COMPARISON OF THE THERMAL AND PRESSURE DROP CHARACTERISTICS OF A CONVENTIONAL FIN BLOCK AND PARTIALLY METAL FOAM EMBEDDED HEAT SINKS

A THESIS SUBMITTED TO
THE GRADUATE SCHOOL OF NATURAL AND APPLIED SCIENCES
OF
MIDDLE EAST TECHNICAL UNIVERSITY

BY

SÜLEYMAN KAANCAN ATAER

IN PARTIAL FULLFILLMENT OF THE REQUIREMENTS
FOR
THE DEGREE OF MASTER OF SCIENCE
IN
MECHANICAL ENGINEERING

SEPTEMBER 2014

Approval of the thesis:

COMPARISON OF THE THERMAL AND PRESSURE DROP CHARACTERISTICS OF A CONVENTIONAL FIN BLOCK AND PARTIALLY METAL FOAM EMBEDDED HEAT SINKS

submitted by **SÜLEYMAN KAANCAN ATAER** in partial fulfilment of the requirements for the degree of **Master of Science in Mechanical Engineering Department, Middle East Technical University** by,

Prof. Dr. Canan Özgen _____
Dean, Graduate School of **Natural and Applied Sciences**

Prof. Dr. Tuna Balkan _____
Head of Department, **Mechanical Engineering**

Assoc. Prof. Dr. Cemil Yamalı _____
Supervisor, **Mechanical Engineering Dept., METU**

Prof. Dr. Kahraman Albayrak _____
Supervisor, **Mechanical Engineering Dept., METU**

Examining Committee Members:

Prof. Dr. Zafer Dursunkaya _____
Mechanical Engineering Dept., METU

Assoc. Prof. Dr. Cemil Yamalı _____
Mechanical Engineering Dept., METU

Prof. Dr. Mecit Sivrioğlu _____
Mechanical Engineering Dept., GAZI

Prof. Dr. Kahraman ALBAYRAK _____
Mechanical Engineering Dept., METU

Assoc. Prof. Dr. Almıla Güvenç Yazıcıoğlu _____
Mechanical Engineering Dept., METU

DATE: 29.09.2014

I hereby declare that all information in this document has been obtained and presented in accordance with academic rules and ethical conduct. I also declare that, as required by these rules and conduct, I have fully cited and referenced all material and results that are not original to this work.

Name, Last name: Süleyman Kaancan Ataer

Signature:

ABSTRACT

COMPARISON OF THE THERMAL AND PRESSURE DROP CHARACTERISTICS OF A CONVENTIONAL FIN BLOCK AND PARTIALLY METAL FOAM EMBEDDED HEAT SINKS

Ataer, Süleyman Kaancan

M.S., Department of Mechanical Engineering

Supervisor: Asso. Prof. Dr. Cemil Yamali

Co-Supervisor: Prof. Dr. Kahraman Albayrak

September 2014, 160 pages

Despite the downsizing of the electronic components, the increase in the power consumption of the electronic components and correspondingly the rise in the loss of power that transforms into heat have given a momentum in the search for different cooling methods for thermal sinks by the thermal engineers. Excessively heated regions that form on the small areas where the heat generating components contact the heat sinks create a thermal resistance for the heat flow from the surface of the component to the chassis and trap the thermal energy. The reasons for the preference of the metal foam for this study are the suitability for the forced convection and the conduction heat transfer methods as well as having a large heat transfer surface area.

In this research, metal foams with 4,8,16 pores/cm aluminium having 93% porosity and copper metal foam having 90% porosity that are integrated into a heat sink with a special geometry was designed and built.

During the process of the experiments, the thermal resistances and the pressure losses of the metal foam integrated heat sinks were tested by applying different heat fluxes and different air speeds to the specimens. Differences in the thermal performances of the heat sinks were observed by enforcing the specially manufactured heaters. In the first part of test scenarios smaller heaters were contacted only to the top side of the

metal foam embedded regions of the heat sink chassis. In the second part of test scenarios the entire top surface of heat sink was heated with longer type heaters.

Within the scope of the experiments, the performances of the designed heat sinks were compared with specially produced fin block which is known as one of the commonly used cooling methods. Experimental results were compared with the results that were obtained from the CFD and interpreted accordingly.

As a result, how much improvement could be achieved was revealed and recommendations were made for the future projects and applications in partial use of metal foam of thermal management. It was observed that partial metal foam utilization is more efficient than a conventional aluminum fin block in thermal management.

Key words: Metal Foam, Soldering Method, Forced Convection, Conduction, Thermal Management

ÖZ

GELENEKSEL KANATÇIKLI BLOK VE KISMI METAL KÖPÜK YERLEŞTİRİLMİŞ ISI ALICILARIN ISIL VE BASINÇ DÜŞÜM KARAKTERİSTİKLERİNİN KARŞILAŞTIRILMASI

ATAER, Süleyman Kaancan

Yüksek Lisans, Makina Mühendisliği Bölümü

Tez Yöneticisi: Doç. Dr. Cemil Yamalı

Ortak Tez Yöneticisi: Prof. Dr. Kahraman Albayrak

Eylül 2014, 160 sayfa

Elektronik komponentlerin küçülmesine rağmen güç tüketimlerinin ve buna paralel olarak komponentlerin ısıya dönüşen elektrik kayıplarının artması, ısıl tasarım mühendislerinin farklı soğutma yöntemleri arayışına hız kazandırmıştır. Isı üreten komponentlerin şaseye temas ettiği küçük yüzeylerinde oluşan aşırı ısıtılmış bölgeler ısıyı hapis eder ve komponent yüzeyinden şaseye gerçekleşen ısı akışına karşı direnç oluşturmaktadırlar. Metal köpüğün hem zorlanmış konveksiyon, hem de iletim ile ısı aktarımı yöntemlerine uygun olması, ayrıca geniş ısı aktarımı yüzeyine sahip olması bu çalışmada tercih edilmesinin nedenleri olmuştur.

Bu araştırmada 4, 8, 16 gözenek/cm yapısında ve %93 poroziteye sahip alüminyum ve %90 poroziteye sahip bakır metal köpüklerin entegre edildiği özel bir geometriye sahip soğutucu bloklar tasarlanmış ve üretilmiştir.

Gerçekleştirilen deneylerde numunelere farklı ısı akıları ve farklı hava hızları uygulanarak metal köpüklerin entegre edildiği soğutucu blokların ısıl direçleri ve basınç kayıpları incelenmiştir. Test senaryolarının birinci kısmında küçük ısıtıcılar sadece soğutucu şasesindeki metal köpüklerin etegre edildiği bölgelerin üst kısmına temas ettirilmiştir. Test senaryolarının ikinci kısmında ise soğutucu blokların üst yüzeyi tamamen uzun ısıtıcılar ile ısıtılmıştır.

Deneyler kapsamında, tasarlanan soğutucunun performansı özel olarak üretilen ve yaygın kullanıma sahip soğutma yöntemlerinden biri olan kanatçık bloğuyla karşılaştırılmıştır. Deney sonuçları HAD'den elde edilen sonuçlar ile karşılaştırılarak yorumlanmıştır.

Çalışma sonucunda metal köpüklerin kısmen kullanımının, ısı yönetiminde ne kadar başarı gösterebileceği incelenerek, gelecek projeler ve uygulamalar için tavsiyelerde bulunulmuştur. Isı yönetiminde, metal köpüğün kısmen kullanılmının, geleneksel aluminyum fin bloğuna göre daha etkili olduğu gözlemlenmiştir.

Anahtar Kelimeler: Metal Köpük, Lehimleme Yöntemi, Zorlanmış Konveksiyon, İletim ile Isı Aktarımı, Isı Yönetimi

To my father & my mother

ACKNOWLEDGEMENTS

I would like to appreciate the recommendation and guidance of Assoc. Prof. Dr. Cemil YAMALI, my advisor. I also wish to thank Prof. Dr. Kahraman ALBAYRAK for his helpful comments and understanding.

An exclusive thank goes to my continuous and major supporter my mother Nuray ATAER and my perfect role model, father Prof. Dr. Ö.Ercan ATAER.

I am also grateful to my former Chief Production Engineer Murat KOÇ for helps on preparing my test specimens, my former commercial manager Zeki Ahmet TEMEL for helps on supplying foam metal materials. I would like to state my special thanks to my former colleagues at MİKES A.Ş. Köksal YILDIZ and Mehmet KAHYA for assistances in my test rig and heat sink installation and production.

I would like to thank my former colleague Senior Mechanical Design Engineer Yavuz DEMIRTOLA for helps on CFD implementation and former Manager Ayşe Hilal ERBAY for thoughtful approaches to my master education. I am appreciated to my officemate Senior System Engineer Sertaç GÜREL, Senior System Engineer Gülkız DOĞAN and Senior Certification Engineer Ayhun ÜNAL for their precious advices on my thesis concept subject.

Finally, I would like to present my thanks to, Mustafa YALÇIN for devoted helps during the experiments.

TABLE OF CONTENTS

LIST OF TABLES

TABLES

LIST OF FIGURES

FIGURES

LIST OF SYMBOLS

A, B, E	simplification coefficients
A_b	base plane area (m^2)
A_{con}	convection area of heat sink (m^2)
A_{cs}	cross section area of duct (m^2)
A_F	frontal area of test specimen (m^2)
A_i	interface area between porous region and clear flow (m^2)
A_0	total heat transfer area of porous fin (m^2)
a	duct channel with (m)
b	duct channel height (m)
b_t	base plane thickness of fin block (m)
$c_{1\epsilon}, c_{2\epsilon}, c_\mu, c_\kappa$	non-dimensional constants
c_p	specific heat of fluid ($J \cdot kg^{-1} \cdot ℃$)
C	form drag coefficient (m^{-1})
D	air width of fin block (m)
D	deformation tensor
D_H	hydraulic diameter of fin block (m)
D_{HF}	hydraulic diameter of duct for foam heat sinks (m)
d_p	pore diameter (m)
e	measurement error
$f_{app.}$	apparent friction
f_k	friction factor
f_σ	Darcy-Weisbach friction factor
H	height of foam specimen (m)
HTC	heat transfer coefficient ($W/m^2 \cdot K$)
$\bar{h}$	average convection heat transfer coefficient ($W/m^2 \cdot K$)
I_f	fan current (A)
I_h	heater current (A)

j^*	Colburn factor
K	permeability of porous zones (m^2)
k_f	thermal conductivity of air at room temperature $(W/m \cdot K)$
k_s	thermal conductivity of solid material of foam $(W/m \cdot K)$
L	length of heat sink (m)
l	length of fin (m)
M	compression factor
$\dot{m}$	mass flow rate of coolant (kg/h)
Nu	Nusselt number
P	pressure of fluid (Pa)
PPI	number of pore per inch
P_{EL}	supplied electric power (W)
p	wetted perimeter (m)
$\dot{Q}$	heat transfer rate (W)
$\dot{Q}_V$	volumetric flow rate (m^3/h)
$\dot{q}_s$	heat flux ($W \cdot m^{-2}$)
R	resultant function
Re	Reynolds number
R_V	viscous term (m^{-2})
R_i	inertial term (m^{-1})
R_{th}	thermal resistance (℃/W)
T_{avgb}	average base plane temperature (℃)
$T_{c,in}$	coolant inlet temperature (℃)
$T_{c,out}$	coolant mean exit temperature (℃)
$\bar{T}$	time averaged temperature.
t	fin thickness of fin block (m)
U_p	pore averaged velocity (m/s)
U	velocity of fluid (m/s)
$\boldsymbol{U}$	superficial velocity in porous zones ($m \cdot s^{-1}$)
U'	fluctuating component of velocity ($m \cdot s^{-1}$)
u_D	Darcy velocity ($m \cdot s^{-1}$)

$\bar{U}$	time averaged velocity
V_{air}	volume of air in metal foam plate (m^3)
V_f	fan voltage (V)
V_h	heater voltage (V)
V_S	volume of metal in metal foam plate (m^3)
V_T	total volume of metal foam plate (m^3)
$\dot{W}$	pumping power (W)
X_T	true value of quantity
x_m	measured value from the device

GREEK SYMBOLS

Δ	change
α	hydraulic conductivity ($m^3 \cdot s \cdot kg^{-1}$)
ε	global porosity of foam metal material
ε_c	porosity of compressed foam metal material
ε_{unc}	porosity of uncompressed foam metal material
ϵ	dissipation rate of turbulence kinetic
$\langle\epsilon\rangle^i$	intrinsic fluid average of ϵ
κ	turbulent kinetic energy per unit mass ($MJ \cdot L^{-1}$)
λ_*	thermal conductivity ratio
μ	viscosity of fluent ($kg \cdot m^{-1} \cdot s^{-1}$)
μ_t	macroscopic turbulent viscosity ($kg \cdot m^{-1} \cdot s^{-1}$)
ν	kinematic viscosity ($m^2 \cdot s^{-1}$)
ρ	density of fluid ($kg \cdot m^3$)
σ_x	normal stress (Pa)
τ_{xy}	shear stress (Pa)
τ_w	wall shear stress (Pa)
Φ	viscous dissipation function (W)
φ	desired porosity
ϕ	surface porosity
Ω^*	foam-finned surface efficiency
ω	uncertainty

SUBSCRIPTS

c	coolant
e	outlet
f	fluid
i	inlet
m	mean
n	n-direction
pm	porous medium
s	solid
V	volumetric
x, y, z	Cartesian directions

SUBSCRIPTS

i	intrinsic (fluid) average

CHAPTER 1

INTRODUCTION

This chapter is an overview of the commonly used electronic cooling methods which have numerous applications. It also contains basic parameters and structure types of metal foam materials encountered in literature. At the end of the chapter the goals of this research are summarized.

1.1. Motivation

Miniaturization of electronic components in the form of integrated circuits (ICs), such as microprocessors, resistors, diodes, plastic leaded chip carriers (PLCCs), *etc.*, increase geometrical complexity of electronic devices in restricted spaces.

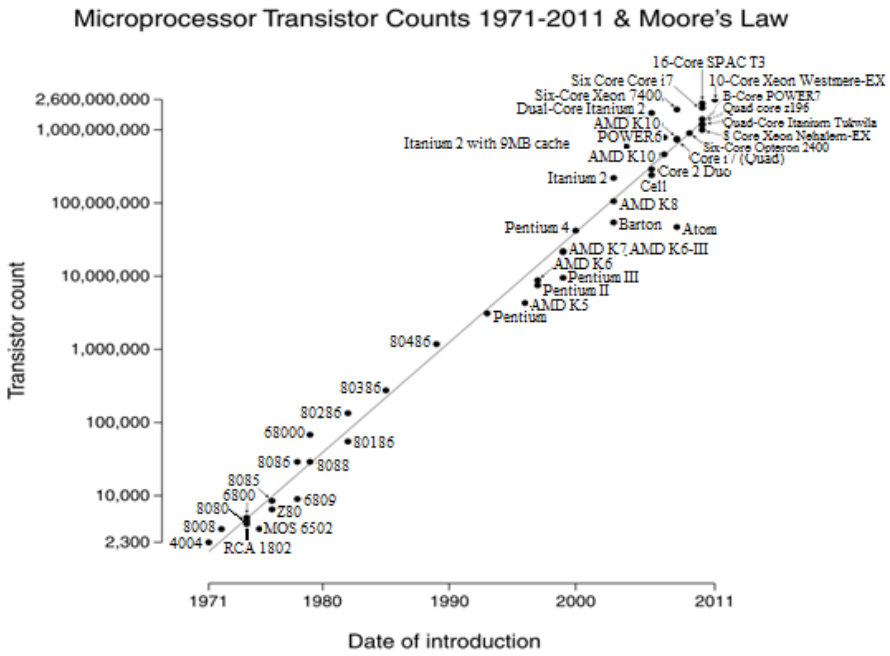

Figure 1.1 Moore's law: Transistor numbers change per years [82]

Gordon Moore, one of the co-founders of Intel, made a prediction about the growth rate of the number of transistors per given area on a die [49, 57].

Known as Moore's law, it specifically predicts the doubling of the number of transistors on a given die area every two years, later updated as 18 months, and has validity on the latest semiconductor fabrication technologies as well. Figure 1.1 demonstrates transistor numbers variation versus years. At the result of this trend, compact and small structured electronic box designs require custom designed cooling systems.

General cooling requirements for electronic devices require spreading of internally generated heat by optimally arranging heat flow paths from source to sink [57]. Otherwise, heat cannot be removed away from the component surface and an uneven temperature distribution profiles, or hot spot(s) occurs [6]. For forming near ideal heat flow paths, thermal design engineers use all three modes of heat transfer; conduction, convection and radiation. Majority of applications use both conduction and convection for cooling electronic assemblies. Electronic devices, especially those used in telecommunications and military systems, can have a mission critical role so they need an uninterrupted power supply to keep data transmission alive which in turn makes a cooling system a must. As another example, jamming operation, an important subfield of telecommunications, provides tactical advantages for military applications. A jammer is an RF (radio frequency) source covering various bands depending on the design and disrupts communication in a given space. This space is basically spherical, with the jammer being at the centre. Diameter of jammed sphere is directly related to the power supply efficiency of jammer.

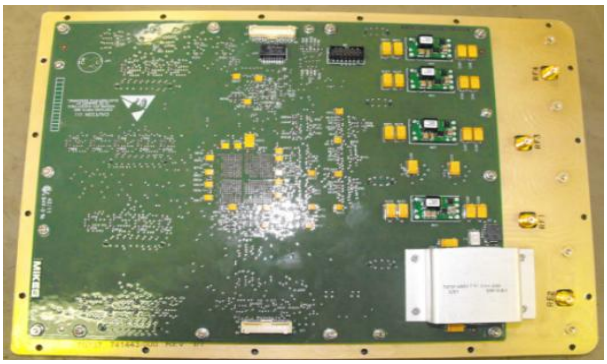

Figure 1.2 RF module of MIKES jammer

In basic terms, jammers have dedicated RF (radio frequency) modules that include digital, analogue, RF PCBs (printed circuit boards) and power supplies for all each band. A cold plate, a traditionally known cooling method, is preferred for RF module cooling. Figure 1.2 shows a photograph of the MIKES jammer's RF module assembly.

Besides, power supplies generally have low efficiencies so most of input electrical energy is converted to heat on their surfaces. If this high heat flux cannot be transferred from the supply surface, mating surface temperature of power supplies reaches the operating temperature limit. Extended use at operating working temperature conditions decrease the overall lifetime of power supplies.

Figure 1.3 Picture of MIKES jammer

Cooling of power supplies directly affects operation and jamming space capacity of jammer. One of the commercial jammer product of MIKES is seen in Figure 1.3. Today's traditional cooling methods are not capable of solving the heating problem of this device. In this study, an alternative high heat dissipation method is examined.

1.2. Overview of Electronic Cooling Technologies

The rate of heat dissipation and the maximum allowable component temperature are basic parameters for adequately comparing cooling techniques [69]. Heat removal rate of component is needed to be high enough through the heat flow so that the temperature of component does not increase to maximum allowable values.

Figure 1.4, taken from Clements [70], demonstrates the wide range of heat removing rates of different cooling fluids and techniques.

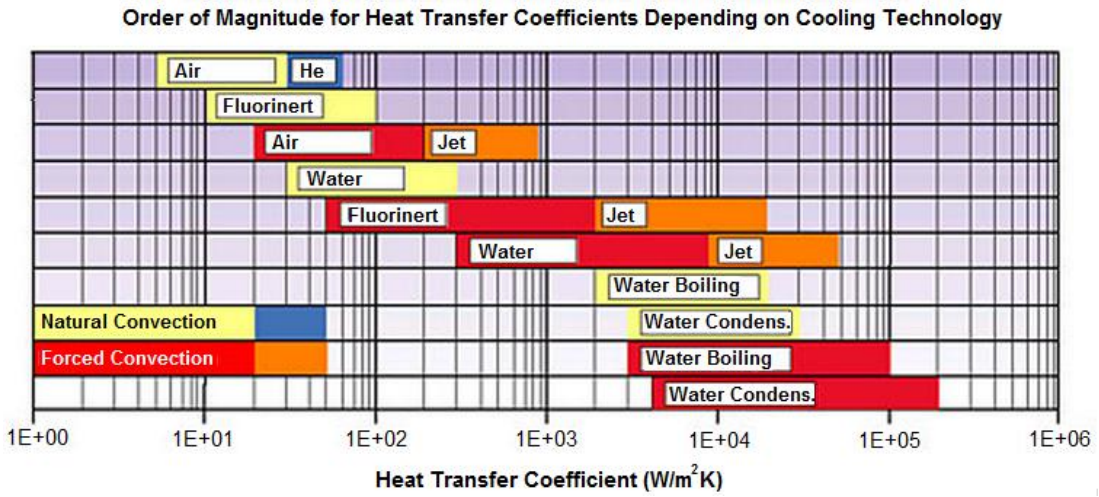

Figure 1.4 Heat transfer coefficient of convection heat removing methods [70]

Figure 1.4 presents cooling capacities of both water and air for natural and forced convection cooling methods. Forced air cooling is the main scope of this study. Of the various ways of removing heat from electronic units, cold plates are generally preferred for military and industrial products. Its basic principle is transferring heat from component surface to metal plates and then spreading heat from metal plate to environment using natural or forced convection. Simple PCB alignment onto the cold plate and heat flow paths are shown in Figure 1.5.

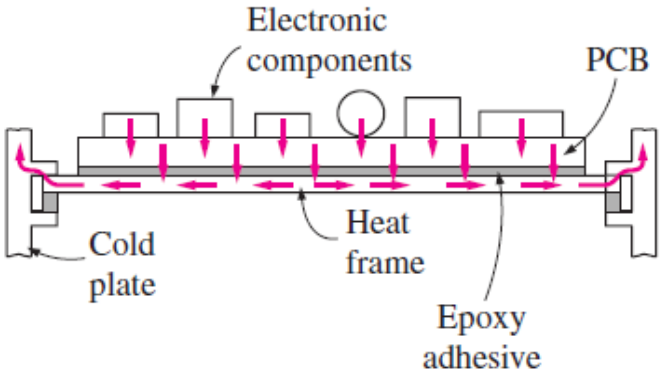

Figure 1.5 Heat flow path inside a cold plate [69]

Conduction capacity is directly related to the metal amount of the cold plate, but weight limits of designs do not permit high metal usage for most applications. In general the design of metal cold plates in natural or forced convection methods employs custom-designed high surface area fins.

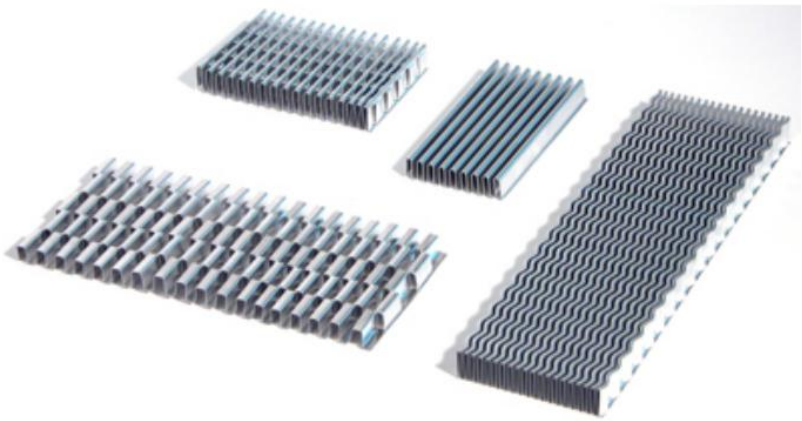

Figure 1.6 Commercial fin products

Fins, used in both natural and forced convection setups, are heat exchangers between electronic unit and environment. As seen in Figure 1.6 there are various commercial custom-design fin types used for various applications. Using such fins with forced air convection, generally a fan-based system can transfer heat at a rate of up to 150 $W/K \cdot m^2$ with admissible noise levels. Another forced air convection type, known as macro jet, has 900 $W/m^2 \cdot K$ maximum heat transfer rate with unbearable high noise level [70]. An example of forced air cooled electronic box is seen in Figure 1.7. In this example air is sucked by fans from electronic components section to finned zones of box.

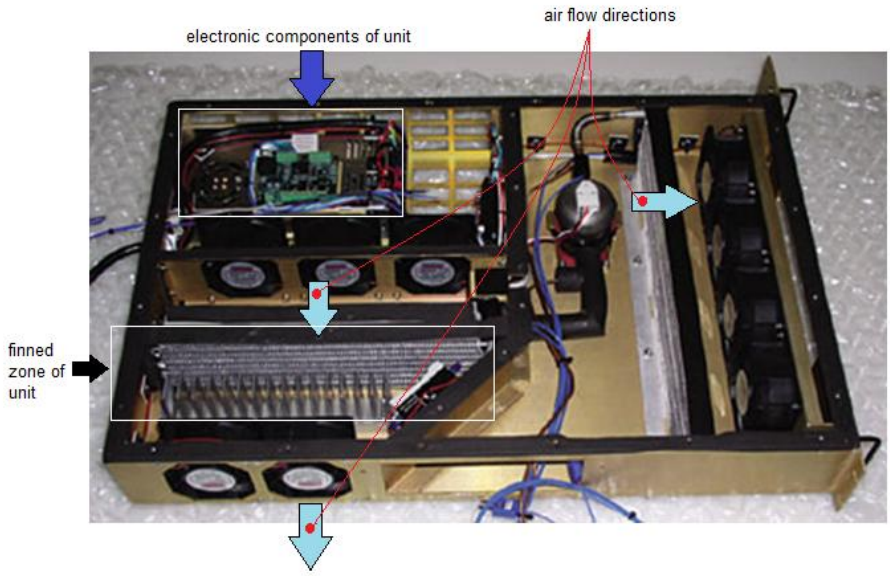

Figure 1.7 Air convection cooled electronic box

One of the alternative cooling methods is micro-fluidic systems, used within the last 20 years in scientific applications [72, 74]. High surface area of micro channels provides better heat transfer values. Therefore, micro channels have lots of application area, i.e. biomedical systems, telecommunication devices, and aerospace industries [75].

Miniaturization process in microelectronics results in brings about high heat flux rates of around 100 W/cm^2. In micro channel applications, liquids which have heat absorbing performance better than gasses are preferred [73]. Figure 1.8 shows scale of micro channels with noticeably smaller dimensions compared to traditional cooling methods.

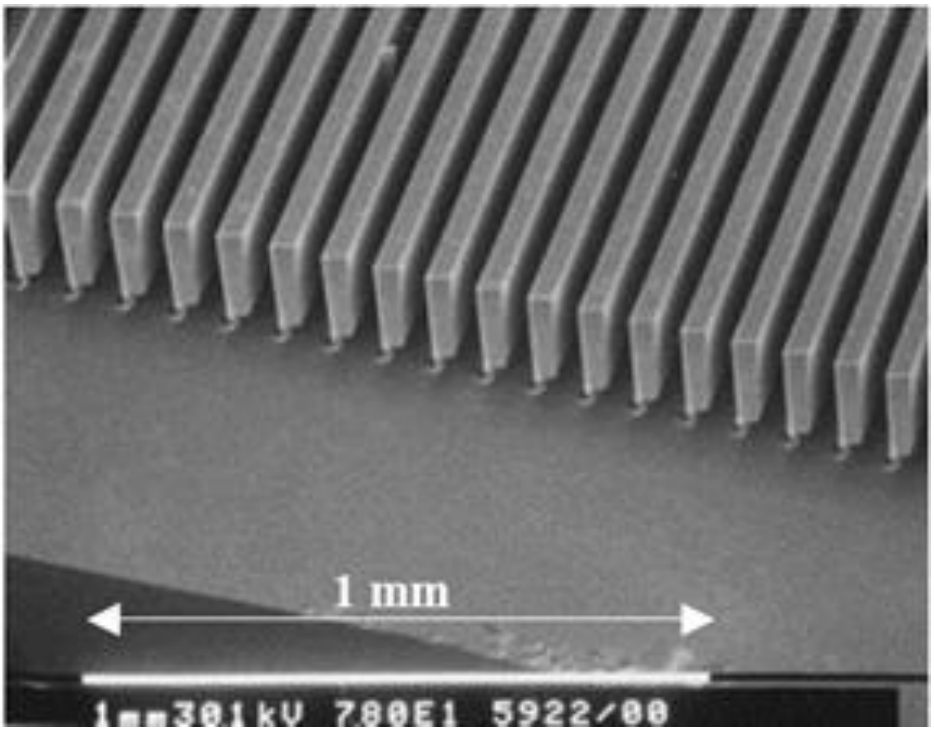

Figure 1.8 Picture of microchannel [71]

Today's established ways of heat spreading heat pipes have lots of commercial applications. Structurally, a heat pipe is made up of a liquid trapped in a metal tube using wick material as shown in Figure 1.9. Heat pipe performance depends on selected working liquid inside and the structure including the wick material. There are various working liquids for heat pipes; water, helium, nitrogen ammonia, sodium and lithium to count a few.

Working principle of a heat pipe is based on condensation and evaporation. One tip of the pipe directly reaches the heat removal surface; hence the working fluid evaporates and starts moving from inside of wick material due to capillary pressure. The other tip of the pipe is in colder conditions so that the vapour condenses and the cycle repeats.

As wick material aluminium, brass, copper and nickel could be used, depending on the design. Heat pipe with water as working fluid has about a hundred times higher thermal conductivity than copper at operating condition of 150^{o}C [59]. High thermal conductance, acting as a thermal flux transformer and low thermal impedance with isothermal surfaces are main advantages of heat pipes.

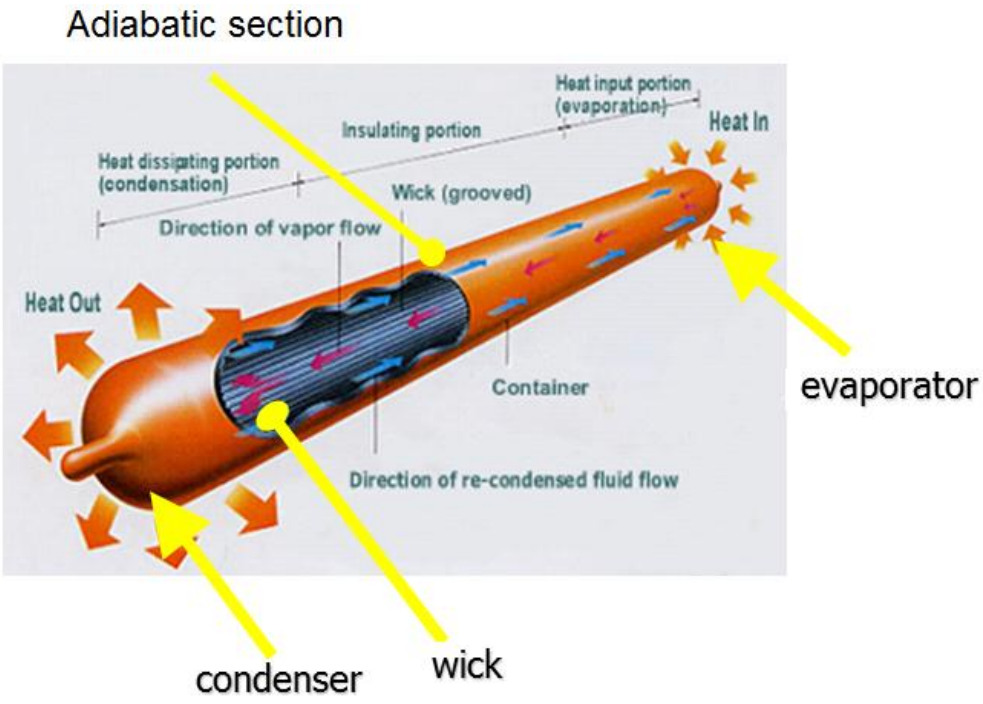

Figure 1.9 Heat flow direction inside the heat pipe

Untraditional materials known as reticulated metal foams (RMFs), have been looked into as potential heat sink materials for the last twenty years. RMFs have higher surface areas together with low densities in comparison to traditional metal heat sinks. Heat removing capacities of RMF's range from 6 W/K·cm^2 (for air as working fluid) to 48 W/K·cm^2 (for water as working fluid) applications.

RMF-based heat sinks are used in certain military applications like inverter-converter controls (ICC) and battery-power converters (BPC) [29]. The main reason of choosing RMFs for forced convection is their serpentine paths that cooling fluid passes and mixes. Therefore heat transfer between fibers of RMFs and cooling fluids is enhanced [68]. RMFs are employed in various heat transfer management applications such as compact heat sinks, heat exchangers for aviation equipment, air cooled condensers and heat shields [58].

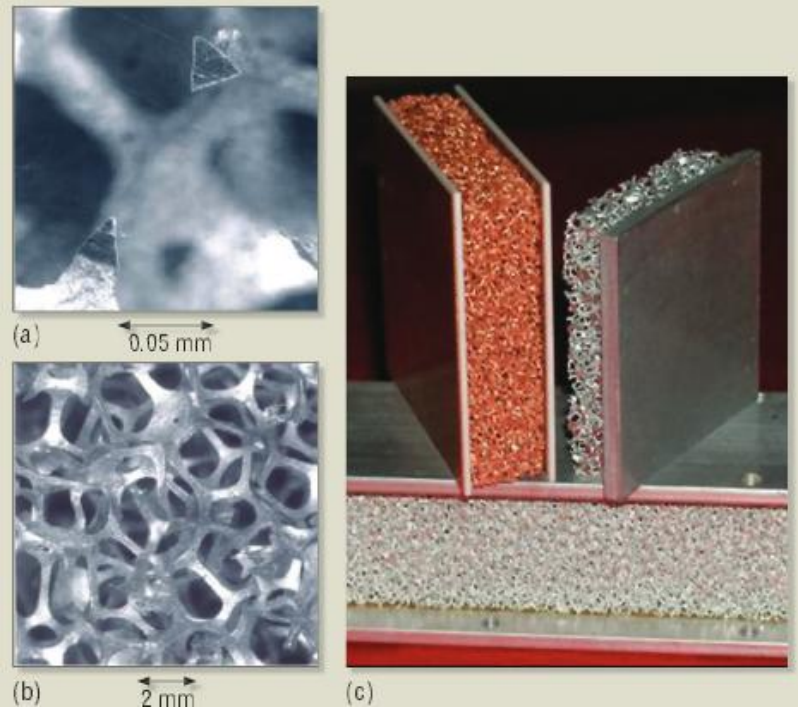

Figure 1.10 Brazed samples of RMFs [29]

Benefits of RMFs include lighter chassis weight, increased forced convection capacity, high heat transfer area per unit volume and machineable structures. Embedding RMFs into a cooling system, which is critical for heat flow on junction areas, is accomplished by soldering or brazing as shown in Figure 1.10 [28]. If RMFs and metal plates of heat sink do not make perfect mechanical contact, heat resistances occur against the heat flow.

1.3. Metal Foam Structures and Applications

Metal foam is classified structurally by cell topology (open cells, closed cells), relative density, cell shape, cell size and anisotropy [58].

Liquid content is another parameter that categorizes foams as dry or wet. Dry foams typically have less than 1 percent liquid content whereas wet foams' liquid fraction may reach 50 percent or higher. Fig. 1.11 shows an example of a dry foam structure.

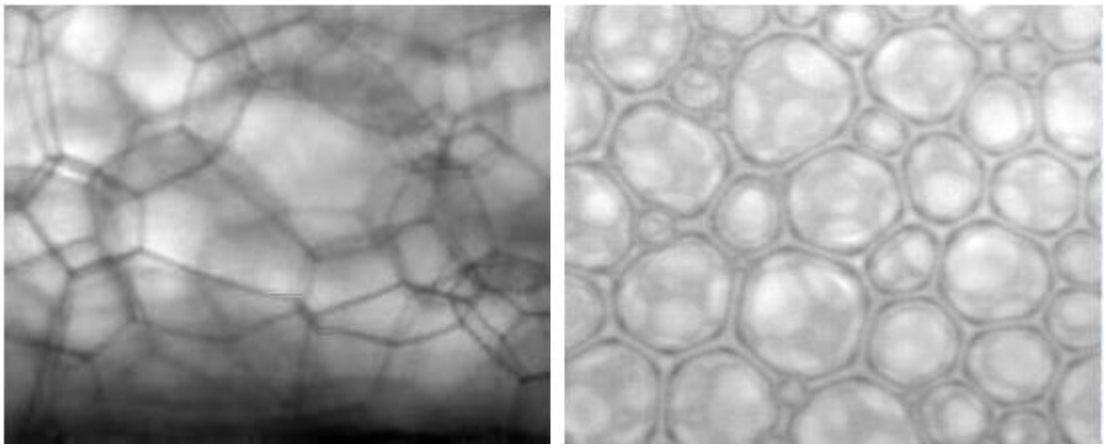

Figure 1.11 Dry foam structure [58]

Closed cell foams have continuous cell walls which separate two different cells completely so that sealed cell compartments are obtained in the foam structure [10]. Cells of closed foam are seen in Figure 1.12.

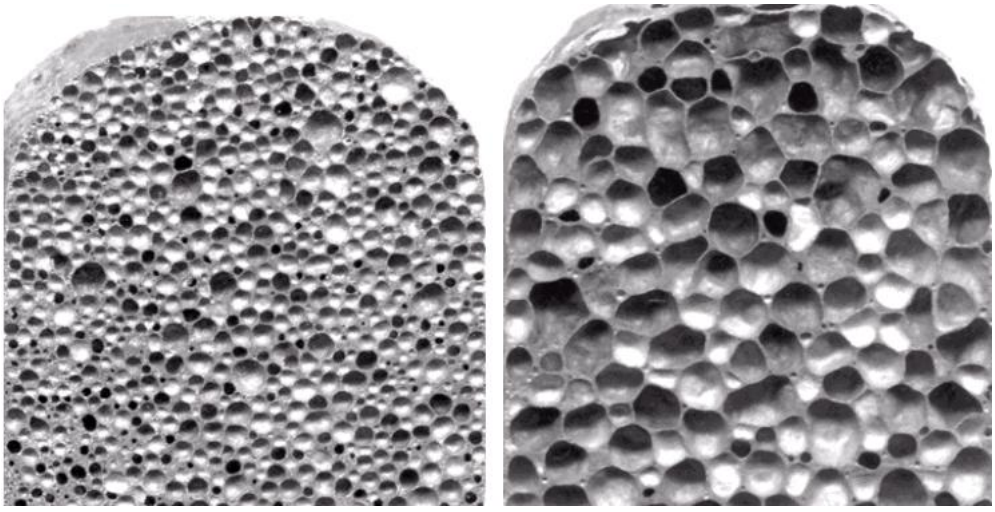

Figure 1.12 Closed cell metal foam structure [58]

Open cell foams (OCMF) exhibit a fibrous structure that has pathways between neighbouring cells so that fluid can easily flow through these pores.
Based on the usage, metal foams can be made from various metals as seen in Figure 1.13.

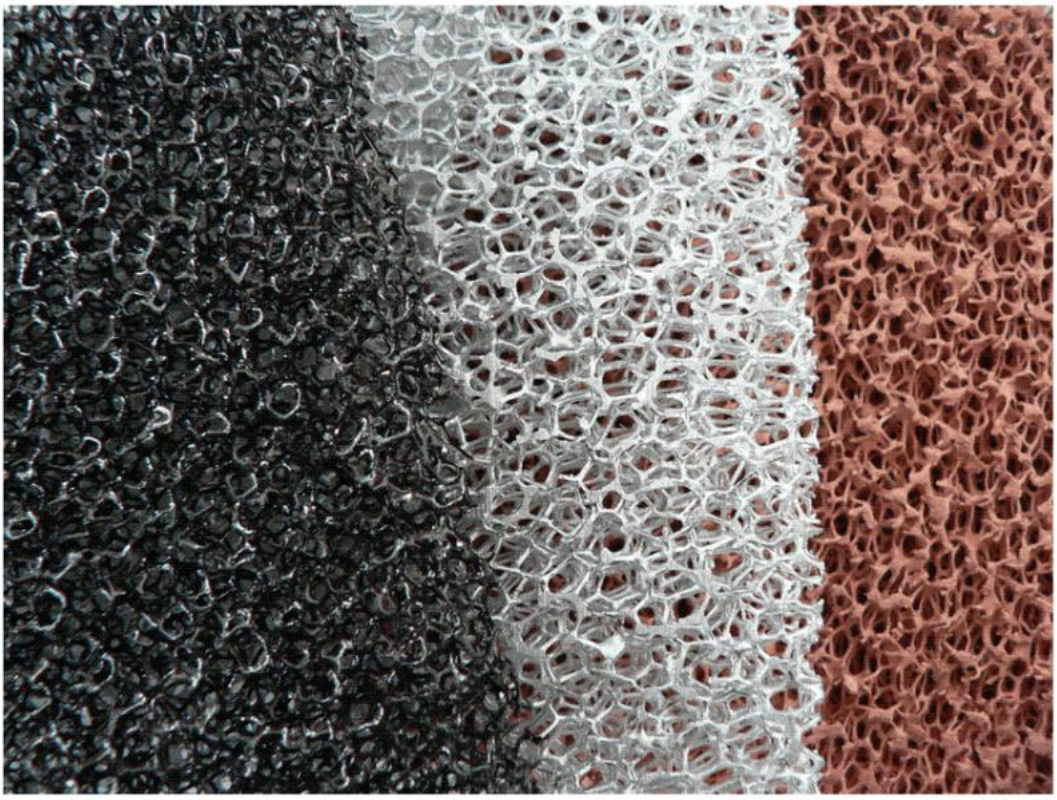

Figure 1.13 Open cell metal foam structure

Due to this open cell structure metal foams have some benefits listed below;

- OCMFs have greater surface areas ranging from 500 m^2/m^3 to over 1000 m^2/m^3 [7],
- Heat dissipation from hot spots into the cooling fluids increases by using OCMFs,
- OCMFs are lighter than other heat removing structures such as fin blocks,
- The base materials of OCMFs can be chosen from copper and aluminium which have higher thermal conductivities.
- OCMFs are amenable to soldering and brazing procedures such that custom made heat sinks can be produced.

1.4. Production Techniques of Metal Foam

In general, metal foam production has nine different manufacturing methods that can be listed as [58]:

1. Gas addition inside the molten Al, Mg alloys,
2. Mixing molten metal with gas-releasing particles during cooling. [Al]
3. Strengthening metal powder with gas-releasing particles. [Al, Zn, Fe, Pb, Au]
4. Building ceramic mold with polymer or wax precursors and then pressure compression onto the molten metal though the ceramic mold. [Al, Mg, Ni-Cr, stainless steel, Cu]
5. Electrodepositing of open cell polymer foams with nickel carbonyl, followed by vacuuming. [Ni, Ti]
6. Titanium powders with entrapped inert put into the titanium housing then rolling and heat treatment applied onto the titanium housing. Finally titanium sandwich panels, used by Boeing, obtained. [Ti]
7. Binding hollow spheres together using sintering. [Ni, Co, Ni-Cr alloys]
8. Pouring liquid metal onto the leading particles. [Al]
9. Eutectic solidification of hydrogen dissolved liquid metals. [Cu, Ni, Al]

Above production techniques create metal foams of materials that were noted in brackets.

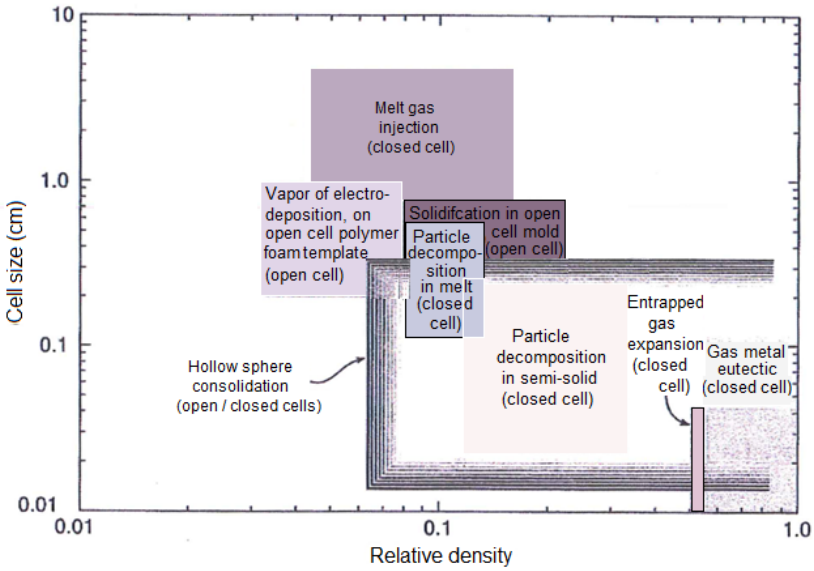

Figure 1.14 Density and cell size ranges of different metal foam manufacturing methods [58]

Producible cell size of metal foam production techniques are presented in Figure 1.14. Open cell metal foam specimens of this research were produced by ceramic mold with polymer or wax precursor manufacturing technique.

1.5. Objective of the Research

The main aim of this work is to investigate the thermal effectiveness of foam embedded heat sink for electronic cooling compared to the conventional techniques like a fin block. In this study, metal foam is used as a heat spreader for relieving heat flow paths. Based on related literature, a block shape is selected as foam specimen geometry. In this study, foam in the form of staircase is soldered at two different locations in the form of staircase as shown in Figure 1.15. This geometry simulates the two adjacent excessively heated hot spots situation which is an undesirable scenario of electronic box designs. The reason of using a second foam section at the downstream side is to observe the heat transfer performance of metal foams when high temperature air is forced for spreading heat from metal foam surface. Staircase alignment of foams increases the amount of metal in the downstream direction which provides higher heat capacity.

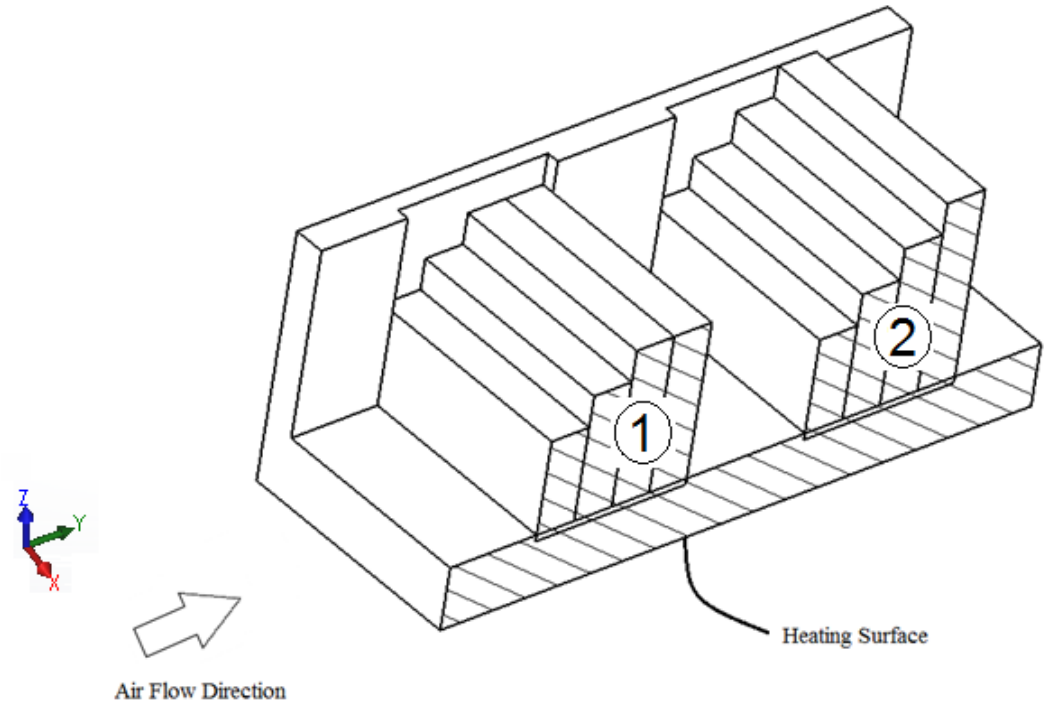

Figure 1.15 Foam embedded heat sink specimen

In the next chapter, literature survey of metal foam structures is summarized. Preparation of metal foam embedded heat sink processes are explained in Chapter 3, where a novel way of coating copper and tin metal foam materials is introduced. The test section of setup on testing is designed in a way similar to Dukhan's test apparatus [37, 38]. Parts and equipment of designed test apparatus and foam materials' physical properties are described in Chapter 4. Definition of variables, experimental results, and experimental errors obtained are also presented in this chapter. Similar experimental scenarios are modelled in CAD software and then imported to commercial FLUENT software. Porous zone equations, required parameter calculations of commercial FLUENT software are specified in Chapter 5. In the scope of this study, thermal performances of custom designed partially metal foam embedded heat sinks are compared with the thermal performance of conventional fin block of current MIKES jammer. Finally, experimental results are compared with commercial software outcome and literature results in Chapter 6.

CHAPTER 2

LITERATURE REVIEW

This chapter reviews experimental and numerical studies about heat dissipation and pressure drop of metal foams. Studies were examined in the following sections and detailed in tables.

2.1. Experimental Heat Transfer Research in Metal Foams

Although studies given in this section involve pressure drop calculations, their priority is examining thermal performance of porous structured metal foams.

Firstly, Kamath et al. [5] tested thermal conductivity and pressure drops of different thickness 10 and 20 PPI aluminium and copper foams. Two distinct properties of this study are locating testing channel of foams as vertical, and not using any permanent joint method. Screws were used for compressing the heater between foams and insulator wooden boxes that cover the outer surface of foams. Kamath calculated the permeability and drag coefficient using Hazen-Dupuit-Darcy equation.

$$\frac{\Delta P}{L} = \frac{\mu}{K}\mathrm{U} + \rho C U^2 = \mathrm{A}U^2 + \mathrm{BU} \tag{2.1}$$

In Equation 2.1, ΔP is pressure drop through the foam sample, L is the length of heat sink, μ is the dynamic viscosity of fluid, K is the permeability of metal foam sample, U is the velocity of fluid, C is form drag coefficient, ρ is density of fluid and A, B are simplification coefficients for fitting experimental results onto the second degree polynomial. In this study investigators used air as working fluid and inlet velocities of air varied between 0.4 m/s to 3 m/s. Test specimens had thicknesses varying from 10 mm to 30 mm and 0.95 porosity copper foams with 0.87 porosity aluminium foams. Test measurement ranges of heater and fan were 10 to 100 W and 6 to 250

Pa., respectively. Seven K-type thermocouples were located on cork wall for comparing temperature values of test specimens and empty channels.

Reynolds number (Re) and aspect ratio have a dominant effect on the Nusselt number (Nu), as shown in Equation 2.2.

$$\mathrm{Nu} = 9.353\lambda_*^{0.0385}\left(\frac{L}{H}\right)^{-0.887}\mathrm{Re}^{0.446} \tag{2.2}$$

In Equation 2.2, H is the height of foam specimen and λ_* is the thermal conductivity ratio of solid to fluid. They conclude this research with two main inferences as follows:

- Metal foams' heat transfer is 2.6 to 3.8 times higher than empty channels.
- Copper foams have %4 more heat transfer ratio than aluminium ones but due to high cost of copper foams, aluminium ones are more preferable.

Mancin et al. have four studies about metal foams and three of them mainly consider heat transfer enhancement of metal foams [3, 24, 25 and 26]. One of his studies [26] examined pressure drop only in aluminium foams which will be investigated in the next chapter.

Mancin et al. [3] calculated heat transfer coefficients of 5, 10, 20 and 40 PPI copper foam blocks whose porosities change between 0.905 and 0.934. In this research, they selected 25, 32.5 and 40 kW/m^2 thermal loads with 0.0055 and 0.0125 $\mathrm{kg/s}$ air mass flow rates for testing samples. Test specimens were compared with their mean wall temperatures, pumping power and interstitial heat transfer coefficient values. Whereas, inlet and outlet temperatures are measured with five T-type thermocouples for each sample, foam brazed copper base plane temperatures are measured with six T-type thermocouples located on bottom and top plate of each sample. Authors fit empirical data to an Equation as given in Equation 2.3 for finding A and B coefficients for each of foam specimens.

$$HTC = A.\dot{m}_f^B \tag{2.3}$$

In Equation 2.3, HTC is the heat transfer coefficient of each sample and $\dot{m}$ is the mass flow rate of coolant. In summary, this research supports that using copper foams for thermal management is an achievable method for electronic cooling.

Mancin et al. [24] compared heat transfer performances and pressure gradients of two distinct heighted 20 PPI aluminium foams. Thermal loads of experimental set up

are 25, 32.5 and 40 kW/m^2 which is similar with previous study [3] given above. 20 mm and 40 mm height, 20 PPI aluminium foams are tested with air mass velocity from varying 2.5 to 7.5 kg·m^{-2}·s^{-1}. They demonstrate empirical data in charts of showing changes of global heat transfer coefficient with air mass velocity for 0.93 porosity samples. This research team selected a model for air flow through porous zones. The model is defined as Forchheimer - extended Darcy (Hazen-Dupuit-Darcy) Equation shown in equation 2.4.

$$\left(-\frac{dP}{dz}\right) = \frac{\mu.\mathrm{U}}{K} + \frac{\rho.C.\mathrm{U}^2}{\sqrt{K}} = \frac{\mu.\mathrm{U}}{K} + C.\rho.\mathrm{U}^2 \tag{2.4}$$

In Equation 2.4, P is the measured pressure of fluid. Hazen-Dupuit-Darcy equation is used in their other researches [25 and 26] as well. Results of developed model support the experimental study of both test specimens. There is no relation between heat flux and heat transfer coefficients. Finally, results show that the heat transfer performance of 20 mm height sample is higher than that of 40 mm height sample.
Mancin et al. [25] investigated heat transfer characteristics of seven 5, 10, 20 and 40 PPI aluminium foam samples with particular porosities. In this study, similar equation used with previous examined investigations like; experimental data fitting to Equation 2.3 and coefficients determination. Experimental test rig of this study is exactly same with previous researches [3 and 24]. Some conclusions of these studies are given as follows:

- HTCs of foam samples increase 1.3 to 1.7 times with decreasing porosity.
- Temperature diminishes exponentially with the displacement from the heated surface.
- Mean wall temperature is crucial parameter for comparing tested samples.
- At higher air inlet velocities, HTCs of aluminium foam samples increase and importance of foam thickness decays.

Dukhan et al. [37 and 39] studied thermal performance of 10 PPI and 20 PPI metal foam heat sinks. Both studies measured temperature from holes inside of the aluminium foam samples. Researchers provided a model for predicting thermal behaviours of metal foam heat sinks. Samples were brazed onto the base heating

plates for eliminating contact resistances. Significant difference between two studies is the directions of measured temperatures of samples. The earlier research of Dukhan [39] obtained one-dimensional heat transfer approach but newest one [37] produced two dimensional approach for convection/conduction of open cell metal foams.

Results of articles are summarized as follows:

- Temperature profiles measured are almost same with the analytically calculated ones.
- 2D convection/conduction model obtained of open cell metal foam is verified with experimental results.

Ateş [7] compared thermal and hydrodynamic performances of microchannel and aluminium metal foam heat exchangers. In his study, microchannel heat sinks with four different channel width and aluminium foam heat sinks with three different pore densities were tested. Some of aluminium foams were compressed with 2 and 3 compressed factor by a special jig. Properties of preferred aluminium foams were 10, 20 and 40 PPI with 92% porosity. Heat exchangers of twelve separate characters were classified with respect to their thermal resistances and pumping powers.

Results of this study summarized as follows:

- Compressing operation increased the performance of foam heat sinks to microchannel levels.
- Although the microchannel heat exchangers with a 300 micron and 420 micron channel width both performed better than metal foam heat sinks, their production cost make compressed aluminium foams a competitive alternative.

Hernandez [31] researched 6101-T6 aluminium foams under the three headings: Fluid flow and pressure drop, forced convection and thermal management. First of all, various porosity and pore density foams were tested in the air duct. Whereas, air velocities were measured from seven different sections of foams, pressure values were measured only at the inlet and outlet of samples. Secondly, heat transfer performance of 10 PPI, 20 PPI and 40 PPI aluminium foams were tested by a 40 W heater. Base plane temperatures were measured from three separate sections of

samples. Lastly, he compared Nusselt numbers, thermal resistances and convection coefficients of aluminium foams with commercially available fin type heat sinks. At the end of this comprehensive study, he reached results below:

- Permeability of specimens decreases with pore density and porosity.
- Base plane temperatures of samples decreases with increasing air velocity.
- Metal foam heat sinks have lower thermal resistances than commercial fin arrays.
- Foams type heat sinks have almost half of commercial heat sinks' weight.

Boomsma et al. [1, 9, and 10] performed lots of researches about compressed and uncompressed aluminium foams' thermal and hydraulic performances. Boomsma prepared an elaborative study which involves twelve test specimens as in Table 2.1. All open cell metal foam samples were made of 6101-T6 aluminium.

Table 2.1 Characteristics of Boomsma's test specimens [10]

Compressed Foam Physical Data

Foam	Compression	Name	Expected Porosity [%]	Measured Porosity [%]
5%	2	95-02	90.0	88.2
	4	95-04	80.0	80.5
	6	95-06	70.0	68.9
	8	95-08	60.0	60.8
8%	2	92-02	84.0	87.4
	3	92-03	76.0	82.5
	4	92-04	68.0	76.1
	5	92-05	60.0	72.2
	6	92-06	52.0	66.9

Uncompressed Foam Physical Data

Foam	Pore Diameter [mm]	Specific Surface Area [m^2/m^3]	Measured Porosity [%]
10 PPI	6.9	820	92.1
20 PPI	3.6	1700	92.0
40 PPI	2.3	2700	92.8

Expected porosity of compressed open cell foams were calculated from Equation 2.5. M designates the compression factor which is ratio of the height of uncompressed foams to the height of compressed foams, ε_c is the porosity of compressed foam metal materials and ε_{unc} is the porosity of uncompressed foam metal materials.

$$\varepsilon_c = 1 - M(1 - \varepsilon_{unc}) \tag{2.5}$$

Foams were compressed from 95% and 92% porosity 40 PPI aluminium foams which can be understood from the names of samples. For example, 95-08 indicates 95% porosity with compression factor of 8 as in Table 2.1. During these investigations, Boomsma evaluated hydrodynamic and heat behaviour of these samples.

Results of studies interpreted as follows:

- Rise of compression factor increases the pressure gradient of compressed samples.
- Experimental results of open cell aluminium foams slightly deviate from Darcy's law.
- Initial porosity of compressed foams, 95% and 92%, does not have remarkable effect on the permeability of specimens.
- At the constant porosity, decreasing pore diameter increases the flow resistance of uncompressed samples.
- Various flow regimes provide distinct permeability and friction coefficient values.
- Open cell aluminium foam heat exchangers decrease the thermal resistance to almost half of current used heat exchangers.

Whereas Bhattacharya et al. [8] found design parameters of RVC (reticulated vitreous carbon) and aluminium foam samples, Peak et al. [14] generated same parameters for only aluminium foam samples. Both studies evaluated thermal conductivity, permeability and inertial coefficients of test specimens. Similar thermal conductivity values were obtained by both researches. It is obvious that, thermal conductivity of RVC samples were too low with respect to aluminium ones. The orders of calculated permeability and inertial coefficient values of studies were proved each other. Results from these two studies are given below.

- At the same pore density, decreasing of porosity increases the thermal conductivity of aluminium foam samples.
- There is a little effect of pore density on the thermal conductivity of metal foams at the same porosity samples.
- Both studies have own specific friction factor as given in articles [8 and 14].

Kim Y. [21] and Calmidi [16] investigated convection heat transfer performances of aluminium foam matrices. In both studies, changes of Nusselt numbers with respect to Reynolds numbers were calculated for all aluminium samples. Kim Y. [21] tested the convective heat transfer characteristic of aluminium foam under the asymmetrically heated channel by a hot bath. Calmidi [16] tested seven distinct aluminium specimens which had various porosity values with three pore density. An analytical model stated and modified for thermal conductivity of metal foams in Calmidi's previous studies, was reproduced in this research.

In the result graphs showed that analytic model and experimental results were substantially matched each other. Authors stated their results as follows:

- At the lower permeable foams, not only the friction factor increases to a higher value but also Nusselt number has significant improvement [21].
- High conductivity of metal foams provides excessively low thermal dispersion in the foam air combination [16].

The goal of Nawaz et al. [47] study is utilization of 10 PPI aluminium 0.93 porosity foam heat exchangers instead of conventional aluminium brazed fins. Aluminium foam is joined to base plane by polysynthetic thermal compound which has 5 W/K·m for base plane. This chemical has lower thermal conductivity compared to Lead-Tin solder paste type joining material (k = 39 W/K·m) [2] which is used in this thesis and detailed in Chapter 4. Empirical results of Nawaz's study [47] are compared with the Camidi's analytical model [16]. As a result of the study, author state that metal foams could be used as a compact heat exchanger if ideal geometry and flow conditions were provided.

Mahjoob and Vafai [27] categorized literature researches about metal foam heat exchangers as follows: Micro structural based correlations for metal foam heat exchangers, metal foam tube heat exchangers, metal foam channel heat exchangers. The purpose of this study is to obtain Nu, Re and pressure drop correlations for each category. The main inference of this study is that inserting metal foam into the tube or channel considerably increased the performance of metal foams.

Finally, Table 2.2 summarizes selected metal foams heat transfer studies. Comprehending all these studies in terms of their goals, their ways of selecting heater values, coolant fluids, pressure ranges and coolant velocities encouraged the author of this thesis to perform a different metal foam embedded heat sink design research. This study is given in detail in Chapter 4.

Table 2.2 Comparison table of open cell metal foams' heat transfer researches

Researchers (Ref. No):	Goal of Research:	Tested Heat Fluxes:	Pressure Range:	Fluid:	Fluid Velocity / Mass Flow Rate:	Geometry:	Material & Properties of Test Specimens:	Assumptions & Approaches:	Year:
Kamath et al. [5]	Comparing heat transfer rate of metal foams w.r.t. empty channel.	10-100 W	6-250 Pa	Air	0.4-3 m/s	250 x 150 x (10,20,30) mm^3	10 and 20 PPI Aluminium and Copper	Contact resistance is negligible	2012
Mancin et al. [3]	Comparing heat transfer coefficient of different PPI copper foams.	25, 32.5 and 40 kW/m^2	7 Bar	Air	2.5-5 m/s	100 x 100 x 20 mm^3	5, 10, 20 and 40 PPI copper foams	Ideal gas assumption for air.	2011
Mancin et al. [24]	Comparing heat transfer coefficient of 20 mm and 40 mm thickness 20 PPI aluminium foams	25, 32.5 and 40 kW/m^2	0-10000 Pa/m	Air	2.0-5.0 m/s	100 x 100 x (20,40) mm^3	20 PPI Aluminium with 0.93 porosity	Forchheimer - extended Darcy (Hazen-Dupuit-Darcy) Equation	2011
Mancin et al. [25]	Determining & comparing HTC of seven different open cell aluminium sample foams	25, 32.5 and 40 kW/m^2	No range defined	Air	2.0-5.0 m/s	6 of samples 100x100x40 mm and last is 100x100x20	5, 10, 20, 40 PPI Aluminium foams with various pore densities	Forchheimer - extended Darcy (Hazen-Dupuit-Darcy) Equation	2010
Dukhan et al. [37]	Providing a circa model for predicting thermal behaviours of aluminium foams	2.99 W/cm^2	Press. trans. ranges: 0-2487 Pa & 0-746 Pa	Air	2.71 m/s for 10 PPI %69.8 porosity 2.50 m/s for 10 PPI %79.6 porosity 2.79 m/s for 20 PPI %78.2 porosity	3 identical sample 10.16 x 10.16 x 5.8 cm^3	10 & 20 PPI 6101-T6 Aluminium(different porosity)	Arpaci's conduction Analysis, Forchheimer - extended Darcy flow model & conservation of energy equations	2007
Dukhan et al. [39]	Obtaining 1D heat transfer approach for metal foam samples.	6-7 W/cm^2	4.1-41.5 Pa	Air	4-17.7 m3/min	101.6 mm x 241.3 mm x 50.8 mm	10 PPI 6101-T6 Aluminium	Fourier's law, Newton's law of cooling	2005
Nawaz et al. [47]	Examination of metal foams availability as a replacement of conventional fins	20 kW	0-1400 Pa	Air	0.6-4.3 m/s	200 mm x 15 mm x 15 mm	6101-T6 Aluminium10 PPI with 0.9272 porosity	Calmidi and Mahajan model for heat transfer coeff., Bhattacharya for pressure gradient	2010
Boomsma et al. [1, 9, 10]	Selection of most efficient aluminium foam heat exchanger by using hydraulic characterization and heat transfer performances.	1100 W (688 kW/m^2)	0 - 3.2 bar	Water	0-2 m/s	40 mm x 40 mm x 20 mm (compressed) 12 mm x 38 mm x 80 mm (uncompressed)	40 PPI 0.92 and 0.95 porosity compressed and 10 PPI, 20 PPI, 40 PPI 0.92 porosity uncompressed (6101-T6 aluminium)	Darcy, Hazen and Ergun approaches were mentioned.	2002

Table 2.2 (Continued)

Bhattacharya et al. [8]	Empirical research for specifying effective thermal conductivity, permeability and inertial coefficients of twelve aluminium foams and fifteen RVC foams.	Not given	0-6.25 mm w.c. (about 65 Pa)	Air & Water	Not given	7.5 cm x 7.5 cm x 4.38 cm (RVC) 62,5 mm x 43,75 mm x 192,5 mm (aluminium)	Aluminium and reticulated vitreous carbon (RVC) above 90% porosity with 5, 10, 20, 40 PPI pore destiny.	Analytical model of Calmidi and Mahajan	2001
Kim et al. [21]	Observing convection performance of aluminium foams in an asymmetrically heated channel.	Hot bath used defined but not detail is given	3 atm compressed air	Air	1.1-5.4 m/s	90 x 188 x 90 mm	10, 20, 40 PPI Aluminium6101 alloy foams with 0.92 porosity	Forchheimer - extended Darcy (Hazen-Dupuit-Darcy) Equation	2000
Peak et al. [14]	Thermal conductivity, permeability and Ergun coefficient of aluminium samples were generated.	heating surface regulated at 50 ^{o}C	0-1600 Pa	Air	0-4 m/s	90 x 190 x 9.1 mm	Aluminium alloy 6101 0.65, 1.25, 2.50 pore diameter with 0.89-0.96 porosity range	Darcy, Hazen and Ergun approaches were mentioned.	2000
Calmidi et al. [16]	Evaluation of harmony of numerical and empirical calculations of Nusselt number.	15-35 W	Not given	Air	Not given	63 x 45 x 196 mm	10, 20, 40 PPI Aluminium6101 alloy foams with 0.92 porosity	Volume-averaged momentum equation for fluid flow in porous media	2000
Ateş [7]	Comparison of heat exchanger performances of microchannel heat sinks and metal foam heat sinks.	60 W	(0-1.1) x 10^4 Pa	Water	0-1.4 m/s	31,9 mm x 14 mm x 14 mm (for foams) 31,9 mm x 14.1 mm x 4 mm (for micro channels)	10, 20, 40 PPI uncompressed and compressed Aluminium6101-T6 metal foams with various porosities & 300, 420, 500 and 900 micron channel width microchannel heat sinks	Modified Darcy Law	2011
Hernandez [31]	Pressure drops, convection coefficient and thermal performances of aluminium foams were compared to each other and to commercial fin arrays.	40 W	15.9 - 472.6 Pa	Air	0.64 - 4.12 m/s	9.875 x 4 x (2-4) (inches)	10, 20, 40 PPI, Aluminium alloy, 6101-T6, various porosities metal foams	Hazen-Dupuit-Darcy Equation	2005

2.2. Experimental Fluid Flow Research in Metal Foams

Bonet, Topin and Tadrist studied flow in porous media and they test dozen of foam samples from different metal or alloys (Cu, Ni, Ni-Cr) [43]. Air and water are used as a working fluid with velocity ranges from 0 to 20 m/s and from 0 to 0.1 m/s, respectively. Their main concern is investigating compressibility and pore size effects on flow field. The pressure values of various pore sized metal foams are measured by twelve pressure sensors located on top side of the test section, through the main flow axis. At high velocity flow fields, the variation between the pressure and the velocity does not linearly change, so the empirical Forchheimer equation is used for high Reynolds flows.

$$\rho \frac{dP(z)}{dz} = -\left(\frac{\mu}{K}\dot{m} + C\dot{m}^2\right) \tag{2.6}$$

From Equation 2.6, pressure occurs from two terms: The one is the viscous term ($\frac{\mu}{K}\dot{m}$) which is same with Darcy equation and the second is the inertia term ($\beta\dot{m}^2$). Researchers obtained both β and K coefficient from all test specimens by using least square fitting method. Viscous effects are shown at smaller pore diameter foam samples. Therefore, uncertainties of K and β coefficients are directly related with pore diameters of samples.

Dukhan and Patel [41] used Ergun correlation for defining flow model of eight different open cell aluminium foam samples. Samples are aluminium 6101-T6, 10 and 20 PPI with particular compression factors owning different porosities from 67.9% to 92.4%.

$$\frac{\Delta P}{L} = A\frac{(1-\varepsilon_{unc})^2\mu}{{\varepsilon_{unc}}^3 d_p^2}\,\mathrm{U} + B\frac{(1-\varepsilon_{unc})\rho}{{\varepsilon_{unc}}^3 d_p}\mathrm{U}^2 \tag{2.7}$$

Testing velocity range of foams is 0-3 m/s for air. Pressure ranges of foams are, 0 - 4 kPa/m for high porosity foam samples and 0 - 16 kPa/m for low porosity foam samples. Polynomial curves fit into the collected data which show similarities to Ergun correlation in Equation 2.7. At the end, authors claimed that Ergun approach is a successful method for obtaining pressure and friction disturbance in tested aluminium metal foams.

Dukhan and Ali [38] examine porous metal foams for determining wall and size effects on pressure disturbances. Fourteen different cylindrical 6 inch length sample of metal foam specimens are tested in this study. Seven of samples have diameter changes from 1.27 cm to 8.89 cm, 10 PPI with 89.27% porosity and 20 PPI 90% porosity samples with same pore diameters. During the experiments, air velocity changes from 0 to 30 m/s which are sufficient to obtaining the effect of diameter on the pressure distribution. After merging empirical data to the Darcy-Weisbach friction factor (f_σ) equation, Equation 2.8, A and B values are calculated.

$$f_\sigma = \mathrm{A}(Re_D)^{\mathrm{B}} \tag{2.8}$$

This study concluded with the following results:

- Wall effect has opposite relation between the diameters which increases as the diameter of sample decreases.
- Specimen diameter has a critical importance on wall effect after a critical diameter of 63.5 mm.
- If diameters of samples are equal or greater than 63.5 mm, there left no wall and size effects on pressure drop and empirical values perfectly fit Forchheimer equation.

Another similar study of Dukhan was about pressure drop examination and comparison of compressed and uncompressed 10, 20, 40 PPI open cell aluminium foam samples [12]. Nine samples participated in this research whose surface areas increased nearly 3-4 times of initial surfaces with compression. Contrasting point of Dukhan's study was obtaining relation between drag coefficient and permeability with porosity which shown in Equation 2.9.

$$K = \mathrm{A}\exp[b_1\varepsilon], \qquad C = \mathrm{B}\varepsilon + \mathrm{E} \tag{2.9}$$

Author summarized the study as below:

- Darcian velocity had quadratic relation with the pressure drop and it was higher for lower porosity aluminium samples.
- Not only permeability but also inertia coefficients were correlated with porosity.

Mancin et al. [26] evaluate pressure drop of six distinct pore density aluminium foams during the air flow. The scope of this study is comparing experimental and

theoretical analysis pressure drops of six samples. It is obvious that test conditions of researches were same with author's other researches [3, 24 and 25]. The reason of this, the identical test apparatus was established in University of Padova and used in all. Aluminium foams were brazed to two aluminium plates at top and bottom. Each plate has six thermocouple holes. Inlet velocity of test section varied from 2 to 5 m/s. Equation 2.10 is linear equated version of Equation 2.1. In contends of study, A and B coefficients were calculated from empirical data.

$$\left(-\frac{dP}{dz}\right)\frac{1}{\mathrm{U}} = \frac{\mu}{K} + \frac{\rho.C.\mathrm{U}}{\sqrt{K}} = \mathrm{A} + \mathrm{B.U} \tag{2.10}$$

Authors obtained new equation for characteristic length of samples in Equation 2.11. Validity of this equation depends on selected air inlet velocities and arranged test conditions of this research.

$$D_{HF} = 0.0122\mathrm{PPI}^{-0.849}\ [m] \tag{2.11}$$

In Equation 2.11, D_{HF} is the hydraulic diameter of foam heat sinks and PPI is the number of pore per inch. Investigators concluded results of survey as listed below:

- As predicted, lowest porosity foam specimen showed best performance, which means lowest pressure drop, compared to other samples.
- Highest porosity foam has thirty percent higher pressure drop than lowest porosity sample.
- Highest pressure drop is observed at 40 PPI foam sample which has highest pore number.

Liu et al. [15] practiced an experimental study for examining flow friction characteristic of aluminium foams. Seven different porosity samples were used for finding a correlation of friction factor (f_k) as shown in Equation 2.12. Author mentioned that increasing of pore density raised the pressure drop.

$$f_k = 20.93\frac{1-\varepsilon_{unc}}{Re} + 0.22 \tag{2.12}$$

Another practical study was done by Kim et al. [20]. Difference of this research from the literature was usage of aluminium foam. Instead of louvered fin, rectangular section foams were embedded into the plate fin heat exchanger. While hot water was

being circulated into the copper jackets, air flowed through the aluminium foams with 20 ℃ inlet temperature. Not only temperatures of inlet air and outlet air but also pressures of entrance and exit of air were measured.

For comparison, modified Colburn factors of heat exchanger were calculated from Equation 2.13.

$$j^* = \frac{A_F}{A_0}\frac{\Delta T}{\Delta T_m}\mathrm{Pr}^{2/3} \tag{2.13}$$

In the Equation 2.13, $j^*$is the Colburn factor of foam heat exchangers, ΔT designates inlet and outlet air temperature difference, ΔT_m designates the logarithmic mean temperature difference, A_F designates the frontal area of test specimen and A_0 designates the total heat transfer area of porous fin. As a result of this experimental study, following inferences were obtained by researchers.

- At lower Reynolds numbers low permeable aluminium foams had lower friction factor than louvered fins. On the other hand, higher friction factor were observed at higher Reynolds numbers for aluminium foams.
- Increasing pore density and decreasing porosity decrease modified Colburn factors of porous samples.
- They emphasized that although both porous and louvered fins showed similar performance, louvered fins had better in pressure drop.

Recent study about fluid flow of open cell metal foam was prepared by Antohe et al. [34]. Hydraulic characteristics of nine compressed foams were tested by air and Poly-alpha-olefin (PAO). Antohe determined permeability and inertia coefficients which are between $1.0\times10^{-10}\mathrm{m}^{-2} < \mathrm{K} < 12\times10^{-10}\mathrm{m}^{-2}$ and $0.3\ \mathrm{m}^{-1} < \mathrm{C} < 0.9\ \mathrm{m}^{-1}$. Authors claimed that obtaining these parameters from curve fitting was more correct than using a one data point. According to this study, dependence between permeability and inertia coefficient with the velocity range was observed. It should not be forgotten that these results and indications are valid in the defined fluids and velocities of each study.

Table 2.3 summarizes the basic parameters and conditions of fluid flow studies about porous metal fields.

Table 2.3 Comparison table of open cell metal foams' fluid flow researches

Researchers (Ref. No):	Aim of Research:	Pressure Range:	Fluid:	Fluid Vel. / Mass Flow Rate:	Geometry:	Material & Properties of Test Specimens:	Assumptions & Approaches:	Year:
Mancin et al. [26]	Experimental and theoretical examinations of pressure drops of aluminium foam samples.	0-12000 Pa/m	Air	2.0-5.0 m/s	100x100x40 mm	5, 10, 20, 40 PPI Aluminium foams with various pore densities (0.903 to 0.956)	Forchheimer - extended Darcy Equation	2010
Dukhan et al. [12]	Enhancing data of pressure loss of porous metals, obtaining empirical model for permeability and creating approach for pumping power for foam heat sinks	0-18 $kPa.s/m^2$	Air	0-3 m/s	10.16 x 24.13 x 5.08 cm3	10, 20, 40 PPI compressed and uncompressed 6101-T6 Aluminium foams with various pore densities (92-94 % porosity)	Forchheimer - extended Darcy Equation	2006
Dukhan et al. [38]	Finding critical diameter of foam samples that pressure drop becomes independent from sample diameter.	0-1400 $(Pa.s/m^2)$	Air	0-30 m/s	6 inch length x (0.5, 1, 1.5, 2, 2.5, 3 and 3.5) dia.	10 & 20 PPI Aluminium foams	Darcy law & Forchheimer Eq.	2012
Dukhan et al. [41]	Empirical prove of Ergun approach for metal foams.	0-16 kPa/m	Air	0-3 m/s	10.16 x 10.16 x 5.8 cm3	10 & 20 PPI Aluminium 6101-T6 Compressed and various porosity	Ergun Equation	2007
Liu et al. [15]	Determining friction effects of the metal foams.	0-550 kPa	Air	255-2550 l/min	20 cm length x 6.5 cm dia. cylinder	Aluminium, 5, 10, 20, 40 PPI and 7 different porosity open cell metal foams	Ergun Equation	2005
Kim et al. [20]	Comparison of thermal and hydraulic performances of 6 various aluminium foam heat exchangers with louvered fin type heat exchanger.	0- 500 Pa	Air	0.48 - 3.64 m/s	9 mm x 90 mm x 30 mm	10, 20, 40 PPI, Aluminium alloy, 6101-T6, 0.89, 0.92, 0.94 and 0. 96 porosities 6 metal foam samples	Forchheimer extended Darcy model	2000
Antohe et al. [34]	Hydraulic characterization of nine compressed aluminium foam by Poly-alpha-olefin (PAO) and air.	0 - 500 kPa	PAO & Air	1.22 m/s PAO 0.033-1.436 m/s (Air)	76.2 mm x 50.8 mm x 1 mm	Aluminium 6101-O alloy, (30-90% porosity)	Forchheimer extended Darcy equation	1997
Bonet et al. [43]	Investigating compressibility and pore size effects on flow field	(1-2.2) x 10^5 Pa	Air & Water	0 to 20 m/s for air 0 to 0.1 m/s for water	50 x 150 x (1.5-10.3) mm3	500 - 5000 µm pore size metal or alloys (Cu, Ni, Ni-Cr)	Forchheimer & Ergun approaches were used	2007

2.3. Simulation and Numerical Researches in Metal Foams

In this section, two simulation studies are examined for having knowledge about metal foams in CFD domain.

Kopanidis et al. [4] examined 3D simulation methodology of open cell metal foams. Geometry of samples was generated by CAD-CAE systems and exported IGES format from the Surface Evolver as in Figure 2.1. For the both 10 PPI and 40 PPI simulation k-e turbulence model was selected by Kopanidis. 40 PPI structured geometry had 4-5 times higher pressure drops than 10 PPI structured geometry.

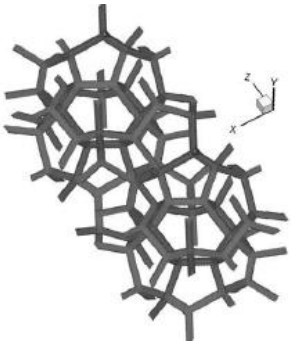

Figure 2.1 Construction of metal foam in CFD domain [4]

Authors claimed that 3D Navier-Stokes energy equations were calculated for 10 PPI and 40 PPI metal foam geometry. Simulation results were compared with the experimental studies of identical foam samples. Importance of entrance effects on pressure drop and heat transfer coefficient were stated at the conclusion section. Temperature distribution inside the designed 10 PPI model at the constant 2.9 m/s inlet velocity and constant hot plate 323 K temperature boundary conditions is given in Figure 2.2.

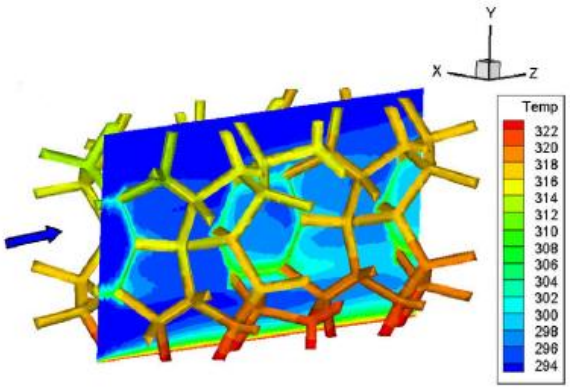

Figure 2.2 Conjugate heat transfers in CFD domain [4]

Secondly, Boomsma et al. [36] presented a new model for flow through open cell foam structure medium. Similarly, geometry of foams was created by Surface Evolver program and meshes were generated by Hypermesh software. At the mesh generation process, 3-D tetrahedral meshes were built from 2-D triangular surface meshes. Representative Elementary Volume (REV) concept, basic calculation approach of CFD, was appeared in this article. REV, which carries characteristic properties of foam materials, is a computable bounded small volume for optimizing processor capacity. Fluid stream lines into the pressure distribution of solved REV are indicated in Figure 2.3.

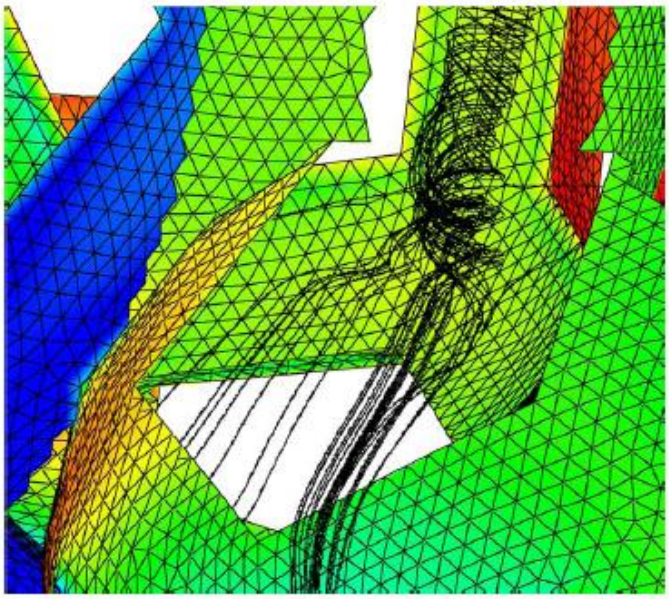

Figure 2.3 View of fluid streamlines through the foam ligaments [36]

Three separate solutions with separate mesh numbers were calculated for observing the mesh dependency of results. Change of pressure drop between distinct meshes was 1% which showed that results were mesh-independent. Due to lack of wall effect into the simulation, calculated pressure values of simulation were 25% lower than experimental results. In the scope of this thesis, both experimental and simulation studies are performed.

Experimental part is given in Chapter 4 and CFD simulation is given in and Chapter 5 of this thesis.

CHAPTER 3

PREPARATION OF TEST SPECIMENS

For this study, unique heat sink geometry with embedded aluminium or copper foams is produced. Embedding the foams to aluminium 6061 chassis is achieved by various steps such as soldering, cutting and coating. Details of these steps are described in detail in this chapter.

3.1 Cutting Metal Foams by Electro Discharge Machining

EDM is one of the non-traditional machining methods and it provides accurate cutting dimensions of materials. The idea of EDM is removing material with electric current between electrodes. Gap distance between electrodes and sparks is arranged by control algorithms of the machine.

A cutting mold prepared for metal foams prevents the damaging of foams in EDM cutting operation. Mold is shown in Figure 3.1. This cutting mold has a cavity for holding foam, so that brass wire of EDM cuts both foam and mold at the same time. Cutting mold is fastened to bench of machine by means of screws.

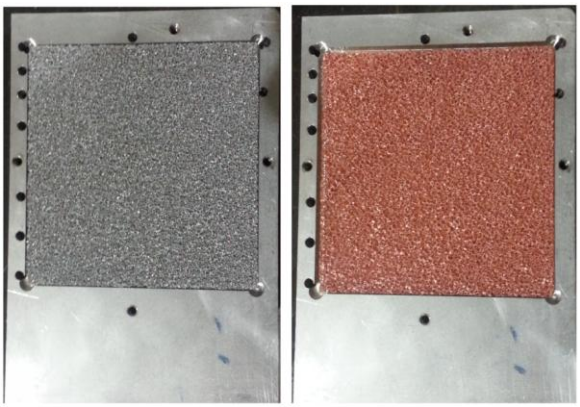

Figure 3.1 EDM Mold of aluminium and copper foams

An electro discharge cutting process of foams, which is performed as it is submerged in water, is shown in Figure 3.2.

Figure 3.2 EDM cutting operations of metal foams

0.25 mm diameter brass wire is selected for catching accurate precision in defined dimensions in the metal foam cutting operation.

3.2. Deep Hole Drilling of Heat Sink Chassis

Thermocouple locations are obtained by deep hole drilling process. The machine used in this step works like EDM cutting machine and it has different removable blades. A blade of one millimetre in diameter and thirty millimetres in length is used for heat sink chassis drilling. Deep hole drilling machine used can be seen in Figure 3.3.

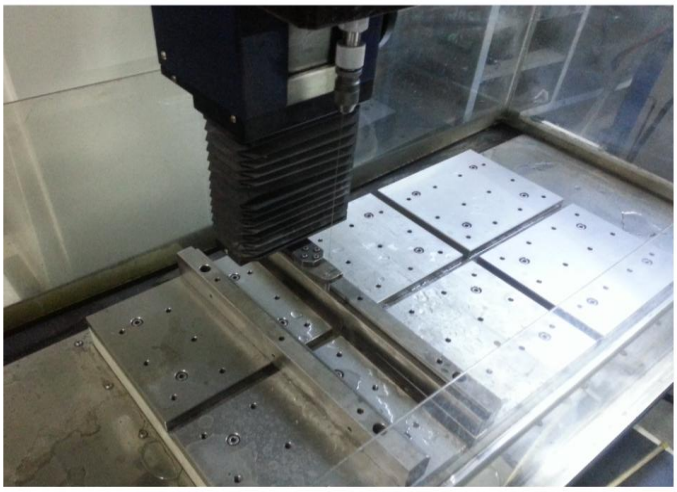

Figure 3.3 Photograph of deep hole electrical discharge drilling machine

In this process, blade caused melting of aluminium which was then removed from the chassis until the hole reached a depth of thirty millimetres. Six foam chassis and bare fin block were drilled with this method; each of chassis had nine holes as shown in Figure 3.4.

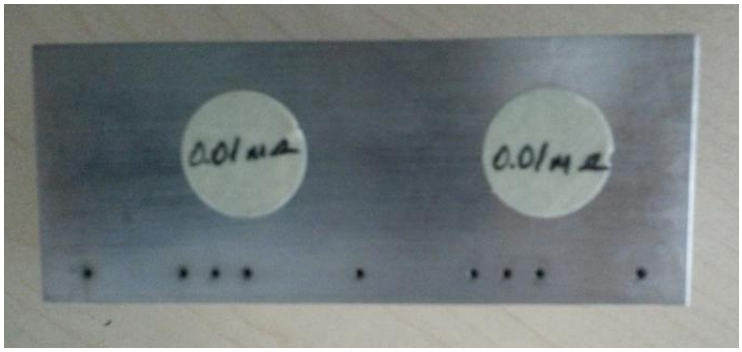

Figure 3.4 Specimen holes after deep drilling

3.3. Finishing and Coating of Metal Foams and Chassis

Both aluminium foams and their chassis are coated with tin and copper. The reason of copper coating of all foam heat sink chassis is, to make them suitable for soldering operation. Bare aluminium cannot solder itself so copper coating is used for creating a soldering layer on to the aluminium. After copper coating operations, all foams and their chassis are coated with tin for protection from corrosion effects. Bare aluminium fin block is only coated with yellow chromate for environmental protection. Some dimensions of fin block and foam heat sink chassis are viewed in Figure 3.5 and detailed technical drawings are given in Appendix A.

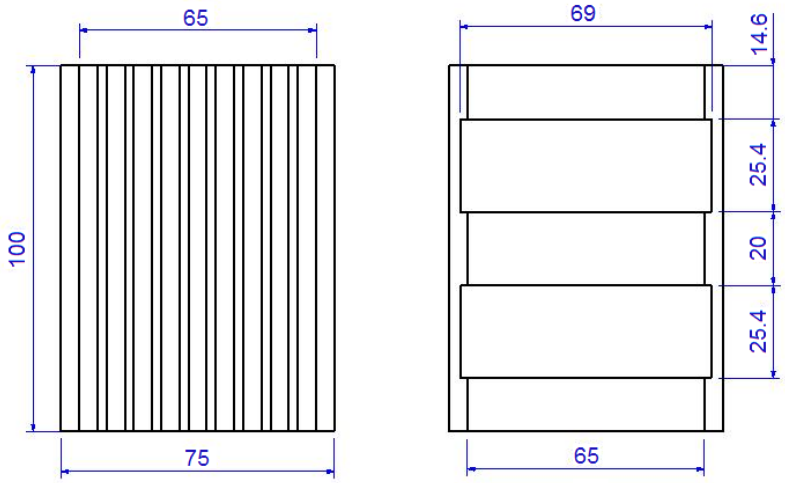

Figure 3.5 Technical presentation of fin block and foam chassis

Copper and tin coated aluminum chassis of foams and yellow chromate coated fin block is presented in Figure 3.6.

Figure 3.6 Photograph of test specimen chassis after coating process

After tin coating, appearance of all foams becomes same bright silver colour shown in above Figure 3.7. At this stage, six different foams are cut and coated so that they become ready for soldering process.

Figure 3.7 Photograph of metal foams after coating process

3.4. Soldering of Metal Foams

Soldering and brazing are most common joining methods of metal foams. The most important advantage of these methods is using high thermal conductivity of assistant materials. Both brazing and soldering methods require dissimilar infrastructures. MİKES, a Turkish avionics company, permits usage of its SLC Vapour Phase Soldering Machine for this research. Therefore, soldering methods become applicable for metal foam joining in extent of this study. Soldering process can be divided in two parts: Presoldering operations and Soldering of Foams to Specimens Chassis in Vapour Phase Soldering Machine. These are detailed in following subtitles. Thermal conductivity of solder, which is composed of 63% tin and 37% lead, is 39 W/℃·m [2].

3.4.1. Presoldering operations of metal foams

Cream solder is applied onto the two locations of chassis. Quantity of solder is spreaded with a planar stick and an equal smooth solder is obtained. Solder is also applied both on to the left and right walls of specimens. All chassis have two junction pockets as shown in Figure 3.8.

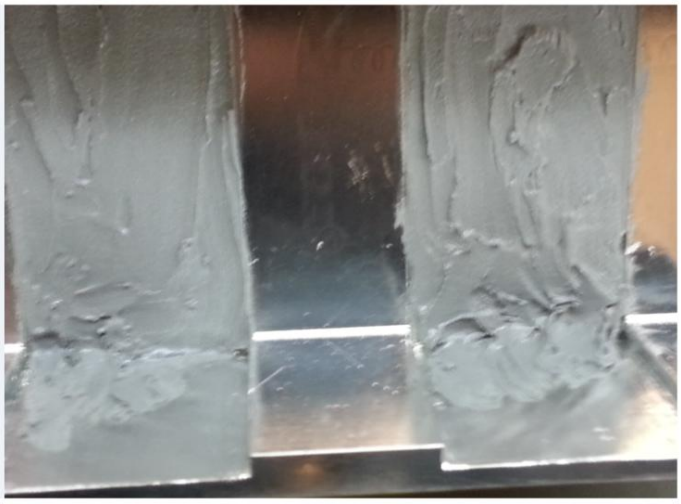

Figure 3.8 Cream solder application onto metal chassis

Excessive solder is cleaned with wet cotton so solder is only located on 1 mm depth in the junction pockets of chassis. The photograph of foam embedded heat sink in the soldering process is demonstrated in Figure 3.9.

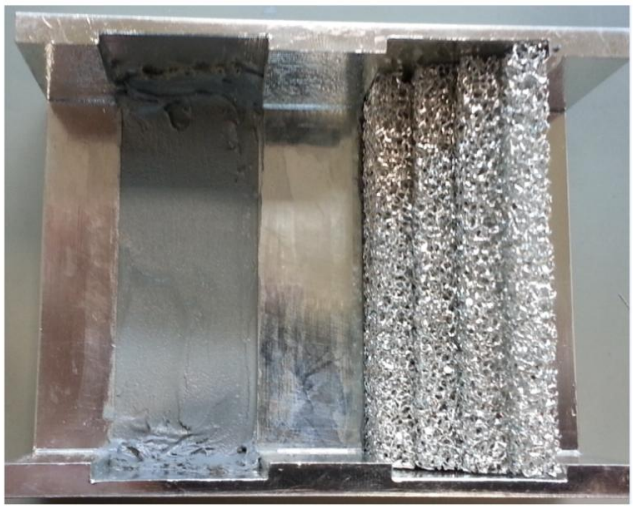

Figure 3.9 Cream solder application process after one side of foam located

Metal foams are inserted into the cream solder applied pockets of aluminium chassis as designed before. Four different length foams are installed to each pocket. Lengths of foams are 16 mm, 21 mm, 26 mm and 31 mm. The reason of using various lengths in this design is reducing required pumping fan power. Details of this design take part in Chapter 4 and Chapter 5.

Figure 3.10 Junction of foam to chassis before melting

Laser labels are used for separating foam samples like in Figure 3.10. Label defines foam material and pore number per centimetre. Foam materials have 4, 8, 16 pore

densities which corresponds to 10, 20, 40 pore per inch (PPI). PPI is a well-known parameter which is used in literature as described in Chapter 2.

3.4.2. Soldering of foams to chassis

SLC 600 Vapour Phase Soldering machine is used for soldering operations of metal foams to aluminium chassis. This machine commonly solders electrical components on to bare PCB. Figure 3.11 shows the basic structure of soldering machine. Machine has two different working fluids for melting solder paste and has one pump for recycling fluid mixture [54].

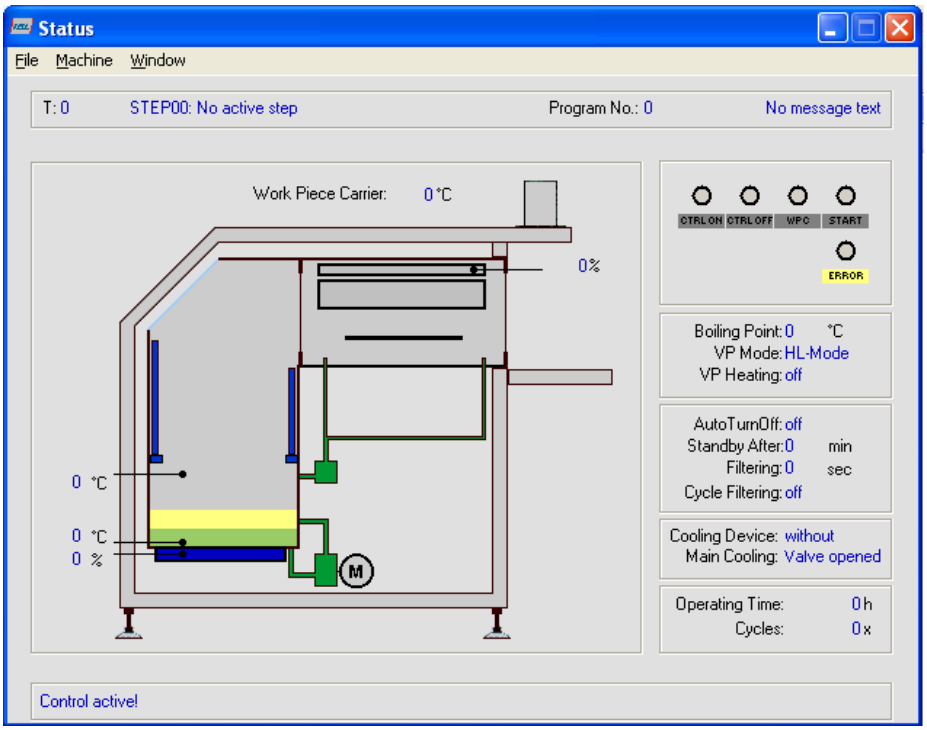

Figure 3.11 Screen shot of SLC 600 vapour phase machine's user interface software [54]

Alignment of foam embedded heat sink into the SLC vapour phase machine is seen in Figure 3.12.

Figure 3.12 Photograph of test specimen of metal foams in SLC vapour phase machine

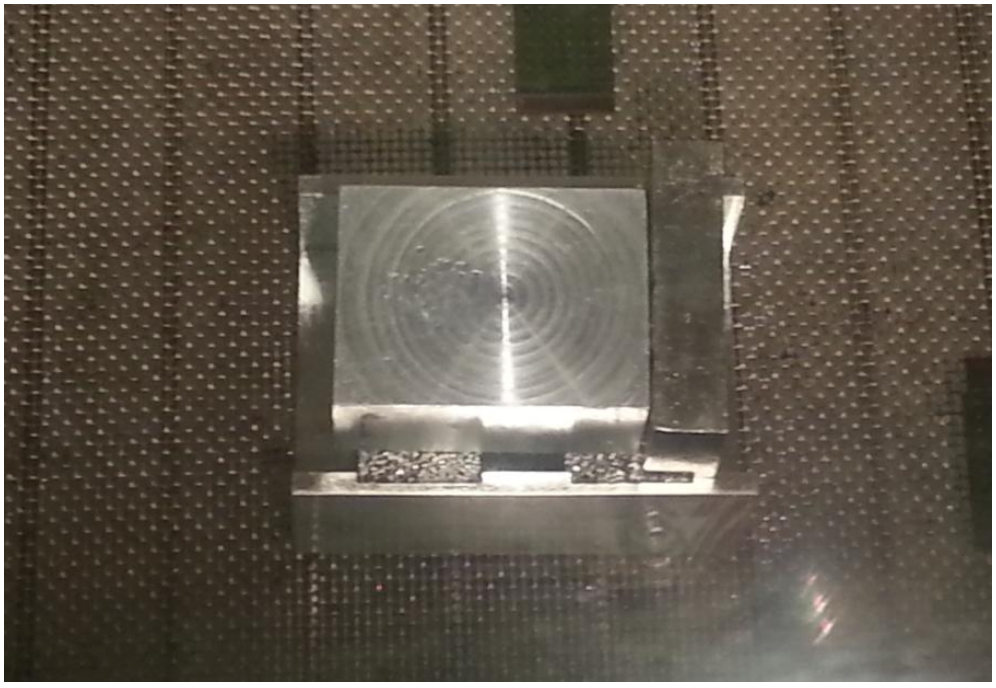

Figure 3.13 Detail photograph of test specimen in vapour phase machine with weights

Two separate metal blocks are used as a weight for increasing pressure onto the junction of foams, Figure 3.13. They provide lower thermal resistance and higher strength in junction parts.

Final status of the heat sinks before the testing is shown in Figure 3.14.

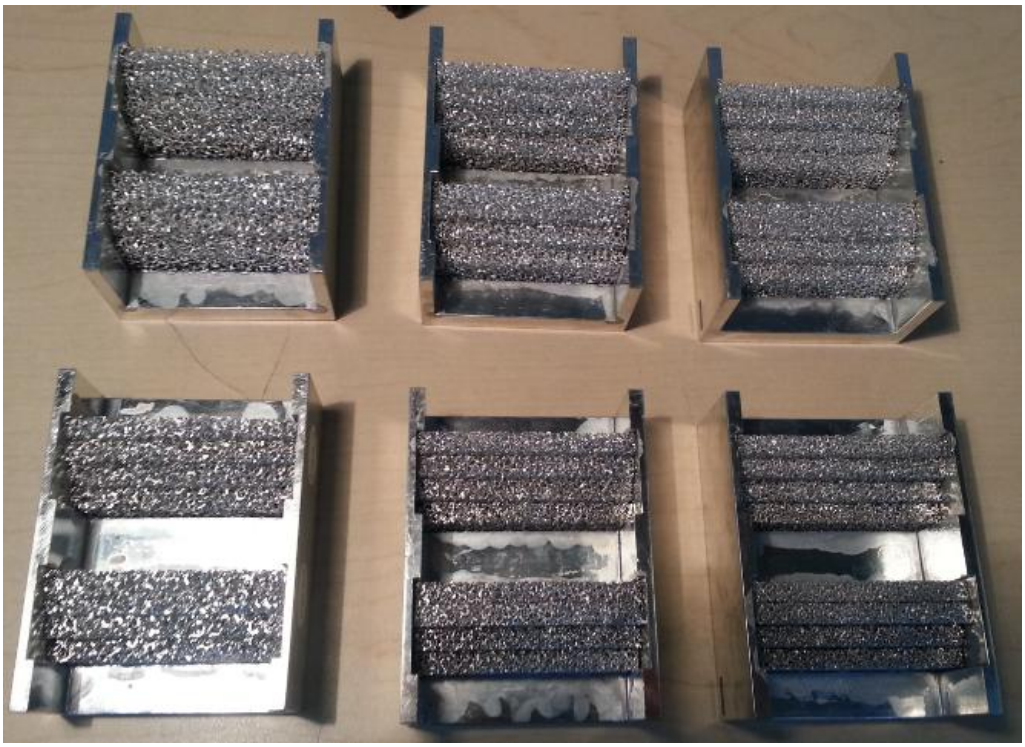

Figure 3.14 Final form of soldered metal foam test specimens

After soldering operation, electrical resistivity between foam and aluminium chassis is measured with miliohmmeter. Electrical resistivity was measured to be lower than 0.01 mΩ, which means foams and chassis behave like a single metal body.

CHAPTER 4

EXPERIMENTAL PROCEDURE AND RESULTS

4.1. Motivation of Experimental Study

Studies about metal foams show that metal foams are capable of being significant heat sinks especially for military applications. Technological improvements reduce PCB layouts and the size of electronic components; therefore, cooling of the required location has a vital role on the operational life of the component. At this stage, restricted usage of metal foams and conventional fin blocks shall be accurately compared. However, even if the thermal and the hydraulic performance calculation techniques of the fin type heat sinks are numerically and analytically known, there is still a lack of knowledge in the calculation methods of the metal foams. The single phase fluid flow of the metal foams and the heat transfer approaches used in the current studies, are summarized in Chapter 2. When the manufacturing process is considered, the structure formation and pore density of the metal foams make experimental studies a necessity. What makes the experimental studies paramount is not only the uniqueness of foam embedded heat sink but also the uncertainties arising from the manufacturing process of metallic foams As a result of these studies, analysing the usage of a small quantity of metal foam, rather than finned chassis can provide useful suggestions for future applications.

4.2. Test Scenarios

The primary goal of this experiment was to observe the hydraulic and the thermal behaviour of an aluminium fin block, the open cell copper and aluminium foam embedded heat sinks. The heat sinks having identical external dimensions were

placed on the testing section of the test rig. Seven different heat sinks were tested for four separate heaters with two distinct air velocities. A total of fifty six test cases were run, as shown in Table 4.1. At the foam embedded heat sinks, only the metal foam materials were used to remove the heat from the surface of the heater to the air. Meanwhile, a conventional fin block was made from processed aluminium. The metal foam materials of the foam embedded heat sinks had three distinct types of pore density for both the aluminium and copper plates. This study differs from similar studies in partial heating scenarios where only a small heater is used on top of the metal foams. Designs and materials of the heat sinks were detailed on the next part of this section.

Table 4.1 Experiment scenarios

	Air velocity = 4 m/s							
	Heaters (Watt)	Aluminium			Copper			Fin Block
		10 PPI	20 PPI	40 PPI	10 PPI	20 PPI	40 PPI	
Whole Heater	80	28 Cases						
	160							
2 dif. Sec. Heater	60							
	120							
	Air velocity = 6 m/s							
	Heaters (Watt)	Aluminium			Copper			Fin Block
		10 PPI	20 PPI	40 PPI	10 PPI	20 PPI	40 PPI	
Whole Heater	80	28 Cases						
	160							
2 dif. Sec. Heater	60							
	120							

4.3. Experimental Test Rig

The experimental apparatus used in this study, the locations of measuring devices, the properties of the test samples, the detailed figures and the description of the test procedures are described in this section.

4.3.1. Fin block geometry

Fin block heat sink which is 75 mm wide and 100 mm long, was produced from aluminium 6061-T6 alloy. Thickness of the block is 40 mm, 10 mm of which formed base plate thickness of the specimen. On the right side of the base plate, there are

nine thermocouple holes which are 30 mm deep to measure the temperature distribution of the fin block. The tested fin block is illustrated in Figure 4.1. Technical drawing of the fin block is given in Appendix A. A similar fin block structure was used in the current Jammer chassis and also in most of the commercial products.

Figure 4.1 Pictures of the aluminium fin block

4.3.2. The Geometry of the designed foam embedded heat sinks

All used metal foams were supplied and manufactured by Goodfellow Company. Aluminium foams were made from aluminium 6101 and copper with a purity of 99.9%. Detail illustrations of foams are shown in Figure 4.2. The labels of foam packages, which describe technical properties such as porosity, size, weight etc., may also be seen in Figure 4.2.

Figure 4.2 Pictures of the metal foams and packages

External dimensions of the supplied foam plates are 150 mm wide, 150 mm long and 6.35 mm thickness as shown in Figure 4.3.

Three particular pore densities were selected for this study through a literature survey. Pore density refers to the number of pores per centimetre or per inch. Pore densities of samples are 4 pores per cm, 8 pores per cm and 16 pores per cm for both copper and aluminium plates.

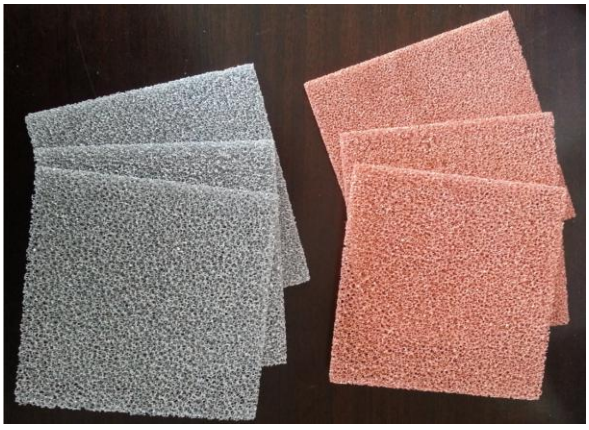

Figure 4.3 Pictures of the metal foams

The aforementioned pore densities correspond to 10 pore per inch (PPI), 20 PPI and 40 PPI which are commonly preferred by researchers. Foam plates were cut in to the given dimensions in Figure 4.4 in order to produce heat sinks. EDM method was used for cutting foams in accurate dimensions which are 69 mm wide with 16, 21, 26 and 31 mm long as shown in Figure 4.4.

Each heat sink has 2 pieces which are 16 mm long, 2 pieces which are 21 mm long, 3 pieces which are 26 mm long and 1 piece which is 31mm long, parts of which were cut from the same foam plate.

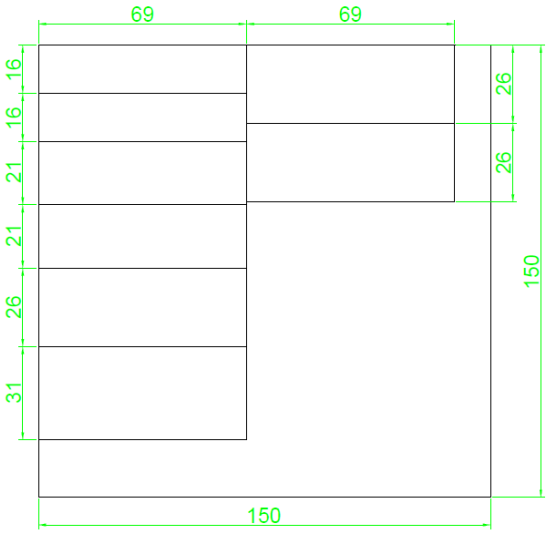

Figure 4.4 Cutting layouts of the foam sheets

The porosity of open cell aluminium foams is given to be 93% but there is no data for the porosity of the copper foam. To avoid this deficiency, Equation 4.1 was used for porosity calculation of copper foams. The masses of copper foam plates are stated on the labels. As a result, by using air and copper densities, solid and fluid volumes are calculated. Finally, the ratio of fluid (air) volume over total volume gave 0.905 porosity of the copper foam.

$$\varepsilon = \frac{V_{air}}{V_T} = \frac{V_T - V_S}{V_T} \tag{4.1}$$

Although aluminium foams have homogeneous structure, all three copper plates have closed cells in a line as shown in Figure 4.5. Therefore, the high density of copper makes manufacturing process of foams more complicated. Physical properties of the tested foams are located in the Table 4.2.

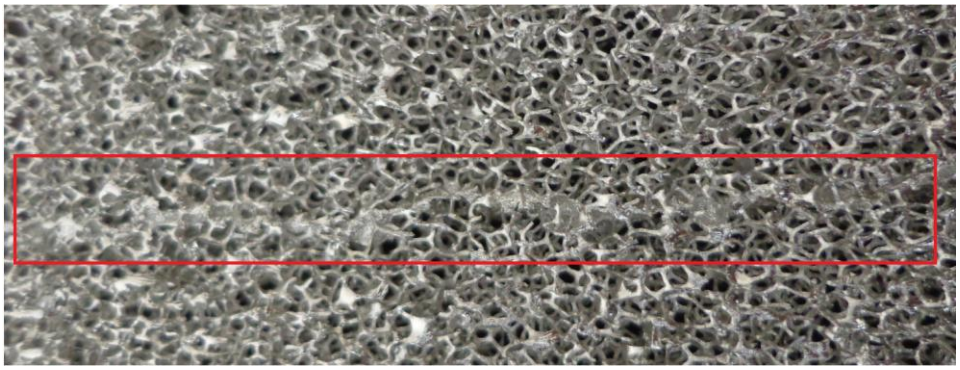

Figure 4.5 Closed cells picture of copper foam plate

Last column of Table 4.2 indicates the total foam convection areas which are the volume of the cut parts times the area density of the metal foam.

Table 4.2 The physical properties of the used foam plates

Foam	Average Pore Diameter (m)	Porosity	Area Density (m^2/m^3)	Area(m^2)
AL 10PPI	0.00508	0.93	809.1	0.058442
AL 20PPI	0.0029	0.93	1240.2	0.089581
AL 40PPI	0.001702	0.93	1800.8	0.130074
CU 10PPI	0.0050	0.905	831.0	0.060024
CU 20PPI	0.00254	0.905	1273.8	0.092006
CU 40PPI	0.00165	0.905	1849.5	0.133595

The heights of the foam layer heat sinks are shown in Figure 4.6.

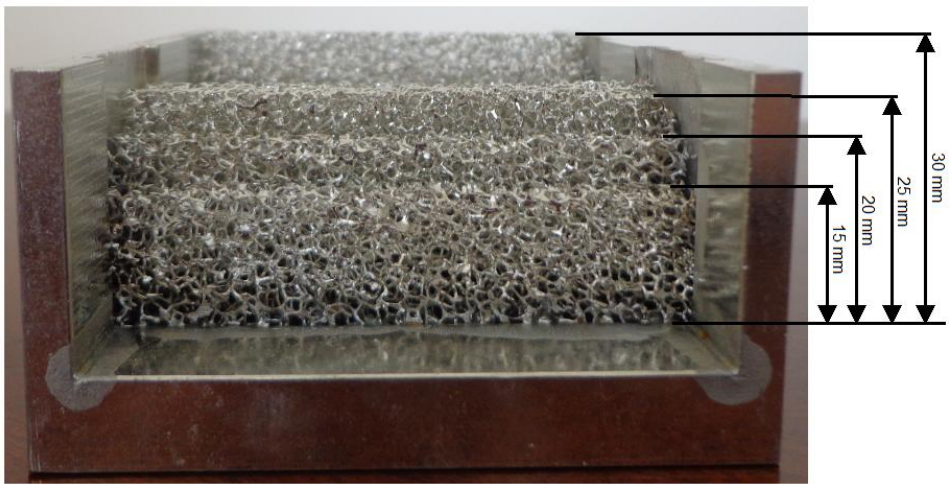

Figure 4.6 Porous layers of foam embedded heat sink

The photograph showing all foam embedded heat sinks in Figure 4.7.

Figure 4.7 Pictures of foam embedded heat sinks

Chassis of metal foam embedded heat sinks were produced from aluminium 6061-T6 alloy as defined in Chapter 3. External dimensions the of chassis are 100 mm long, 75 mm wide and 40 mm thick, which are identical with fin block dimensions. Moreover, each chassis has two separate 1 mm deep pockets on the base plane and the lateral inside surfaces where soldering operation occurred. Before the soldering, both chassis and foam parts were coated as stated in Chapter 3. Although both first

and the second pocket of the chassis have rising foam height according to the air direction, the last foam height of the first pocket is 5 mm shorter than that of the second pocket. The main reason of this decision was to provide fresh and low temperature air onto the foamless area of the heat sink. Thus, by raising the temperature, an increase in the heat transfer was aimed. In the second pocket, air was forced to pass through the foam by not leaving foamless gap as seen in Figure 4.8. The technical drawing of the bare chassis foam heat sink and the assembly status are stated in Appendix A.

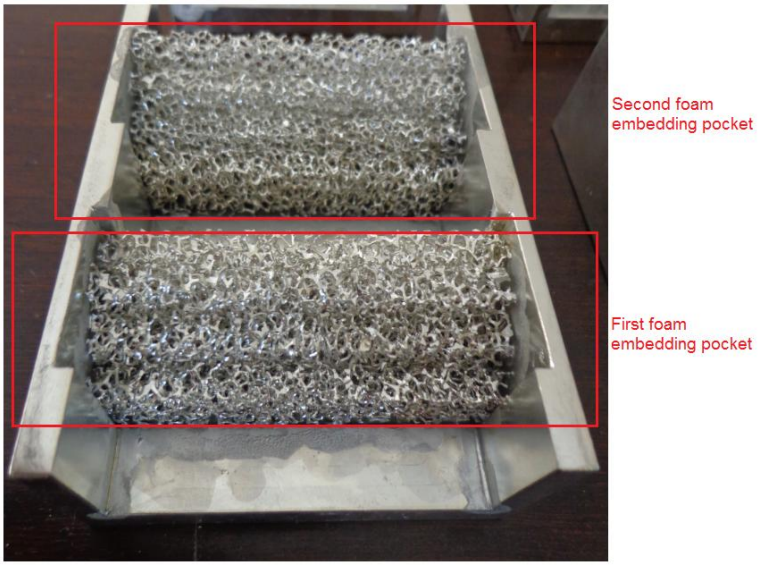

Figure 4.8 Pictures of the foam soldered pockets

There are several reasons why metal foams were used in different heights. The first is to reduce the pressure difference of the heat sink by decreasing the foam thickness. The second is to use the cooling capacity of air efficiently and the last reason is catching appropriate heat transfer point between the conduction and the convection heat transfer methods.

4.3.3. The components of the test rig

In the scope of this experimental study, a test rig having a capability to observe thermal and hydrodynamic performance comparisons of heat sinks is planned to be established. The performance of heat sinks was evaluated with respect to each other by the inlet and the outlet fluid temperatures, the average base plane temperatures and the pressure drops through the heat sinks. The components of test rig, their technical properties and the models are shown in Table 4.3.

Table 4.3 Component of test rig

Test Rig Components			
Item No:	**Component:**	**Brand / Model:**	**Properties\Function\Measuring Ranges:**
1	Fan	EBMPAPST G2E120-AR77-01	AC centrifugal Fan, Max pressure: 330 Pa Max Vol. rate: 260 m^3/h
2	Heaters	Custom design heaters are produced in the desired dimensions.	Heater capabilities: 60W, 120W, 80W, 160W
3	Hot Wire Anemometers # 1	AIRFLOW TA2	Velocity range: 0-15 m/s Temperature range: 0- 80 ^oC
4	Hot Wire Anemometers # 2	KM 4003	Velocity range: 0-30 m/s Temperature range: -30- 200 ^oC
5	Adapter	Custom Design, made from polyoxymethylene (POM)	Reduction of air flow area from fan exit to test section inlet.
6	Test Section Duct Assembly	Custom Design, made from (POM)	Providing air flow pass through the heat sinks, locating thermocouples
7	Heater Plates	Custom Design made from Bakelite (Pertinax)	Thermal Conductivity: 0.21 W/mK Thermal Exp. Coeff.: $1.6\times10^{-4}\ C^{-1}$
8	Fan Holders	Custom Design, made from (POM)	Stabilizing fan during the operation.
9	Insulation Material	EPS Heat Insulation Plate	Thermal Conductivity: 0.032 W/mK Insulating test section from Base Plate
10	Base Plate	Custom Design, 6061 Aluminium Plate (60 cm x 25 cm x 1 cm)	Combining all set-up components on the same plane
11	Voltmeter of Fan	Agilent U1272A	AC Current range: 0.3 mA - 10 A AC Voltage range: 30 mV - 1000 V
12	Ammeter of Fan	UNIT-T Clamp	AC Current range: 2-400 Ampere AC Voltage range: 2-600 Volt
13	Voltmeter of Heater	Avometer M3004/ MEGGER INS.	AC Current range: 10 mA - 10 A AC Voltage range: 10 mV - 1000 V
14	Ammeter of Heater	Avometer M3004/ MEGGER INS	AC Current range: 10 mA - 10 A AC Voltage range: 10 mV - 1000 V
15	AC Motor Driver	ES200-004A	Output: 750 W, Input Voltage: 200VAC Input Current: 6.5A, Output Current: 3.6A
16	Frequency meter	Agilent U1241B	AC Current range: 0.4 mA - 20 A AC Voltage range: 1000 mV - 1000 V
17	Thermocouples	Cole-Parmer EW-08542-04	Digi-Sense Thermocouple,Wire,TYPE-T,30-GAUGE, FEP Insulation,
18	Power Supply	Powerstat 216B	Superior Electric Powerstat 216B Variable Autotransformer, Input Volt: 240V Output Volt: 0-280V Frequency: 50-60 Hz
19	Data Logger	Agilent 34970A	Up to 120 Channels, 11 function measuring capability, voltage, ampere, and temperature recorder within 1 second's intervals.
20	Laptop	TOSHIBA	Collecting & Processing data taken from Data logger

The adapter component of the test rig converts the rectangular cross-section exit area of fan to the cross section area of the test section, so that air can flow through the test specimens. In this study, all the specimens were aimed to be tested under the same conditions such as; identical air velocities and the thermal loads. Pressure drops of the heat sinks were calculated via the power consumption of the fan.

At the first step of the test rig assembly, item no 5 (see Table 4.3), the adapter, was attached to the test section (item no 6) with four hexagonal-headed M6 screws, by implementing the O-Ring gasket into the hole of test section. Secondly, the honeycombs which prevent the fluctuation of the anemometer AIRFLOW TA2 were placed inside of the adapter. Following this procedure, in order to install the fan, four screws which are hexagonal headed and 20 mm long M6 were fastened by pressing gasket of the adapter part. The subassembly of the test rig was installed to the POM spacers that pressed the insulation materials between the duct assembly and the aluminium plate with fourteen 4M 30 mm length screws. Polyoxymethylene (POM) was ideal to make the test section duct assembly, the adaptor, the fan holders and the spacers of the test rig due to the low thermal conductivity, the low thermal expansion co-efficiency and easy machining properties. Despite the low thermal properties of the POM material, negligible heat losses occured in the experiments. These heat losses were ignored in the calculations. Schematic view of the test rig is shown in Figure 4.9.

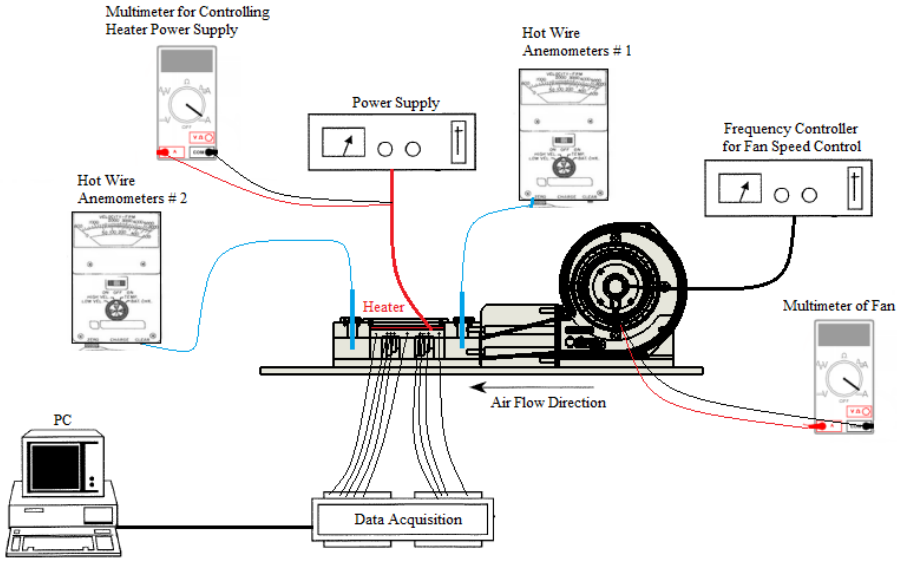

Figure 4.9 Schematic view of the test rig

Two different types of heater plates were required for two separate heaters. The plates were designed and manufactured by using Pertinax heat-resistant material. The heaters were compressed between the heat plate and the heat sink by six M4 10 millimetre long screws to avoid thermal resistance. The partial and the whole heaters are illustrated in Figure 4.10.

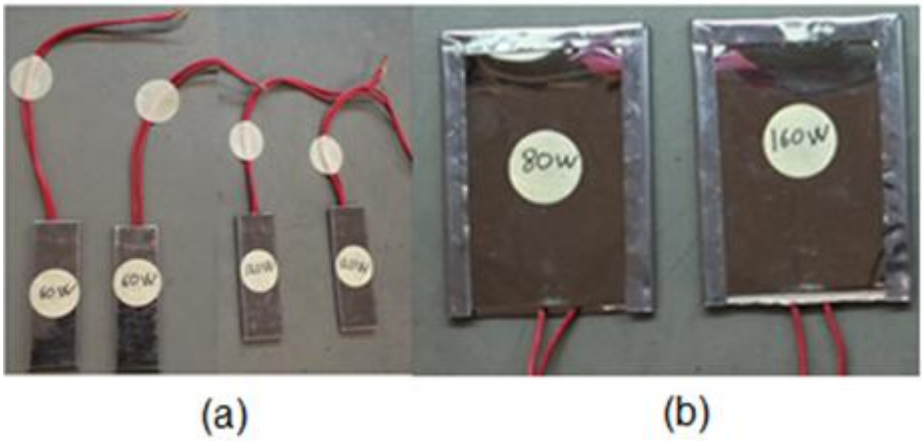

Figure 4.10 (a) Partial heaters (item no 2 in Table 4.3); (b) whole heaters (item no 2 in Table 4.3)

For the base plane of the heat sinks, nine T-type ± 1 (℃) accurate thermocouples were used to measure the temperature. Thermocouples were placed in the 30 mm deep holes from the lateral surface of heat sinks as shown in Figure 4.11.

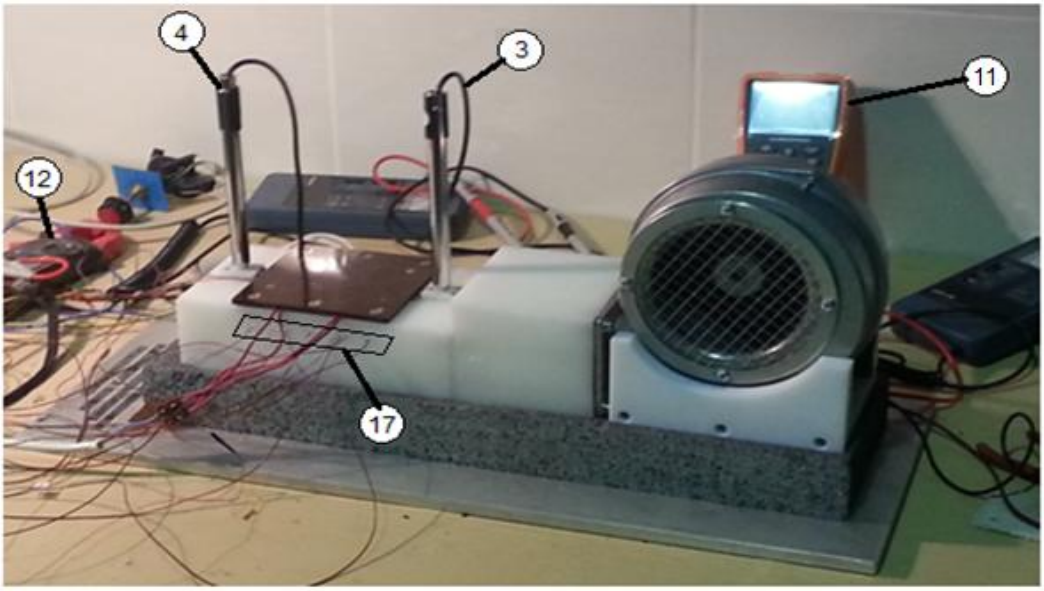

Figure 4.11 Picture of test rig

The T-type thermocouples were coated with high conductivity thermal epoxy to avoid air contact on the inside of the heat sinks. Although the inlet air temperatures were measured with AIRFLOW TA2, the outlet temperatures could not be measured by using it since the air temperature approached its maximum temperature limit. Consequently, the outlet air was measured from nine different locations of the test section outlet with KM 4003 anemometer.

The air velocity was measured with AIRFLOW TA2 and set to the desired value by an AC Motor Driver (item no 15). To prevent the occurrence of any particular problems, the arranged frequency was measured with Agilent U1241B (item no 16). The second adjustable parameter of this test rig is heater load which is controlled by the power supply (item no 18). The powers of heaters were calculated by the multiplication of current by the voltage of power supply. As seen in Figure 4.12, the power values were set from the power supply switch then both the current and the voltage of power supplies were checked with an external ampermeter and voltmeter for each case.

(a) (b)

Figure 4.12 (a) Power supply of the test rig (item no 18 in Table 4.3); external voltmeter and ammeter (item no 13 and 14 in Table 4.3)

Detailed view of the test rig components is given in Figure 4.13 and Figure 4.14 with stated item numbers in Table 4.3.

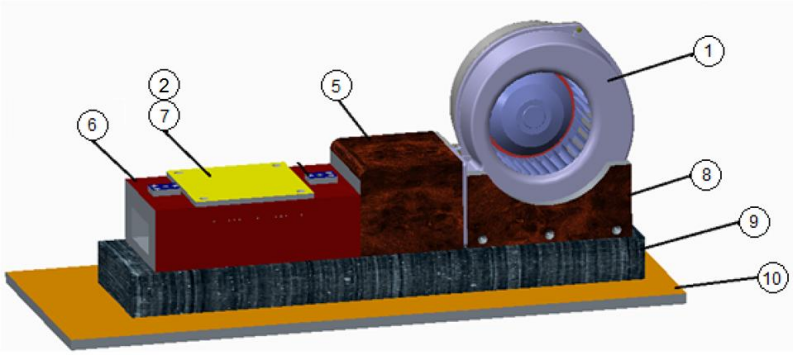

Figure 4.13 CAD geometric model of the test rig

The data logger (item no 19) measured and recorded temperature at one second intervals and transferred data to laptop by an RS-232 connection. Commercial Agilent 34970A software allowed the tracking and saving temperature data in Microsoft Office format.

Temperature stability was established in 30-40 minutes. Once it was established, the temperature values were taken. Steady-state condition was observed for all experiment cases and these cases were repeated under each separate air velocity and heater condition. Uncertainty values of measuring devices are stated on Table 4.4.

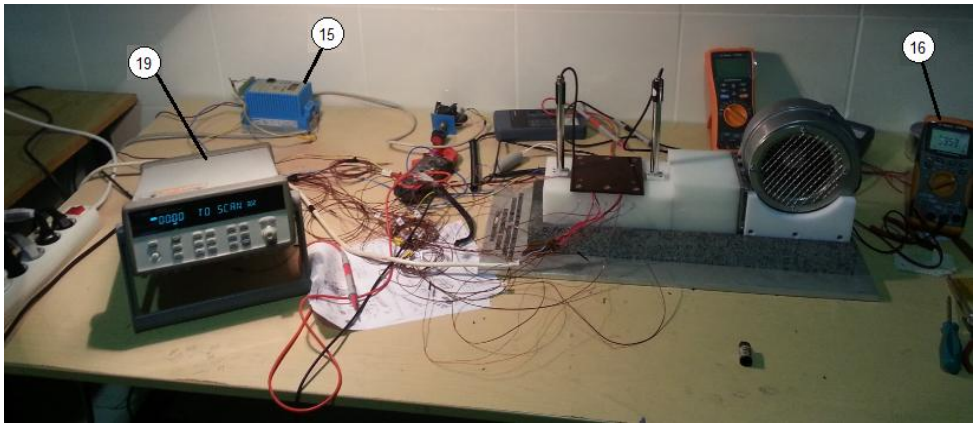

Figure 4.14 General view of the test rig

A detail cross-section view of test section of test rig is displayed in Figure 4.15. The locations of the hot wire anemometers, the heaters location, the honeycombs and the heat sink are presented in this figure.

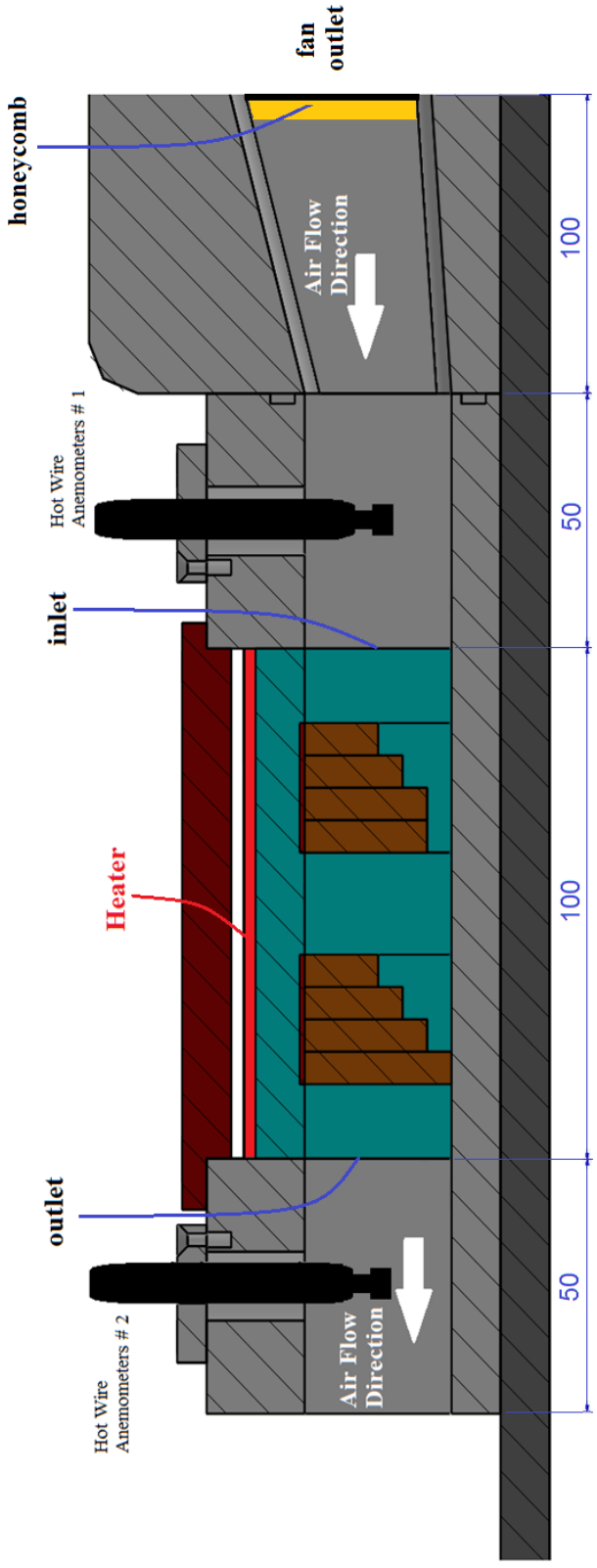

Figure 4.15 The cross section view of the test section which shows the location of the foam embedded heatsink, the heater and the direction of air

4.4. Uncertainty Analysis of Measurements

In this chapter, the uncertainties which generated from experiment components are calculated and presented in tables. In this part of study, the reasons and the calculation method of the measuring uncertainties will be explained in detail. The uncertainty analysis provides proximity of measured value to true value. Some of the reasons of uncertainties were the calibration of measuring device, the environmental effects on measured variables, reading accuracy capability of the device and the incompatible results of the repeated measurements. The equations below demonstrate the calculations of uncertainties [61, 7]. The measurement error:

$$e = x_m - X_T \tag{4.2}$$

x_m Measured value from the device

X_T True value of quantity

The error value in above equation is the maximum error of measurement devices which is given in the devices' datasheet. Common types of errors are fixed errors, the mistakes and the accidental errors which were caused by different repeated readings without an obvious reason [64]. To prevent the effects of these types of errors, measurements were repeated by switching the measurement devices.

The uncertainty for rectangular probability distribution is defined as follows [62]:

$$\omega = \frac{e}{\sqrt{3}} \tag{4.3}$$

Uncertainty is the multiplication of quoted value from manufacturer's specification to the stated level of confidence [62] is as follows:

$$\omega = 1.5\frac{u_f}{\sqrt{3}} \tag{4.4}$$

u_f is uncertainty of measurement devices. It is given in the manufacturer specifications. The resultant function is demonstrated with R and whether it has a relation with independent variables or not.

$$R = R(x_1, x_2, x_3, \dots, x_n) \tag{4.5}$$

If uncertainty of R depends on the every component of the errors, this situation is defined as n^{th} order uncertainty [63]. And this n^{th} order uncertainty is calculated as follows:

$$\omega_R = \left[\left(\frac{\partial R}{\partial x_1}\omega_1\right)^2 + \left(\frac{\partial R}{\partial x_2}\omega_2\right)^2 + \cdots + \left(\frac{\partial R}{\partial x_n}\omega_n\right)^2\right]^{1/2} \tag{4.6}$$

If the resultant function is a resultant function of variables raised to the exponents,

$$R = R({x_1}^{a1}{x_2}^{a2} \dots {x_n}^{an}) \tag{4.7}$$

The partial differentiations performed for calculating the resultant uncertainty is shown in Equation 4.8.

$$\frac{\partial R}{\partial x_i} = {x_1}^{a1}{x_2}^{a2}(a_i){x_1}^{ai-1} \dots {x_n}^{an} \tag{4.8}$$

For more simplification, both sides is divided to R function,

$$\frac{1}{R}\frac{\partial R}{\partial x_i} = \frac{a_i}{x_i} \tag{4.9}$$

Finally the following equation is obtained when the derivative of resultant function (Equation 4.9) is replaced in the Equation 4.6.

$$\frac{\omega_R}{R} = \left[\sum \left(\frac{a_i \omega_{x_i}}{x_i}\right)^2\right]^{1/2} \tag{4.10}$$

Table 4.4 The uncertainties of the test rig components

Uncertainty of the Test Rig Components			
Item No:	Component:	Model/Brand:	Accuracy:
3	Hot Wire Anemometers # 1	AIRFLOW TA2	±2% Full scale deflection (FSD), ± 1 digit
4	Hot Wire Anemometers # 2	KM 4003	± 3% of reading, ± 1 % full scale
11	Voltmeter of Fan	Agilent U1272A	1 % + 5 No. of Least Significant Digit
12	Ampermeter of Fan	UNIT-T Clamp	2.5 % + 5 No. of Least Significant Digit
13	Voltmeter of Heater	AVOMETER M3004	2 % + 5 No. of Least Significant Digit
14	Ampermeter of Heater	AVOMETER M3004	2 % + 5 No. of Least Significant Digit
17	Thermocouples	Cole-Parmer EW-08542-04	Error limit T-type ± 1oC (-65 to 130°C)

Equation 4.10 was used for uncertainty calculations of the parameters below.

Reynolds numbers of fin block was defined as:

$$\mathrm{Re} = \rho \mathrm{u} \frac{D_H}{\mu} \tag{4.11}$$

D_H indicates, hydraulic diameter of fin block and is given as:

$$D_H = \frac{4A_{cs}}{p} = \frac{4lt}{2(l+t)} \tag{4.12}$$

A_{cs} cross section area of duct (m^2)

p wetted perimeter (m)

l length of fin (m)

t fin thickness (m)

Dimensions used in the equations above for the fin block are presented in Figure 4.16.

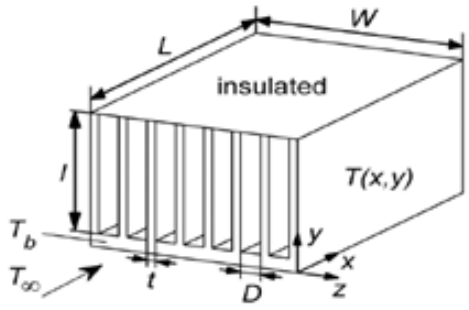

Figure 4.16 Dimensional designations of reference studies [76]

Hydraulic diameter is substituted into the Equation 4.11, so:

$$\mathrm{Re} = \rho \mathrm{u} \frac{D_{HF}}{\mu} = \frac{\mathrm{u}2lt}{(l+t)\nu} \tag{4.13}$$

ν kinematic viscosity (m^2/s)

The uncertainty of Reynolds number was calculated as in Equation 4.14.

$$\frac{\omega_{\mathrm{Re}}}{\mathrm{Re}} = \left[\left(\frac{\omega_{\mathrm{u}}}{\mathrm{u}}\right)^2 + \left(\frac{\omega_l}{l}\right)^2 + \left(\frac{\omega_t}{t}\right)^2 + \left(\frac{-\omega_l}{l+t}\right)^2 + \left(\frac{-\omega_t}{l+t}\right)^2 + \left(\frac{-\omega_\nu}{\nu}\right)^2\right]^{1/2} \tag{4.14}$$

Average base plane temperature differences of heat sinks calculate as in Equation 4.15.

$$\Delta T_{avgb} = \frac{\sum_1^9 T_b}{9} - T_{c,in} \tag{4.15}$$

T_{avgb} average base plane temperature (℃)

The uncertainty of average base plane temperature is related with the thermocouples errors as shown in Equation 4.16.

$$\frac{\omega_{T_{avgb}}}{T_{avgb}} = \left[\left(\frac{\omega_{T_1}}{T_1}\right)^2 + \left(\frac{\omega_{T_2}}{T_2}\right)^2 + \left(\frac{\omega_{T_3}}{T_3}\right)^2 + \left(\frac{\omega_{T_4}}{T_4}\right)^2 + \left(\frac{\omega_{T_5}}{T_5}\right)^2 + \left(\frac{\omega_{T_6}}{T_6}\right)^2 + \left(\frac{\omega_{T_7}}{T_7}\right)^2 + \left(\frac{\omega_{T_8}}{T_8}\right)^2 + \left(\frac{\omega_{T_9}}{T_9}\right)^2\right]^{1/2} \tag{4.16}$$

The Nusselt numbers of heat sinks are defined in the chapter as follows:

$$\mathrm{Nu} = \frac{\dot{q}_s D_{HF}}{k_f A_{con}(T_{avgb} - T_{c,in})} = \frac{\rho \mathrm{u} c_p 2a^2 b^2 (T_{c,out} - T_{c,in})}{k_f A_{con}(T_{avgb} - T_{c,in})(a+b)} \tag{4.17}$$

$\dot{q}_s$ heat flux ($\mathrm{W \cdot m^{-2}}$)

A_{con} convection area of heat sink ($\mathrm{m^2}$)

c specific heat of fluid ($\mathrm{J \cdot kg^{-1} \cdot ℃}$)

$T_{c,in}$ coolant inlet temperature (℃)

$T_{c,out}$ coolant mean exit temperature, (℃)

Where D_{HF} is the hydraulic diameter of foam embedded heat sinks which is different from fin block's hydraulic diameter is calculated by Equation 4.18.

$$D_{HF} = \frac{4A_{cs}}{p} = \frac{4ab}{2(a+b)} \tag{4.18}$$

a high of duct (m)

b wide of duct (m)

Assembly drawing of the surface of test section to adaptor part of test rig is shown in Figure 4.17.

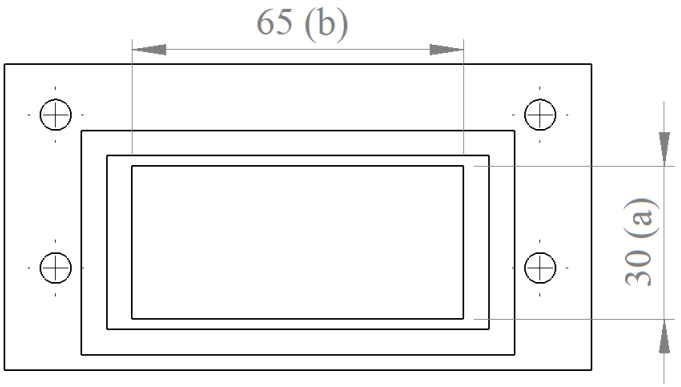

Figure 4.17 View of air entrance side of test section duct

The uncertainty of Nusselt Number was calculated by:

$$\frac{\omega_{\mathrm{Nu}}}{\mathrm{Nu}} = \left[\left(\frac{\omega_{\rho}}{\rho}\right)^2 + \left(\frac{\omega_{\mathrm{u}}}{\mathrm{u}}\right)^2 + \left(\frac{\omega_{c_p}}{c_p}\right)^2 + \left(\frac{2\omega_{\mathrm{a}}}{\mathrm{a}}\right)^2 + \left(\frac{2\omega_b}{\mathrm{b}}\right)^2 + \left(\frac{\omega_{T_{c,out}}}{T_{c,out}}\right)^2 + \left(\frac{-\omega_{T_{c,in}}}{T_{c,in}}\right)^2 + \left(\frac{-\omega_{k_f}}{k_f}\right)^2 + \left(\frac{-\omega_{A_{con}}}{A_{con}}\right)^2 + \left(\frac{-\omega_{T_{avgb}}}{T_{avgb}}\right)^2 + \left(\frac{\omega_{T_{c,int}}}{T_{c,int}}\right)^2 + \left(\frac{-\omega_a}{\mathrm{a}+\mathrm{b}}\right)^2 + \left(\frac{-\omega_b}{\mathrm{a}+\mathrm{b}}\right)^2\right]^{1/2} \quad (4.19)$$

The average convection coefficient of foam embedded heat sinks is given in Equation 4.20.

$$\bar{h} = \frac{q}{A_{con}(T_{avgb} - T_{c,in})} = \frac{V_h I_h}{A_{con}(T_{avgb} - T_{c,in})} \quad (4.20)$$

I_h heater current (A)

V_h heater voltage (V)

The average convection coefficient's uncertainty was calculated by:

$$\frac{\omega_{\bar{h}}}{\bar{h}} = \left[\left(\frac{\omega_{V_h}}{V_h}\right)^2 + \left(\frac{\omega_{I_h}}{I_h}\right)^2 + \left(\frac{-\omega_{A_{con}}}{A_{con}}\right)^2 + \left(\frac{-\omega_{T_{avgb}}}{T_{avgb}}\right)^2 + \left(\frac{\omega_{T_{c,in}}}{T_{c,in}}\right)^2\right]^{1/2} \quad (4.21)$$

Thermal resistance of the heat sinks is

$$R_{th} = \frac{\Delta T}{q} = \frac{\Delta T_{avgb} - T_{c,in}}{\dot{m}c(T_{c,out} - T_{c,in})} = \frac{\Delta T_{avgb} - T_{c,in}}{\rho \mathrm{u} cab(T_{c,out} - T_{c,in})} \tag{4.22}$$

The uncertainty expression of thermal resistance is:

$$\frac{\omega_{R_{th}}}{R_{th}} = \left[\left(\frac{\omega_{\Delta T_{avgb}}}{\Delta T_{avgb}}\right)^2 + \left(\frac{-\omega_{T_{c,in}}}{T_{c,in}}\right)^2 + \left(\frac{-\omega_{\rho}}{\rho}\right)^2 + \left(\frac{-\omega_{\mathrm{u}}}{\mathrm{u}}\right)^2 + \left(\frac{-\omega_{\mathrm{c}}}{\mathrm{c}}\right)^2 + \left(\frac{-\omega_{\mathrm{a}}}{\mathrm{a}}\right)^2 + \left(\frac{-\omega_b}{\mathrm{b}}\right)^2 + \left(\frac{-\omega_{T_{c,out}}}{T_{c,out}}\right)^2 + \left(\frac{\omega_{T_{c,in}}}{T_{c,in}}\right)^2\right]^{1/2} \tag{4.23}$$

The Pressure differences of heat sinks were calculated from the power consumptions of the fan as:

$$\Delta P = \frac{\dot{W}}{Q} = \frac{\mathrm{Uab}}{I_f V_f} \tag{4.24}$$

$\dot{W}$ pumping power (W)

$\dot{Q}_V$ volumetric flow rate (m^3/h)

I_f fan current (A)

V_f fan voltage (V)

The uncertainty of calculated pressure differences were found as:

$$\frac{\omega_{\Delta P}}{\Delta P} = \left[\left(\frac{\omega_{\mathrm{u}}}{\mathrm{u}}\right)^2 + \left(\frac{\omega_{\mathrm{a}}}{\mathrm{a}}\right)^2 + \left(\frac{\omega_b}{\mathrm{b}}\right)^2 + \left(\frac{-\omega_{I_f}}{I_f}\right)^2 + \left(\frac{-\omega_{V_f}}{V_f}\right)^2\right]^{1/2} \tag{4.25}$$

The uncertainty of pressure gradient was stated as:

$$\frac{\omega_{\Delta P/L}}{\Delta P/L} = \left[\left(\frac{\omega_{\Delta P}}{\Delta P}\right)^2 + \left(\frac{-\omega_L}{L}\right)^2\right]^{1/2} \tag{4.26}$$

An example for uncertainty calculation of convection coefficient was given in Appendix B.

4.5. Pressure Drops of the Fin Block and Metal Foam Embedded Heat Sinks

Pressure drops of the test specimens were calculated via the power of the fan as in Equation 4.24. The Reynolds numbers of fin block which were calculated in Equation 4.13 proved that flow was in laminar regime. The pressure drops, the Reynolds numbers of the fin block and their uncertainties are presented in Table 4.5. The pressure drops of the fin block were lower than all other kinds of metal foam heat sinks.

Table 4.5 The pressure drops of the fin block

	$\dot{m}$ (kg/h)	ΔP (Pa)	Re	$\omega_{\Delta P}$ (%)	ω_{Re} (%)
Bare Fin	33	36	957	10.32	4.70
	50	70	1435	9.22	6.99

Column 2 of Table 4.6 shows the pressure drops of the foam embedded heat sinks calculated by using fan power consumption measurement whereas column 3 shows the pressure drops of the foams having the same structure were calculated with Hazen-Dupuit-Darcy equation [3, 26]. Mancin calculated the pressure drops with Equation 2.4. The Reynolds number of the porous media was calculated as shown in Equation 4.27 where the permeability values of the foam samples were taken from Mancin's studies [3, 26]. Although the porosity and pore density of the tested foams were similar to Mancin's study, the pressure drops have to be different from those of Mancin's study.

$$\mathrm{Re} = \frac{\rho U \sqrt{K}}{\mu} \tag{4.27}$$

For the current study, due to the thickness and the alignment of the foam, pressure drop values had to be lower than those of Mancin's. The pressure drop data, calculated via the power of the fan were approximately 35-40% of Mancin's data (see also Figure 4.18). Alvarez's [31] study also confirmed the calculated data with a similar experiment. In Alvarez's study, pressures of the same pore density samples were decreased by reducing the thickness. The staircase alignment of the foams reduced the pressure drops of the specimens as demonstrated in Table 4.6. The pressure drop variation versus pore density is shown in Table 4.6 and Figure 4.18. It is obvious that increase of pore density and air frontal velocity enhance the pressure drops of foam heat sinks. It is known that whereas aluminium foam samples have

93% porosity, copper ones have 90.5% porosity. The effect of this porosity difference is also seen in Table 4.6. In fact, higher porosity aluminium heat sinks have higher pressure drop values compared to copper heat sinks.

Table 4.6 Tabulated Pressure Drop Results

	1	2	3	4	5
	Mass Flow Rate in Experiment	Pressure Drop (Measured)	Pressure Drop (Calculated from HDD Eqn.)	Pressure Drop Measurement Uncertainty	Calculated Re Num.
Foam	$\dot{m}$ (kg/h)	ΔP (Pa)	$\Delta P_{cal.}$ (Pa)	$\omega_{\Delta P}$ (%)	$Re_{cal.}$
AL10PPI	33	80	199.87	8.92	131
	50	157	436.93	8.07	196
AL20PPI	33	93	256.14	8.74	87
	50	208	547.32	8.04	130
AL40PPI	33	148	379.35	8.43	76
	50	292	815.85	8.19	114
CU10PPI	33	71	181.26	8.56	105
	50	141	388.08	7.72	158
CU20PPI	33	84	244.04	7.96	70
	50	189	504.27	7.25	105
CU40PPI	33	139	356.53	8.27	61
	50	250	743.95	7.46	92

The air velocity directly increases the pressure drops and the Reynolds numbers of all the tested specimens. At the Mancin's study, a rectangular box was selected as the geometry of foams. The effect on the pressure drop of the staircase structure of the heat sinks can be seen in Figure 4.18

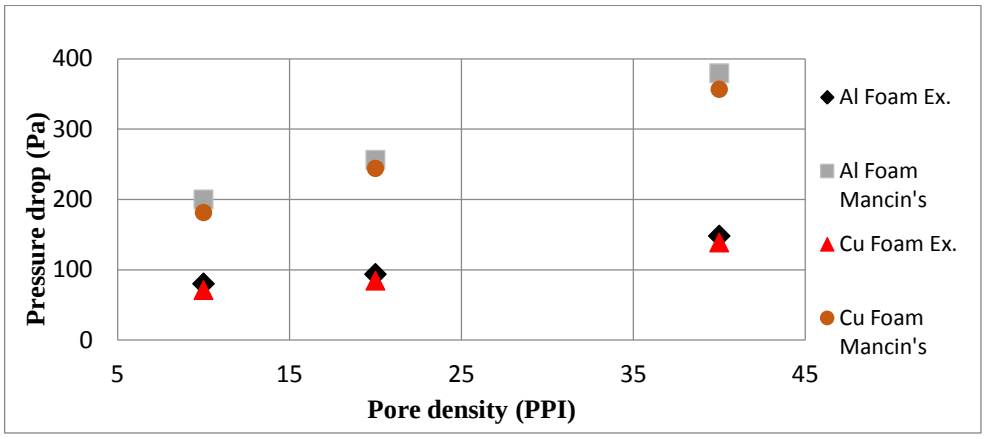

Figure 4.18 Variation of drop of tested heat sinks and Mancin's results [3, 26] with respect to the pore densities

4.6. Heat Transfer Results of Conventional Fin Block

Experimentally calculated Nusselt numbers and the thermal resistance of the fin block were stated in Table 4.7. Equation 4.17 and Equation 4.22 are used for Nusselt numbers and the thermal resistance calculations respectively. The average temperature of the base surface is the average temperature value of the nine thermocouples that were placed in the base plane as in Equation 4.15.

Table 4.7 Nusselt numbers, the heat transfer coefficients and the thermal resistances of fin block

	Heater (W)	$\dot{m}$ (kg/h)	R_{TH} (^oC/W)	Nu	ω_{rt} (%)	ω_{Nu} (%)
Bare Fin	60	33	0.346	5.90	8.29	7.47
	80		0.339	5.41	8.19	7.60
	120		0.365	5.13	7.59	7.75
	160		0.337	5.25	7.95	8.67
	60	50	0.290	6.44	8.46	7.43
	80		0.242	6.51	8.35	7.51
	120		0.305	6.33	7.63	7.21
	160		0.225	6.63	8.03	8.17

The measurement uncertainties of both thermal resistances and Nusselt numbers were lower than 9%. Nusselt number variations at different heater loads are assumed to be related to this inaccuracy. Measured temperatures of all heat sinks' base planes are given in Appendix A. Furthermore, thermal resistances of the fin block at the two partial 60W and 120W heaters are higher than 80W and 160W whole heaters. At the two partial heaters case, the shortage of the heat transfer surface area had a vital role in forcing of the heat flow from the heater to the air.

4.7. Heat Transfer Results of Metal Foam Embedded Heat Sinks

In this experiment, the convection coefficients, Nusselt numbers and hydraulic diameter of metal foams were calculated from Equation 4.20, Equation 4.17 [31] and Equation 4.18 [10]. Nusselt numbers of the foam embedded heat sinks are higher than the fin block as demonstrated in Table 4.8 and Table 4.9. The thermal resistance, Nusselt numbers, the convection coefficients of the tested foam embedded heat sinks are presented in Table 4.8 and Table 4.9. While Table 4.8 shows the results of the foam embedded heat sinks at 4 m/s air inlet velocity, Table 4.9 shows the results of foam embedded heat sinks at 6 m/s air inlet velocity.

Table 4.8 The heat transfer coefficients, Nusselt numbers and the thermal resistances of the metal foam embedded heat sinks at 4 m/s air velocity

	Heater (W)	$\dot{m}$ (kg/h)	R_{TH} ($^oC/W$)	$\bar{h}$ ($W/m^{2o}C$)	Nu	$\omega_{R_{th}}$ (%)	ω_h (%)	ω_{Nu} (%)
Al 10PPI	60	33	0.290	39.79	62.75	8.34	5.91	7.64
	80	33	0.324	39.94	62.99	7.91	5.42	7.48
	120	33	0.352	38.52	60.75	7.77	4.95	7.77
	160	33	0.324	39.28	61.94	7.83	4.57	8.53
Al 20PPI	60	33	0.287	27.35	43.13	8.05	5.56	7.34
	80	33	0.331	26.18	41.29	7.75	5.11	7.22
	120	33	0.333	26.24	41.37	7.65	4.65	7.61
	160	33	0.266	25.81	40.71	8.30	4.36	9.21
Al 40PPI	60	33	0.260	18.03	28.44	8.46	5.74	7.58
	80	33	0.261	17.62	27.78	8.14	5.24	7.67
	120	33	0.250	17.30	27.27	8.33	4.77	8.62
	160	33	0.264	17.47	27.55	8.47	4.33	9.34
CU 10PPI	60	33	0.273	42.41	66.88	8.66	6.13	7.79
	80	33	0.241	43.86	69.16	8.21	5.64	7.86
	120	33	0.251	42.99	67.80	8.20	5.16	8.40
	160	33	0.319	43.99	69.37	7.93	4.81	8.28
CU 20PPI	60	33	0.105	37.08	58.47	8.94	6.53	8.64
	80	33	0.145	32.27	50.88	8.53	5.58	8.60
	120	33	0.138	31.86	50.24	9.42	5.21	10.35
	160	33	0.141	30.92	48.76	10.36	4.77	12.12
CU 40PPI	60	33	0.185	24.19	38.14	8.59	6.03	7.82
	80	33	0.196	23.06	36.36	8.52	5.68	7.97
	120	33	0.217	23.44	36.96	8.06	4.90	8.09
	160	33	0.229	23.77	37.48	8.23	4.61	8.65

On the other hand, pore density increases the heat transfer area of the foams and Nusselt numbers decays with a rising pore density, on the other hand, the increase pore density reduces thermal resistance of all heat sinks except for 20PPI copper foam. This exception is originated from the closed cells of the copper foam as defined in Figure 4.5. Calculated uncertainty values were almost lower than 10% for all parameters. High thermal conductivity of the copper samples ensured the superior thermal performance to copper foams. The effects of air velocity can appear when the heat transfer coefficients and thermal resistances of Table 4.8 are compared to those of Table 4.9. 10 PPI copper embedded heat sinks had the highest heat transfer coefficients. The 10 PPI aluminium embedded heat sinks took the second place.

Table 4.9 The heat transfer coefficients, Nusselt numbers and the thermal resistances the of metal foam embedded heat sinks at 6 m/s air velocity

	Heater (W)	$\dot{m}$ (kg/h)	R_{th} ($^oC/W$)	$\bar{h}$ ($W/m^2.^oC$)	Nu	$\omega_{R_{th}}$ (%)	ω_h (%)	ω_{Nu} (%)
Al 10PPI	60	50	0.207	49.50	78.06	8.49	6.15	7.55
	80	50	0.219	59.13	93.24	8.15	5.68	7.37
	120	50	0.237	49.69	78.36	8.02	5.27	7.57
	160	50	0.207	53.40	84.21	7.76	4.87	7.94
Al 20PPI	60	50	0.182	34.72	54.75	8.38	5.89	7.48
	80	50	0.207	34.14	53.83	7.94	5.36	7.24
	120	50	0.220	34.75	54.80	7.85	4.99	7.37
	160	50	0.189	34.56	54.50	7.80	4.60	8.02
Al 40PPI	60	50	0.170	22.39	35.31	8.54	5.91	7.56
	80	50	0.220	22.34	35.23	8.19	5.42	7.27
	120	50	0.214	22.39	35.31	8.03	4.98	7.50
	160	50	0.191	22.57	35.58	7.97	4.56	8.14
CU 10PPI	60	50	0.178	53.68	84.64	8.93	6.42	7.90
	80	50	0.205	56.21	88.64	8.44	5.91	7.60
	120	50	0.236	55.37	87.32	8.09	5.38	7.49
	160	50	0.203	56.56	89.19	7.94	5.04	7.91
CU 20PPI	60	50	0.074	42.02	66.26	9.02	6.48	8.59
	80	50	0.086	42.71	67.35	8.21	5.61	8.21
	120	50	0.084	41.15	64.89	9.12	5.47	9.68
	160	50	0.134	41.48	65.41	8.50	5.07	8.74
CU 40PPI	60	50	0.119	31.90	50.30	8.74	6.26	7.84
	80	50	0.171	33.60	52.99	8.45	5.82	7.48
	120	50	0.151	32.18	50.75	8.12	5.22	7.67
	160	50	0.152	31.66	49.92	8.20	5.00	8.05

The increase of pore density impeded the air flow through the metal foam. As a result, the convective heat transfer from the metal foam to air reduced by increasing pore density as expected.

Finally, it is understood that thermal resistance is directly dependent on pore density of foam samples. All thermal resistances, except for 20PPI copper, were lessened with pore density. As stated in results, the Nusselt numbers decline along with the rise of heat transfer areas decreases. This means that the increase of pore density increases the conduction heat transfer of foam metals.

Figure 4.19 and Figure 4.20 show the thermocouple temperatures of the base plane at the stated conditions. Due to the locations of the heaters, temperatures on the foam sides were higher than TC9 and TC5 in Figure 4.19. In addition, the metal foam parts in Figure 4.20 provided temperature values to get close to each other.

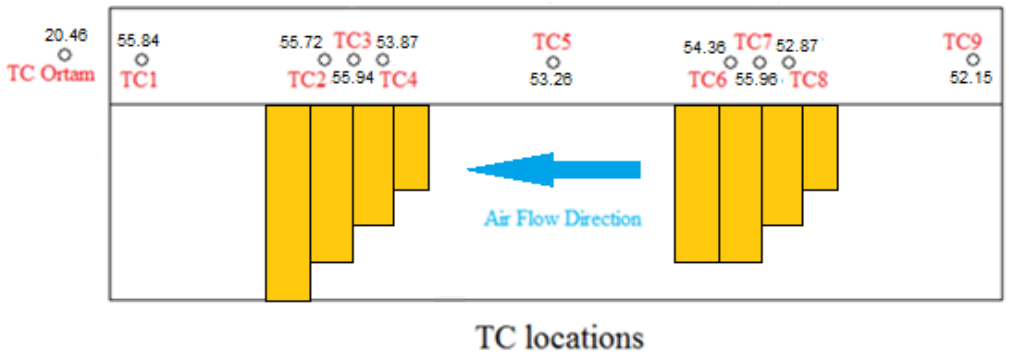

Figure 4.19 Surface temperatures of CU 20PPI at a 2 section 120 watt heater at 6 m/s air velocity

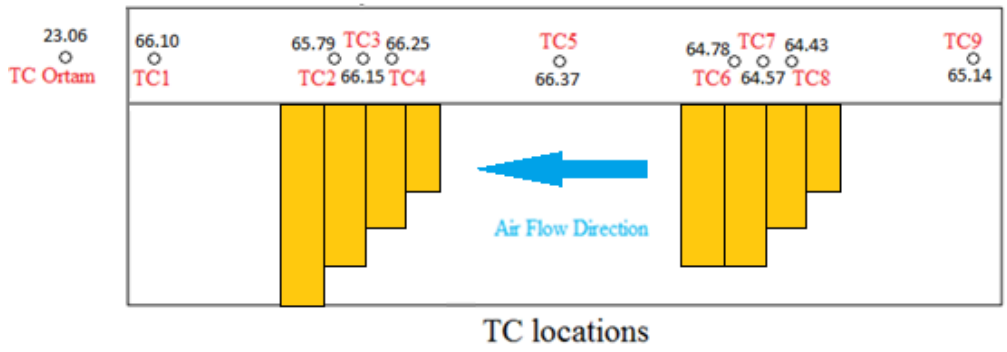

Figure 4.20 Surface temperatures of CU 20PPI at a whole 160 watt heater at 6 m/s air velocity

Heat transfer coefficients (HTC) of each sample showed similar values at various heaters as mentioned in Mancin's study [3]. In addition, the order of the heat transfer

coefficients with respect to pore density of the present study and Mancin's study supports one another [3]. Another study carried out by Mancin indicated that 10 PPI aluminium sample had lower mean wall temperature than 20PPI and 40 PPI foams which are at the same porosity, as in Figure 4.21.

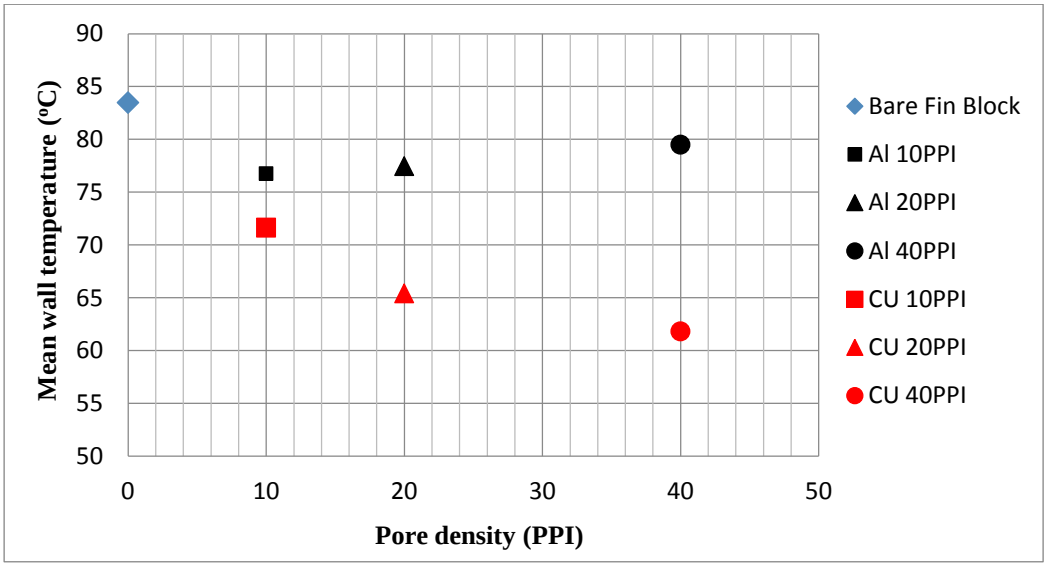

Figure 4.21 Mean wall temperature as a function of pore density at 160 W heater and 6 m/s frontal air velocity

At the copper samples, increase of pore density decreases the mean wall temperature of the heat sinks as seen in Figure 4.21. On the contrary, mean wall temperatures of the aluminium heat sinks increase with pore density. This can be interpreted as, higher porosity and lower thermal conductivity of the aluminium foams slowed the heat flow from foam surface to air. Pore density versus mean wall temperature, resistance graphs of other heaters at 6 m/s are given in Appendix C.

4.8. The Performance Comparison of the Heat Sinks

This study has one ultimate goal that is to determine the heat sink which will give the lowest base temperature at a specified heater load and inlet air temperature, with the lowest air pressure drop. Graphs from 4.24 to 4.25 were prepared for the evaluation of the heat sinks with the best performance heat sinks for this goal. The thermal resistances of the heat sinks were calculated by implementing Equation 4.22.

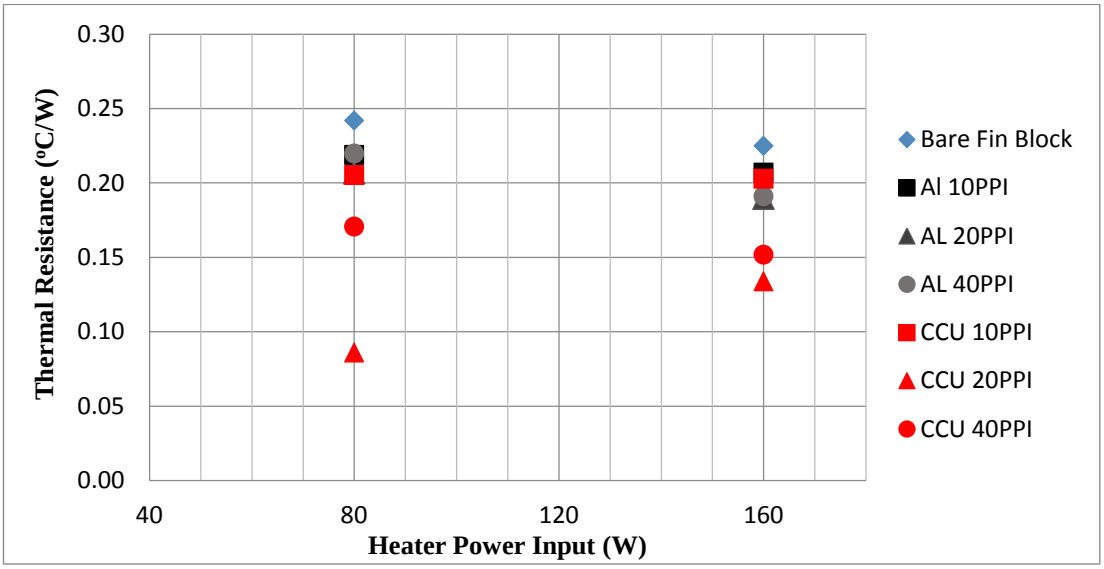

Figure 4.22 Variation of R_{th} as a function of heater power at 50 kg/h mass flow rate (whole heaters)

As it can be seen in Figure 4.22 thermal resistances of heat sinks drop down at 160 W heater loads. There could be a breakeven point beyond which heat sink works effectively. The effectiveness of the heat sink depends on the heater load and the geometrical configuration of the heat sink, which seems to be worth investigating in further studies.

20PPI foam embedded heat sinks do not fit in this generalization. The reason of this discrepancy can be originated from the closed cells structure of the copper foam plates. It is clearly understood from the Figure 4.22 that the fin block has the highest thermal resistances at both heat loads. While the thermal resistances of the aluminium foams are close to each other, thermal resistances of copper foams illustrate differences. The effect of the thermal conductivity of copper samples is seen in 20PPI and 40PPI copper foam embedded heat sinks which have the lowest thermal resistances.

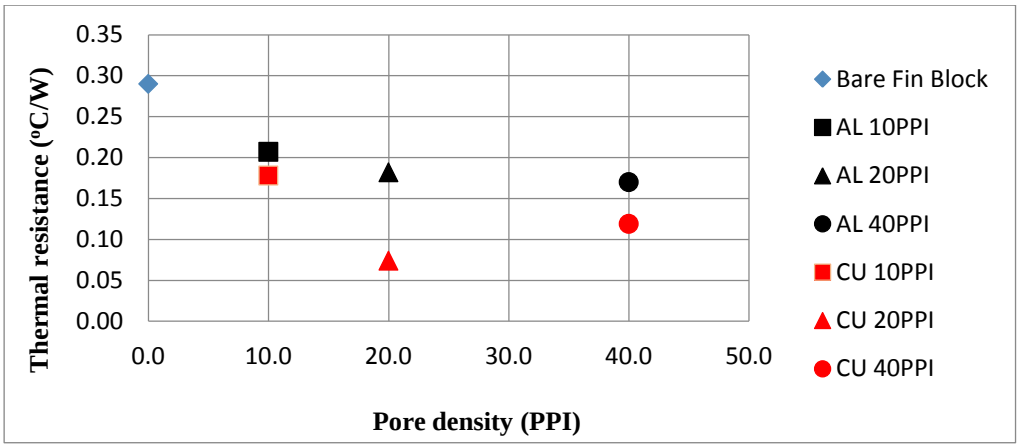

Figure 4.23 Variation of R_{th} as a function of pore density at a 60W heater and 6 m/s frontal air velocity

It is observed that the increase of pore density decreases the thermal resistance of heatsinks except for 20 PPI copper sample as seen in Figure 4.23. Even with the limited usage of metal foam, the thermal resistance of metal foam embedded heat sinks are significantly lower than the thermal resistance of the fin block as shown in Figure 4.23. Pore density versus thermal resistance graphs of other heaters at 6 m/s are given in Appendix C. The pressure drop and the thermal resistance are the design criteria of heat sinks as stated in Figure 4.24. Both the thermal resistance and the pressure drop values of 20PPI copper embedded heat sink are the lowest values. Therefore, 20PPI copper embedded heat sink was found to have the highest heat sink performance in the experiments.

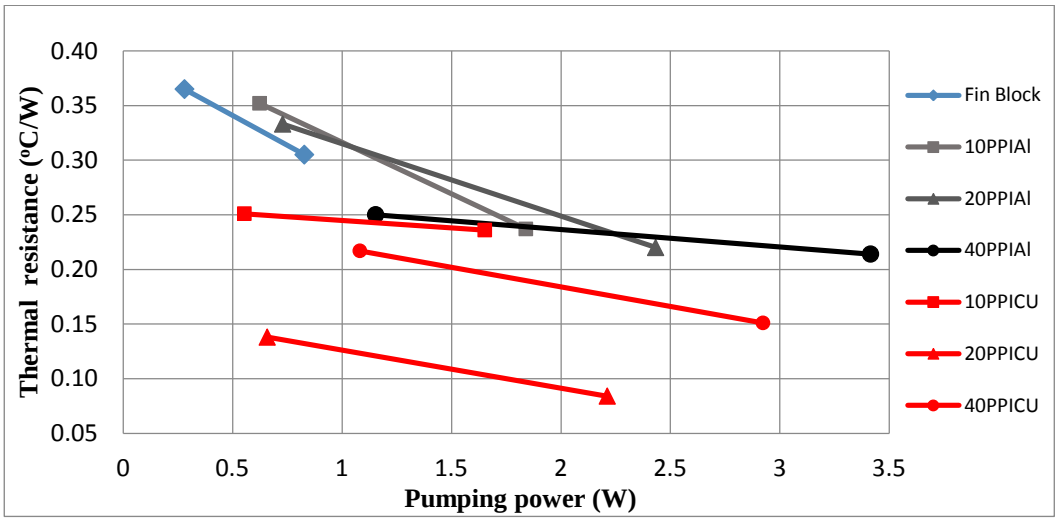

Figure 4.24 Variation of R_{th} as a function of pumping power at 120W heating

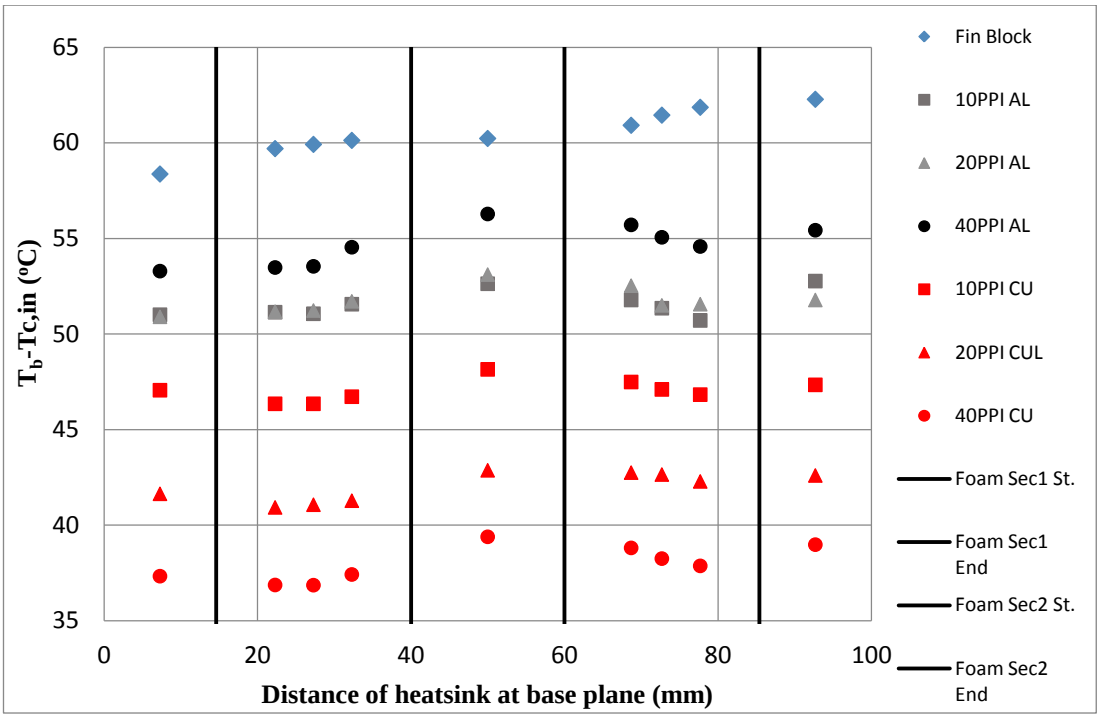

Figure 4.25 Variation of base plane temperatures as a function of distance at 160 W heater

Figure 4.25 demonstrates the base plane temperatures of the samples and the vertical lines indicate the foam boundaries of the heat sinks. It is seen that the temperatures increased in the first foam section while fresh air provided from 5 mm gap decreased the second foam section. At the fin block the temperature continued to increase, which is undesired for the operational life of the electronic components. Finally, the 40PPI copper foam heat sink provided the lowest base plane temperatures however 20PPI copper foam heat sink was the most effective considering the pressure drop and the thermal resistance together. Moreover, the 20PPI foam heat sink produced less noise compared to the 40PPI foam heat sink. The metal foam structured heat exchangers reduced the thermal resistance by nearly two thirds when compared to a conventional fin block.

CHAPTER 5

COMPARISON OF THE THERMAL PERFORMANCE OF PARTIALLY METAL FOAM EMBEDDED HEAT SINK WITH A CONVENTIONAL FIN BLOCK USING NUMERICAL METHODS

In this chapter numerical analyses of partially metal foam embedded heat sink specimen are performed. Also, the numerical analyses of a similar geometry fin block, which was used in experiments, are performed to show that the utilization of the metal foam embedded sink is a more effective method to cool the electronic equipment. During this numerical comparison, the attention has been given to select the similar variables as in the experiments in order to provide an accurate verification. Commercially available FLUENT software was used to perform the related numerical analyses. In this chapter, the numerically analysed geometries, the boundary conditions and the FLUENT approaches onto the porous zones are also stated. The meshes of the geometries and the implementation steps of these geometries into the FLUENT are stated in Appendix D.

5.1. Numerical Models of Fin Block and Foam Embedded Heat Sink

The geometric models of both the fin block and the partially foam embedded heat sink are defined in following sections. Technical drawings of the specimens are given in Appendix A. In order to simplify the analysis, only the heat sink geometries are modelled and the walls are considered as adiabatic.

5.1.1. Models of foam embedded heat sink

The numerically modelled partially metal foam embedded heat sink is presented in Figure 5.1. As it can be seen in Figure 5.1 that the metal foam embedded heat sink was designed as a part of the channel below the surface to be cooled. It was intended to be kept at acceptable levels. The temperature of the surface was cooled, which is the part of the channel, by passing air through channel. The heat emitting electronic components were assumed to be at the unseen bottom surface of the heat sink (see Figure 5.1), which is desired to remain cool. It was aimed that this base plane to be cooled by the soldered metal foams. The heights of the metal foams, which were positioned perpendicular to the flow direction increase as seen in the flow direction. Although the utilization of constant height rectangular cross section foam geometry was planned initially, it was thought that because of the increase in air temperature while passing through the metal foam, which decreases cooling capacity of the air at the downstream side, the geometry was considered to be inappropriate for heat sink design. Therefore, longer foams were selected at the downstream in comparison to the upstream foams.

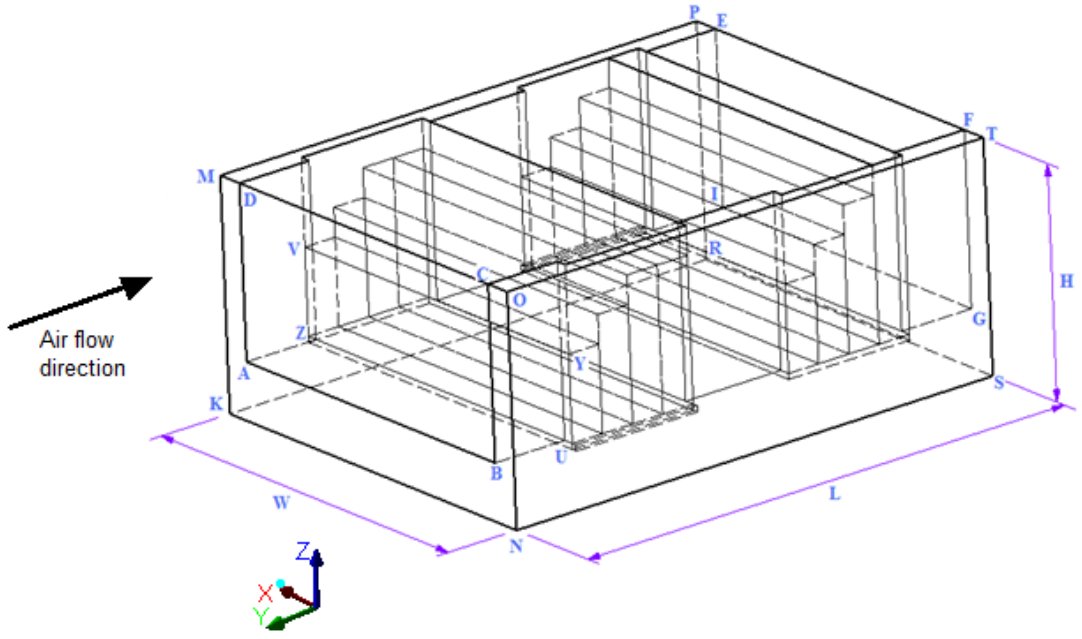

Figure 5.1 Solution domain of foam embedded heat sink model

5.1.2. The model of the fin block

To show the cooling superiority of the metal foam embedded heat sink and to compare the thermal performances of the metal foam embedded heat sink with a fin block, a fin block model, which removes heat from base plane by a fin array, was used in numerical analyses is seen in Figure 5.2. At the model, it was assumed that the fins were located on the one side of the base plane and the heat generating electronic components were located on other side of base plane. Fins, which are plate fins, were arranged parallel to the flow direction. While the air passed through the channels between the plate fins, it takes heat from the fin surfaces so that the base plate dissipated the heater loads. To obtain the accurate results in performed comparisons, similar air flow rate, geometrical dimensions and other thermodynamic parameters were chosen in numerical analyses.

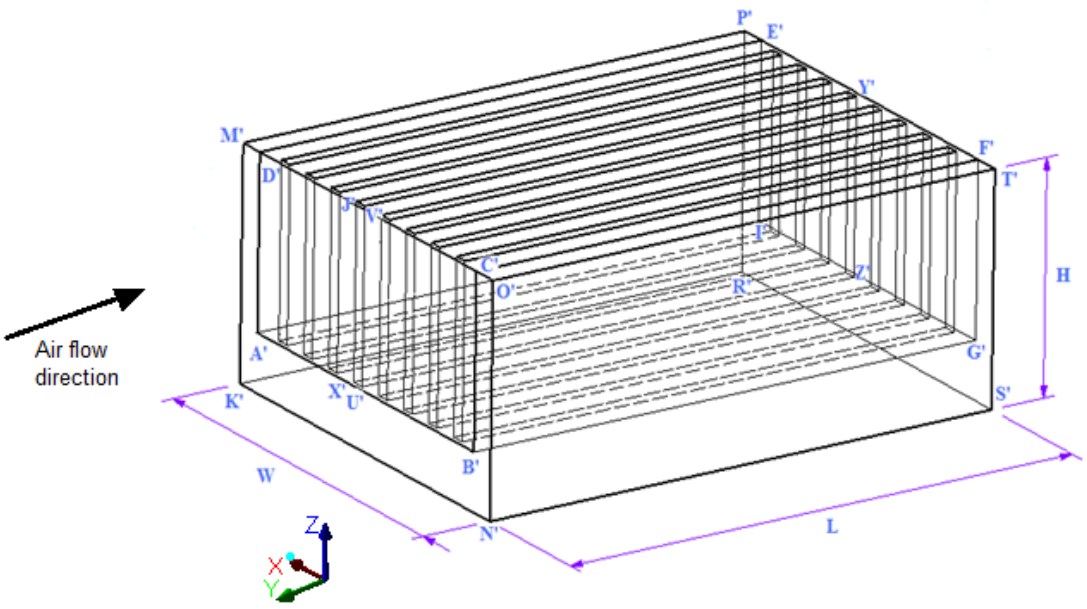

Figure 5.2 Solution domain of the fin block model

5.1.3. Contact surfaces of the foams

During the experiments soldering was used to bond the metal foams and the base plane. Although the soldered layer was very thin it created a thermal resistance against the heat flow from the base plane to the metal foam. Therefore, this contact surface was thought as a zone with a volume in the numerical modeling. The thermal conductivity of this new zone was calculated from Equation 5.1. Green areas in Figure 5.3 present junction zones of solder and the metal foam.

$$k_{eff} = \varepsilon k_f + (1 - \varepsilon) k_s \tag{5.1}$$

k_{eff} overall thermal conductivity of junction parts

ε porosity of soldered metal foam

k_f thermal conductivity of solder

k_s thermal conductivity of the metal foam

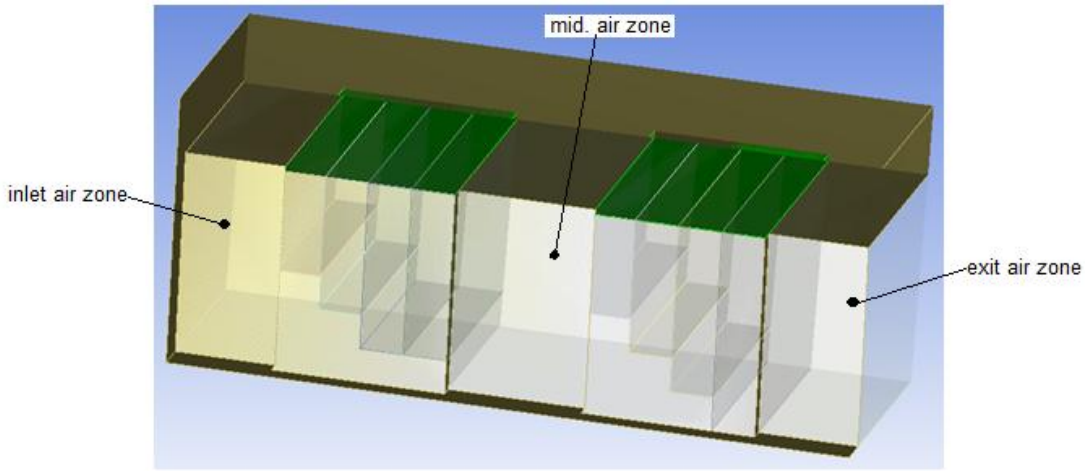

Figure 5.3 The presentation of the foam contact zones on the section view of the metal foam embedded heat sink geometry

5.1.4. The heater locations of the test specimens

At the numerical model, heaters, which simulate the heat generation of the electronic components and heats the base plane, are shown in Figure 5.4. Heat sources are placed in two different ways. The first ones are one-inch thick strip heat sources which are perpendicular to the air flow direction at certain intervals (Figure 5.4 (a)), the second one is a uniformly distributed heat source on the whole base plane (Figure 5.4 (b)).

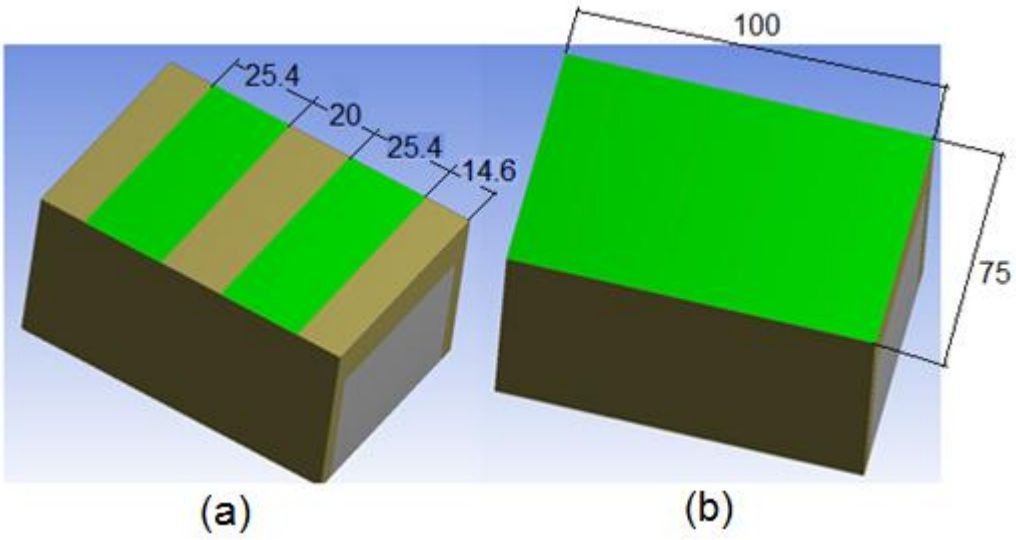

Figure 5.4 (a) Partial heaters; (b) the demonstration of the whole heater on the model of numerical analyses

The heat flux values were entered to FLUENT as the boundary conditions. The fluxes and the dimensions of heater dimensions are tabulated as in Table 5.1. These heat flux values were calculated by division of heater power by heaters contact areas.

Table 5.1 Imported heat flux values for CFD

Heater conf.	Heater Power (W)	Dimensions of heaters (mm) (W × L)	Real heat flux of heaters (W/m^2)	CFD imported heat fluxes (W/m^2)
2 partial Heaters	60	25.4x75 (2 pcs.)	31496	15750
	120	25.4x75 (2 pcs.)	62992	31500
Whole Heater	80	75x100 (1 pc)	10667	10650
	160	75x100 (1 pc)	21333	21300

5.1.5. General Equations

The three dimensional laminar incompressible continuum, momentum and energy equations were used for the fin block model and foamless zones of the foam embedded heat sinks. Also, the three dimensional conduction equations were used for heating surfaces and inside the fin block.

Conduction equation:

Physical properties of aluminium, i.e., the thermal conductivity, density, specific heat, were assumed to be constant during the analyses. There is also no heat generation occurring inside the aluminium.

$$\nabla^2 T = 0 \tag{5.2}$$

At the Cartesian coordinates Equation 5.2 can be presented as below.

$$\frac{\partial^2 T}{\partial x^2} + \frac{\partial^2 T}{\partial y^2} + \frac{\partial^2 T}{\partial z^2} = 0 \tag{5.3}$$

Conservation of mass equation:

Mass conservation equation is presented as in Equation 5.4.

$$\frac{\partial \rho}{\partial t} + \frac{\partial (\rho u)}{\partial x} + \frac{\partial (\rho v)}{\partial y} + \frac{\partial (\rho w)}{\partial z} = 0 \tag{5.4}$$

Assumption simplified Equation 5.4 to Equation 5.5.

$$\frac{\partial u}{\partial x} + \frac{\partial v}{\partial y} + \frac{\partial w}{\partial z} = 0 \tag{5.5}$$

Momentum equation:

General expression of momentum equation is stated in Equation 5.6.

$$\frac{\partial (\rho \mathbf{u})}{\partial t} + \left(\mathbf{u}\vec{\nabla}\right)(\rho \mathbf{u}) = -\nabla P + \mu(\nabla^2 \mathbf{u}) + \vec{g}\rho_f \tag{5.6}$$

Considering the continuity assumptions momentum equations at the Cartesian coordinates can be written as below.

Momentum equation at the x-direction

$$\left(u\frac{\partial u}{\partial x}+v\frac{\partial u}{\partial y}+w\frac{\partial u}{\partial z}\right)=-\frac{1}{\rho}\frac{\partial P}{\partial x}+\nu\left(\frac{\partial^2 u}{\partial x^2}+\frac{\partial^2 u}{\partial y^2}+\frac{\partial^2 u}{\partial z^2}\right) \tag{5.7}$$

Momentum equation at the y-direction

$$\left(u\frac{\partial v}{\partial x}+v\frac{\partial v}{\partial y}+w\frac{\partial v}{\partial z}\right)=-\frac{1}{\rho}\frac{\partial P}{\partial y}+\nu\left(\frac{\partial^2 v}{\partial y^2}+\frac{\partial^2 v}{\partial y^2}+\frac{\partial^2 v}{\partial y^2}\right) \tag{5.8}$$

Momentum equation at the z-direction

$$\left(u\frac{\partial w}{\partial x}+v\frac{\partial w}{\partial y}+w\frac{\partial w}{\partial z}\right)=-\frac{1}{\rho}\frac{\partial P}{\partial z}+\nu\left(\frac{\partial^2 w}{\partial x^2}+\frac{\partial^2 w}{\partial y^2}+\frac{\partial^2 w}{\partial z^2}\right) \tag{5.9}$$

Energy Equation:

General form of energy equation is given in Equation 5.10.

$$\frac{\partial(\rho\mathbf{u})}{\partial t}+(\mathbf{u}\nabla)(\rho T)=\frac{k}{c_p}(\nabla^2 T) \tag{5.10}$$

Considering the continuity assumptions energy equation at the Cartesian coordinates can be written as in Equation 5.11.

$$\left(u\frac{\partial T}{\partial x}+v\frac{\partial T}{\partial y}+w\frac{\partial T}{\partial z}\right)=\frac{k}{\rho c_p}\left(\frac{\partial^2 T}{\partial x^2}+\frac{\partial^2 T}{\partial y^2}+\frac{\partial^2 T}{\partial z^2}\right) \tag{5.11}$$

Two different methods were selected to solve the thermal behaviour of the foam embedded heat sink. At the first method, the whole flow in the heat sink is assumed to be laminar; therefore, below expressions are solved for this analysis. Velocity of porous zone is calculated from Equation 5.12.

$$\boldsymbol{U} = \varepsilon_{unc} U_p \tag{5.12}$$

$\boldsymbol{U}$ Darcy velocity (m/s)

U_p pore averaged velocity (m/s)

The Conservation of mass equation in a porous zone:

$$\frac{\partial}{\partial t}(\varepsilon\rho_f) + \nabla.(\rho_f \boldsymbol{U}) = 0 \tag{5.13}$$

The continuity equation of porous zones at the Cartesian coordinates can be written as below.

$$\frac{\partial(\varepsilon\rho_f)}{\partial t} + \frac{\partial(\rho_f \boldsymbol{U})}{\partial x} + \frac{\partial(\rho_f \boldsymbol{U})}{\partial y} + \frac{\partial(\rho_f \boldsymbol{U})}{\partial z} = 0 \tag{5.14}$$

Momentum equation in a laminar porous zone:

The general form of momentum equation for the laminar flow inside the porous medium is stated in Equation 5.15. A new source (***F***) term is added at the right side of the equation.

$$\frac{\partial(\rho_f \varepsilon \boldsymbol{U})}{\partial t} + \nabla.(\rho_f \boldsymbol{U}\boldsymbol{U}) = -\nabla P + \mu(\nabla^2 \boldsymbol{U}) + \rho_f \vec{g} + \boldsymbol{F} \tag{5.15}$$

For homogenous porous media $\boldsymbol{F}$ is presented:

$$\boldsymbol{F} = -\left(\frac{\mu \boldsymbol{U}}{K} + C\rho \boldsymbol{U}^2\right) \tag{5.16}$$

K is the directional permeability coefficient of porous zones and C is directional drag coefficient of porous zones.

Momentum equation in porous media at the x-direction

$$-\frac{\partial P}{\partial x} = \frac{\mu \boldsymbol{U}}{K_x} + C_x \rho \boldsymbol{U}^2 \tag{5.17}$$

Momentum equation in porous media at the y-direction

$$-\frac{\partial P}{\partial y} = \frac{\mu \boldsymbol{U}}{K_y} + C_y \rho \boldsymbol{U}^2 \tag{5.18}$$

Momentum equation in porous media at the z-direction

$$-\frac{\partial P}{\partial y} = \frac{\mu \boldsymbol{U}}{K_z} + C_z \rho \boldsymbol{U}^2 \tag{5.19}$$

Energy Equation in a porous zone:

Equation 5.20 is used for laminar porous zones by FLUENT.

$$\left(\rho c_p\right)_{\text{pm}} \left(\frac{\partial T_{\text{pm}}}{\partial t} + \boldsymbol{U} \cdot \nabla T_{\text{pm}}\right) = \nabla \cdot \left(k_{\text{eff}} \nabla T_{\text{pm}}\right) \tag{5.20}$$

T_{pm} temperature of a porous medium (℃)

The first term of Equation 5.21 is calculated form Equation 5.20.

$$\left(\rho c_p\right)_{\text{pm}} = \left(\rho c_p\right)_{\text{s}} (1 - \varepsilon) + \left(\rho c_p\right)_{\text{f}} (\varepsilon) \tag{5.21}$$

When the continuity assumptions in energy equation in porous medium are considered they lead to:

$$\left(\boldsymbol{U} \frac{\partial T_{\text{pm}}}{\partial x} + \boldsymbol{U} \frac{\partial T_{\text{pm}}}{\partial y} + \boldsymbol{U} \frac{\partial T_{\text{pm}}}{\partial z}\right) = \frac{k_{\text{eff}}}{\left(\rho c_p\right)_{\text{pm}}} \left(\frac{\partial^2 T_{\text{pm}}}{\partial x^2} + \frac{\partial^2 T_{\text{pm}}}{\partial y^2} + \frac{\partial^2 T_{\text{pm}}}{\partial z^2}\right) \tag{5.22}$$

In the other method, the metal foam regions of the heat sink were solved by the k-epsilon turbulence procedure. The general momentum equation of k-epsilon turbulence procedure in porous media is given in the following equations.

For κ

$$\rho\left[\frac{\partial}{\partial t}\left(\varepsilon\langle\kappa\rangle^{i}\right)+\nabla.\left(\boldsymbol{U}\langle\kappa\rangle^{i}\right)\right]=\nabla\cdot\left[\left(\mu+\frac{\mu_{t_\varepsilon}}{\sigma_\kappa}\right)\nabla\left(\varepsilon\langle\kappa\rangle^{i}\right)\right]$$
$$-\rho\langle\overline{U'U'}\rangle^{i}:\nabla\boldsymbol{U}+c_\kappa\rho\varepsilon\frac{\langle\kappa\rangle^{i}|\boldsymbol{U}|}{\sqrt{K}}-\rho\varepsilon\langle\epsilon\rangle^{i} \quad (5.23)$$

In Equation 5.23, κ is the turbulent kinetic energy per unit mass, ϵ is the dissipation rate of turbulence kinetic, μ_t is the macroscopic turbulent viscosity, μ_{t_ε} is the macroscopic turbulent viscosity of porous zones, $\langle\kappa\rangle^{i}$ is the intrinsic fluid average of κ, $\langle\epsilon\rangle^{i}$ is the intrinsic fluid average of ϵ, σ_κ is the turbulent Prandtl number of κ, σ_ϵ is the turbulent Prandtl number of ϵ, U' is the fluctuating component of velocity and c_κ is the non-dimensional constants.

For ϵ

$$\rho\left[\frac{\partial}{\partial t}\left(\varepsilon\langle\epsilon\rangle^{i}\right)+\nabla.\left(\boldsymbol{U}\langle\epsilon\rangle^{i}\right)\right]=\nabla\cdot\left[\left(\mu+\frac{\mu_{t_\varepsilon}}{\sigma_\epsilon}\right)\nabla\left(\varepsilon\langle\epsilon\rangle^{i}\right)\right]$$
$$+c_{1\epsilon}\left(-\rho\langle\overline{U'U'}\rangle^{i}:\nabla\boldsymbol{U}\right)\frac{\langle\epsilon\rangle^{i}}{\langle\kappa\rangle^{i}}+c_{2\epsilon}\rho\varepsilon\left\{c_\kappa\frac{\langle\epsilon\rangle^{i}|\boldsymbol{U}|}{\sqrt{K}}-\frac{\langle\epsilon\rangle^{i^2}}{\langle\kappa\rangle^{i}}\right\} \quad (5.24)$$

With

$$-\rho\langle\overline{U'U'}\rangle^{i}=\mu_{t_\varepsilon}2\langle\bar{\mathbf{D}}\rangle^{v}-\frac{2}{3}\varepsilon\rho\langle\kappa\rangle^{i}\mathbf{I} \quad (5.25)$$

$$\mu_{t_\varepsilon}=\rho c_\mu\frac{\langle\kappa\rangle^{i^2}}{\langle\epsilon\rangle^{i}} \quad (5.26)$$

In above equations, $c_{1\epsilon}, c_{2\epsilon}, c_\mu, c_\kappa$ are the non-dimensional constants, **D** is the deformation tensor.

Energy Equation in a porous zone:

Equation 5.27 is used for the turbulent porous zones by FLUENT.

$$\left(\rho c_p\right)_{\mathrm{pm}} \frac{\partial \langle T_{\mathrm{pm}} \rangle^i}{\partial t} + \left(\rho c_p\right)_{\mathrm{f}} \nabla \cdot \left(\boldsymbol{U} \cdot \nabla \langle T_{\mathrm{pm}} \rangle^i\right)$$

$$= \nabla \cdot \left(k_{\mathrm{eff}} \nabla T_{\mathrm{pm}}\right) + \nabla \cdot \left[\frac{1}{\Delta \mathrm{V}} \int_{\mathrm{A_i}} \mathbf{n}\left(k_f \overline{T}_{\mathrm{f}} - k_s \overline{T}_s\right) \mathrm{dS}\right]$$

$$-\left(\rho c_p\right)_{\mathrm{f}} \nabla \cdot \left[\varepsilon(\langle\, {}^i\overline{U}\ {}^i\overline{T}_{\mathrm{f}} \rangle^i + \langle \overline{U' T_f'} \rangle^i)\right] \qquad (5.27)$$

In Equation 5.27, ΔV is REV, S is the swirl parameter, A_i is the interface area between porous region and the clear flow, $\overline{U}$ is the time averaged velocity, $\overline{T}$ is the time averaged temperature.

5.1.6. The boundary conditions of the models

The solution domains and the coordinate systems are given in Figure 6.1 for the foam embedded heatsink and Figure 5.2 for the fin block. In the both models, air flows through the negative y direction. At the foam embedded heat sink, ABCDA is the inlet surface, EFGIE is the outlet surface, KNSRK is the heating surface, ZUYVZ is one of the air entrance surfaces into the metal foam and MKNOCBADM, EPRSTFGIE, NOTSN, KMPRK, OTPMO surfaces are the adiabatic non-heating surfaces as presented in Figure 5.1. At the fin block, A'B'C'D'A' is the inlet surface, E'F'G'I'E' is the outlet surface, K'N'S'R'K' is the heating surface, U'V'Y'V'U' and J'V'U'X'J' are a couple of the interaction surfaces from the fin to air and M'K'N'O'C'B'A'D'M', E'P'R'S'T'F'G'I'E', N'O'T'S'N', K'M'P'R'K', O'T'P'M'O' surfaces are the adiabatic non heating surfaces as presented in Figure 5.2.

The inlet boundary conditions for both models

$$u_{y=0} = 0, \qquad v_{y=0} = v_0, \qquad w_{y=0} = 0, \qquad T_{y=0} = T_{in} \qquad (5.28)$$

The outlet boundary conditions for both models

$$\left.\frac{\partial u}{\partial y}\right|_{y=L} = 0, \qquad \left.\frac{\partial v}{\partial y}\right|_{y=L} = 0, \qquad \left.\frac{\partial w}{\partial y}\right|_{y=L} = 0, \qquad \left.\frac{\partial T}{\partial y}\right|_{y=L} = 0, P_{y=L} = P_0 \quad (5.29)$$

The wall boundary conditions for both models

A no-slip condition was selected at the bottom surface, the top, the fin and the chassis surfaces of the foam embedded heatsink.

The bottom surface of the heat sink constant heat flux (heating surface)

$$-k\frac{\partial T}{\partial z}\Big|_{z=0} = \dot{q}_s \tag{5.30}$$

The bottom surface of the heat sink (no heating surfaces at the partial heater cases)

$$-k\frac{\partial T}{\partial z}\Big|_{z=0} = 0 \tag{5.31}$$

The top surface of the heat sink

$$-k\frac{\partial T}{\partial z}\Big|_{z=H} = 0 \tag{5.32}$$

The fin surfaces and the foam surfaces

At the foam and the fin surfaces, the fluid temperature and the solid temperature are equal.

$$T_s = T_f \tag{5.33}$$

The lateral surfaces of the heat sinks

A coordinate system is located at the centre of the width of the models; therefore, the lateral surfaces are W/2 distant from the origin.

$$-k\frac{\partial T}{\partial x}\Big|_{x=W/2} = 0 \tag{5.34}$$

$$-k\frac{\partial T}{\partial x}\Big|_{x=-W/2} = 0 \tag{5.35}$$

5.2. CFD Approaches of Porous Zones

Porous zone approach of CFD is applicable for various industrial examples such as the fuel cells, the filters of the catalytic converters, tobacco products or the metal foams. A transport phenomenon has more importance for the multiphase and heterogeneous systems [52]. The porous media definition of CFD is a solid fibre structure that creates complex pore shapes. The connection and the shapes of this structure play a significant role in the flow behaviour of the porous media. The global porosity is also defined as the void volume over the total volume. This property is used in most of the porous media equations and it is designated by ε. The global porosity can be calculated by using Equation 5.36.

$$\varepsilon = 1 - \frac{\text{Solid Volume}}{\text{Matrix Volume}} \tag{5.36}$$

ε global porosity

The geometry of the porous zones is defined in CFD with two main dimensions which are,

- Pore or grain scale, d
- Porous media length scale, W >> d

The porous media length shows the differences depending on the designed geometries.

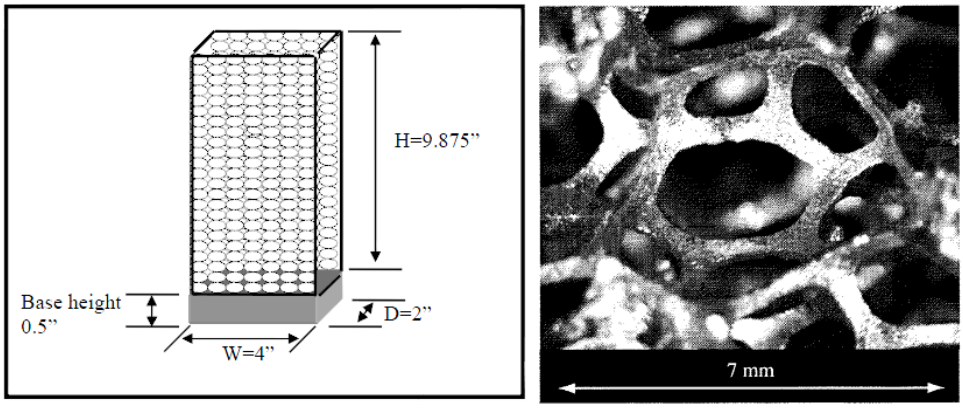

Figure 5.5 Dimensional comparison of the width and the pore diameter of the metal foam samples [31]

In general, solving the flow field at the pore scale is impractical as a result the volumetric averaging method is used to solve the larger flow fields. The comparison of the pore diameter versus the width of the sample is illustrated in Figure 5.5.

5.2.1. Representative elementary volume

Representative elementary volume is defined as the volume of the porous material which is large enough to characterize the material and small enough to maintain the positional description. Subsequently, that optimal number of the processors is used for the porous medium calculations. The schematic presentation of the REV approach is seen in Figure 5.6.

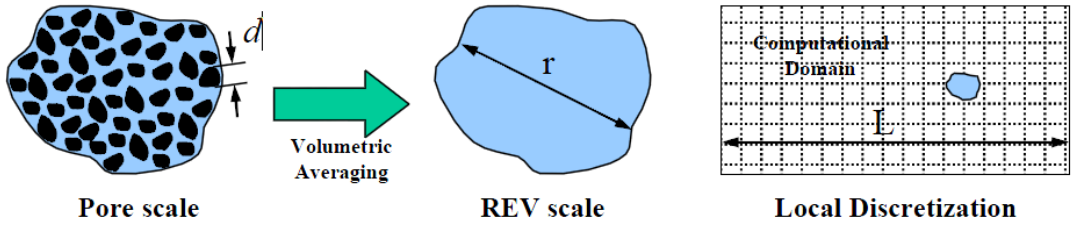

Figure 5.6 Representative elementary volume [52]

The porous zone model of CFD is similar to the Hazen Dupuit Darcy model in that the porous structure creates a resistance through the flow. The magnitude of the resistance is calculated from the viscous and the inertia parameters which were imported into the CFD domain. The resistance parameters can be obtained either analytically or empirically. In the CFD domain,

- Porous zones are defined as a fluid zone.
- Momentum equations involve sink terms which present the resistance forces of the solid materials onto the fluid.

In other words, the porous body is designed as the block geometry and selected as a fluid zone. Then resistive parameters are imported to the blocks, so that flow through the blocks is impeded. The porous media improvement is subject to the following conditions:

- Because of the REV, the porous structure does not require an exact modelling of the porous structure. A superficial velocity is calculated,

which demonstrates the average fluid velocity through three directions of the porous zone.

- The interaction areas between the porous media and the turbulence zones are approximated.

5.3. CFD Results of the Test Specimens

A total of four experimental cases were solved using CFD and the comparisons of the results are presented in the following graphs. The measured inlet air temperatures were entered as the initial inlet conditions to FLUENT. The change of the base plane temperature versus the position between the inlet and the exit of the fin block are shown below.

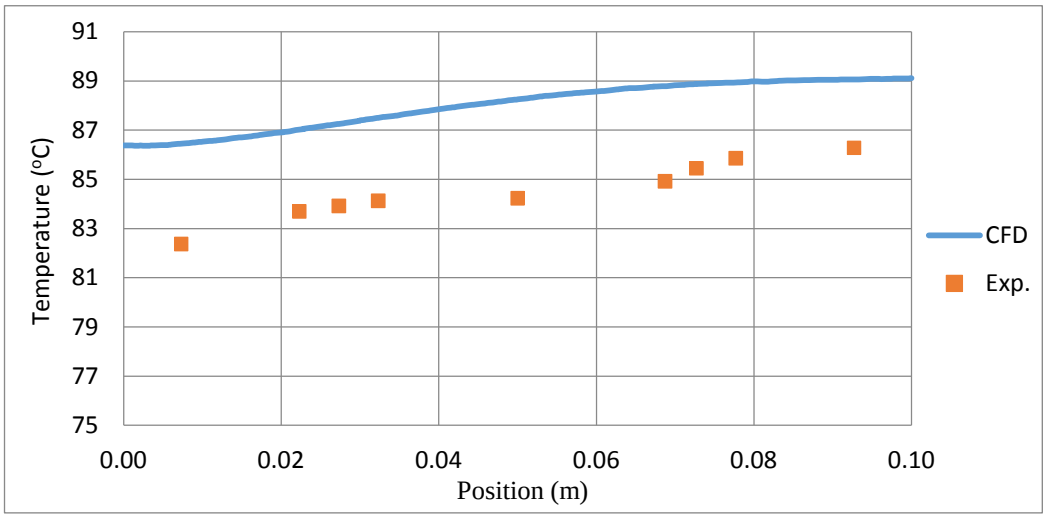

Figure 5.7 Variation of base plane temperatures of the fin block as a function of distance at the 160 W heater and 6 m/s air velocity

As seen in Figure 5.7 both the experimental and CFD results of the temperature distributions of the fin block increase along with the increase of the air temperature at the distant sections.

In the two-piece heaters scenarios, there is a rise in temperatures at the heaters sections which is shown in Figure 5.8. For both of the heaters, the temperature difference between CFD and the experimental results reach a maximum of 5℃ as seen in Figure 5.8. It is considered that the reason of this temperature difference is the disregarded heat loses of the test rig.

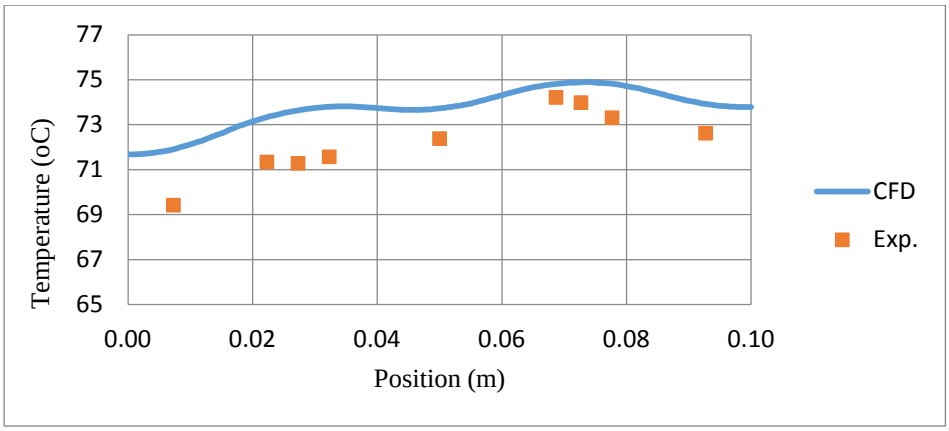

Figure 5.8 Variation of the base plane temperatures of the fin block as a function of the distance at the 120 W partial heater and 6 m/s air velocity

The heat transfer coefficient of the fin block at 4 m/s frontal air velocity is 34.5 (W/m^2·K) as seen in Figure 5.9.

Area-Weighted Average Surface Heat Transfer Coef.	(w/m2-k)
wall-fluid-solid	34.451668

Figure 5.9 Solver display of the CFD software for HTC of fin block

The Nusselt number of the fin block is calculated by using Equation 4.17. Then the Nusselt numbers of fin block at the 160 W heater and 4 m/s frontal air velocity is 4.97. The difference between the CFD Nusselt number and the experimental Nusselt number was approximately 5%.

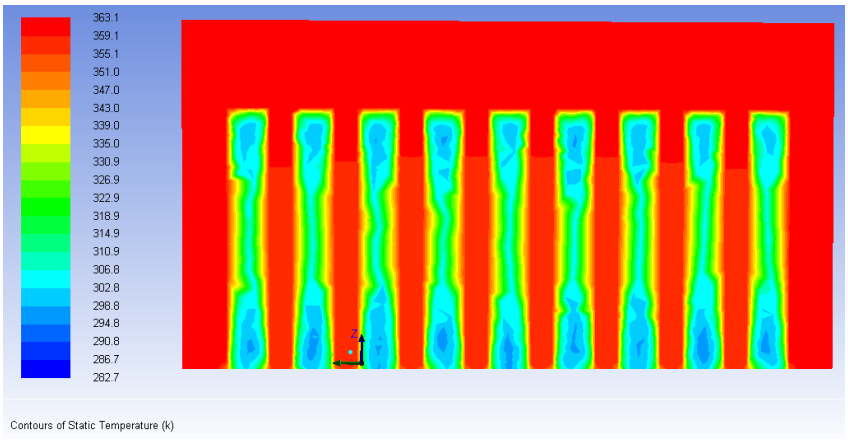

Figure 5.10 The temperature distribution of the vertical half section view fin block at the 160 W heater and 6 m/s air velocity

The temperature distribution of the vertical half section of the fin is presented in Figure 5.10. As it is understood from the temperature distribution, the heat transfer takes place on the all of the air contact surfaces of the fin block which is shown in Figure 5.10. Especially, most of the heat flows from the central regions of the fins to air.

The 20PPI CU embedded heat sink showed best thermal performance in the experiments; therefore this heat sink is modelled and solved in the CFD domain. The base plane temperature versus the position variation of the 20PPI CU foam embedded heat sink is demonstrated in Figure 5.11 and 5.12.

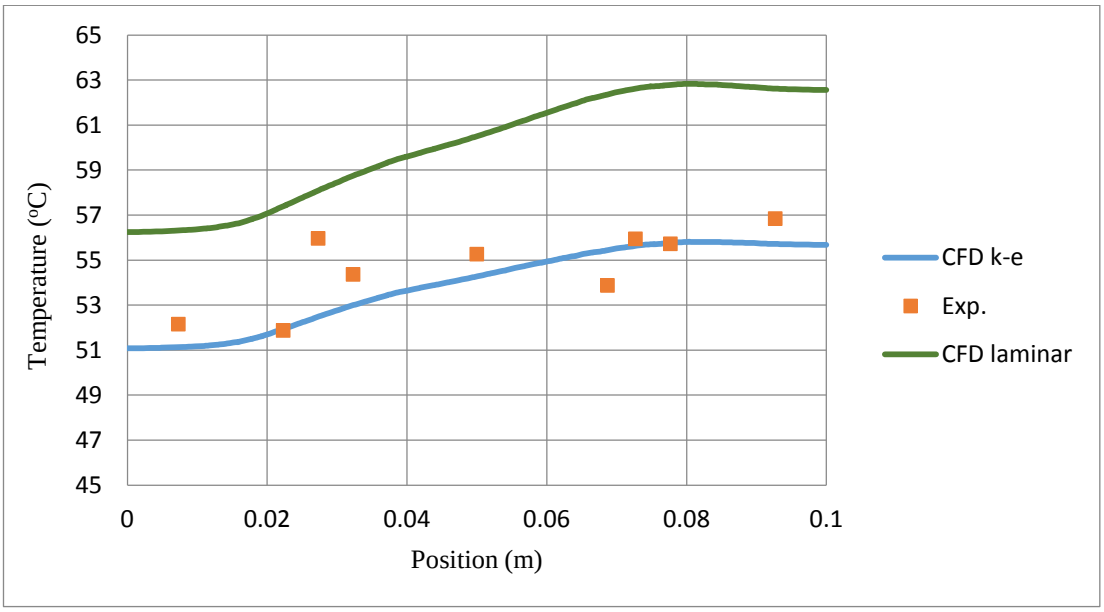

Figure 5.11 Variation of the base plane temperatures of the 20 PPI copper foam embedded heat sink as a function of distance at the 120 W partial heater and 6 m/s air velocity

As seen in Figure 5.11 and Figure 5.12 the results of the viscous k-epsilon turbulent model of CFD are mostly similar to the experimental results. It is also noticed that the laminar model results are higher than the measured temperature values. The cooling capability of the foam materials is given in Figure 5.12 at the 0.02 m to 0.04 m and 0.06 m to 0.08 m ranges. Also the unheated sections are apparent in Figure 5.11.

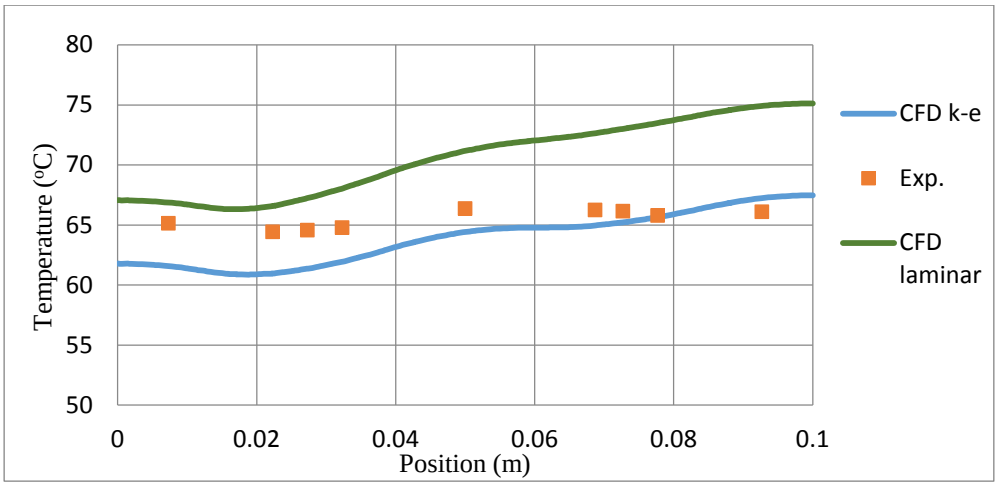

Figure 5.12 Variation of base plane temperatures of 20 PPI copper foam embedded heat sink as a function of distance at the 160 W heater and 6 m/s air velocity

The temperature gradient map of the lateral half sections demonstrates that a considerable amount of heat transfer exists in the metal foam region. Since the dominant green colour of the foam regions presented in Figure 5.13 and Figure 5.14 depict the average temperature of foam and air. In both analyses, air flows along the -y direction. As stated in the figure below at the k-epsilon turbulent model solution, more heat transfer takes place from metal foam to air. The differences between the experimental and the CFD results originate from the uncertainties of the measuring devices and the manufacturing deviations of the foam embedded heat sinks.

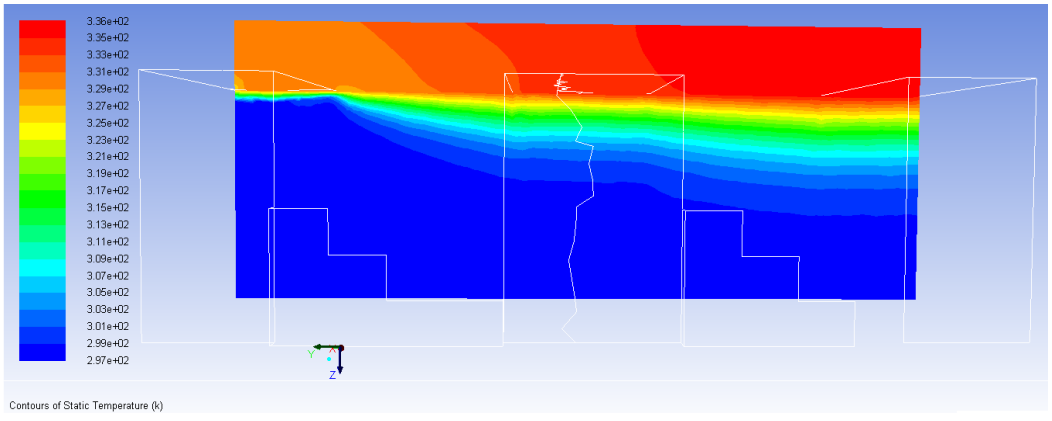

Figure 5.13 The lateral half section view of the temperature distribution of the 20 PPI CU embedded heat sink at the 120 W partial heaters and 6 m/s air velocity at the laminar model solution

Thin white limits are used for portraying approximate positions of the foam. The second metal foam section of the heat sink showed a significant thermal performance as seen in Figure 5.14.

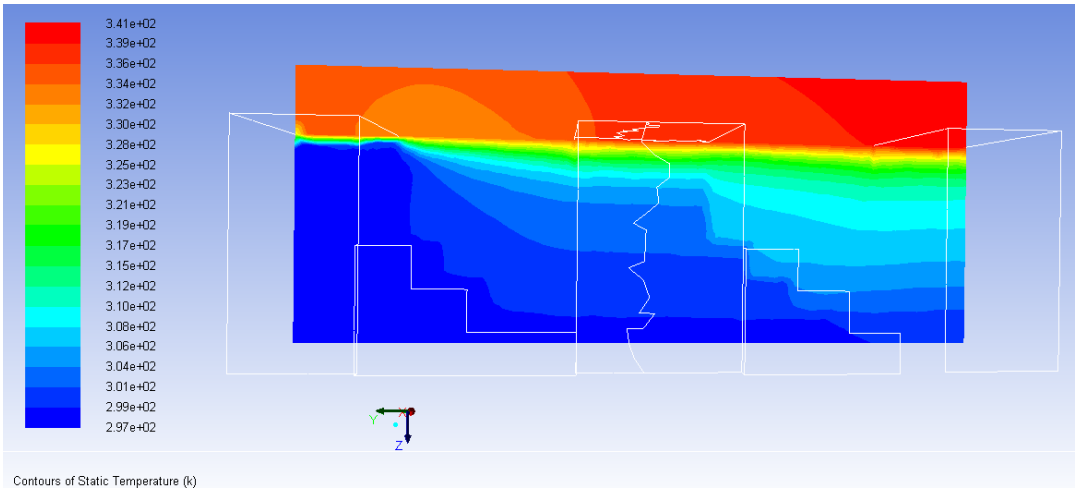

Figure 5.14 The lateral half section view of the temperature distribution of the 20 PPI CU embedded heat sink at the 160 W whole heater, 6 m/s air velocity and the viscous k-epsilon turbulent model solution

An additional temperature distribution gradient of maps and air velocity figures of 20PPI CU embedded heat sink are presented in Appendix D.

5.4. Discussion of CFD Analysis Results

Finding the correct pressure drop on the porous zones depends on the selected Rv and Ri coefficients. Input of the physical and technical parameters that is used in analyses, are supplied from literature and the vendor data of the foam metals. These essential parameters require experimental study to obtain the exact pressure and temperature values. For the foam embedded heat sink, the k-epsilon turbulent model results are more realistic than the laminar model results as they can be understood from the figures.

The CFD software is capable of calculating the required fan capacity and the foam thickness therefore; the conceptual foam embedded heat sink chassis can be analyzed after an extensive literature research. The CFD software is a suitable tool to compare the thermal performances of the fin block and the copper foams. The CFD software

successfully performed the thermal analyses of both the fin block and the foam embedded heat sinks.

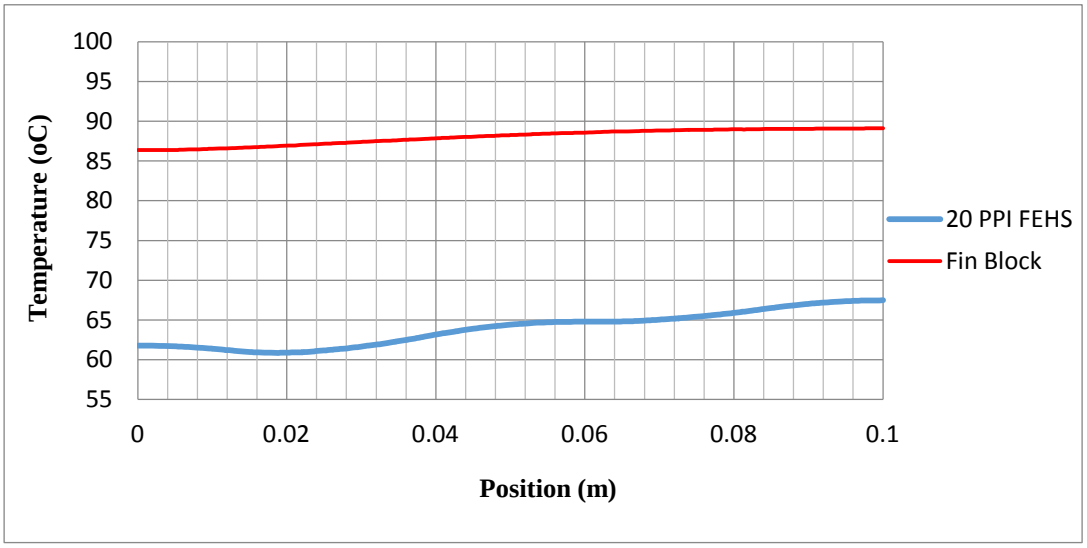

Figure 5.15 The variation of the base plane temperatures of the 20 PPI copper foam embedded heat sink and the fin block as a function of distance at the 160 W heater and 6 m/s air velocity

Figure 5.15 demonstrates the comparison results of FLUENT software of the fin block and the foam embedded heat sink. In this illustration, the 20PPI copper foam embedded heat sink can be seen having a superior thermal performance than the fin block. The base plane temperature difference of the heat sinks reached 25 ℃ at the foam section, between 0.02 and 0.04 m locations. The current study represents that the utilization of the metal foam embedded heat sinks will have a positive impact on the performance and the operational lives of electronic components.

The assessment of the utilization of the metal foam heat sinks and advice for future experimental studies are given in Chapter 6.

CHAPTER 6

CONCLUSIONS

6.1. Comparison and Evaluation of the Results

The purpose of the current study is to generate a comparison between the thermal and the hydrodynamic characteristics of the partial metal foam embedded heat sinks and those of conventional fin block. All commercial and military products have some sort of electronic box structures which transfer the generated heat to the environment. Electronic box structures contain embedded heat sinks not only to increase the operational life of the product but also enable optimally more demanding environmental conditions.

Six geometrically similar foam embedded heat sinks and one fin block heat sink were produced for the experimental stage of this thesis. During the experiments, four distinct heat fluxes and two different air entrance velocities were applied to the heat sinks produced.

The pressure drop of the foam embedded heat sinks increased up to four times more than that of the fin block. However, the aluminium foam embedded heat sinks have one-third of the weight of the fin block. As expected, the copper embedded heat sinks have lower thermal resistance than the aluminium heat sinks and the fin block.

The manufacturing process of heat sinks which are explained in Chapter 3 has some deviations due to the manufacturing tolerances. These acceptable deviations created differences between the empirical and the CFD results as presented in Chapter 5. The CFD results of both the fin block and the 20PPI copper foam embedded heat sink are explained in Chapter 6. The K-epsilon turbulent model resulted in a better match with the experiments than the laminar model in the analysis of the foam heat sinks.

The selected mesh types, the designed models, the boundary and the initial conditions are given in Appendix D.

In the experimental results, the independence of the heater loads from the heat transfer coefficients in foam embedded heat sinks was observed, which was very much like in Mancin's study. The thermal resistance of the aluminium foam embedded heat sinks decreased with the increasing pore density as in Mancin's study.

At the whole heater scenarios, the temperatures at the foam sections were as low as 1 to 1.5 degree, which were lower than temperatures at the foamless sections. This temperature difference provides a longer operational life for the critical electronic components and eliminates hot spots on the chassis of the electronic boxes.

Apart from the tested performances of the heat sinks, the manufacturing capability and the production cost have an incontestable effect on the heat sink selection. The lack of the domestic metal foam manufacturers forces designers to import metal foams from abroad. To lower the initial cost, the metal foam materials should be mass produced and have to be used in the partially embedded designed heat sinks. Not only the corrosiveness of copper but also the higher cost of copper foam makes its utilization difficult in the military applications. Compared to the aluminium foams, the use of the copper foams requires special attention.

6.2. Suggestions for Future Experiments and Applications

The metal foams need to be selected carefully and sufficiently according to their field of application. This study emphasizes that the issues of the limited use of metal foam can develop more compact, lightweight and highly competitive technological products. To overcome the high cost of the metal foams, the domestic production of the foam metal should be promoted in the research and development centres. With the acquisition of this technology both the industry and the universities will create a serious research potential and generate various application areas.

This study also builds up the knowledge about the hydrodynamic and the heat transfer performance of the partial metal foam utilization in the heat sinks. For future experimental studies and applications, following suggestions are given:

- To eliminate the dimensional differences, the heaters should be manufactured before the test specimens.
- Brazing of the foam samples instead of soldering can decrease the thermal resistance of the junction between the foams and the aluminium chassis.
- Using longer and transparent duct assembly to visualize the fluid movements inside of the foam samples for experimental purposes is suggested.
- Measuring the pressure drop with pressure transducer at the inlet and at the exit as well as the pitot tubes at the inside of the test specimens is advised.
- It is recommended to test foams with a higher heat flux and the lower area heaters, in order to provide more knowledge about the thermal performance of the metal foams.
- Performing more test scenarios with more air inlet velocity variation allows a chance for observation of more fluid behaviour in metal foams.

REFERENCES

[1] K. Boomsma, D. Poulikakos, F. Zwick, “Metal foams as compact high performance heat exchangers”, Mechanics of Materials, Vol. 35 Pages 1161-1176, 2003.

[2] Loh C.K., Chou Bor-Bin, Nelson Dan and Chou D.J., “Study of thermal characteristics on solder and adhesive bonded folded fin heat sink”, The Seventh Intersociety Conference, Vol. 2 Pages 1-7, 2000

[3] Simone Mancin, Claudio Zilio, Andrea Diani, Luisa Rossetto, “Experimental air heat transfer and pressure drop through copper foams”, Experimental Thermal and Fluid Science, Vol. 36 Pages 224-232, 2012.

[4] A. Kopanidis, A. Theodorakakos, E. Gavaises, D. Bouris, “3D numerical simulation of flow and conjugate heat transfer through a pore scale model of high porosity open cell metal foam”, International Journal of Heat and Mass Transfer, Vol. 53 Pages 2539-2550, 2010.

[5] Pradeep M. Kamath, C. Balaji, S.P. Venkateshan, “Convection heat transfer from aluminium and copper foams in a vertical channel - an experimental study”, International Journal of Thermal Sciences, Vol. 64 Pages 1-10, 2013.

[6] Kazuhiko Fukutani and Ali Shakouri, “Optimization of thin film microcoolers for hot spot removal in packaged integrated circuit chips”, 22nd IEEE SEMI-THERM Symposium, Pages 130-134, 2006.

[7] ATEŞ A. M., “Experimental Comparison of Fluid and Thermal Characteristics of Microchannel and Metal Foam Heat Sinks”, Msc. Thesis, METU, 2011.

[8] Bhattacharya A., Calmidi V.V., Mahajan R.L., “Thermophysical properties of high porosity metal foams”, International Journal of Heat and Mass Transfer, Vol. 45, pages: 1017-1031, 2002

[9] Boomsma K. and Poulikakos D., “The effects of compression and pore size variations on the liquid flow characteristics in metal foams”, Journal of Fluids Engineering, Vol. 124, pages: 263-271, 2002

[10] Boomsma K.S., “Metal Foams as Novel Compact High Performance Heat Exchangers for the Cooling of Electronics” PhD. Thesis, Swiss Federal Institute of Technology Zurich, 2002.

[11] Noh J.S., Lee K.B., Lee C.G., “Pressure loss and forced convective heat transfer in an annulus filled with aluminium foam”, International Communications in Heat and Mass Transfer, Vol. 33, Pages: 434–444, 2006

[12] Dukhan N., “Correlations for the pressure drop for flow through metal foam”, Experimental Fluids, Vol. 41, Pages: 665–672, 2006

[13] Salas K.I. and Waas A.M., “Convective heat transfer in open cell metal foams”, American Institute of Aeronautics Paper, Vol. 1669, Pages: 1-19, 2006

[14] Paek J. W., Kang B. H., Kim S. Y., Hyun J. M., “Effective thermal conductivity and permeability of aluminium foam materials”, International Journal of Thermophysics, Vol. 21, No. 2, Pages: 453-464, 2000

[15] Liu J.F., Wu W.T., Chiu W.C., Hsieh W.H. “Measurement and correlation of friction characteristic of flow through foam matrixes” Experimental Thermal and Fluid Science, Vol.30, Pages: 329–336, 2006

[16] Calmidi V. V., Mahajan R. L., “Forced convection in high porosity metal foams”, ASME Journal of Heat Transfer, Vol. 122, and Pages: 557-565, 2000

[17] Shih W.H., Chiu W.C., Hesieh W.H., “Height effect on heat-transfer characteristics of aluminium-foam heat sinks”, Journal of Heat Transfer, Vol. 128, Pages: 530-537, 2006.

[18] Lu W., Zhao C.Y., Tassou S.A., “Thermal analysis on metal-foam filled heat exchangers. Part I: Metal-foam filled pipes”, International Journal of Heat and Mass Transfer, Vol. 49, Pages: 2751–2761, 2006.

[19] Lu W., Zhao C.Y., Tassou S.A., “Thermal analysis on metal-foam filled heat exchangers. Part II: Tube heat exchangers”, International Journal of Heat and Mass Transfer, Vol. 49, Pages: 2762–2770, 2006.

[20] Kim S.Y., Peak J.W., Kang B.H., “Flow and heat transfer correlations for porous fin in a plate-fin heat exchanger”, ASME Journal of Heat Transfer, Vol. 122, Pages: 572-578, 2000.

[21] Kim S.Y., Kang B.H., Kim J.H., “Forced convection from aluminium foam materials in an asymmetrically heated channel”, International Journal of Heat and Mass Transfer, Vol. 44, Pages: 1451–1454, 2001.

[22] Lee D.Y., Vafai K., “Analytical characterization and conceptual assessment of solid and fluid temperature differentials in porous media”, International Journal of Heat and Mass Transfer, Vol. 42, Pages: 423–435, 1999.

[23] Marafie A., Vafai K., “Analysis of non-darcian effects on temperature differentials in porous media”, International Journal of Heat and Mass Transfer, Vol. 44, Pages: 4401–4411, 2001.

[24] Mancin S., Zilio C., Rosetto L., Cavallini A., “Foam height effects on heat transfer performance of 20 ppi aluminium foams”, Applied Thermal Engineering, Vol. 49, Pages: 55–60, 2012.

[25] Mancin S., Zilio C., Cavallini A., Rosetto L., “Heat transfer during air flow in aluminium foams”, International Journal of Heat and Mass Transfer, Vol. 53, Pages: 4976–4984, 2010.

[26] Mancin S., Zilio C., Cavallini A., Rosetto L., “Pressure drop during air flow in aluminium foams”, International Journal of Heat and Mass Transfer, Vol. 53, Pages: 3121–3130, 2010.

[27] Mahjoob S., Vafai K., “A synthesis of fluid and thermal transport models for metal foam heat exchangers”, International Journal of Heat and Mass Transfer, Vol. 51, Pages: 3701–3711, 2008.

[28] Ozmat B., Leyda B., Benson B., “Thermal applications of open cell metal foams”, ASME 2001 International Mechanical Engineering Congress& Exposition, 2001

[29] Ozmat B., “Reticulated metal foams build better heat sinks”, Power Electronics Technology, Pages: 30–35, November 2007

[30] Leong K.C., Jin L.W., “Effect of oscillatory frequency on heat transfer in metal foam heat sinks of various pore densities”, International Journal of Heat and Mass Transfer, Vol. 49, Pages: 671–681, 2006.

[31] Hernández Á. R. Á., “Combined Flow and Heat Transfer Characterization of Open Cell Aluminium Foams”, Msc. Thesis, University Of Puerto Rico, 2005.

[32] Jeng T.M., S., Zilio C., Cavallini A., Rosetto L., “Heat transfer behavior in a rotating aluminium foam heat sink with a circular impinging jet”, International Journal of Heat and Mass Transfer, Vol. 51, Pages: 1205–1215, 2008.

[33] Boomsma K., Poulikakos D. “On the effective thermal conductivity of a three-dimensionally structured fluid-saturated metal foam” International Journal of Heat and Mass Transfer, Vol. 44, Pages: 827–836, 2001.

[34] Antohe B. V., Lage J. L., Price D. C., Weber R. M., “Experimental determination of permeability and inertia coefficients of mechanically compressed aluminium porous matrices” Journal of Fluids Engineering, Vol. 119, Pages: 404-412, 1997.

[35] Antohe B. V., Lage J. L., Price D. C., Weber R. M., “A general two-equation macroscopic turbulence model for incompressible flow porous media” International Journal of Heat and Mass Transfer, Vol. 40, No. 13, Pages: 3013-3024, 1996.

[36] Boomsma K., Poulikakos D., and Ventikos Y., “Simulations of flow through open cell metal foams using an idealized periodic cell structure” International Journal of Heat and Fluid Flow, Vol. 24, Pages: 825–834, 2003.

[37] Dukhan N., Chen K. C., “Heat transfer measurements in metal foam subjected to constant heat flux” Experimental Thermal and Fluid Science, Vol. 32, Pages: 624–631, 2007.

[38] Dukhan N., Ali M., “Strong wall and transverse size effects on pressure drop of flow through open-cell metal foam” International Journal of Thermal Sciences, Vol. 57, Pages: 85–91, 2012.

[39] Dukhan N., Quinones-Ramos P. D., Cruz-Ruiz E., Velez-Reyes M., Scott E. P. “One-dimensional heat transfer analysis in open-cell 10-ppi metal foam” International Journal of Heat and Mass Transfer, Vol. 48, Pages: 5112–5120, 2005.

[40] Dukhan N., Hooman K. “Comments on two analyses of thermal non-equilibrium Darcy–Brinkman convection in cylindrical porous media” International Journal of Heat and Mass Transfer, Vol. 66, Pages: 440–443, 2013.

[41] Dukhan N., Patel P. “Equivalent particle diameter and length scale for pressure drop in porous metals” Experimental Thermal and Fluid Science, Vol. 32, Pages: 1059–1067, 2008.

[42] Shen L., Chen Z. “Critical review of the impact of tortuosity on diffusion” Chemical Engineering Science, Vol. 62, Pages: 3748-3755, 2007.

[43] Bonnet J.P., Topin F. Tadrist L. “Flow laws in metal foams: compressibility and pore size effects” Transport in Porous Media, Vol. 73, Pages: 233-254, 2008.

[44] Miranda B. M. S., “A Numerical Study Of Convection In A Channel With Porous Baffles" MS. Thesis, Texas A&M University, 2003.

[45] Lu T. J., Stone H. A. and Ashby M. F. “Heat transfer in open-cell metal foams” Acta Metallurgical Inc., Vol. 46, and No: 10, Pages: 3619-3635, 1998.

[46] Gupta A., Dean N.F. “Metal foam heat sinks for laptop cooling application in a heat pipe-heat sink arrangement” Transfer in Open-Cell Metal Foams” Thermal Challenges in Next Generation Electronic Systems, Millpress, 2002.

[47] Nawaz K., Bock J., Dai Z., Jacobi A.M. “Experimental studies to evaluate the use of metal foams in highly compact air-cooling heat exchangers” International Refrigeration and Air Conditioning Conference, Pages: 1-11, 2010.

[48] Annapragada R., Gaarimella S. V., Murthy J.Y. “Permeability and thermal transport in compressed open-celled foams” Cooling Technologies Research Center Research Publications, Paper 95, 2008.

[49] Moore E.M, “Cramming more components onto integrated circuits” Electronics, Vol. 38, 1965.

[50] Andreas èOchsner, Graeme E. Murch and Marcelo J.S. de Lemos., “Cellular and Porous Materials: Thermal Properties Simulation and Prediction”, Weinheim: Wiley-VCH, 2008

[51] Heat Transfer in Porous Media, “Advanced Heat Transfer Modelling” ANSYS Inc., 2006.

[52] ANSYS Fluent Tutorial Guide, ANSYS Inc., 2008.

[53] CFD Online “Viscous Resistance” http://www.cfd-online.com/ [09.07.2014]

[54] Bıçak İ., “3-1.5.8 (SLC600 Vapour phase soldering machine) Buhar fazli lehimleme makinasi kullanim kilavuzu” MİKES, 2005

[55] Kurtuluş F.D. “Hot Wire Measurements” AE 547 Lecture Notes, METU, 2013.

[56] Nield D. A., Bejan A., “Convection in Porous Media”, Springer, 2006.

[57] Steinberg D. S., “Cooling Techniques for Electronic Equipment”, John Wiley & Sons, Inc., 1991.

[58] Ashby M.F., Evans A.G., Fleck N.A., Gibson L.J., Hutchinson J.W., Wadley H.N.G., “Metal Foams: A Design Guide”, Butterworth Heinemann, 2000.

[59] Reay D., Kew P., “Heat Pipes Theory, Design and Applications”, Butterworth Heinemann, 2006.

[60] George F. P., William G. G., “Essentials of Multiphase Flow and Transport in Porous Media”, Wiley, 2008

[61] Holman J.P. “Experimental Methods for Engineers” McGraw-Hill, 7th Edition, 2001.

[62] “Uncertainty" http://inside.mines.edu/~mmyoung/phgn471/uncertainty.htm [12.06.2014]

[63] Moffat R.J. “Contributions to the theory of single-sample uncertainty analysis” Journal of Fluids Engineering, Vol. 104, Pages: 250-260, 1982

[64] Kline, S. J., and F. A. McClintock. “Describing uncertainties in single-sample experiments” Mechanical Engineering, Vol. 75, No. 1, January 1953: 3-8.

[65] Arunn Narasimhan “Essentials of Heat and Fluid Flow in Porous Media”, Boca Raton, FL: CRC, Taylor & Francis/Ane Books Pvt. Ltd. 2013

[66] Derek B. Ingham and Iaon Pop “Transport Phenomena in Porous Media”, Oxford; Danvers, MA: Pergamon, 1998.

[67] Kaviany, M., “Principles of Heat Transfer in Porous Media”, New York: Springer-Verlag, c1995.

[68] Öchsner A., Murch G. E., Lemos M. J. S. “Cellular and Porous Materials Thermal Properties Simulation and Prediction” Wiley-VCH Verlag GmH & Co. KGaA, 2008.

[69] Çengel A.Y., “Heat Transfer a Practical Approach” WCB McGraw-Hill, 1998.

[70] Lasance C. J.M., Simons R. E. “Advances in high-performance cooling for electronics” Electronic Cooling Magazine, 2005.

[71] S.G. Kandlikar, W.J. Grande, “Evolution of microchannel flow passages – thermohydraulic performance and fabrication technology”, Heat Transfer Eng.24 (1) (2003) 3–17.

[72] G.L. Morini, "Single-phase convective heat transfer in micro channels: a review of experimental results", Int. J. Therm. Sci. 43 (2004) 631–651.

[73] G.M. Mala, D. Li, J.D. Dale, "Heat transfer and fluid flow in micro channels", Int. J.Heat Mass Transfer 40 (13) (1997) 3079–3088.

[74] Zhong Qiana, Haimin Wangba, "Numerical study of performance of a micro chip cooler", Energy Procedia 16 (2012) 314 – 319

[75] Mushtaq I. Hasan, "Numerical investigation of counter flow microchannel heat exchanger with MEPCM suspension", Applied Thermal Engineering 31 (2011)

[76] Lindstedt M., Karvinen, "Optimization of plate fin arrays with laminar and turbulent convection", Journal of Physics, Conference Series 395, Pages: 1-8, 2012.

[77] Kays W. M. and London A. L., "Compact Heat Exchangers", McGraw-Hill, 1984.

[78] Loh C. K., Chou D.J. "Comparative analysis of heat sink pressure drop using different methodologies", Semiconductor Thermal Measurement and Management Symposium, 2004. Twentieth Annual IEEE, Pages 148-153, 2004.

[79] Bejan A., “Convection Heat Transfer”, John Wiley & Sons, Inc., 1984.

[80] Bejan A., “Heat Transfer”, John Wiley & Sons, Inc., 1993.

[81] Bejan A., Kraus Allan, “Heat Transfer Handbook”, John Wiley & Sons, Inc., 2003.

[82] http://en.wikipedia.org/wiki/Moore's_law [05.09.2014]

[83] Marcelo J.S., “Turbulence in porous Media”, Elsevier, 2006.

APPENDIX A

TECHNICAL DRAWINGS OF TEST SPECIMENS AND COMPONENTS

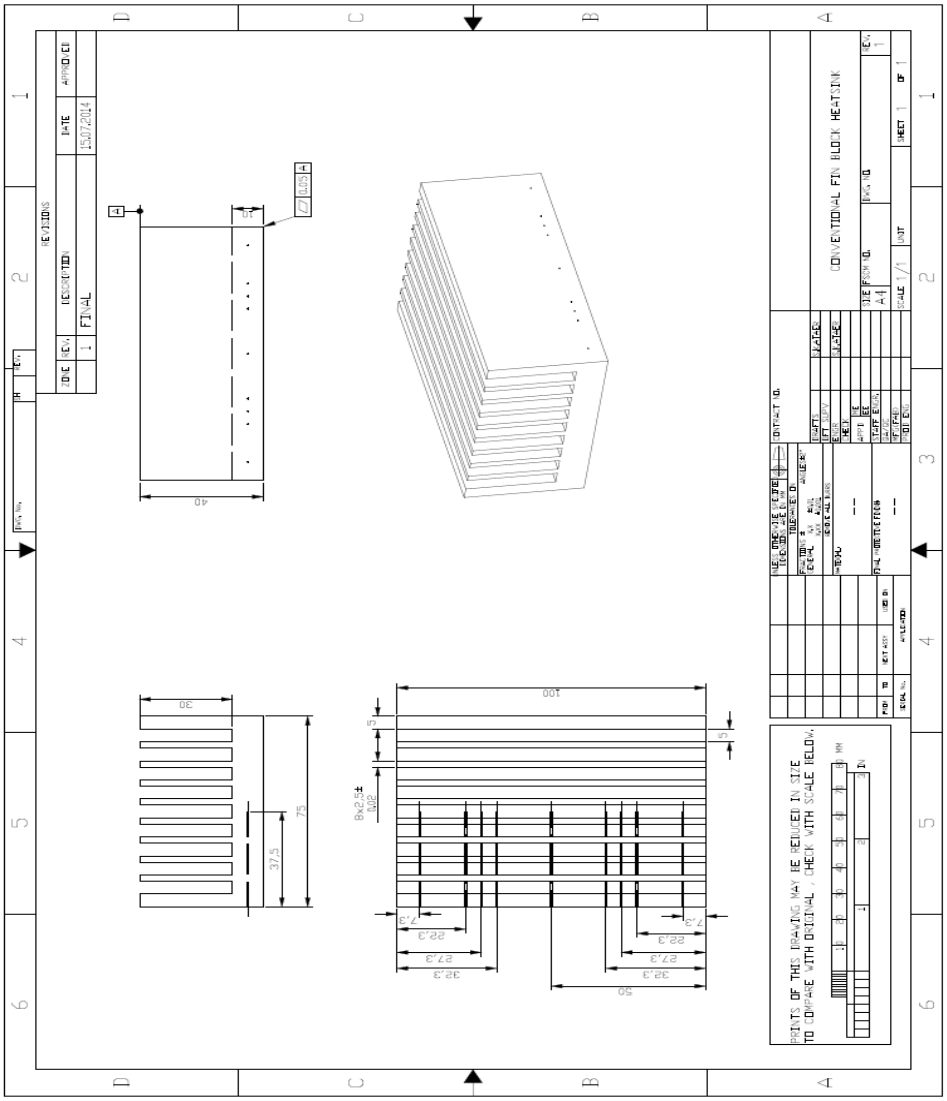

Figure A.1 Technical drawing of fin block

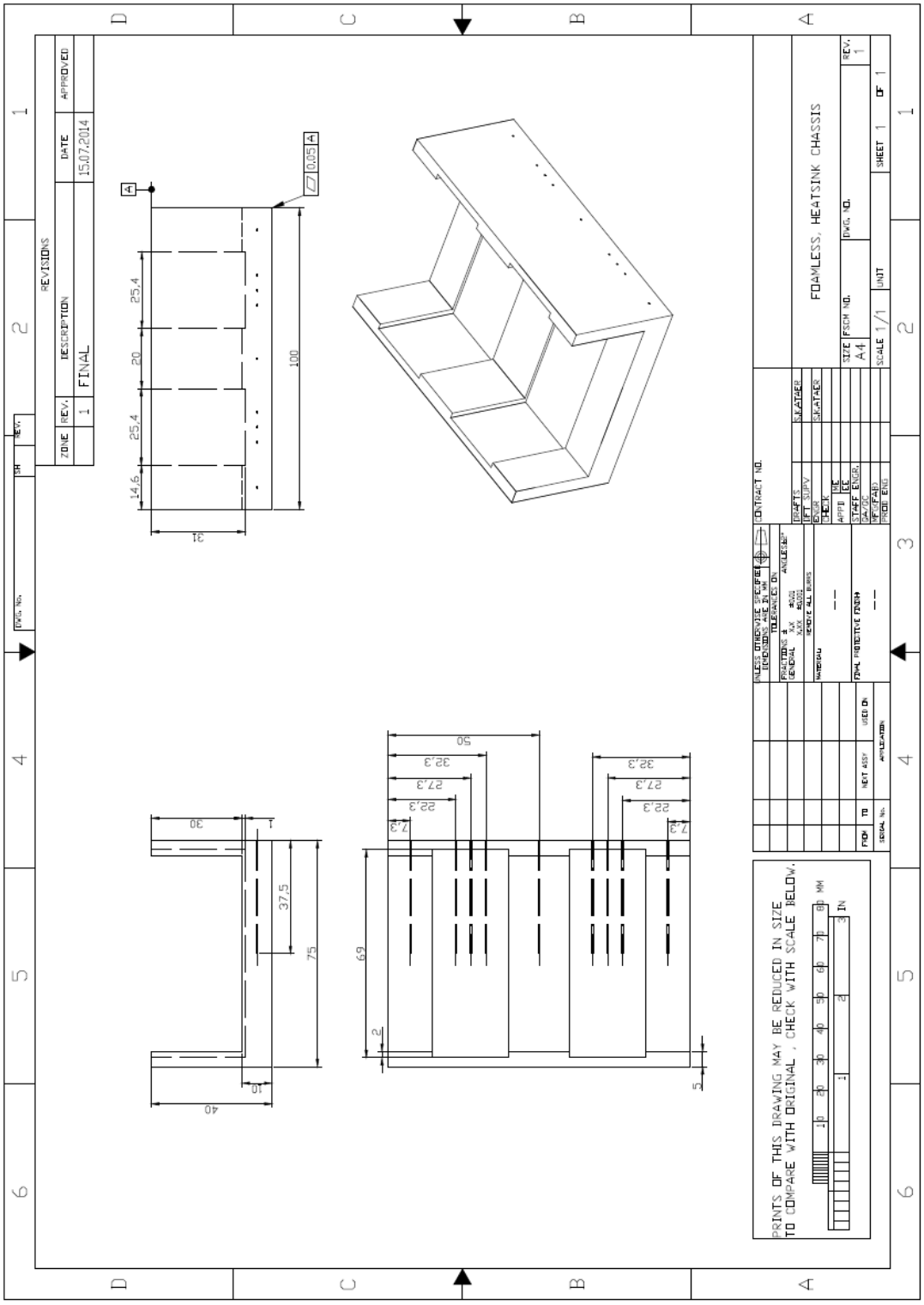

Figure A.2 Technical drawing of bare chassis of foam embedded heat sink

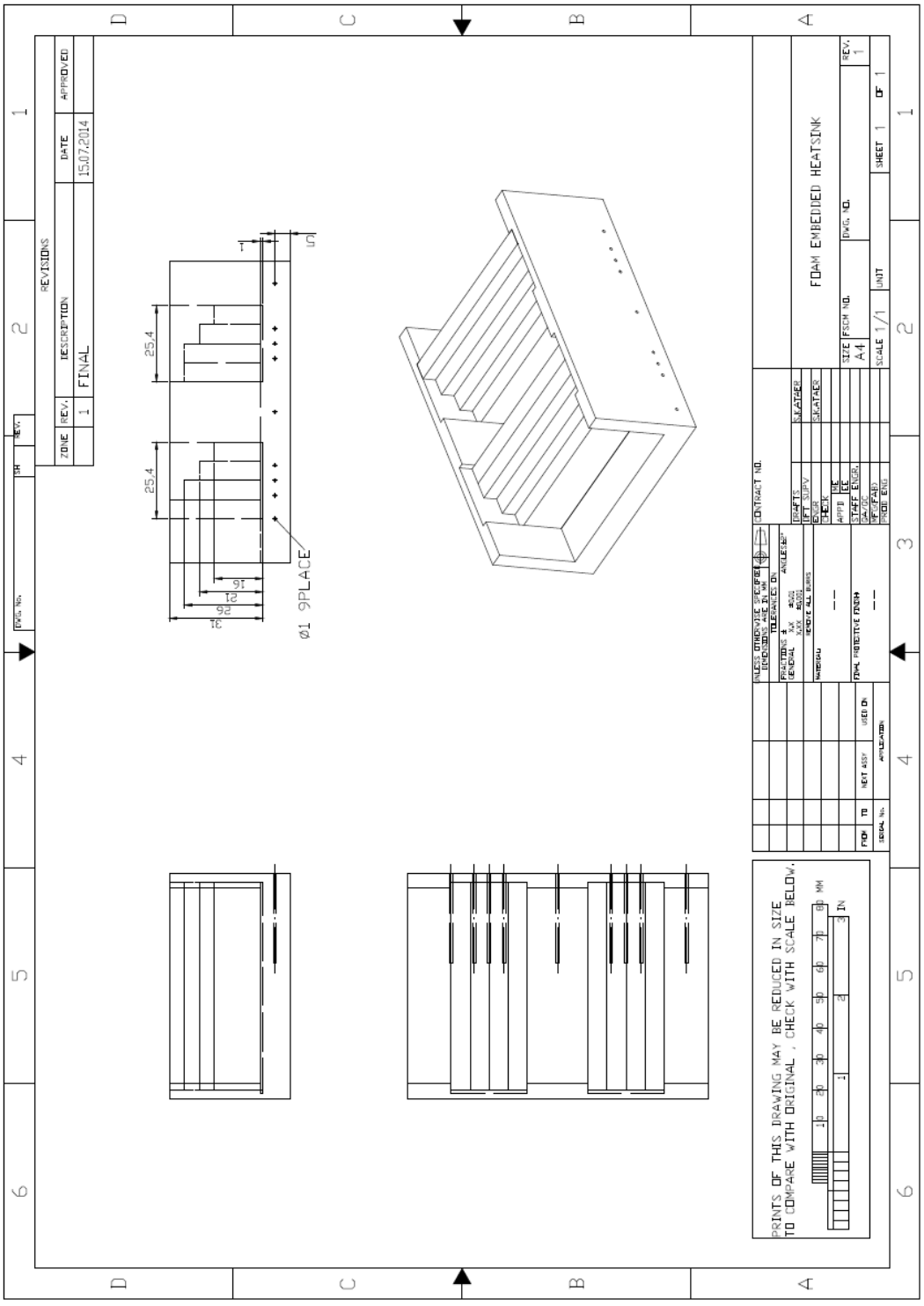

Figure A.3 Technical drawing of foam embedded heat sinks concept design

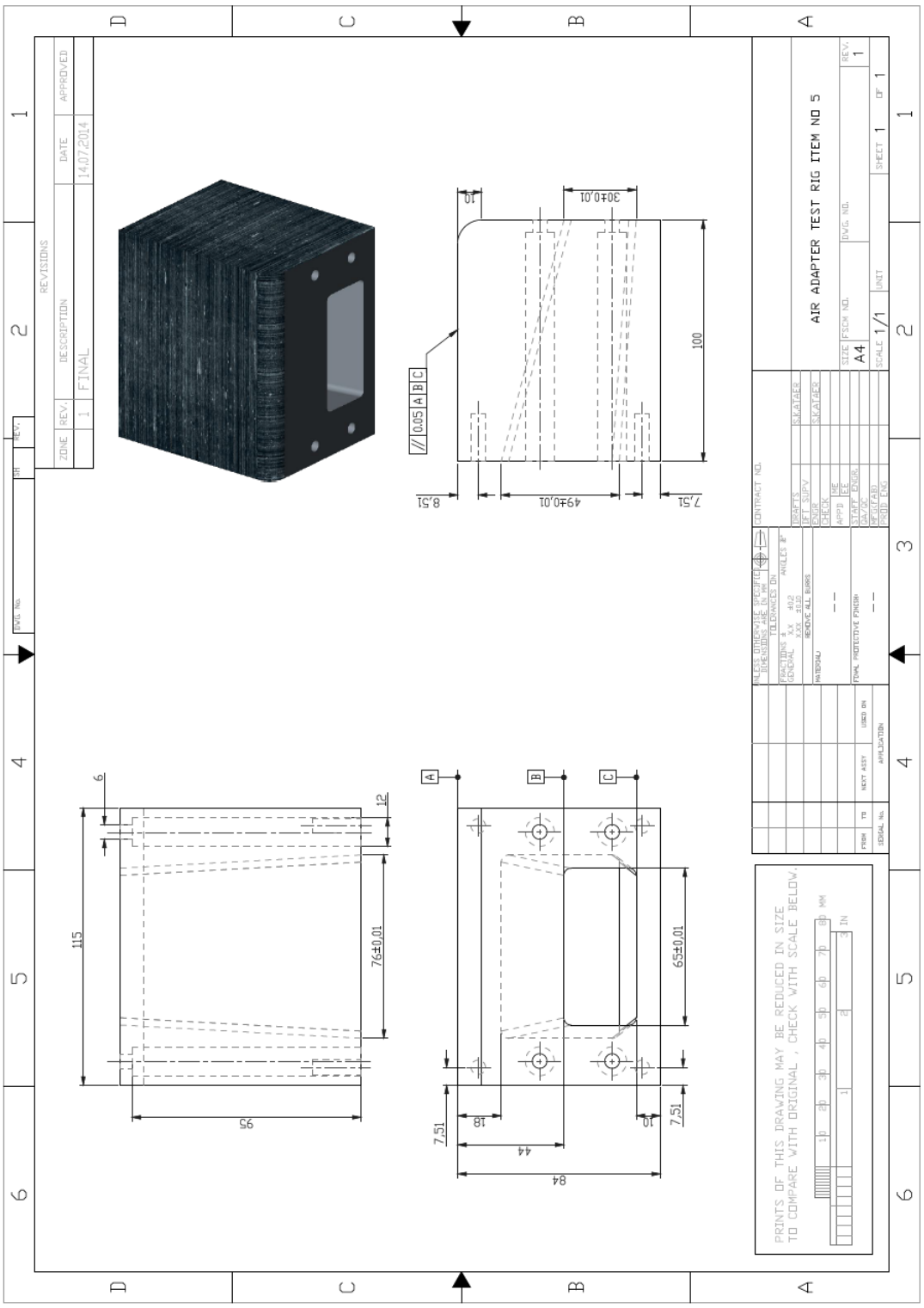

Figure A.4 Technical drawing of adapter component of test rig

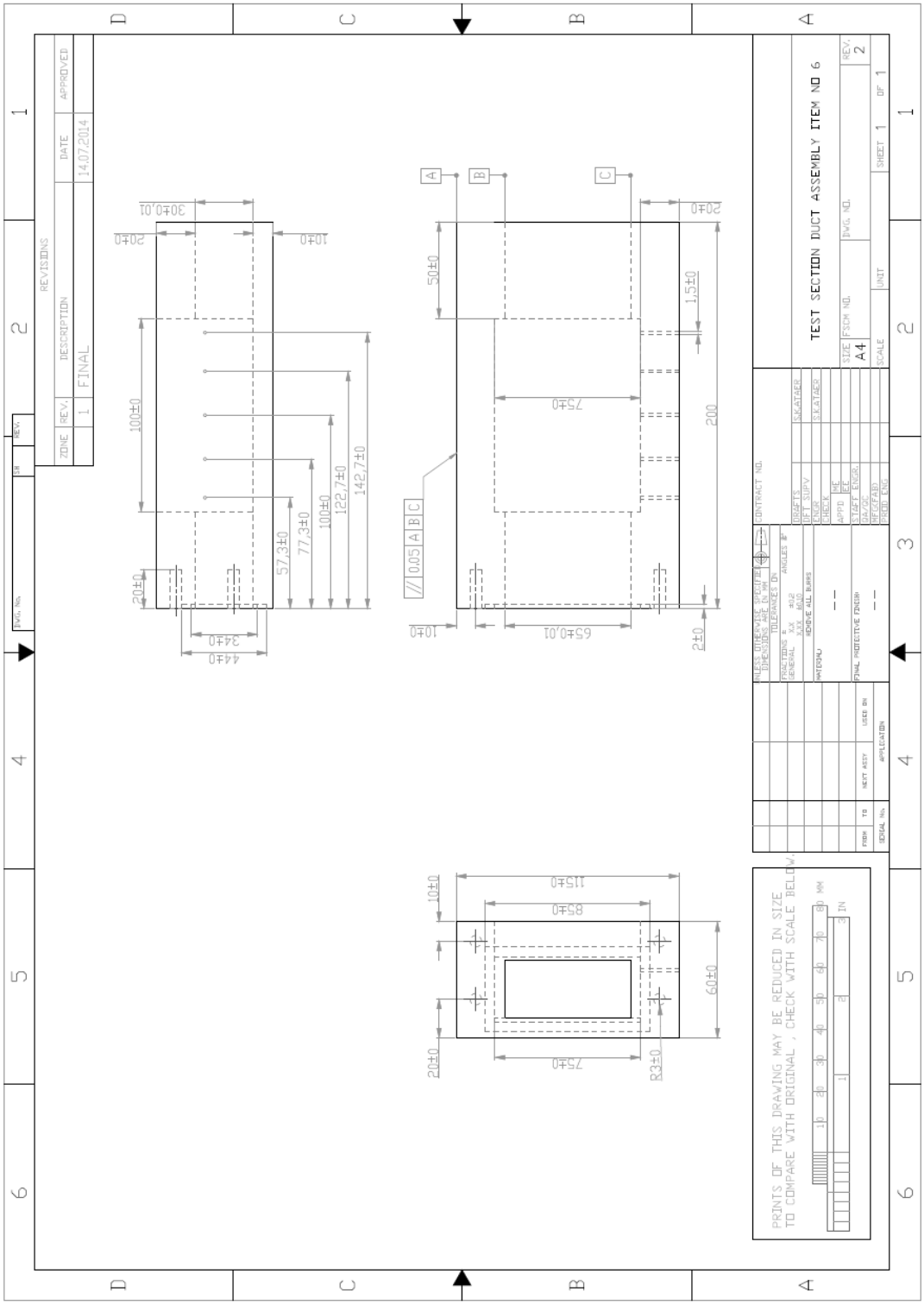

Figure A.5 Technical drawing of test section duct assembly component of test rig

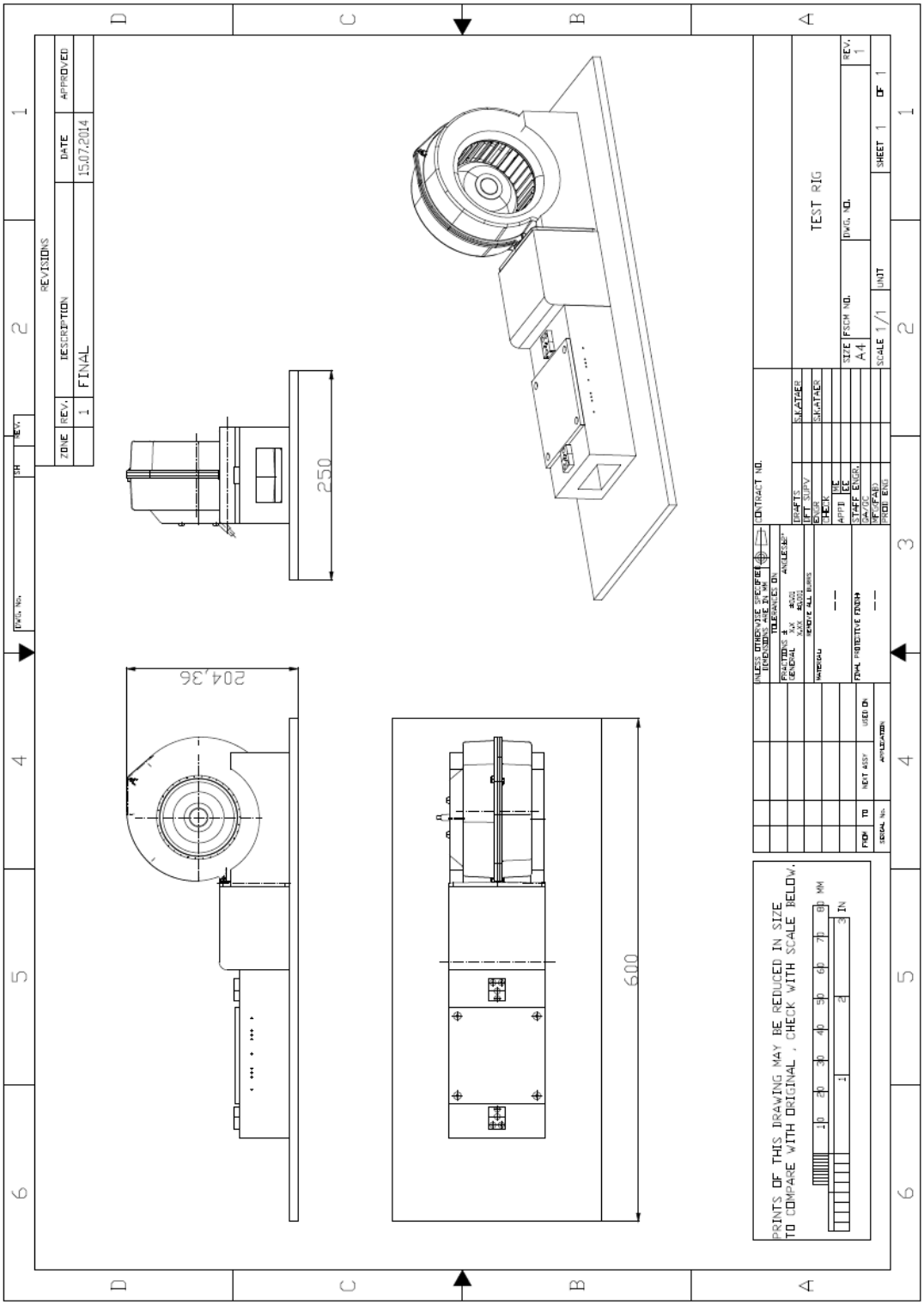

Figure A.6 Technical drawing of test rig

APPENDIX B

EXAMPLE OF UNCERTAINTY CALCULATION

Uncertainty calculation of the convection coefficient of 20PPI copper embedded heat sink at a 6 m/s air velocity and 120 W two section heaters is calculated as example. Uncertainty formulation of convection coefficient is obtained in Chapter 4 as below:

$$\frac{\omega_{\bar{h}}}{\bar{h}} = \left[\left(\frac{\omega_{V_h}}{V_h}\right)^2 + \left(\frac{\omega_{I_h}}{I_h}\right)^2 + \left(\frac{-\omega_{A_{con}}}{A_{con}}\right)^2 + \left(\frac{-\omega_{T_{avgb}}}{T_{avgb}}\right)^2 + \left(\frac{\omega_{T_{c,in}}}{T_{c,in}}\right)^2\right]^{1/2}$$

Error values are taken from datasheets of measuring devices and each uncertainty term is calculated with equation below.

$$\omega = e/\sqrt{3}$$

Average temperature uncertainty of base temperature is the resultant uncertainty of nine T-type thermocouples. It is calculated by the equation derived in Chapter 4 as:

$$\frac{\omega_{T_{avgb}}}{T_{avgb}} = \left[\left(\frac{\omega_{\mathrm{T}_1}}{\mathrm{T}_1}\right)^2 + \left(\frac{\omega_{\mathrm{T}_2}}{\mathrm{T}_2}\right)^2 + \left(\frac{\omega_{\mathrm{T}_3}}{\mathrm{T}_3}\right)^2 + \left(\frac{\omega_{\mathrm{T}_4}}{\mathrm{T}_{41}}\right)^2 + \left(\frac{\omega_{\mathrm{T}_5}}{\mathrm{T}_5}\right)^2 + \left(\frac{\omega_{\mathrm{T}_6}}{\mathrm{T}_6}\right)^2 + \left(\frac{\omega_{\mathrm{T}_7}}{\mathrm{T}_7}\right)^2 + \left(\frac{\omega_{\mathrm{T}_8}}{\mathrm{T}_8}\right)^2 + \left(\frac{\omega_{\mathrm{T}_9}}{\mathrm{T}_9}\right)^2\right]^{\frac{1}{2}}$$

Temperatures values are taken from Figure C. 46.

Error of each T–type thermocouple is ± 0.8°C so the uncertainity of thermocouples on the base plane of heat sink becomes:

$$\omega_{T1} = \omega_{T2} = \ldots = \omega_{T9} = 1/\sqrt{3}$$

$$\frac{\omega_{T_{avgb}}}{T_{avgb}} = \left[\left(\frac{1/\sqrt{3}}{56.84}\right)^2 + \left(\frac{1/\sqrt{3}}{55.72}\right)^2 + \left(\frac{1/\sqrt{3}}{55.94}\right)^2 + \left(\frac{1/\sqrt{3}}{53.87}\right)^2 + \left(\frac{1/\sqrt{3}}{55.26}\right)^2 + \left(\frac{1/\sqrt{3}}{54.36}\right)^2 + \left(\frac{1/\sqrt{3}}{55.96}\right)^2 + \left(\frac{1/\sqrt{3}}{51.87}\right)^2 + \left(\frac{1/\sqrt{3}}{52.15}\right)^2\right]^{\frac{1}{2}} = 0.03173$$

Error of each AIRFLOW TA2 anemometer thermocouple has ±2 % full scale deflection (FSD) so uncertainity of inlet temperature is:

$$\omega_{Tc,in} = 0.02 \times 80/\sqrt{3}$$

80 demonstrates difference of maximum and minimum temperature values of AIRFLOW TA2 anemometer. Both heater ampere and heater volt are measured by AVO M3004 whose error is ±2%.

$$\omega_{V_h} = 0.02/\sqrt{3} \;\&\; \omega_{I_h} = 0.02/\sqrt{3}$$

Surface area data of metal foam are taken from the manufacturer's datasheet and compared with literature. Error value of foam's surface area is 0.2%.

$$\omega_{A_{con}} = 0.002/\sqrt{3}$$

Values at 6 m/s and 120 W

T_{avgb}: 54.70 ^oC

$T_{c,in}$: 23.00 ^oC

A_{con} : 0.092 m^2

V_h : 152.3 V

I_h : 0.79 A

$$\frac{\omega_{\bar{h}}}{\bar{h}} = \left[\left(\frac{0.02/\sqrt{3}}{152.3\ V}\right)^2 + \left(\frac{0.02/\sqrt{3}}{0.79\ A}\right)^2 + \left(\frac{-0.002/\sqrt{3}}{0.092\ m^2}\right)^2 + (-0.03173)^2 + \left(\frac{0.02 * 80/\sqrt{3}}{23.00\ ^oC}\right)^2\right]^{1/2} = 0.05469$$

APPENDIX C

THERMOCOUPLE TEMPRATURES OF TEST SPECIMENS

Temperature values on figures are measured at the 30 mm depth on the base plane of test specimens.

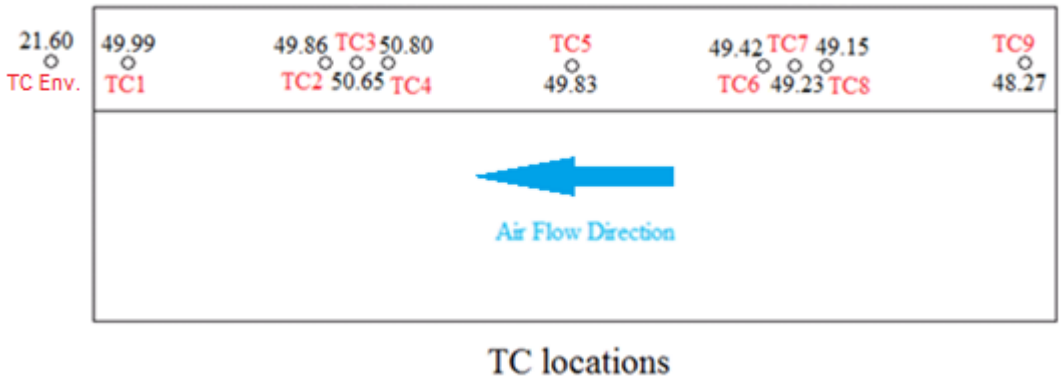

Figure C.1 Surface temperatures of bare fin block at 2 section at 60 Watt heater and 4 m/s air velocity

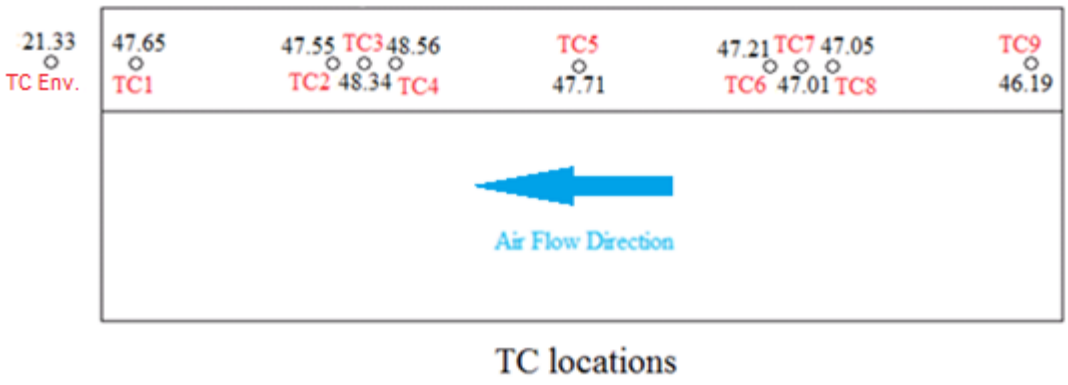

Figure C.2 Surface temperatures of bare fin block at 2 section at 60 Watt heater and 6 m/s air velocity

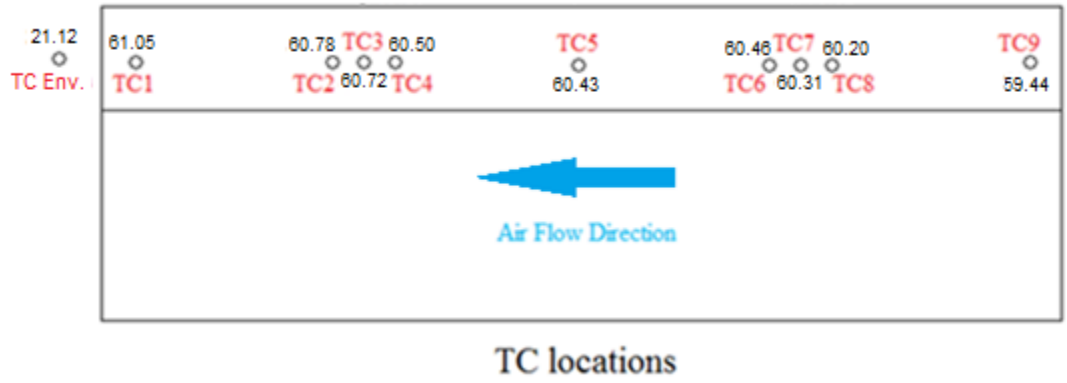

Figure C.3 Surface temperatures of bare fin block at 80 Watt heater and 4 m/s air velocity

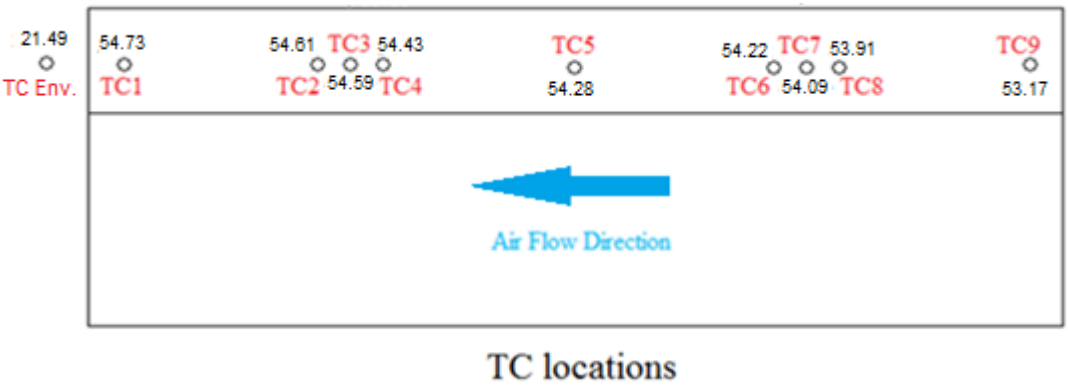

Figure C.4 Surface temperatures of bare fin block at 80 Watt heater and 6 m/s air velocity

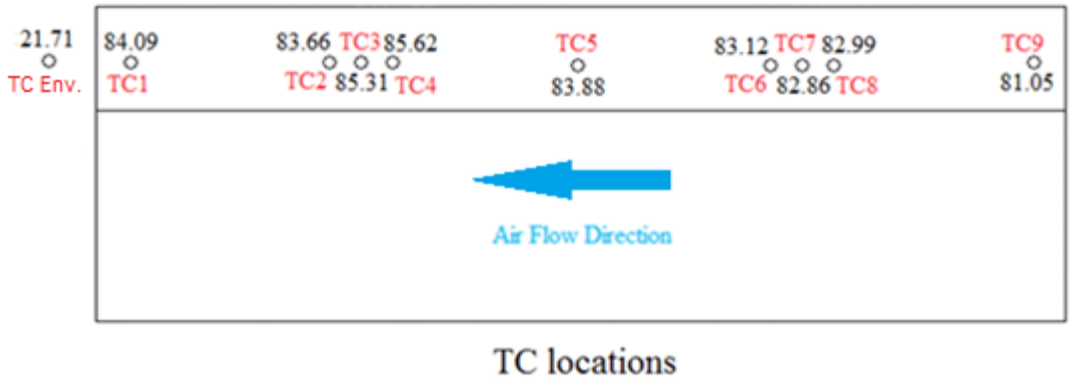

Figure C.5 Surface temperatures of bare fin block at 2 section 120 Watt heater and 4 m/s air velocity

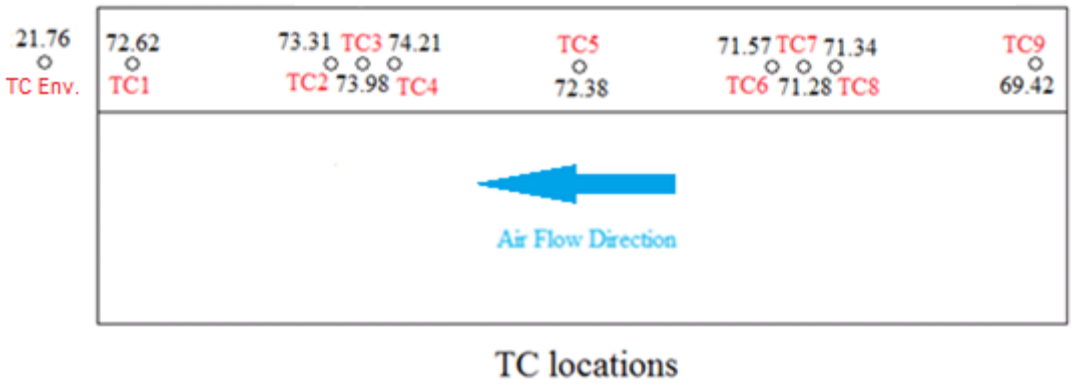

Figure C.6 Surface temperatures of bare fin block 2 section at 120 Watt heater and 6 m/s air velocity

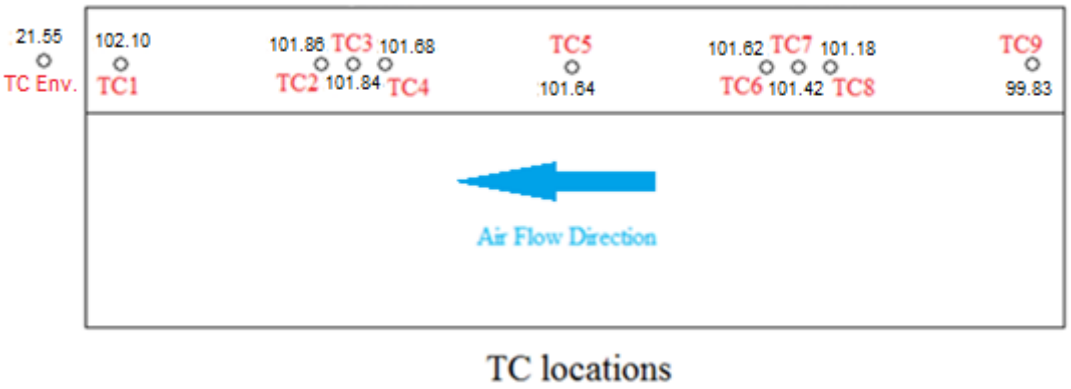

Figure C.7 Surface temperatures of bare fin block at 160 Watt heater and 4 m/s air velocity

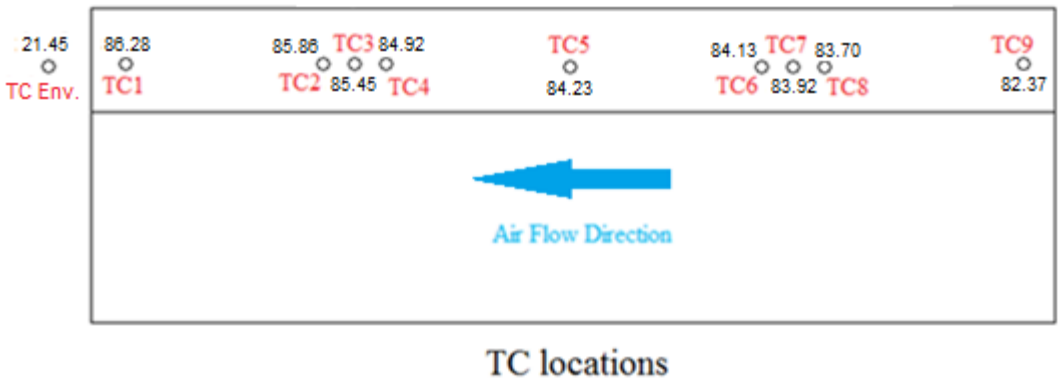

Figure C.8 Surface temperatures of bare fin block at 160 Watt heater and 6 m/s air velocity

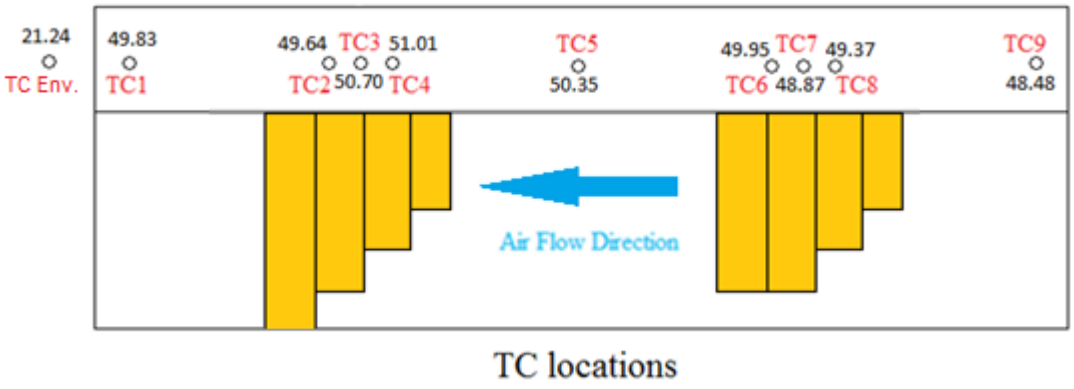

Figure C.9 Surface temperatures of 10PPI AL embedded heat sink at 2 section 60 Watt heater and 4 m/s air velocity

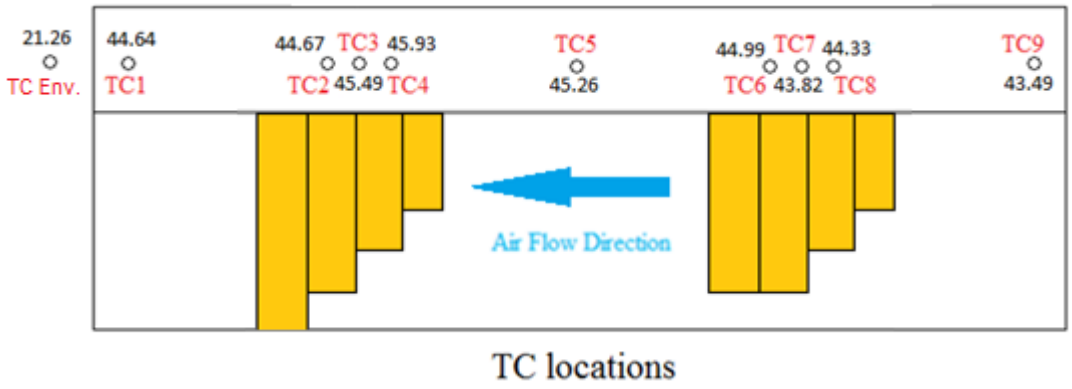

Figure C.10 Surface temperatures of 10PPI AL embedded heat sink at 2 section 60 Watt heater and 6 m/s air velocity

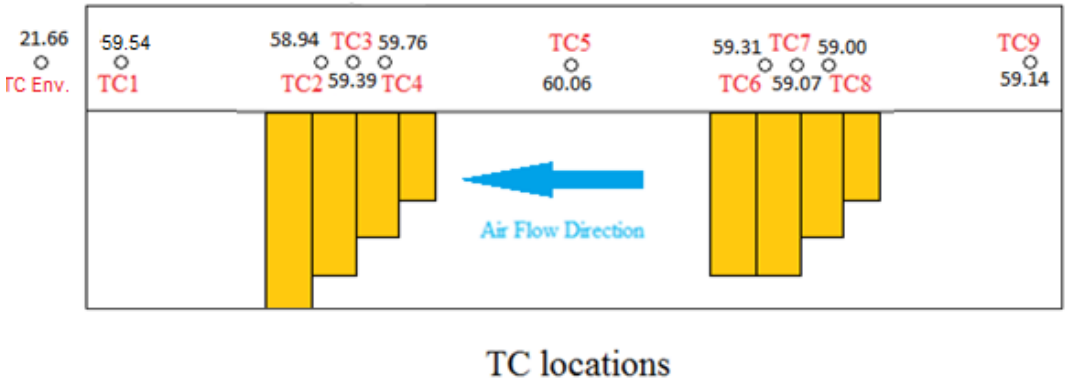

Figure C.11 Surface temperatures of 10PPI AL embedded heat sink at 80 Watt heater and 4 m/s air velocity

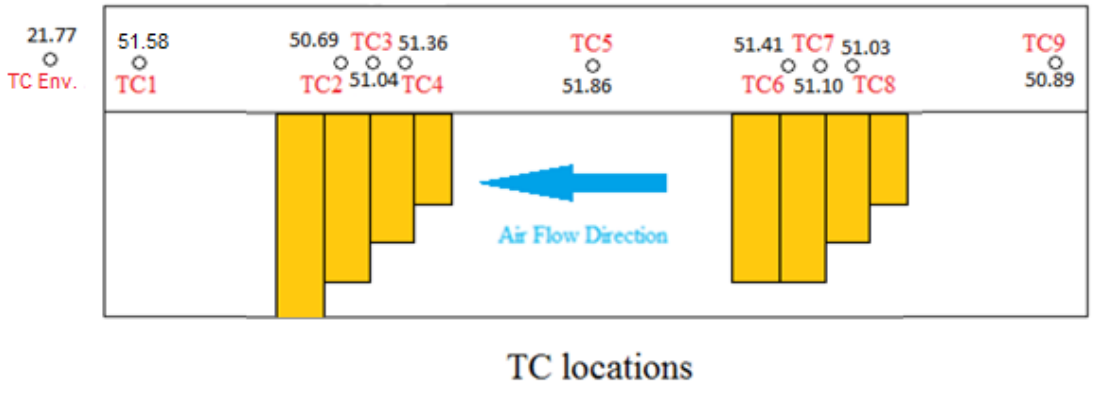

Figure C.12 Surface temperatures of 10PPI AL embedded heat sink at 80 Watt heater and 6 m/s air velocity

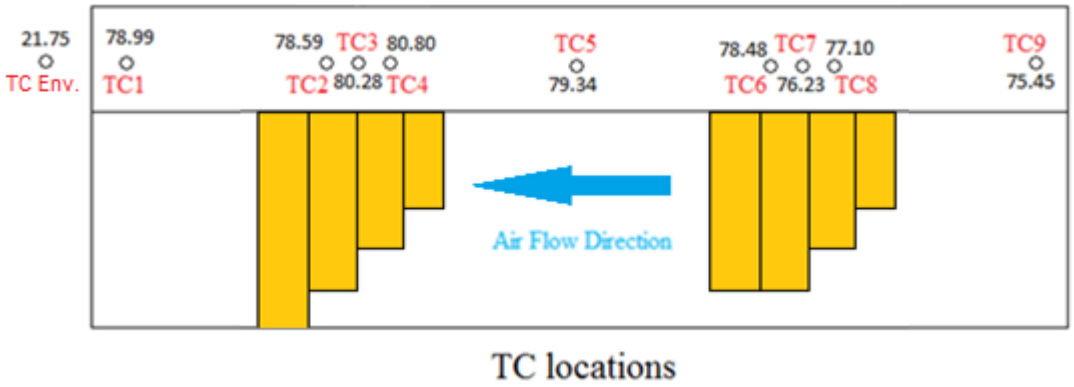

Figure C.13 Surface temperatures of 10PPI AL embedded heat sink at 2 section 120 Watt heater and 4 m/s air velocity

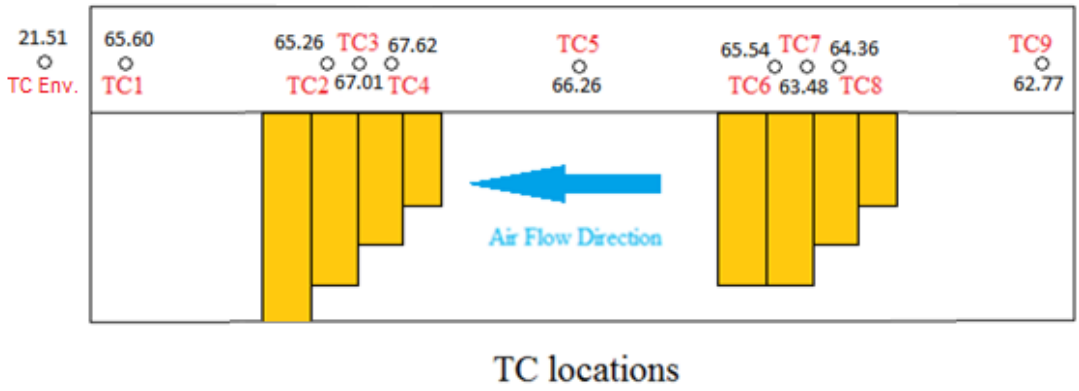

Figure C.14 Surface temperatures of 10PPI AL embedded heat sink at 2 section 120 Watt heater and 6 m/s air velocity

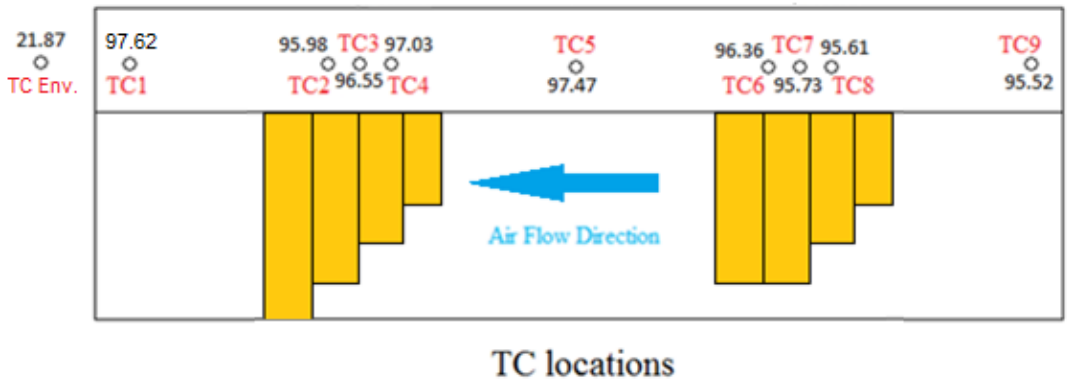

Figure C.15 Surface temperatures of 10PPI AL embedded heat sink at 160 Watt heater and 4 m/s air velocity

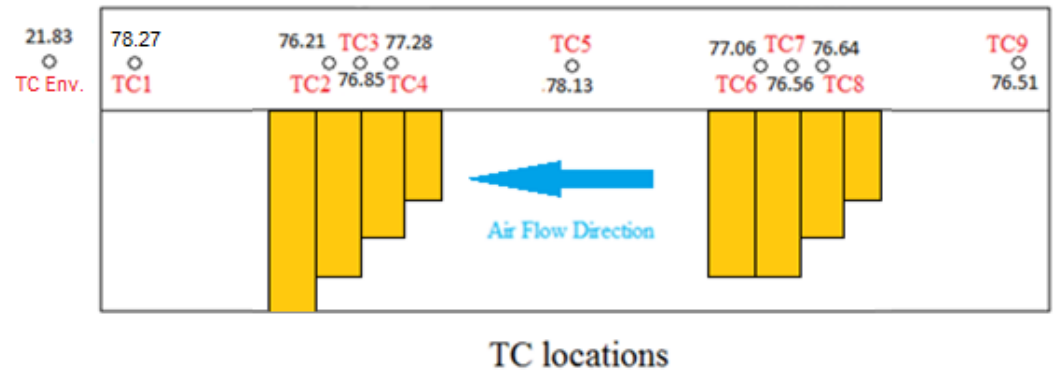

Figure C.16 Surface temperatures of 10PPI AL embedded heat sink at 160 Watt heater and 6 m/s air velocity

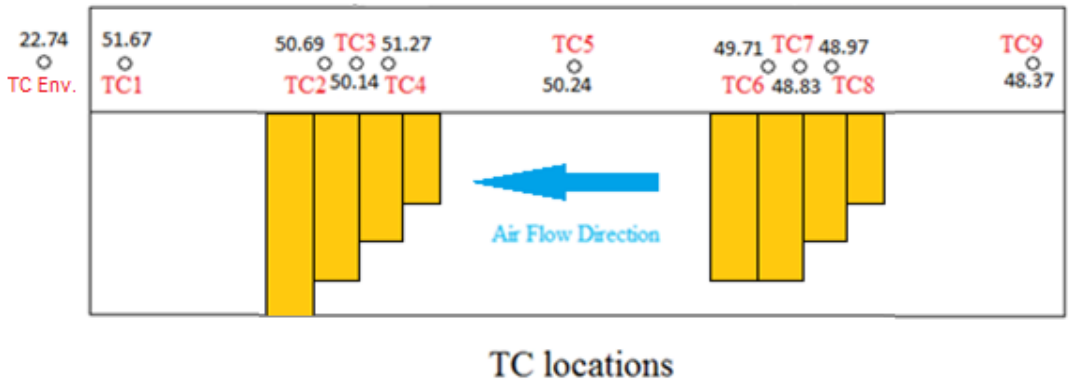

Figure C.17 Surface temperatures of 20PPI AL embedded heat sink at 2 section 60 Watt heater and 4 m/s air velocity

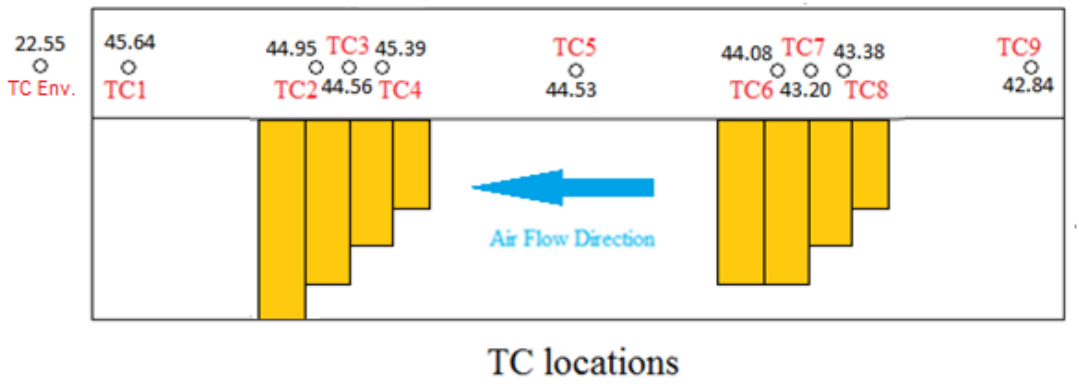

Figure C.18 Surface temperatures of 20PPI AL embedded heat sink at 2 section 60 Watt heater and 6 m/s air velocity

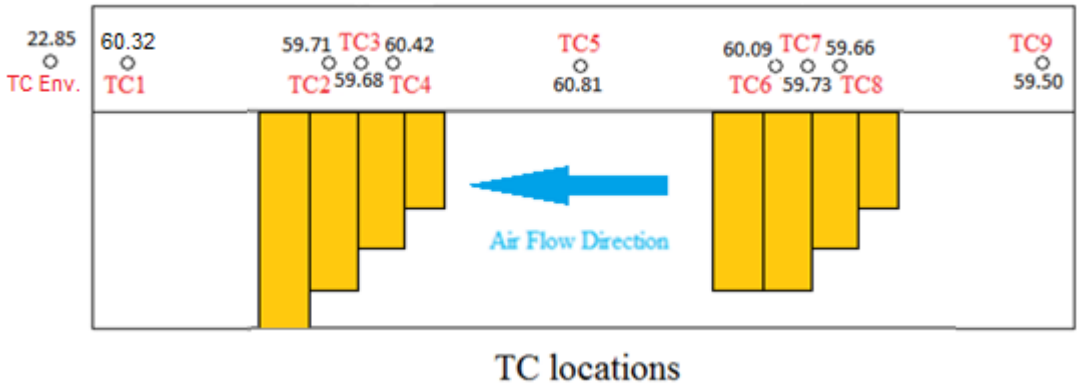

Figure C.19 Surface temperatures of 20PPI AL embedded heat sink at 80 Watt heater and 4 m/s air velocity

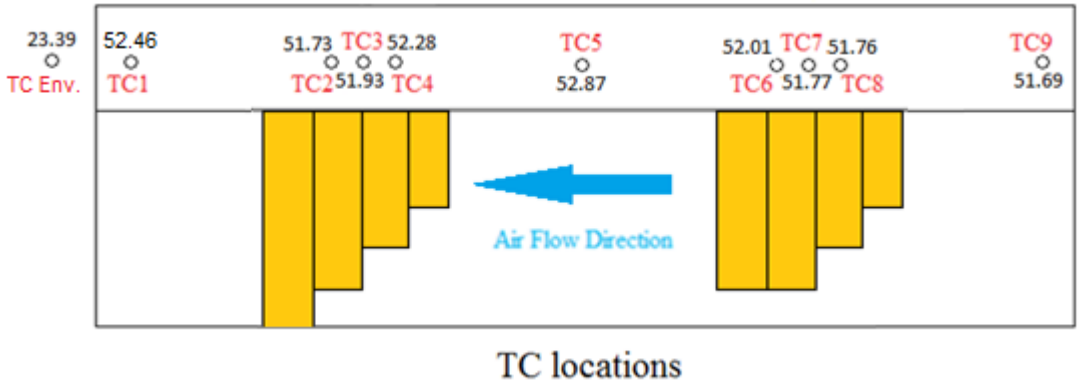

Figure C.20 Surface temperatures of 20PPI AL embedded heat sink at 80 Watt heater and 6 m/s air velocity

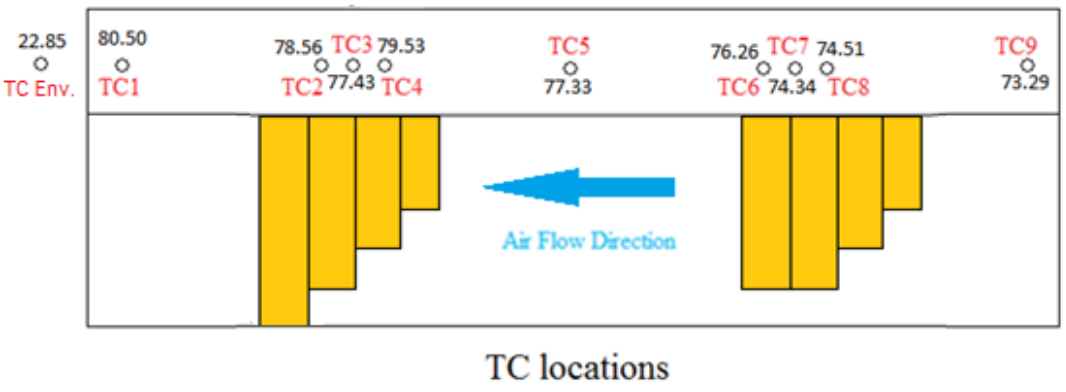

Figure C.21 Surface temperatures of 20PPI AL embedded heat sink at 2 section 120 Watt heater and 4 m/s air velocity

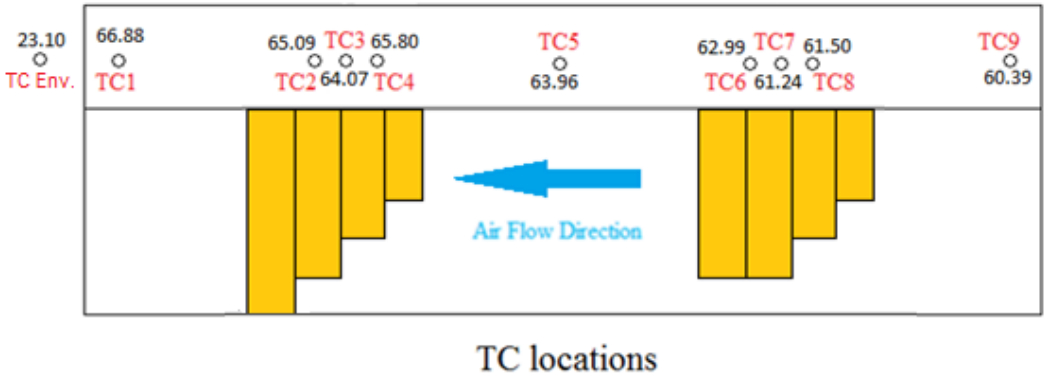

Figure C.22 Surface temperatures of 20PPI AL embedded heat sink at 2 section 120 Watt heater and 6 m/s air velocity

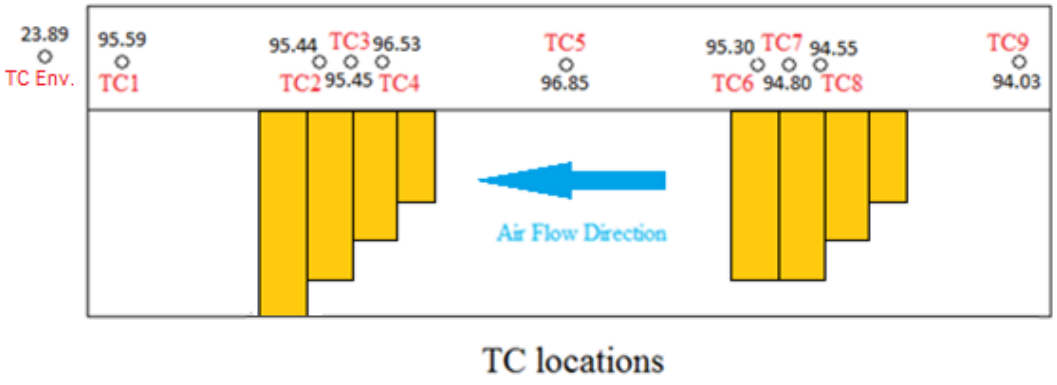

Figure C.23 Surface temperatures of 20PPI AL embedded heat sink at 160 Watt heater and 4 m/s air velocity

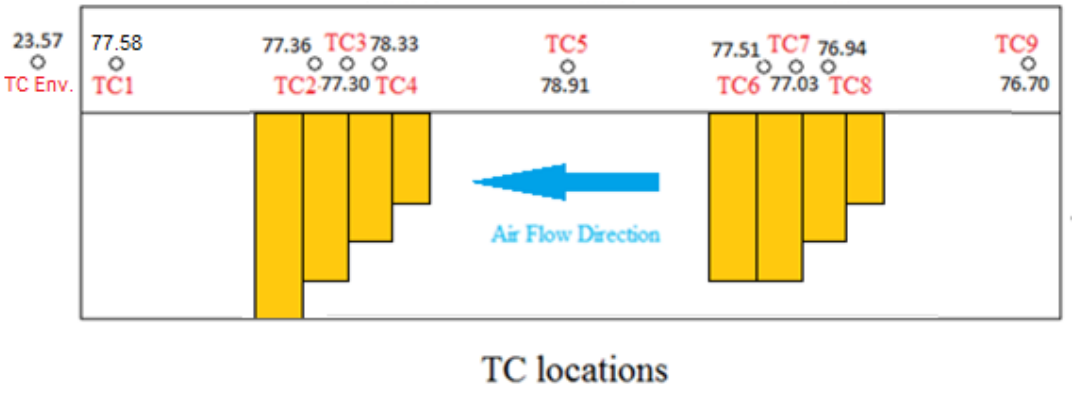

Figure C.24 Surface temperatures of 20PPI AL embedded heat sink at 160 Watt heater and 6 m/s air velocity

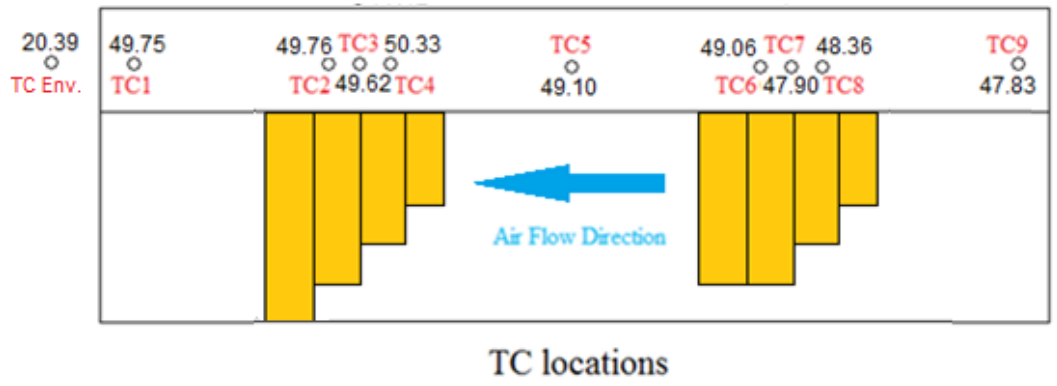

Figure C.25 Surface temperatures of 40PPI AL embedded heat sink at 2 section 60 Watt heater and 4 m/s air velocity

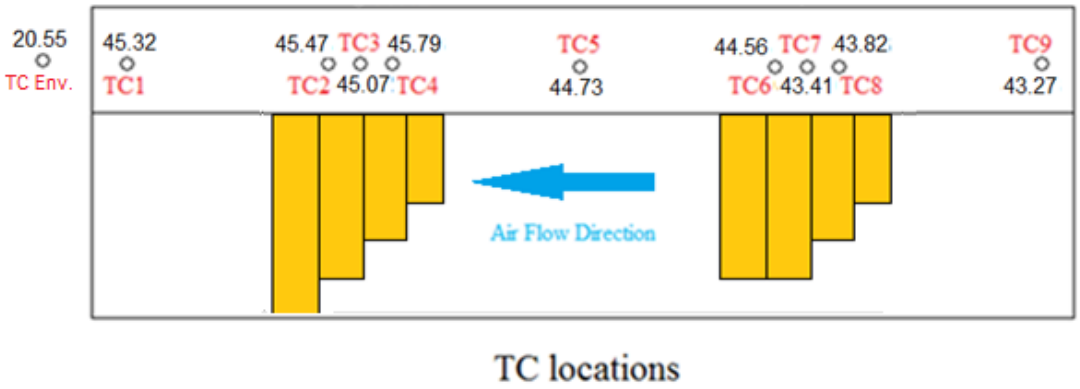

Figure C.26 Surface temperatures of 40PPI AL embedded heat sink at 2 section 60 Watt heater and 6 m/s air velocity

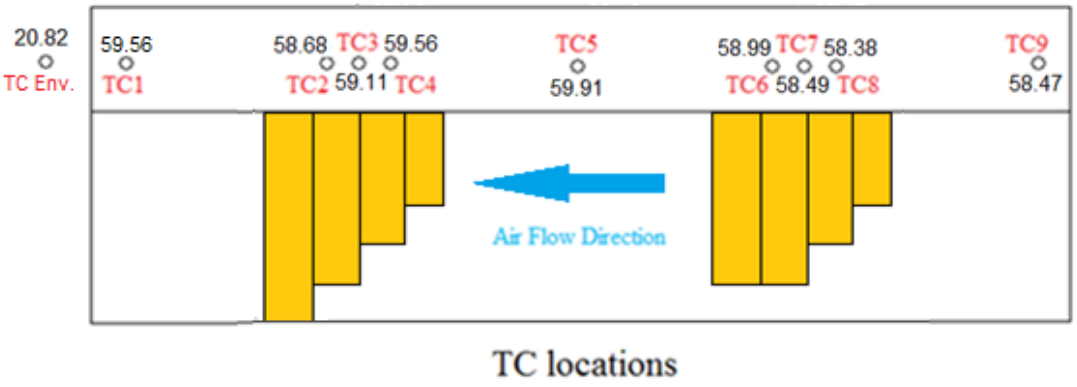

Figure C.27 Surface temperatures of 40PPI AL embedded heat sink at 80 Watt heater and 4 m/s air velocity

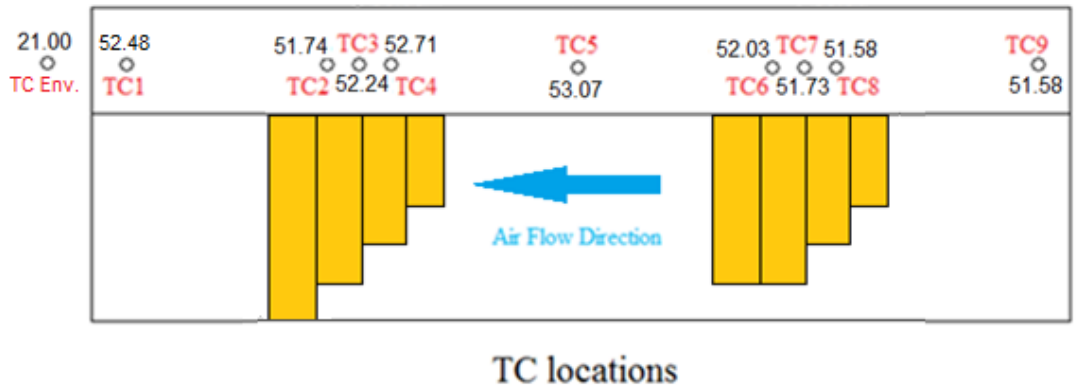

Figure C.28 Surface temperatures of 40PPI AL embedded heat sink at 80 Watt heater and 6 m/s air velocity

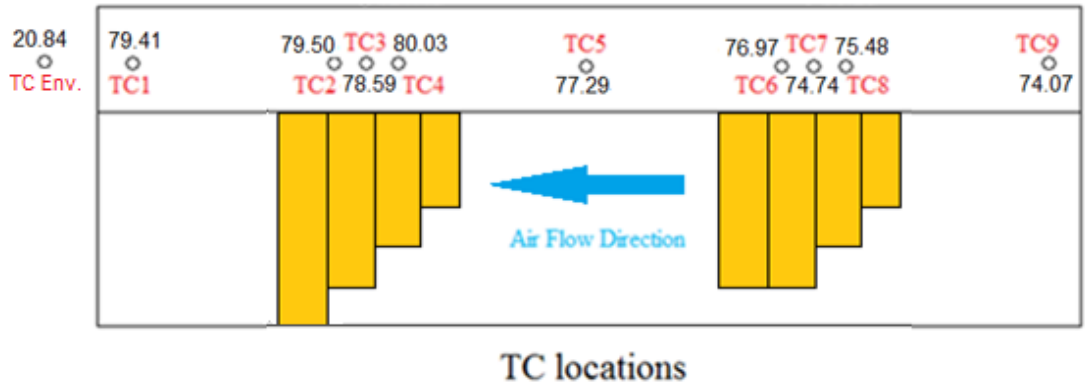

Figure C.29 Surface temperatures of 40PPI AL embedded heat sink at 2 section 120 Watt heater and 4 m/s air velocity

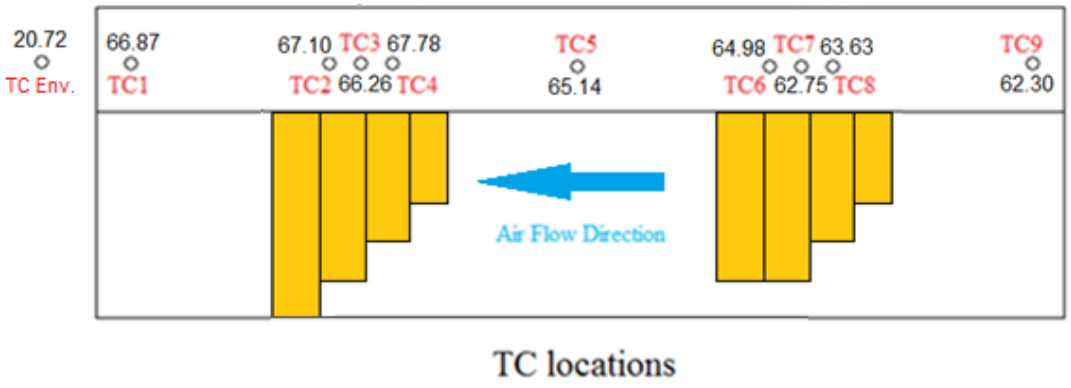

Figure C.30 Surface temperatures of 40PPI AL embedded heat sink at 2 section 120 Watt heater and 6 m/s air velocity

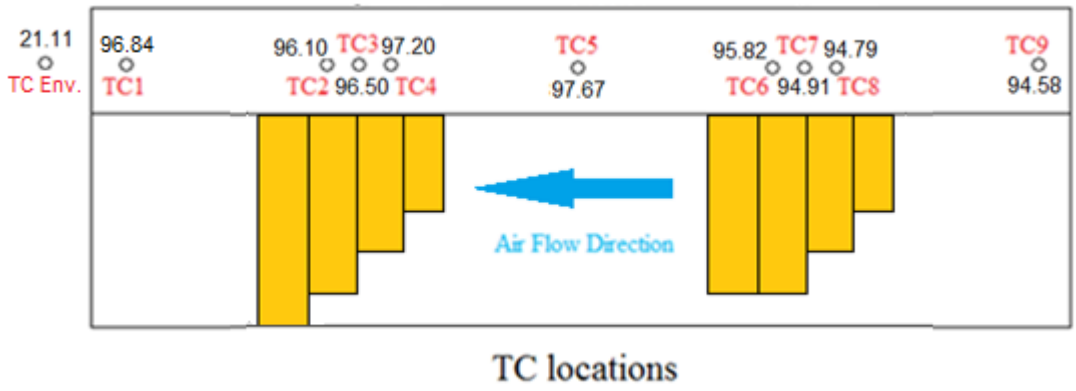

Figure C.31 Surface temperatures of 40PPI AL embedded heat sink at 160 Watt heater and 4 m/s air velocity

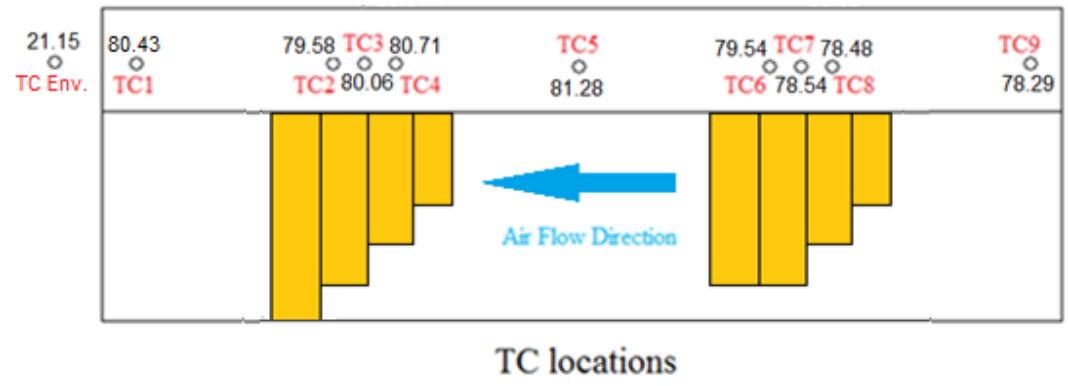

Figure C.32 Surface temperatures of 40PPI AL embedded heat sink at 160 Watt heater and 6 m/s air velocity

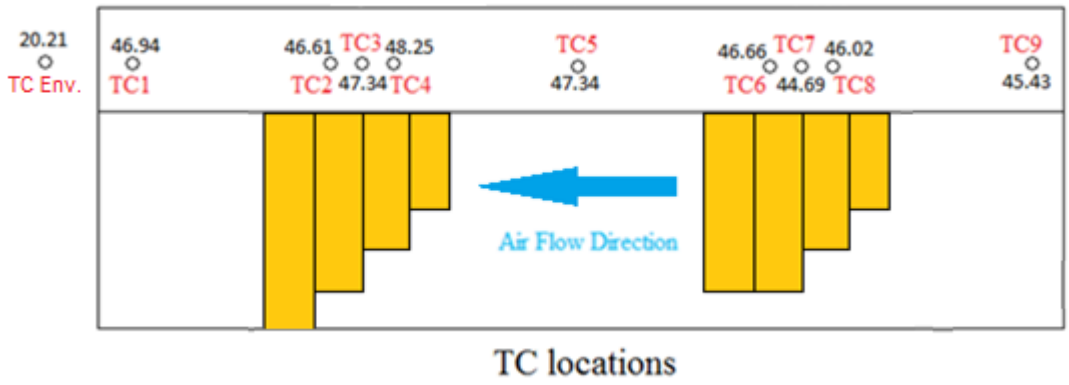

Figure C.33 Surface temperatures of 10PPI CU embedded heat sink at 2 section 60 Watt heater and 4 m/s air velocity

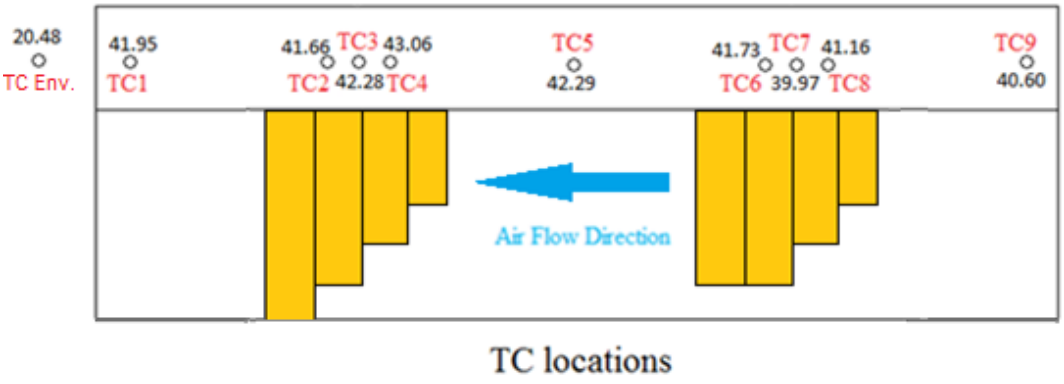

Figure C.34 Surface temperatures of 10PPI CU embedded heat sink at 2 section 60 Watt heater and 6 m/s air velocity

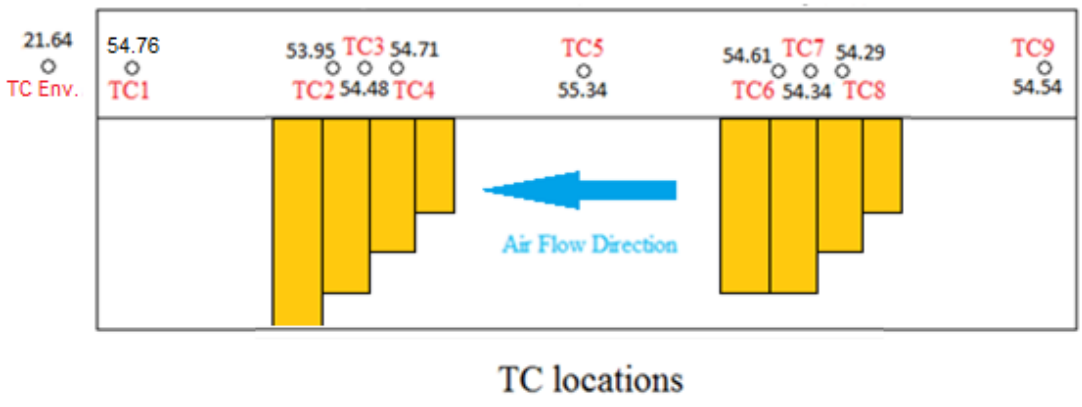

Figure C.35 Surface temperatures of 10PPI CU embedded heat sink at 80 Watt heater and 4 m/s air velocity

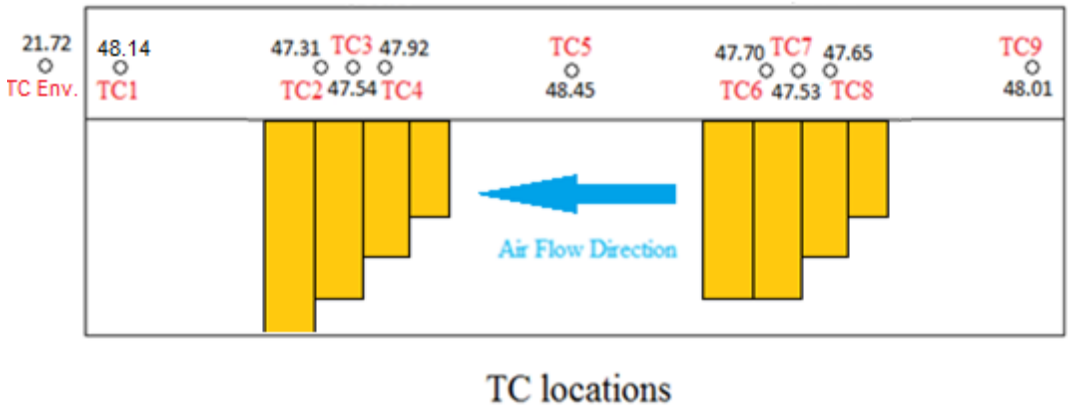

Figure C.36 Surface temperatures of 10PPI CU embedded heat sink at 80 Watt heater and 6 m/s air velocity

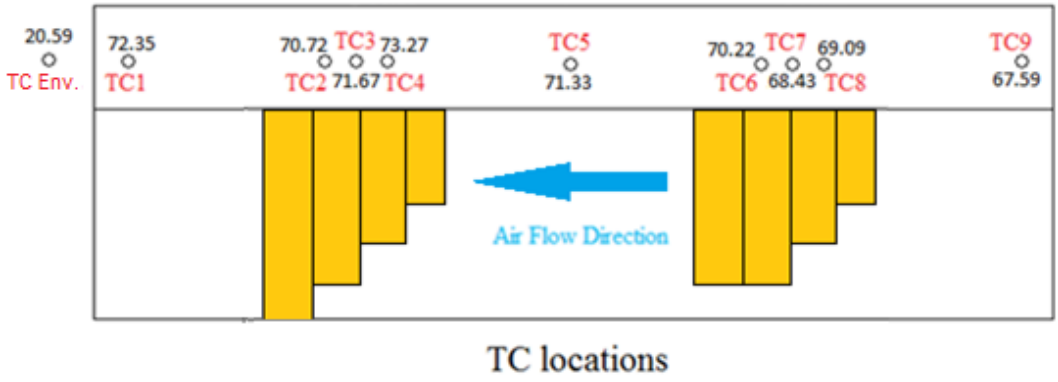

Figure C.37 Surface temperatures of 10PPI CU embedded heat sink at 2 section 120 Watt heater and 4 m/s air velocity

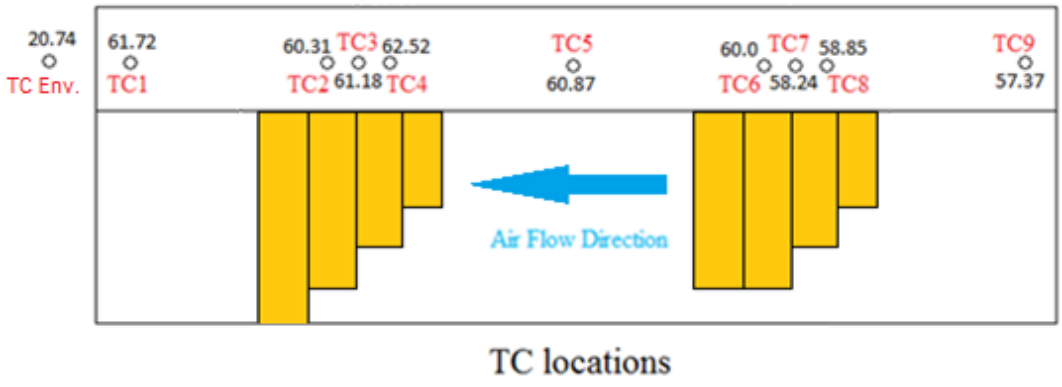

Figure C.38 Surface temperatures of 10PPI CU embedded heat sink at 2 section 120 Watt heater and 6 m/s air velocity

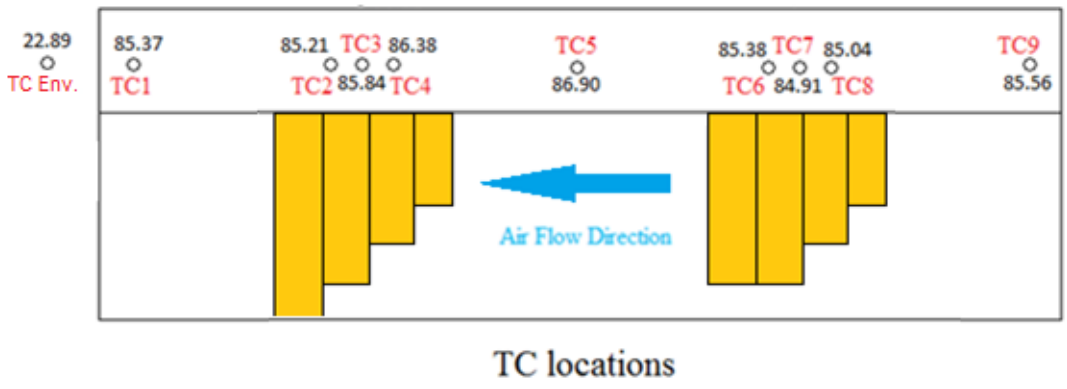

Figure C.39 Surface temperatures of 10PPI CU embedded heat sink at 160 Watt heater and 4 m/s air velocity

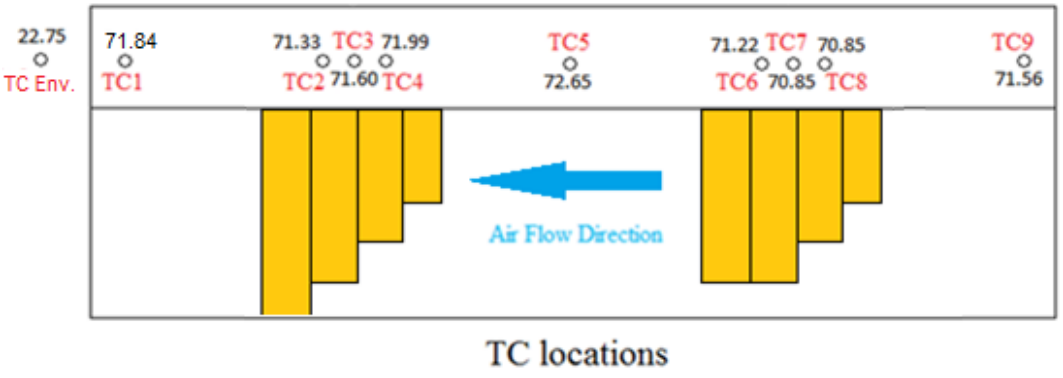

Figure C.40 Surface temperatures of 10PPI CU embedded heat sink at 160 Watt heater and 6 m/s air velocity

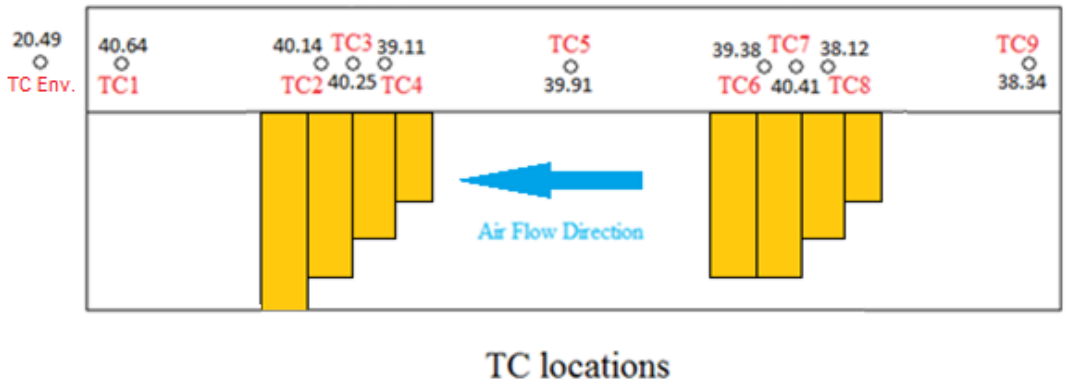

Figure C.41 Surface temperatures of 20PPI CU embedded heat sink at 2 section 60 Watt heater and 4 m/s air velocity

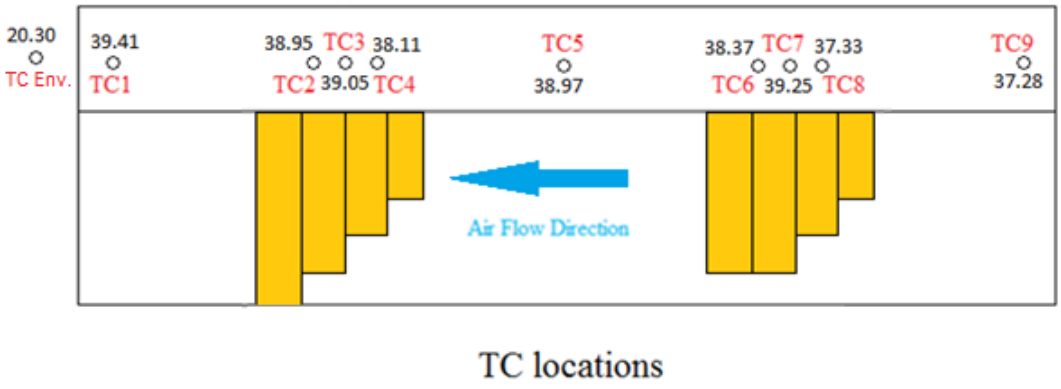

Figure C.42 Surface temperatures of 20PPI CU embedded heat sink at 2 section 60 Watt heater and 6 m/s air velocity

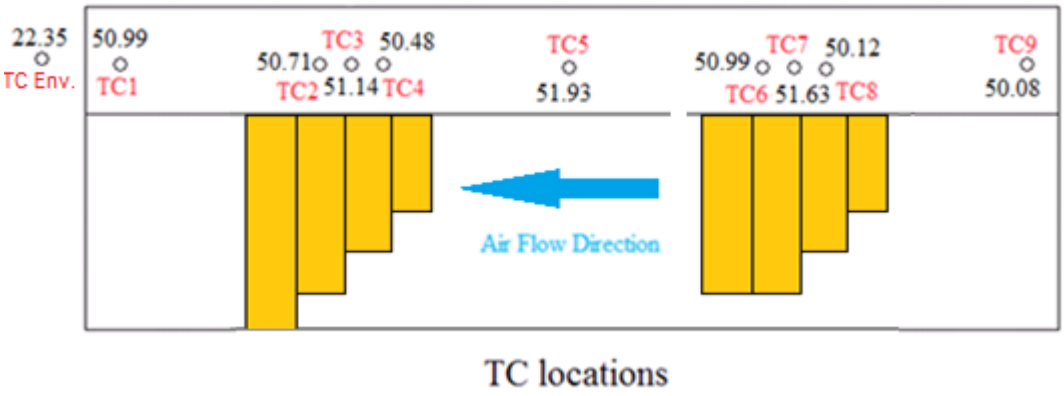

Figure C.43 Surface temperatures of 20PPI CU embedded heat sink at 80 Watt heater and 4 m/s air velocity

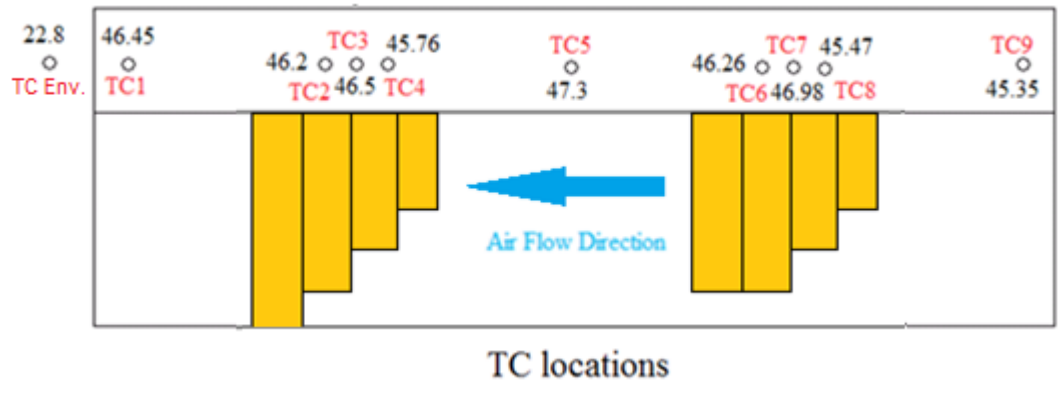

Figure C.44 Surface temperatures of 20PPI CU embedded heat sink at 80 Watt heater and 6 m/s air velocity

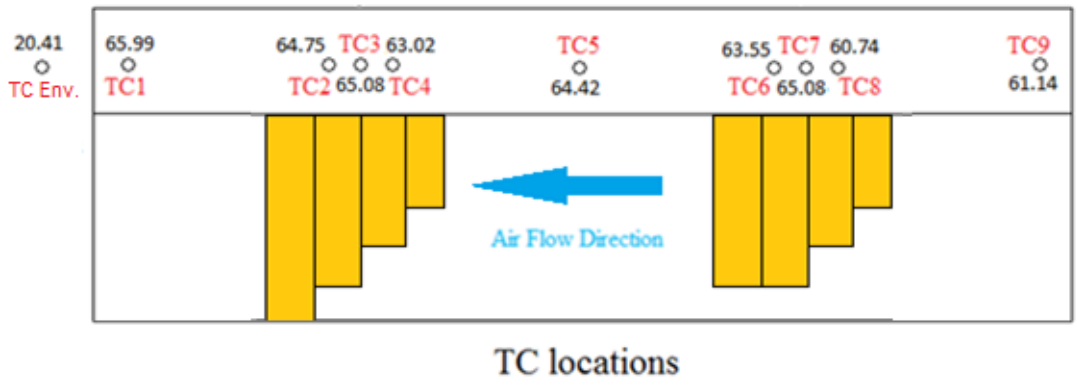

Figure C.45 Surface temperatures of 20PPI CU embedded heat sink at 2 section 120 Watt heater and 4 m/s air velocity

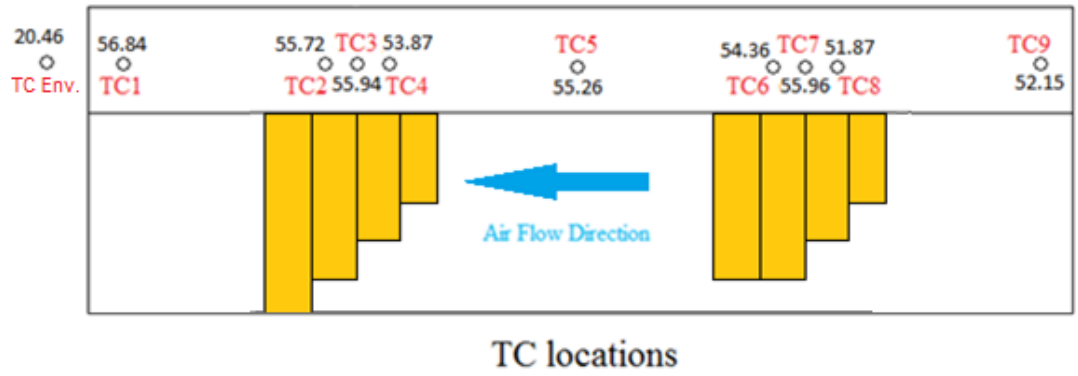

Figure C.46 Surface temperatures of 20PPI CU embedded heat sink at 2 section 120 Watt heater and 6 m/s air velocity

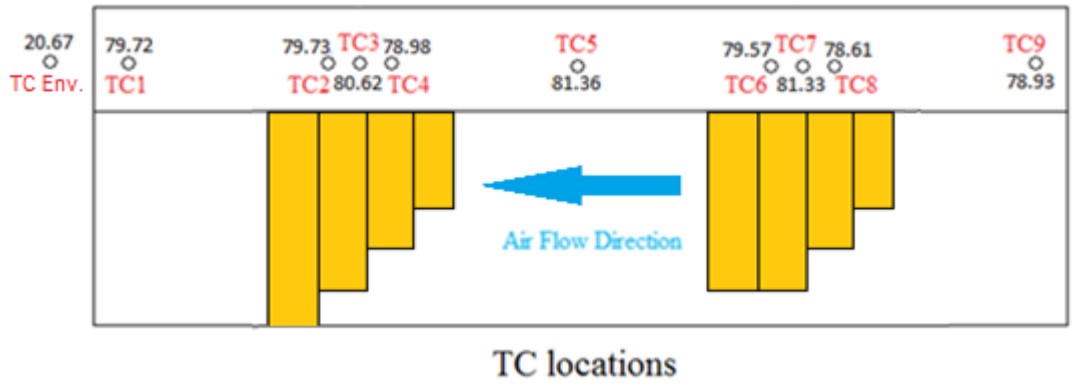

Figure C.47 Surface temperatures of 20PPI CU embedded heat sink at 160 Watt heater and 4 m/s air velocity

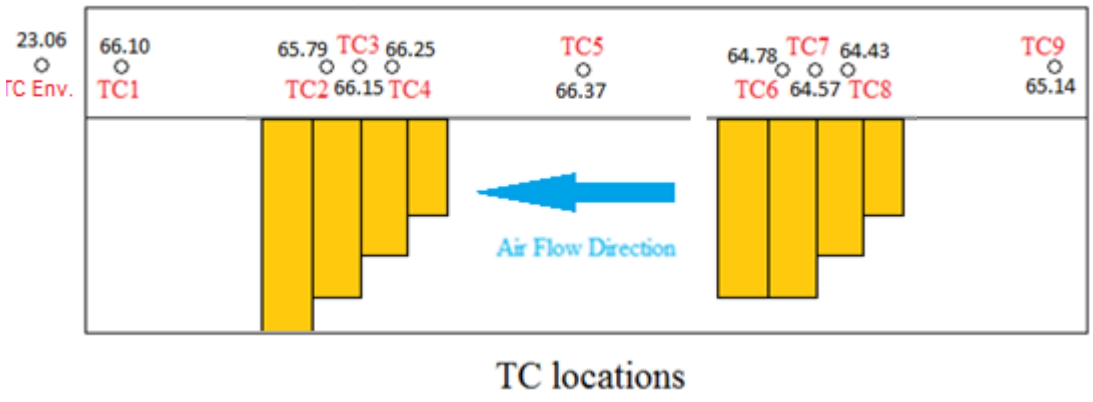

Figure C.48 Surface temperatures of 20PPI CU embedded heat sink at 160 Watt heater and 6 m/s air velocity

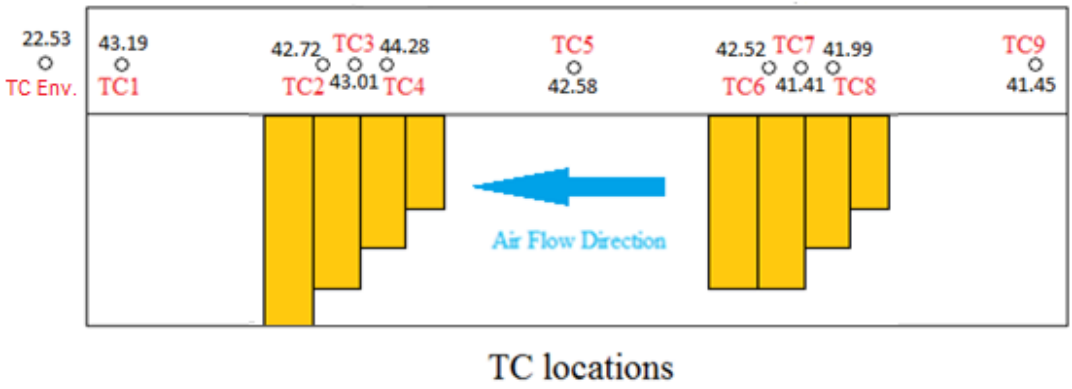

Figure C.49 Surface temperatures of 40PPI CU embedded heat sink at 2 section 60 Watt heater and 4 m/s air velocity

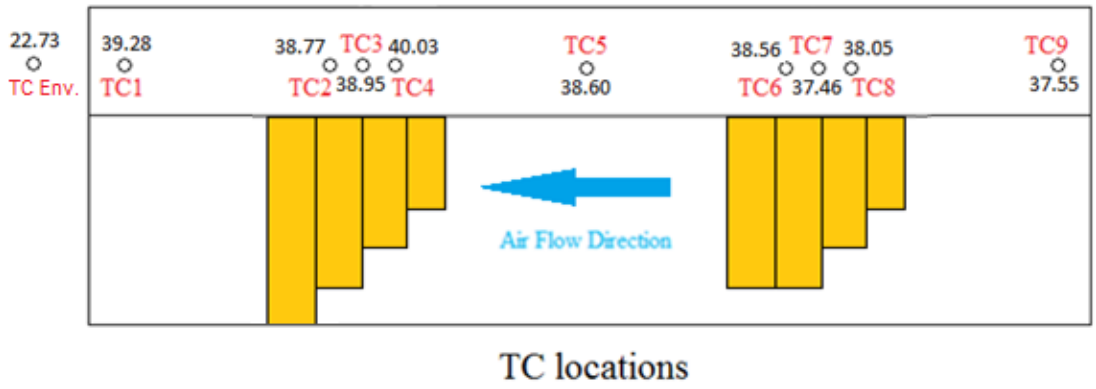

Figure C.50 Surface temperatures of 40PPI CU embedded heat sink at 2 section 60 Watt heater and 6 m/s air velocity

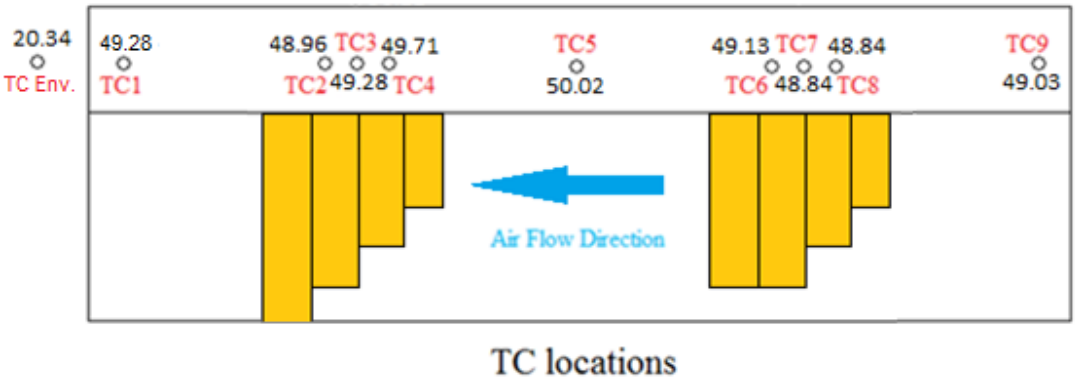

Figure C.51 Surface temperatures of 40PPI CU embedded heat sink at 80 Watt heater and 4 m/s air velocity

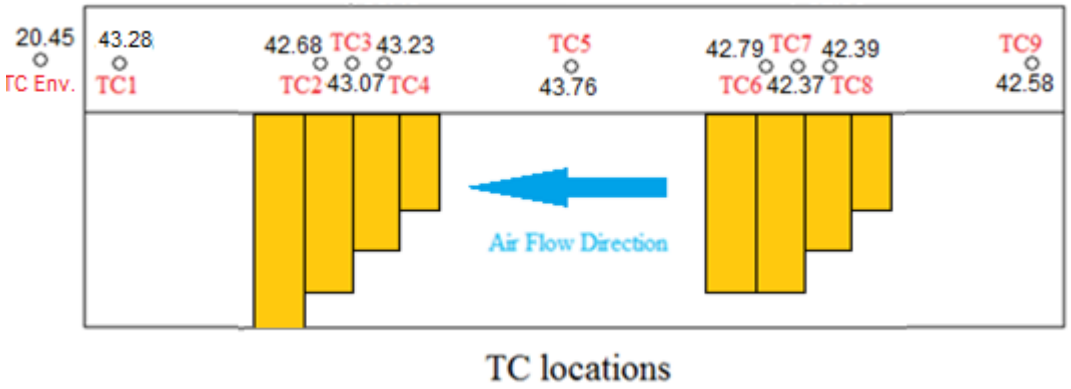

Figure C.52 Surface temperatures of 40PPI CU embedded heat sink at 80 Watt heater and 6 m/s air velocity

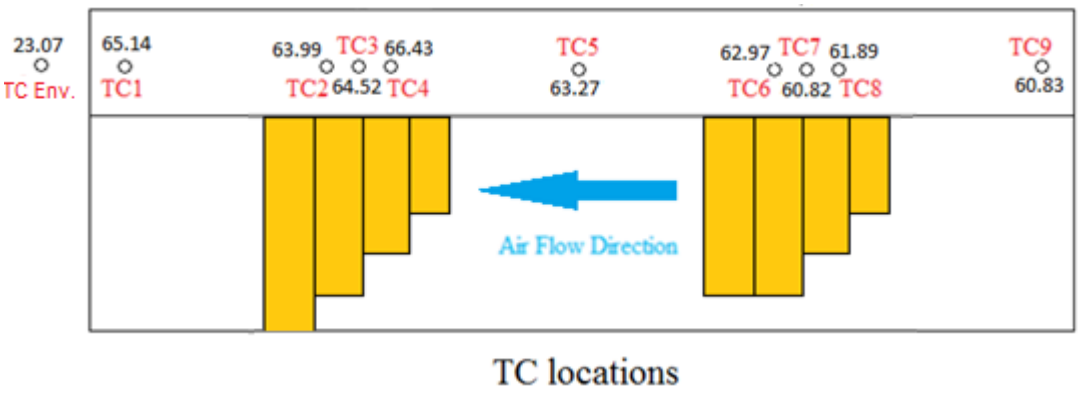

Figure C.53 Surface temperatures of 40PPI CU embedded heat sink at 2 section 120 Watt heater and 4 m/s air velocity

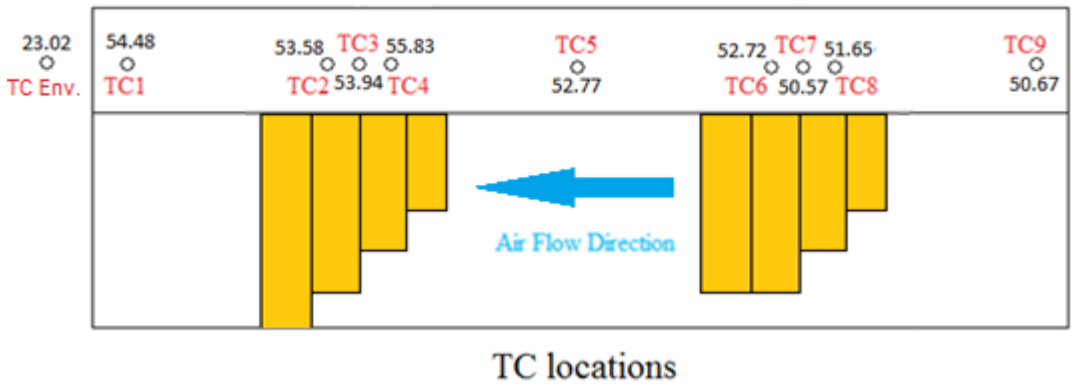

Figure C.54 Surface temperatures of 40PPI CU embedded heat sink at 2 section 120 Watt heater and 6 m/s air velocity

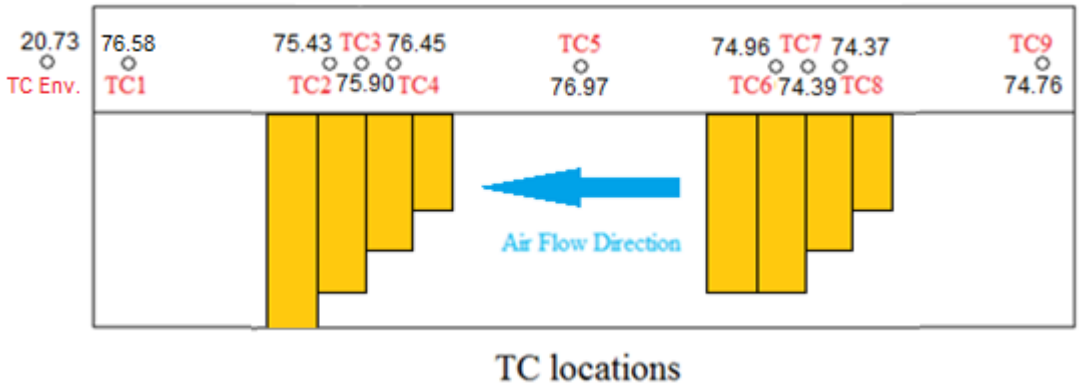

Figure C.55 Surface temperatures of 40PPI CU embedded heat sink at 160 Watt heater and 4 m/s air velocity

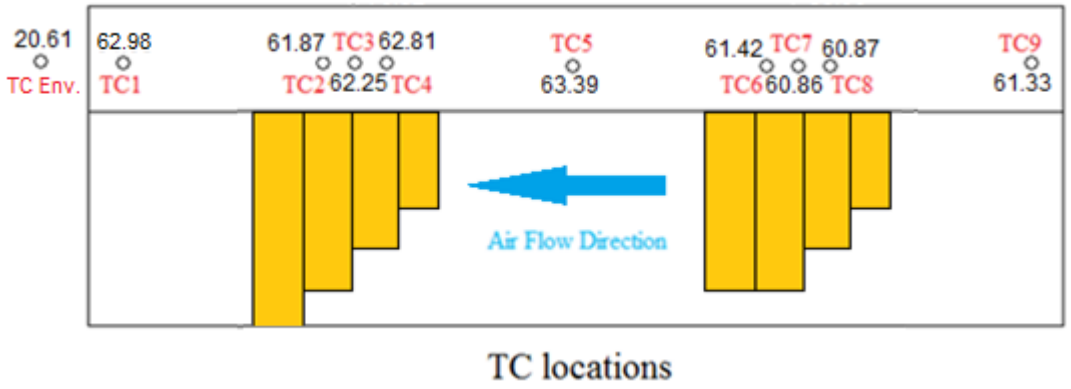

Figure C.56 Surface temperatures of 40PPI CU embedded heat sink at 160 Watt heater and 6 m/s air velocity

MEAN WALL TEMPERATURE AS A FUNCTION OF AIR FRONTAL VELOCITY FOR ALL HEATERS

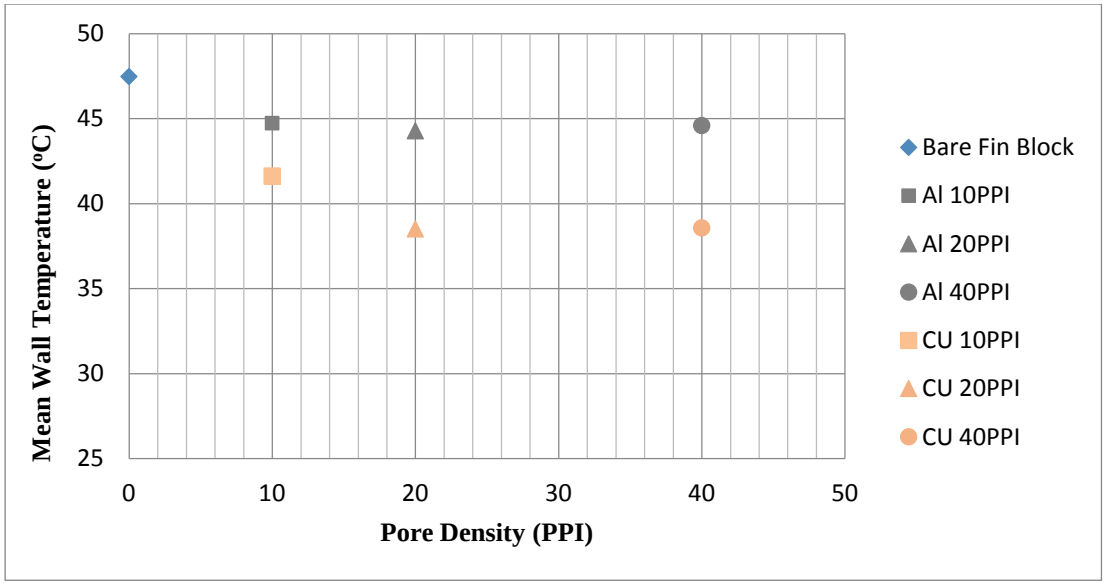

Figure C.57 Mean wall temperature, as a function of pore density at partial 60 W heaters and 6 m/s frontal air velocity

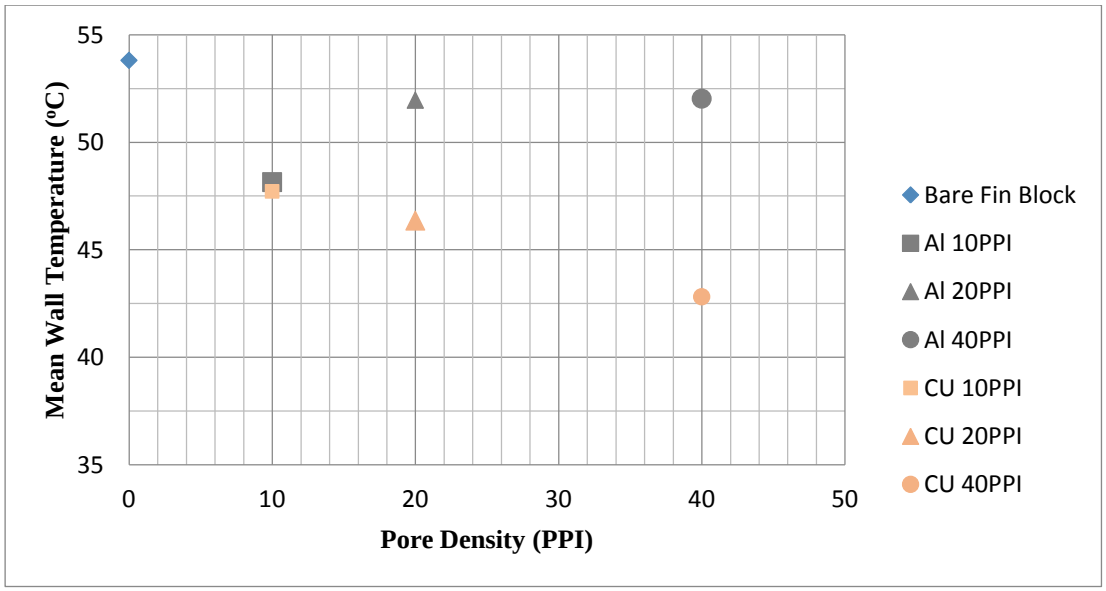

Figure C.58 Mean wall temperature, as a function of pore density at 80 W heater and 6 m/s frontal air velocity

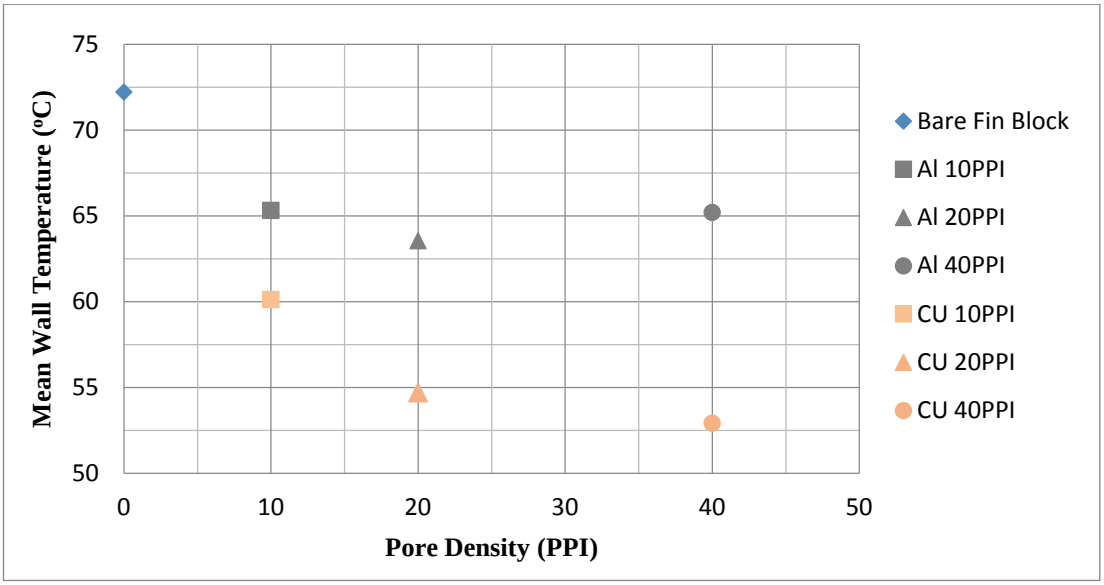

Figure C.59 Mean wall temperature, as a function of pore density at partial 120 W heaters and 6 m/s frontal air velocity

VARIATION of THERMAL RESISTANCE OF AIR FRONTAL VELOCITY FOR ALL HEATERS

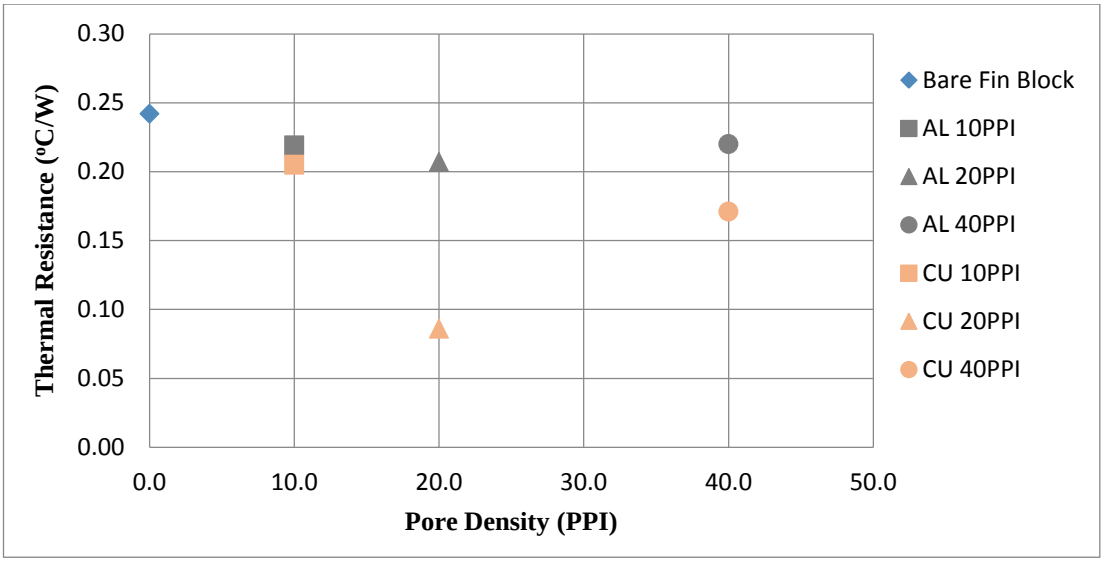

Figure C.60 Variation of R_{th} as a function of pore density at 80 W heater and 6 m/s frontal air velocity

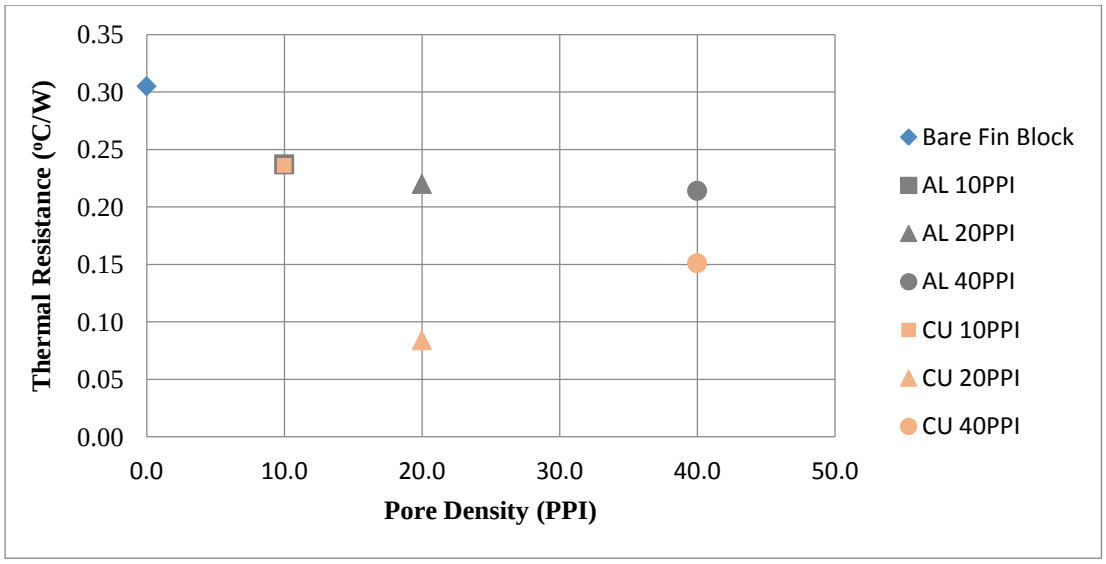

Figure C.61 Variation of R_{th} as a function of pore density at partial 120 W heaters and 6 m/s frontal air velocity

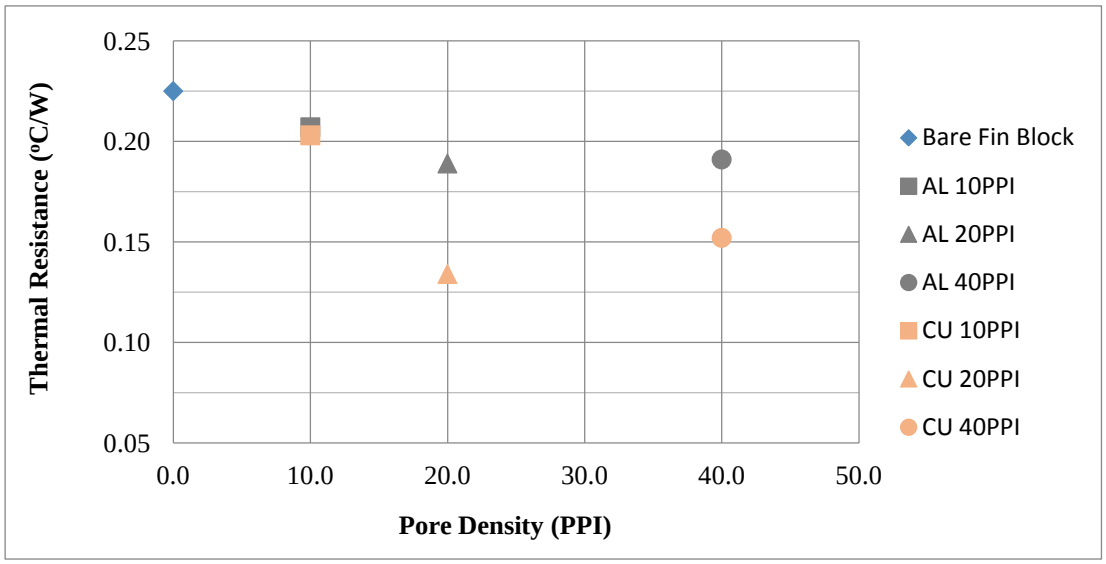

Figure C.62 Variation of R_{th} as a function of pore density at 160 W heater and 6 m/s frontal air velocity

APPENDIX D

PRESENTATION OF CFD RESULTS

Meshes of the Heat Sink Geometries

To analyse the fin block, a tetrahedron assembly mesh was chosen. Nearly half a million mesh elements were used with 0.90 average skewness ratio which is the ratio of the dimension of the mesh elements relative to the dimensions of one another. Mesh structure of fin block is presented in Figure D.1 and mesh parameters of fin block is given in Figure D.7.

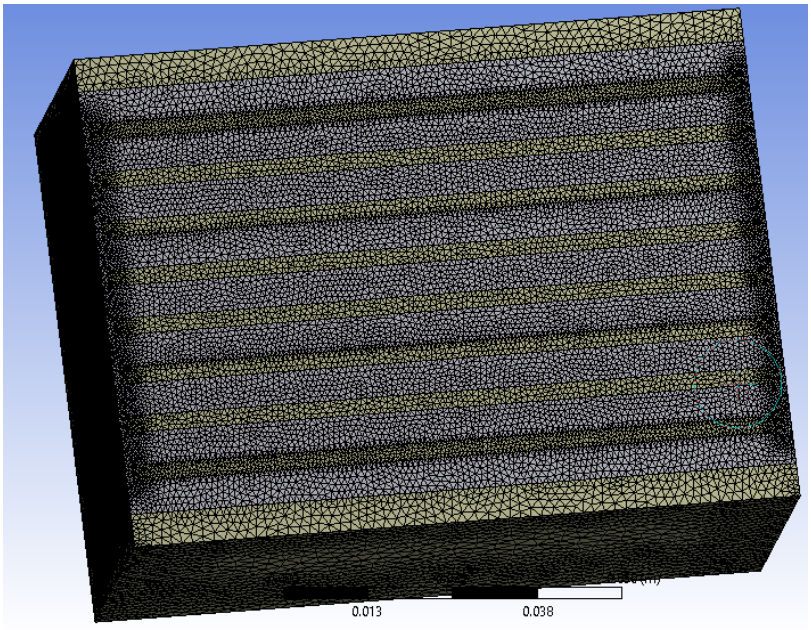

Figure D.1 The demonstration of the meshes of the fin block model in the CFD domain

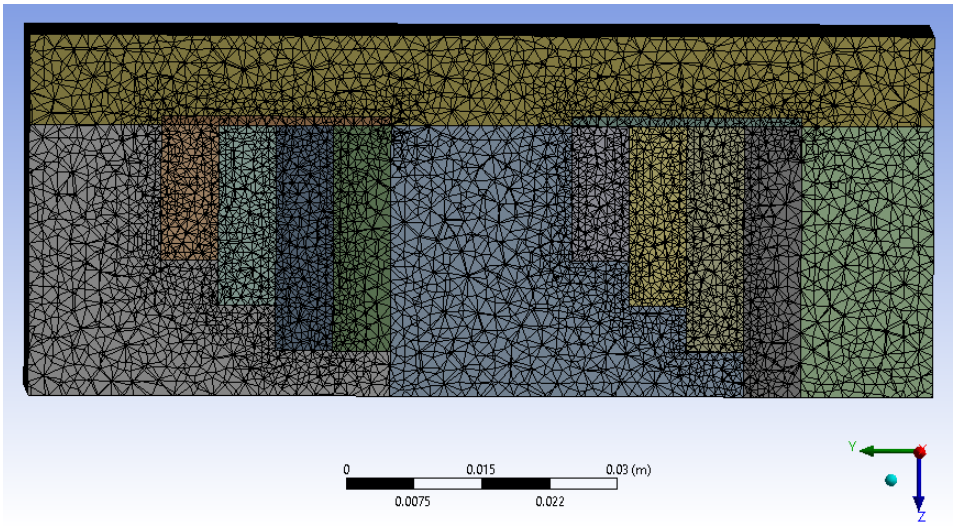

Figure D.2 Section views of the foam embedded heat sink meshes

At the foam embedded heat sinks, the element sizes on the foam entrance surfaces were shrunk to half of the overall geometry of the meshes as presented in Figure D.2. The mesh model of the foam embedded heat sinks has one million mesh elements and nearly 0.90 skewness ratio. The mesh parameters of fin the block are shown in Figure D.8.

The named selections of the surfaces are defined in the mesh module and transferred to a solver module as illustrated in Figure D.3, Figure D.4, Figure D.5 and Figure D.6. The defined names and the boundary conditions are stated in the subtitle Commercial FLUENT Implementation Steps of the Heat Sinks.

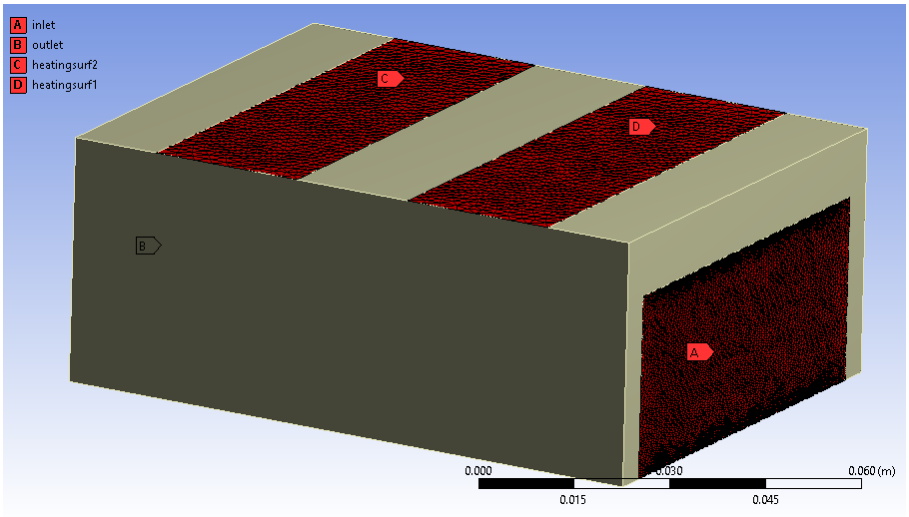

Figure D.3 The demonstration of the name selections of the heat sinks

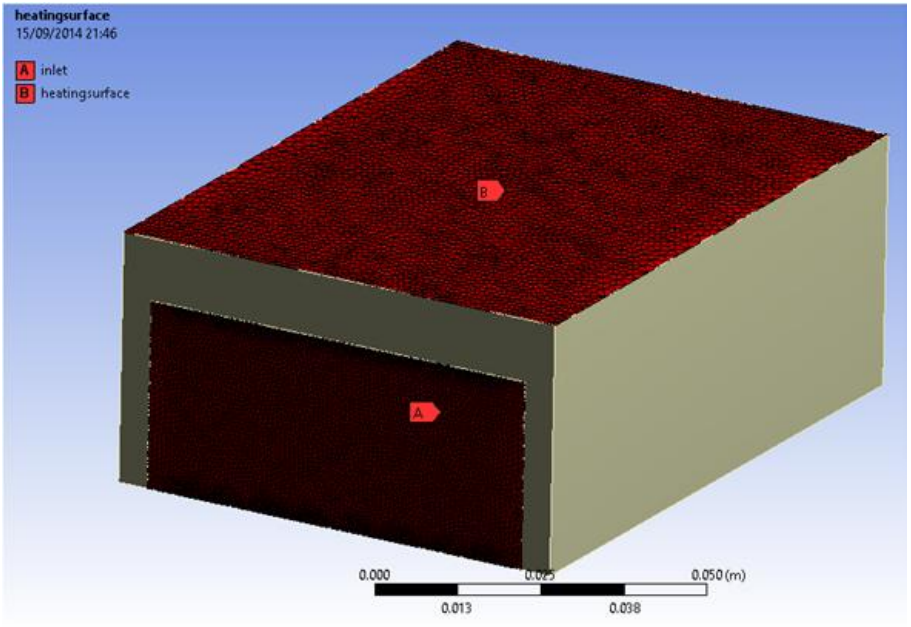

Figure D.4 The selected boundary surfaces of the fin block

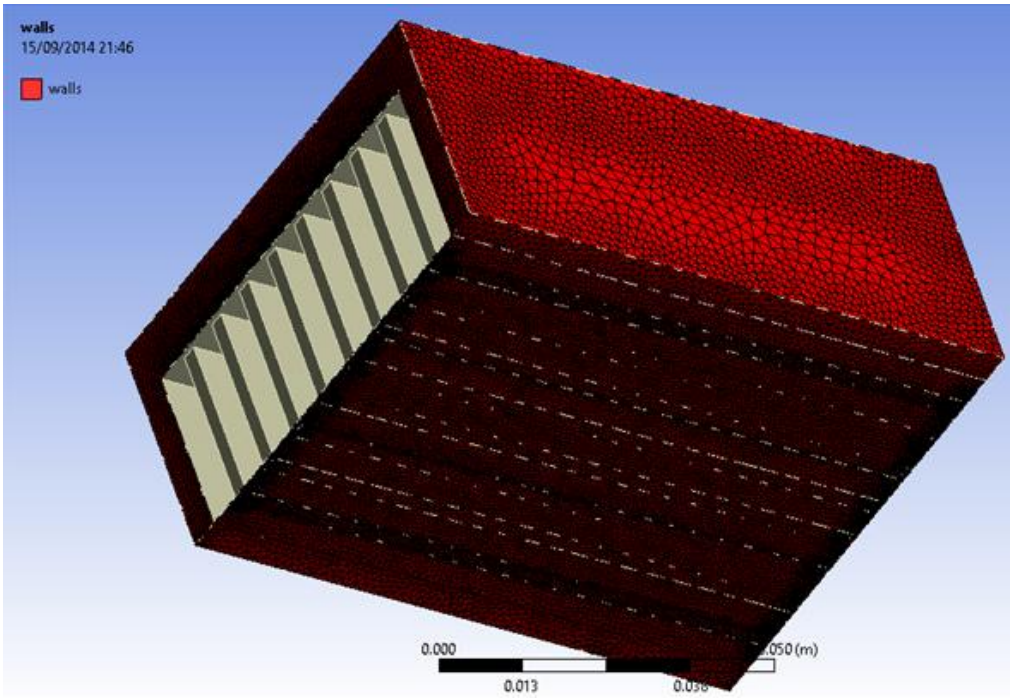

Figure D.5 The adiabatic defined walls of the fin block

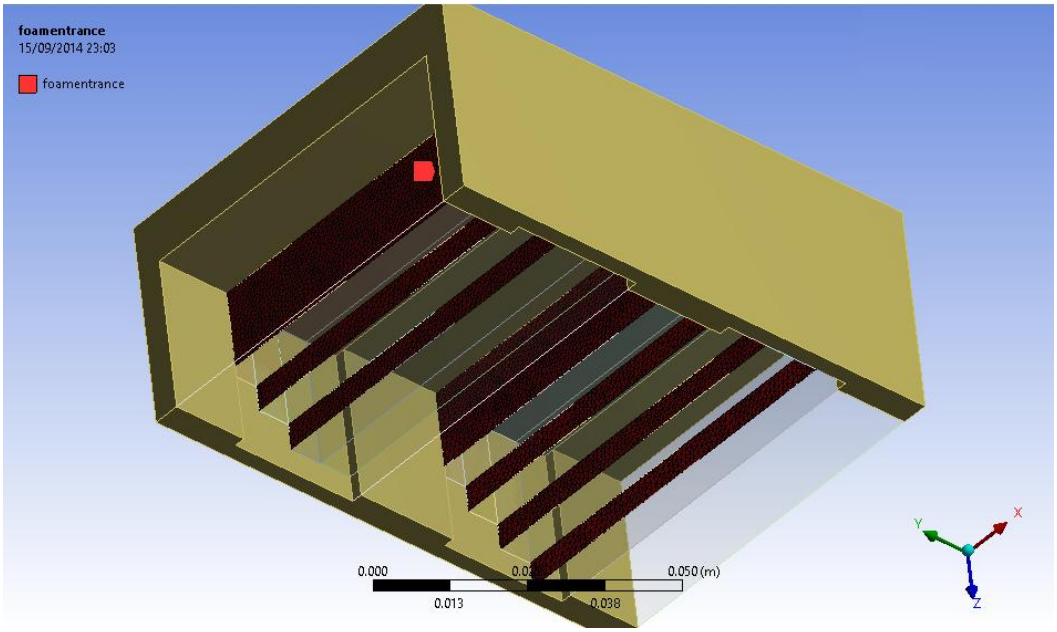

Figure D.6 Air entrance surfaces through the foam sections

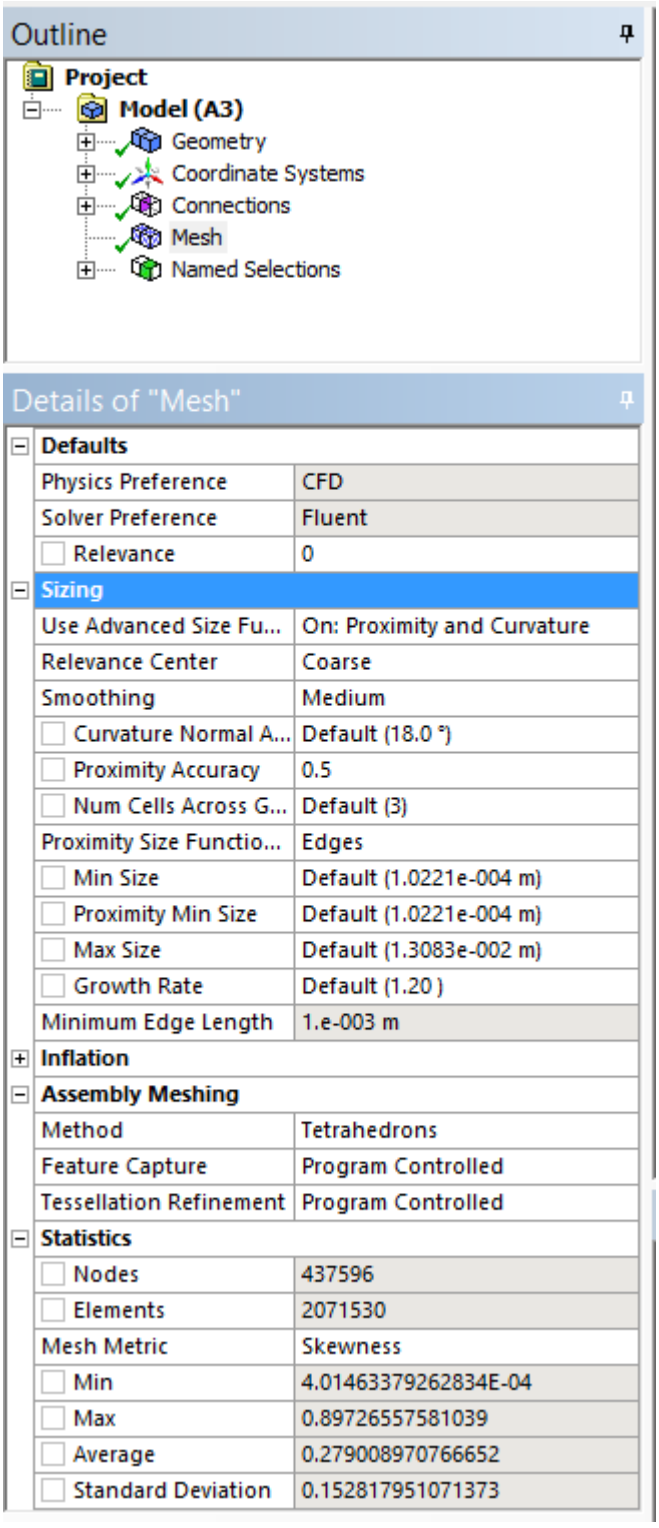

Figure D.7 The mesh properties of the fin block model

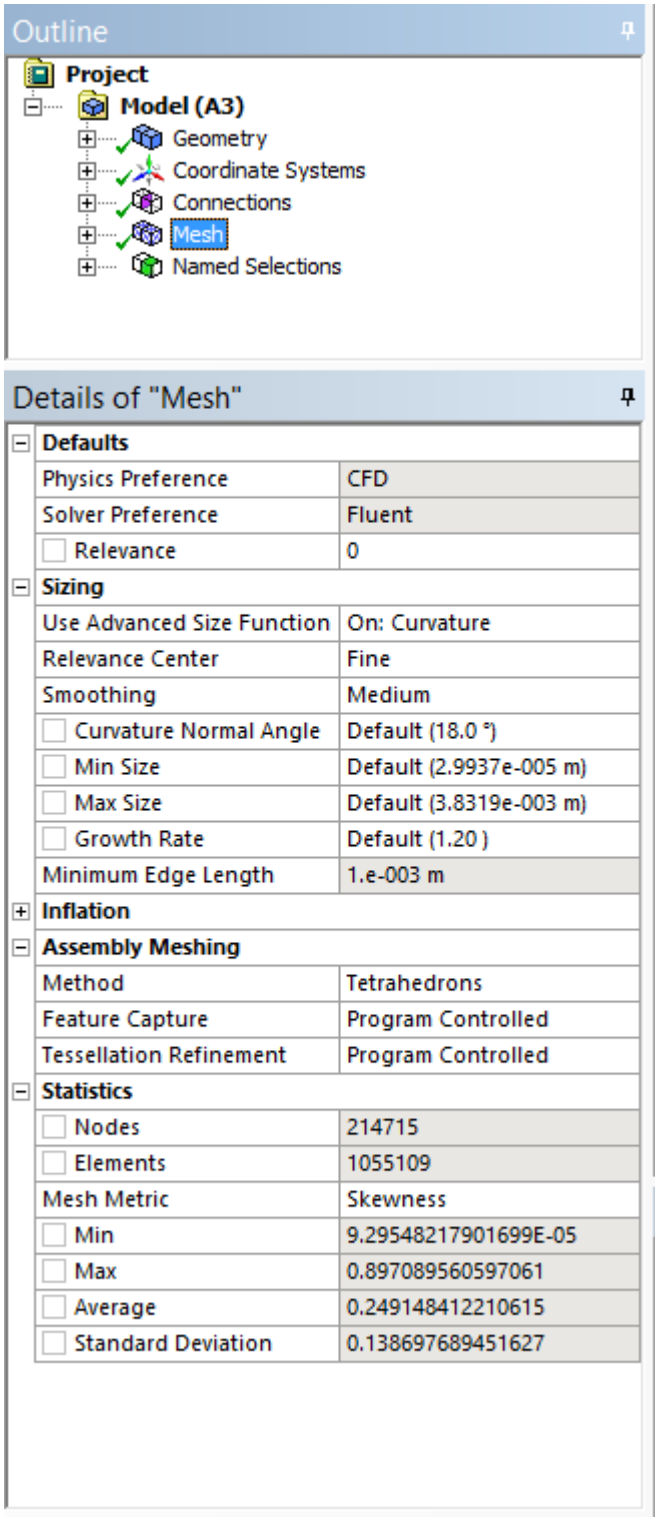

Figure D.8. The mesh properties of the foam embedded heat sink model

Commercial FLUENT Implementation Steps of the Heat Sinks

For the foam embedded heat sink both the laminar and the viscous k-epsilon turbulent models were solved in the CFD domain. The selection reason of the laminar model is the calculated Reynolds number from Mancin's study as in Table 4.6. On the other hand the reasons for the application of the viscous k-epsilon method are the literature studies and the CFD tutorials as stated in [4, 52]. Kopanidis' study suggests that the k-epsilon method stabilizes the solution and provides a reasonablly overall pressure drop. Because of the Reynolds numbers laminar flow model is selected in the fin block analysis. For all analyses energy model is turned on as in Figure D.9.

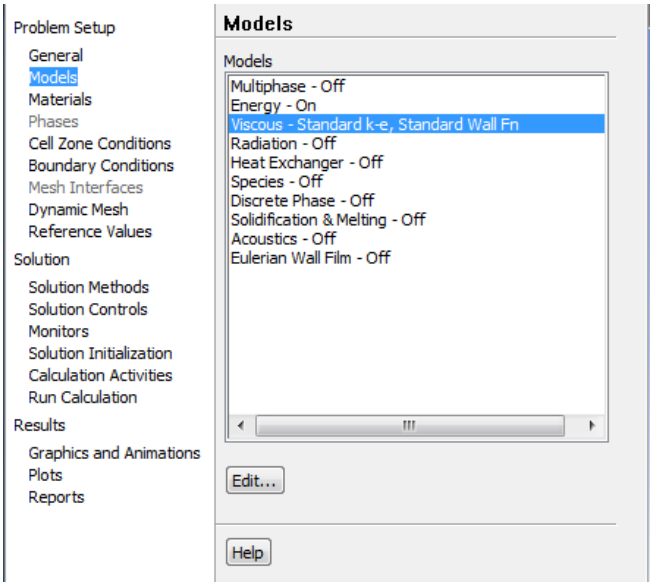

Figure D.9 Model window of CFD

At the fin block analysis, only two cell zone conditions take place. The fluid zone is assigned by air and the solid zone is assigned by the CFD software automatically. The metal foam blocks embedded heat sink model were assigned as the fluid in the geometry module. As a result, these blocks are seen as the fluid on the cell zone conditions. When the porous zone option is selected on the upper side, the bottom porous zone window is activated as seen in this Appendix. The viscous term, the inertial term, the porosity, material of the foam and the thermal model of the porous zone are imported into this window. Figure D.10 visualizes the CFD software implementation window of the viscous resistance and the internal resistance which

are calculated from Equation D.1. Similar equations with Equation D.1 are also estimated from the literature studies [24, 26].

$$R_V = \frac{1}{K} = \left[180\frac{(1-\varepsilon)^2}{\pi^2 d_{pore}^2 \varepsilon^3}\right], \qquad R_i = C = \left[3.5\frac{(1-\varepsilon)}{\pi d_{pore}\varepsilon^3}\right] \quad \text{(D.1)}$$

R_V viscous term (m^{-2})

R_i inertial term (m^{-1})

For a packed column of spheres Ergun found correlations as in Equation D.1 which is also used by commercial FLUENT software for the determination of the inertial and the viscous terms. The empirical coefficients 180 and 3.5 in this correlation depend on the properties of the specimens and the past empirical studies. Whereas the tabulated Rv(cal.) and Ri(cal.) numbers are the result of Equation D.1, Rv(exp.) and Ri(exp.) values are found from the permeability and the inertia coefficients of [24, 26]. The viscous terms of Ergun correlation are nearly 100 times lower than the empiric viscous terms, which means that the pressure gradient varies over a wide range.

Table D.1 Calculated and the empirical resistance coefficients

Samples	Porosity	Pore Dia. (mm)	Rv (cal.) (m^{-2})	Ri (cal.) (m^{-1})	Rv (exp.) (m^{-2})	Ri (exp.) (m^{-1})	k_{ef} Junc. ($W \cdot m^{-2} \cdot {}^{\circ}C^{-1}$)
10 PPI AL	0.93	2,54	1.72E+04	38.1709	5.35E+06	190	51.53
20 PPI AL	0.93	1,27	6.89E+04	76.3418	1.21E+07	240	51.53
40 PPI AL	0.93	0,64	2.76E+05	152.684	1.58E+07	342	51.53
10 PPI CU	0.905	2,54	3.44E+04	56.2162	8.26E+06	160	71.87
20 PPI CU	0.905	1,27	1.38E+05	112.432	1.89E+07	214	71.87
40 PPI CU	0.905	0,64	5.51E+05	224.865	2.44E+07	290	71.87

The calculated Rv and Ri values for the 20PPI copper foam from Table D.1 are imported to the CFD software as in Figure D.10.

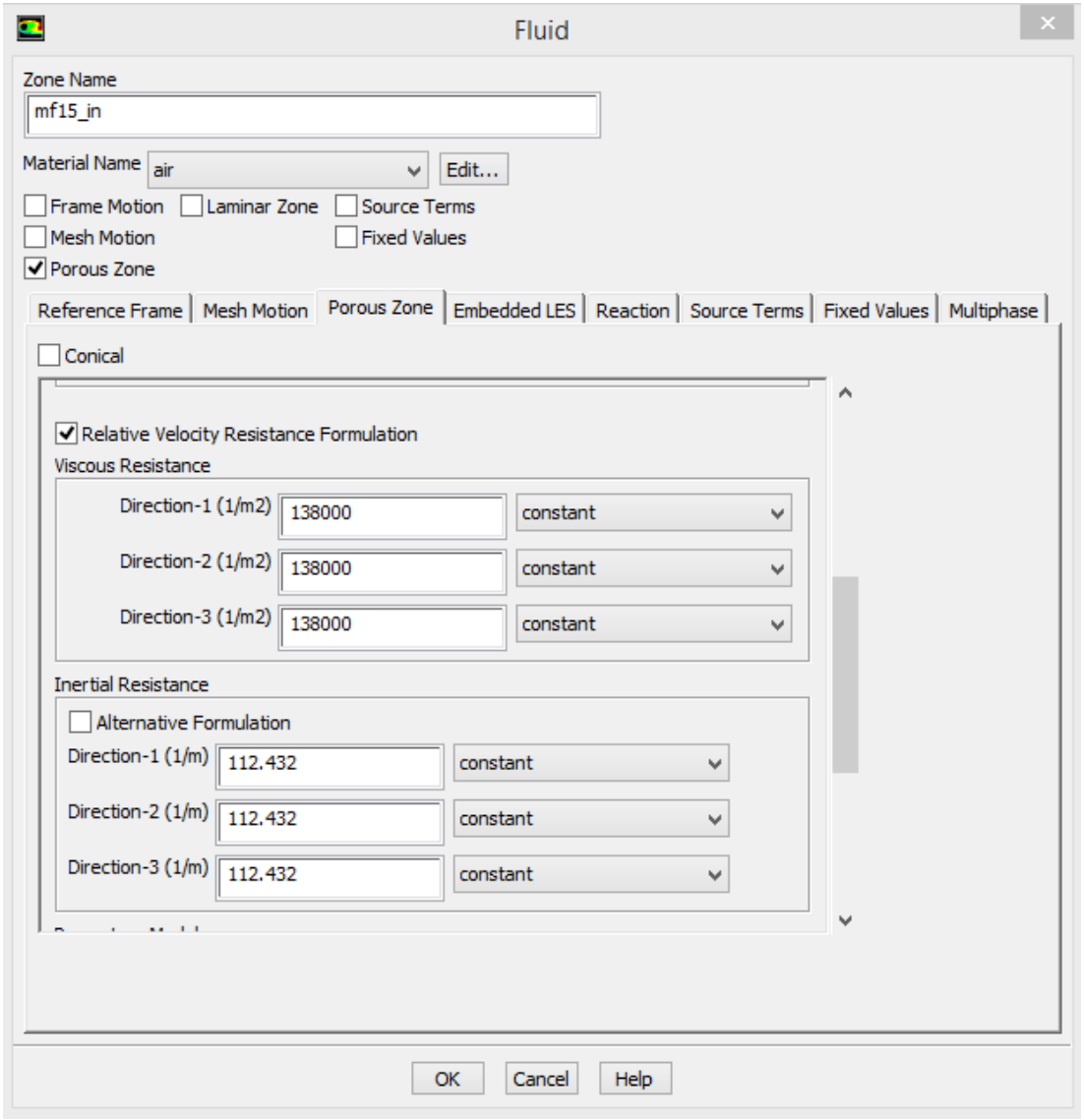

Figure D.10 Cell zone conditions window of the foam blocks

The zones of the foam embedded heat sink are defined as in Table D.2. The components of the heat sinks are named as; chasis_hs for the heat sink, solder_in for the inlet side junction part, solder_ex for the exit side junction part, airinlet for the inlet side air, airmid for middle air, airexit for the exit side air, mf 15_in for the 15 mm long metal foam at the first foam section, mf 25_in_1 for the first 25 mm long metal foam at the first foam section, mf15_out for 15 mm long metal foam at the second foam section. As it is understood from the indication of the metal foams, the number suffixes are used for the foam lengths. The **in** and **out** suffixes are used to demonstrate the first and the second foam sections of the heat sink.

Table D.2 Cell zone conditions of foam embedded heat sink

Names	Mat.	Selected Property	Imported properties of porous metal				
			Rv (m^{-2})	Ri (m^{-1})	Porosity	Solid Mat. Name	Thermal Model
mf15_in	Air	Porous Zone	1.38E+05	112.432	0.905	Copper	Equilibrium
mf20_in	Air	Porous Zone	1.38E+05	112.432	0.905	Copper	Equilibrium
mf25_in_1	Air	Porous Zone	1.38E+05	112.432	0.905	Copper	Equilibrium
mf25_in_2	Air	Porous Zone	1.38E+05	112.432	0.905	Copper	Equilibrium
mf15_out	Air	Porous Zone	1.38E+05	112.432	0.905	Copper	Equilibrium
mf20_out	Air	Porous Zone	1.38E+05	112.432	0.905	Copper	Equilibrium
mf25_out	Air	Porous Zone	1.38E+05	112.432	0.905	Copper	Equilibrium
mf25_out	Air	Porous Zone	1.38E+05	112.432	0.905	Copper	Equilibrium
solder_in	s.j.	None	No input value				
solder_ex	s.j.	None					
chasis_hs	AL	None					
airexit	Air	Laminar Zone					
airinlet	Air	Laminar Zone					
airmid	Air	Laminar Zone					

In the viscous k-epsilon turbulent model, the air zones are selected to be the laminar zones as stated in Table D.2. s.j. presents the defined solder junction material in Chapter 6.1.3. When the laminar model option is selected, the laminar zone option at the cell zone does not appear as in Figure D.11.

The boundary conditions of the fin block model are demonstrated in Table 6.4. Inasmuch as the velocity values are varied as 4 m/s and 6 m/s, heat fluxes are imported as in Table 6.1. For the partial heater analyses, heating surfaces are divided into two different surfaces so that the heat fluxes to be imported separately. Even though, the air velocity was measured two and a half centimetre away from the inlet of heat sinks, these measurements were imported into the commercial FLUENT software with those values. The outlet of the model was given zero gauge pressure and the remaining surfaces were assigned as “wall”. The commercial FLUENT software automatically assigns the interior fluid and solid parts as seen in Figure D.12. The boundary surfaces of fin block model are shown in detail in Figure D.3 and Figure D.4.

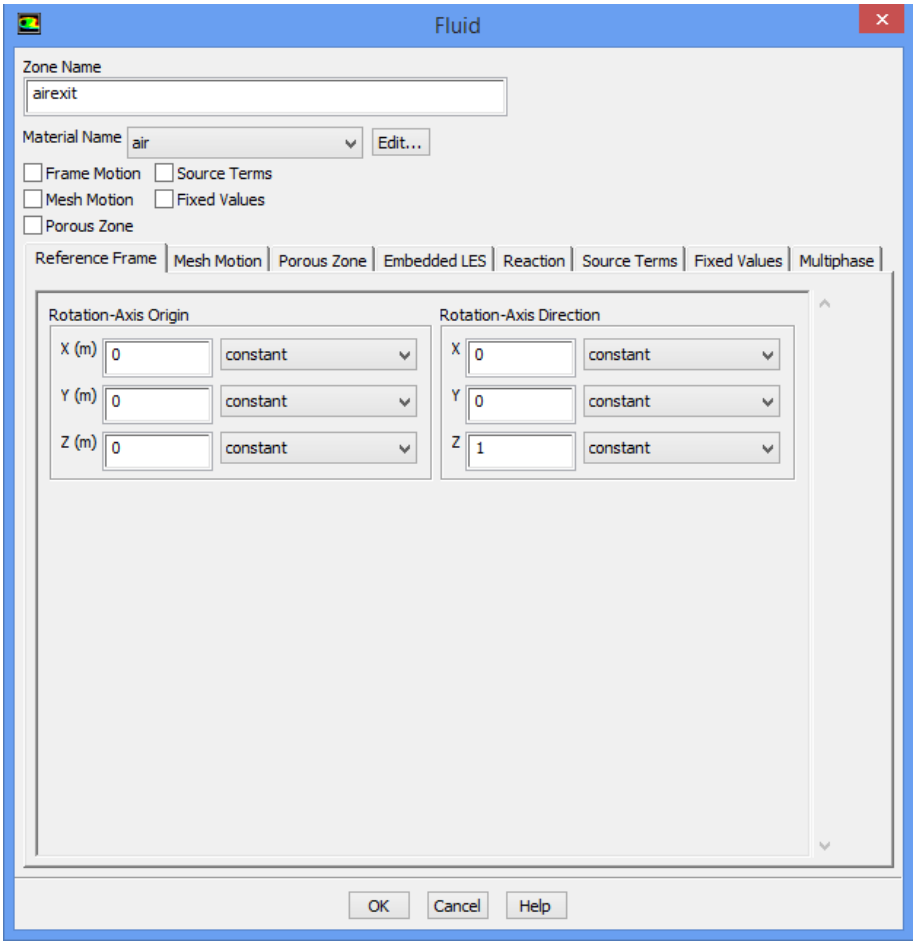

Figure D.11 Air cell zone window of foam embedded heat sink at laminar model

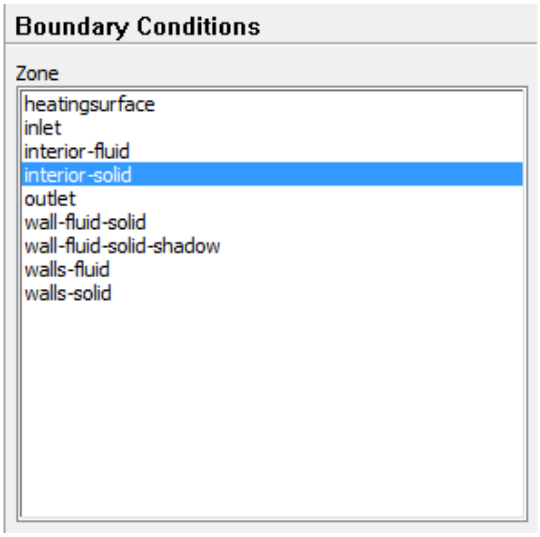

Figure D.12 Boundary condition window of the fin block on the CFD software

Table D.3 Boundary conditions of the fin block

Names of Zones	Type	Thermal
Inlet	velocity-inlet	temperature
Outlet	pressure-outlet	Gauge Pressure
Heating surface	wall	Heat Flux
Walls	wall	isolated
Interior	Interior	No input value

Because of the structure of the model, the CFD software assigns the interior porous medium and the wall boundaries as shown in Figure D.13. The assigned boundary conditions of the foam embedded heat sink are mostly similar to the fin blocks shown in Table D.4. The boundary conditions defined at the outer surfaces of the heat sinks at the mesh module are wall boundary conditions selected by software automatically. This means that no heat transfer takes place on the outer surfaces of the CFD model.

Table D.4 The boundary conditions of the foam embedded heat sink at a partial heater scenario

Names of Zones	Type	Thermal
Inlet	velocity-inlet	temperature
Outlet	pressure-outlet	Gauge Pressure
Heating surface1	wall	Heat Flux
Heating surface2	wall	Heat Flux
Walls	wall	isolated
Interior	Interior	No input value

CFD solves the porous zones with a coupled method which was selected from solution method window of the software as in Figure D.14 [52]. For this analysis, the initial condition was the inlet velocity, which is entered into the solution initialization part with a standard initialization option. The number of the iterations is arranged from the run calculation compartment of the CFD.

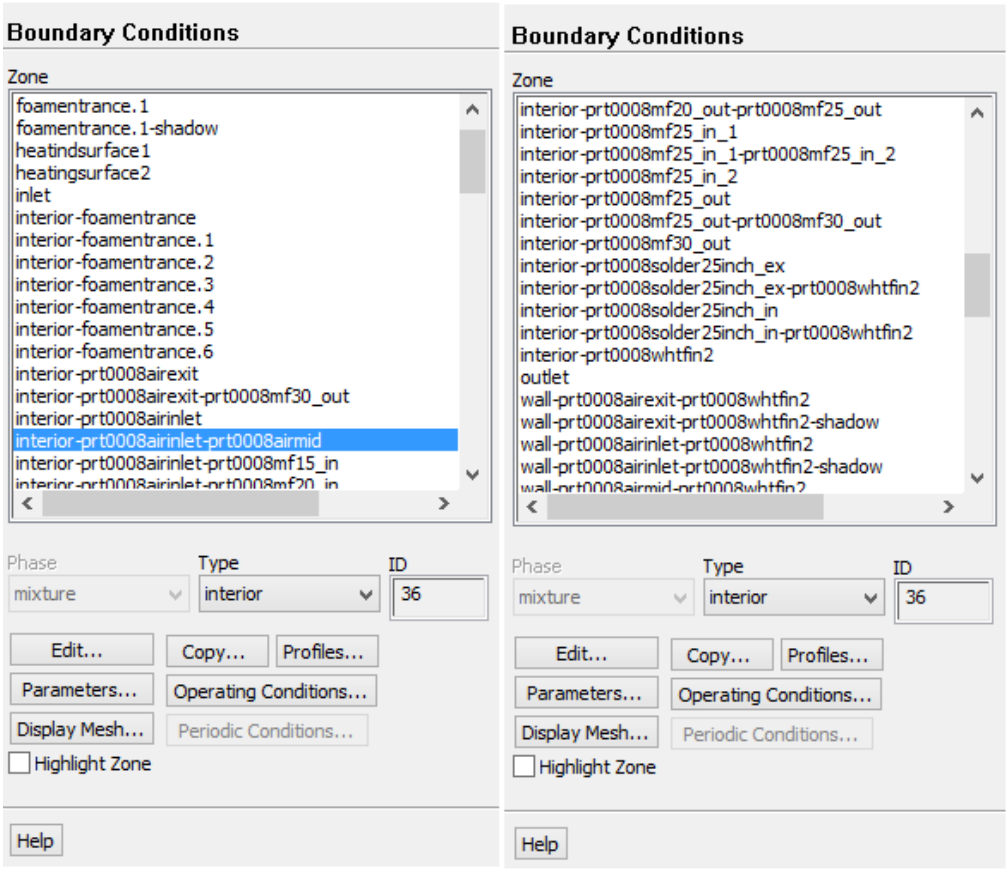

Figure D.13 The boundary condition window of the 20PPI foam embedded heat sink at the 120 W partial heaters

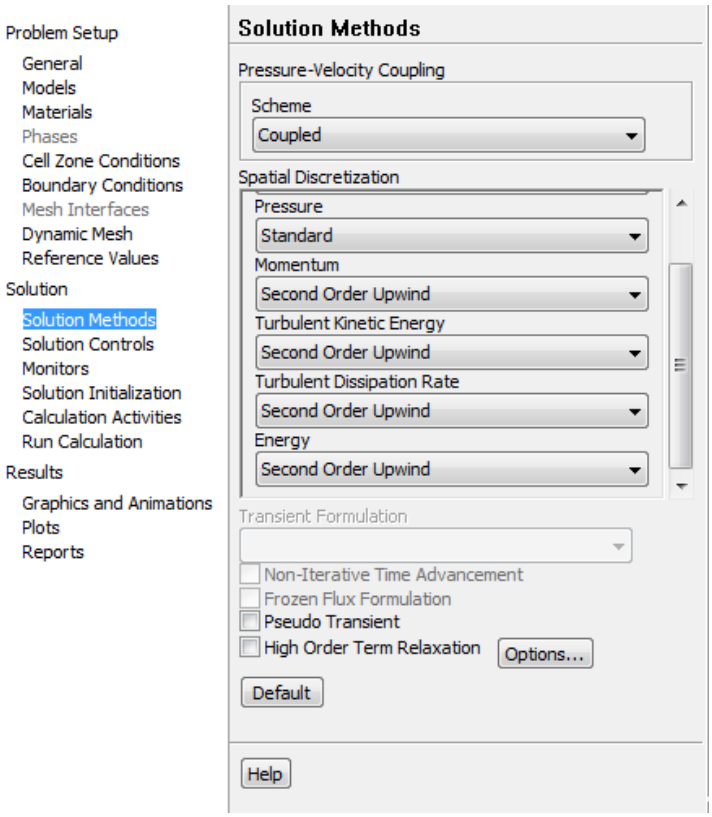

Figure D.14 The solution method window of the foam embedded heat sink on CFD

The post process operations of the analyses that are used to plot the temperature disturbance at the thermocouples level and presenting the temperature distribution at the desired sections, are controlled from the results compartment of the software.

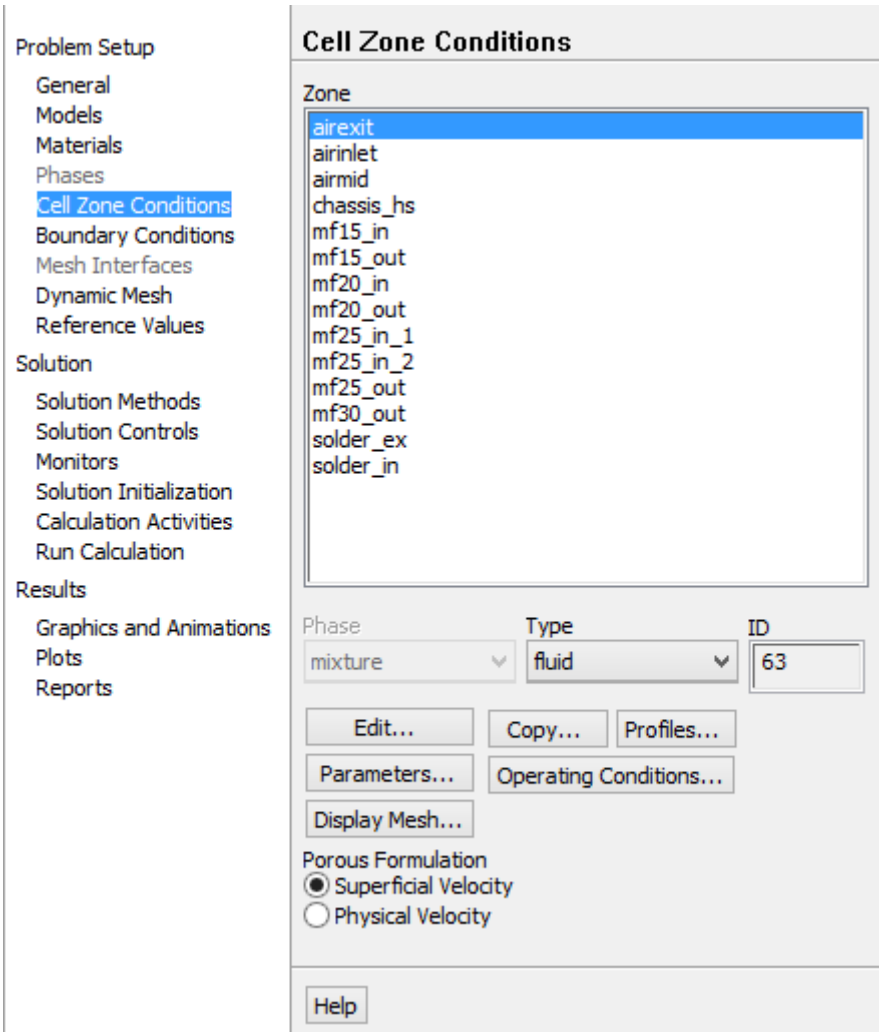

Figure D.15 The cell zone conditions of the foam embedded heat sink

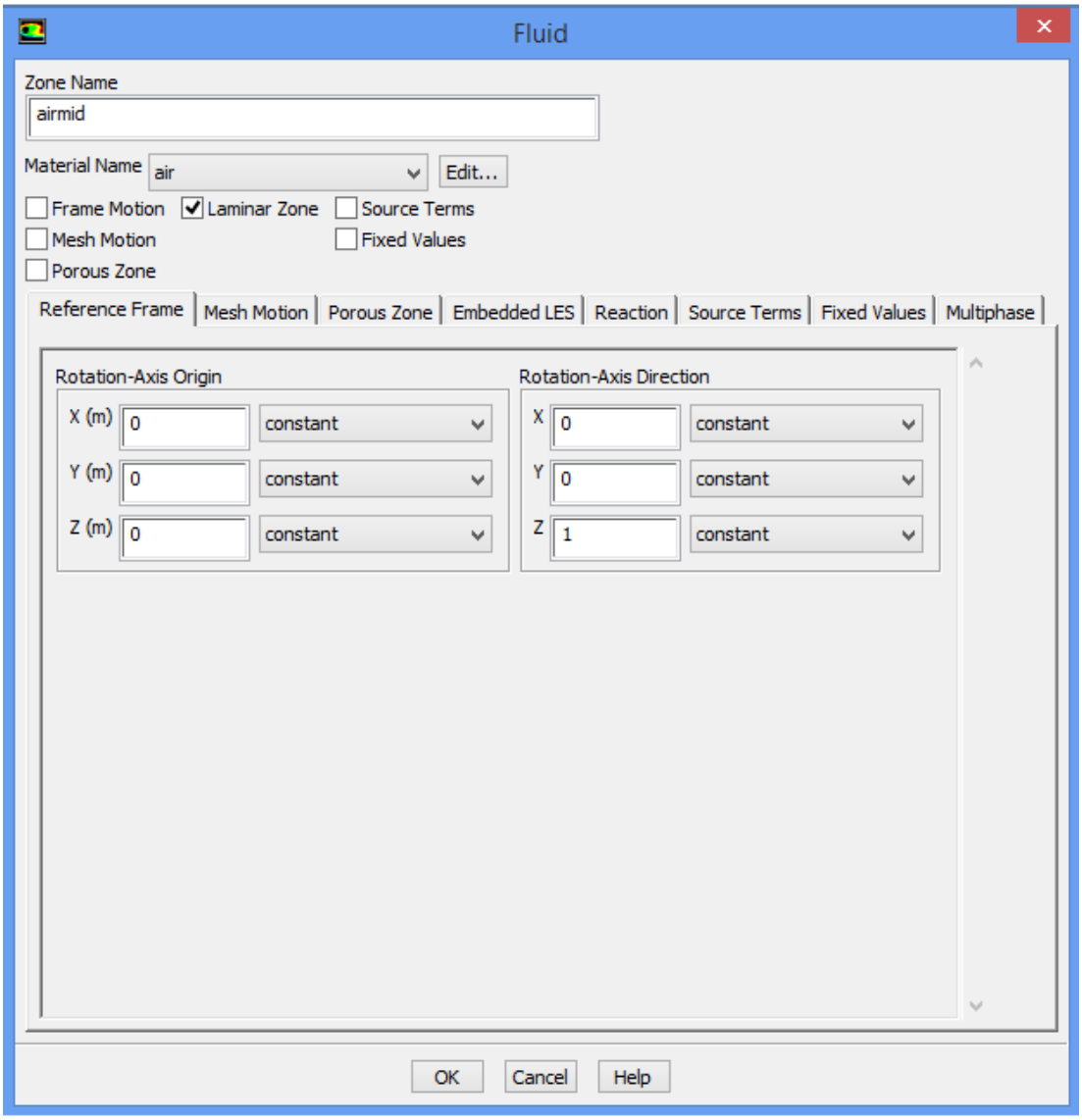

Figure D.16 The laminar zone selection of the foamless zones of model

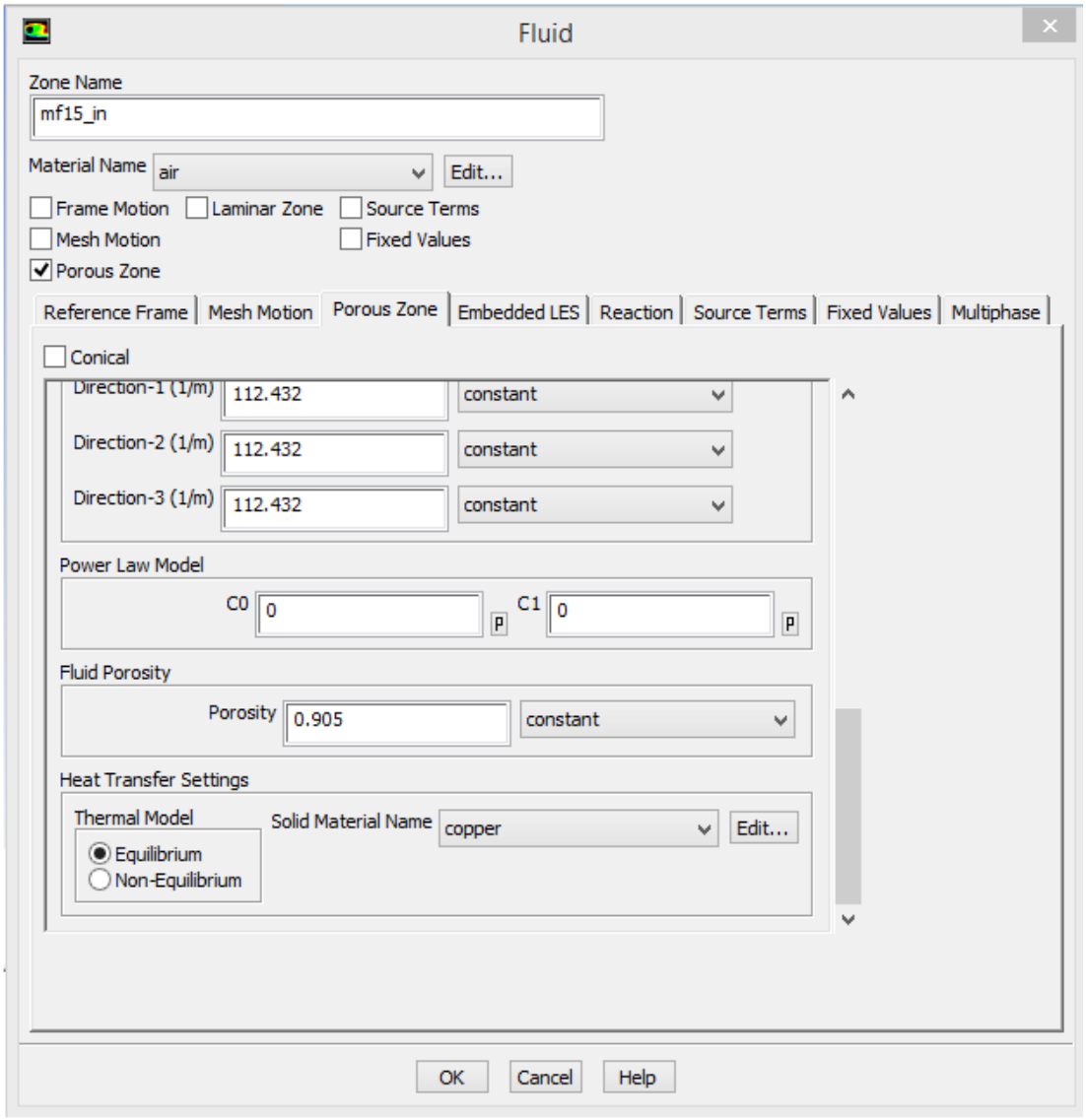

Figure D.17 CFD porous zone porosity and material importing window

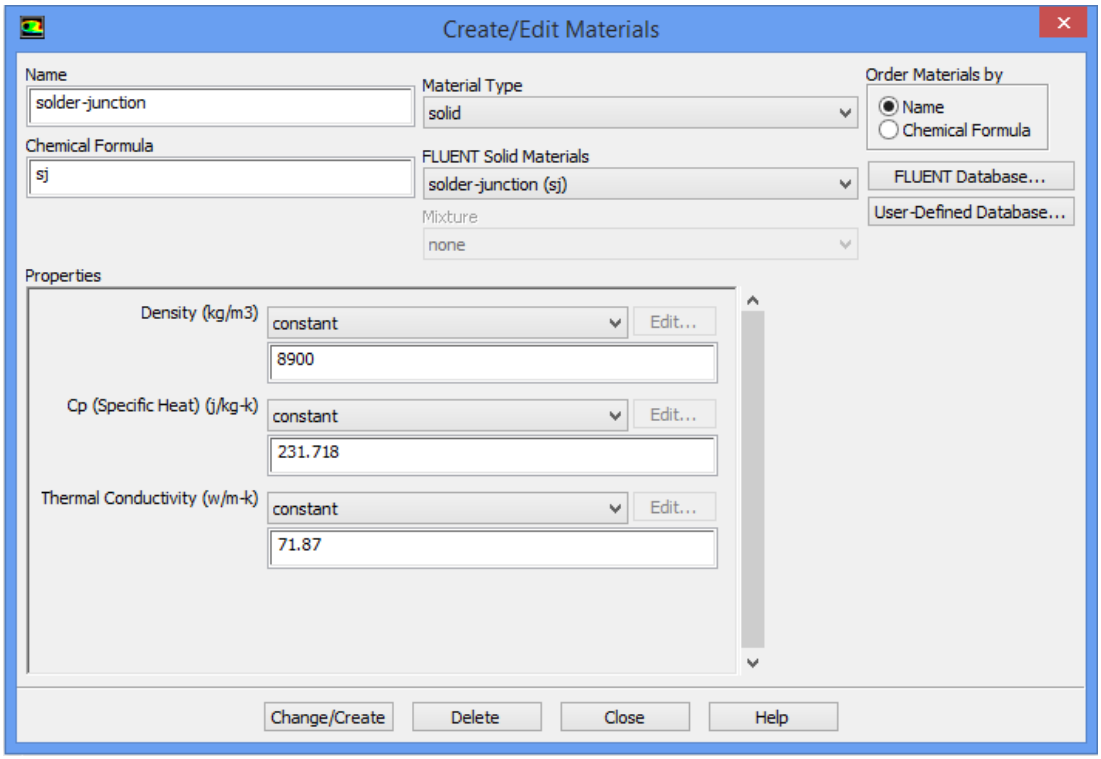

Figure D.18 New material adding window for solder junction zones

CFD Result of the Fin Block

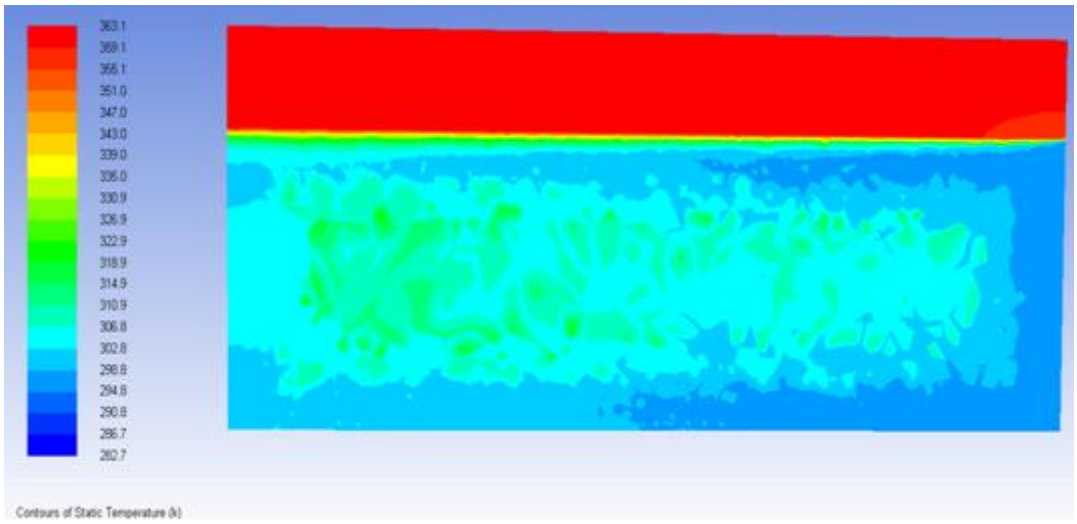

Figure D.19 The lateral half section (y direction) view temperature disturbance of the fin block at the 160 W heater and 6 m/s air Velocity

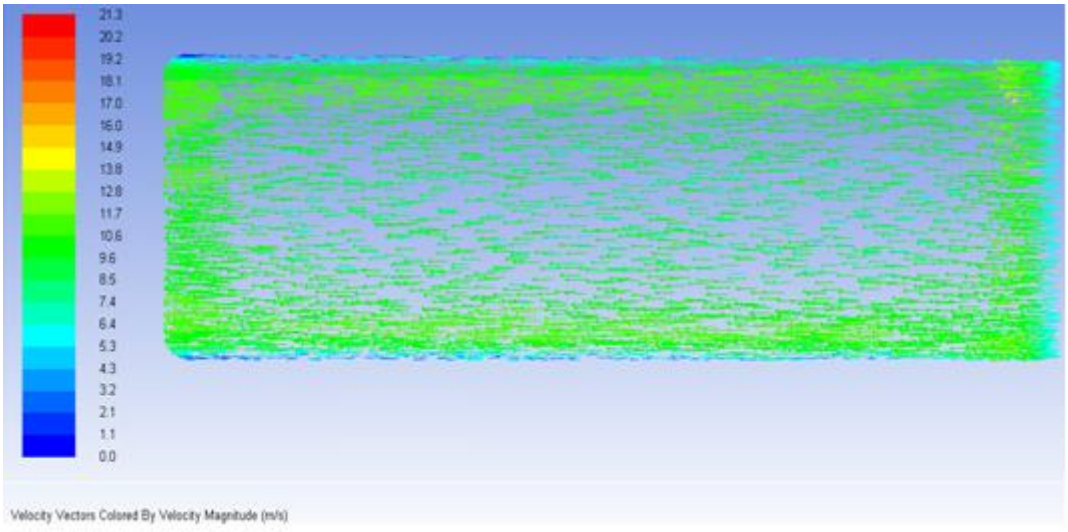

Figure D.20 The lateral section (y direction) view of the velocity vectors of air into the fin block at 6 m/s air velocity

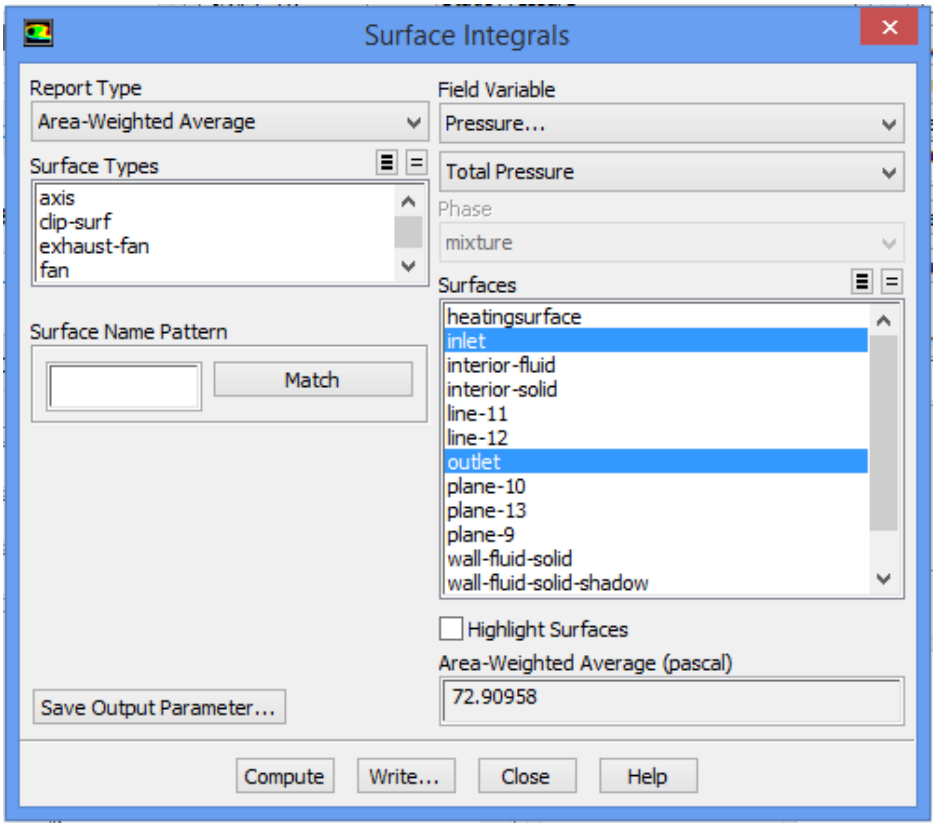

Figure D.21 The pressure drop screen of the fin block at 6 m/s air velocity

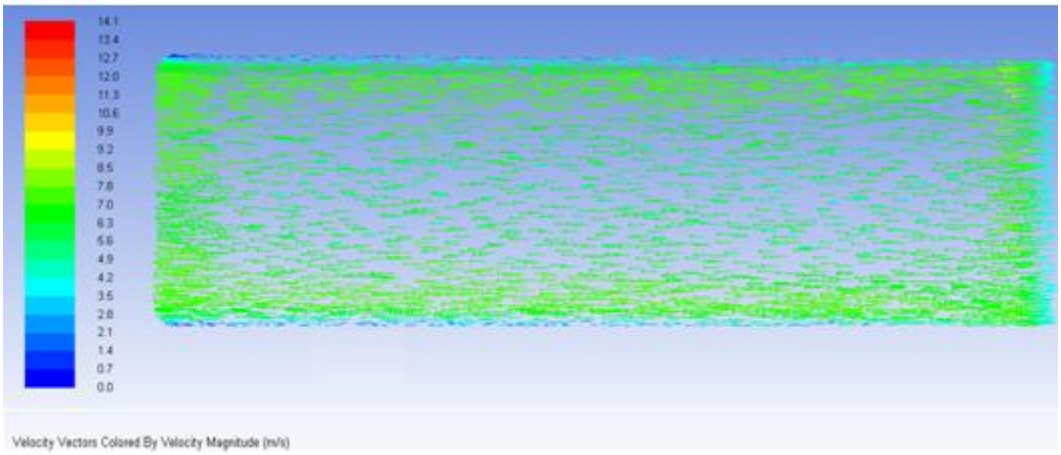

Figure D.22 The lateral section (y direction) view of the velocity vectors of air into the fin block at 4 m/s air velocity

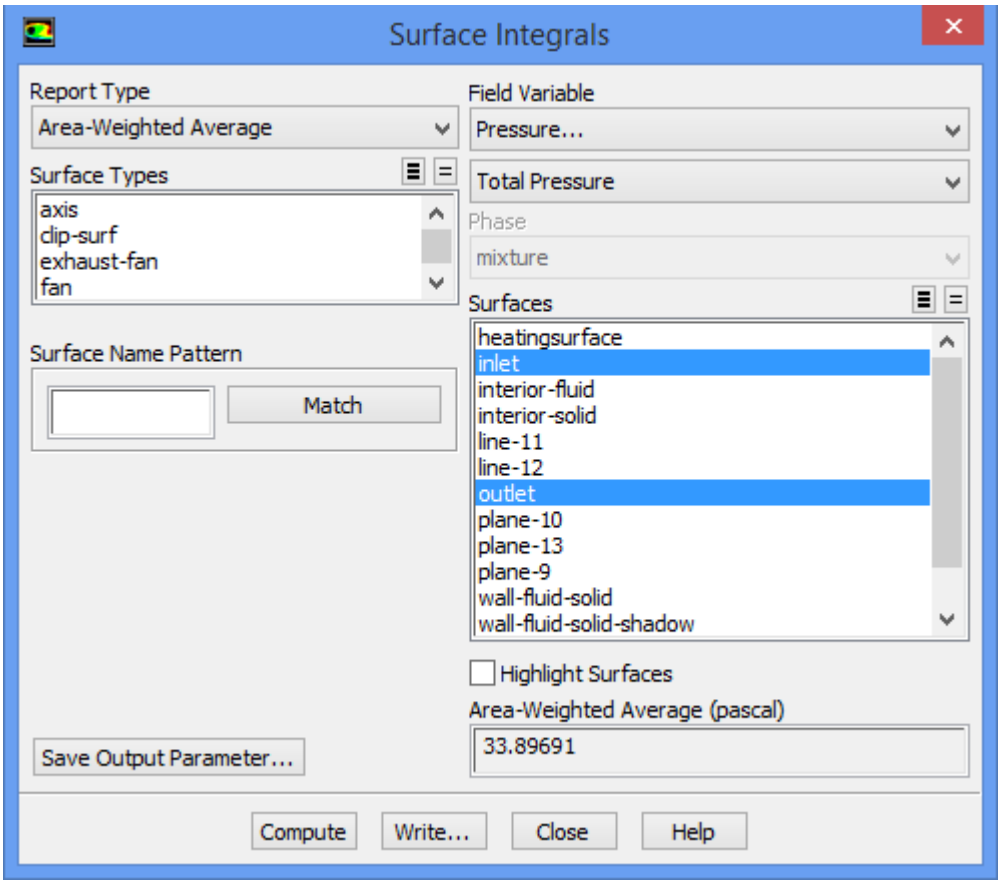

Figure D.23 The pressure drop screen of the fin block at 4 m/s air velocity

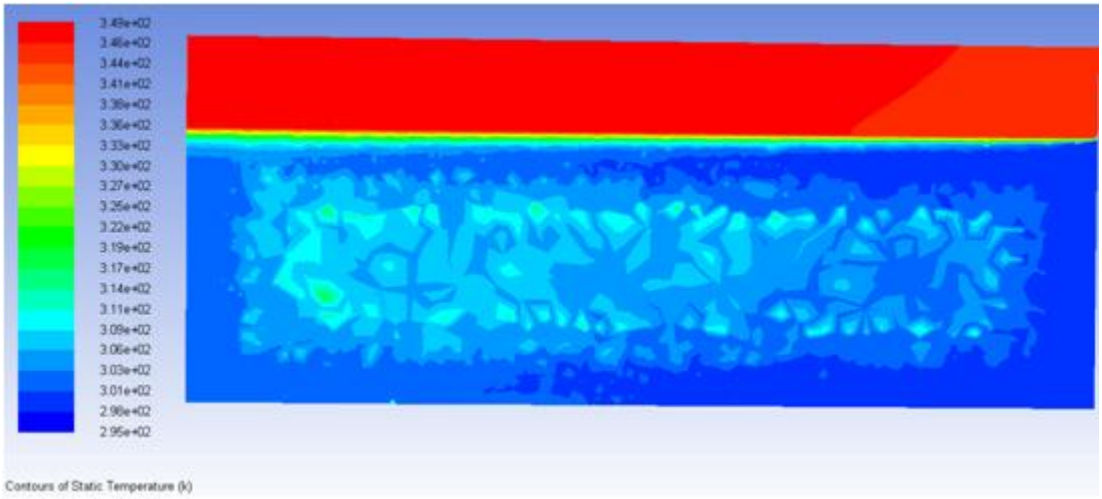

Figure D.24 The lateral half section (y direction) view temperature distribution of the fin block at 120 Watt two section heater and 6 m/s air velocity

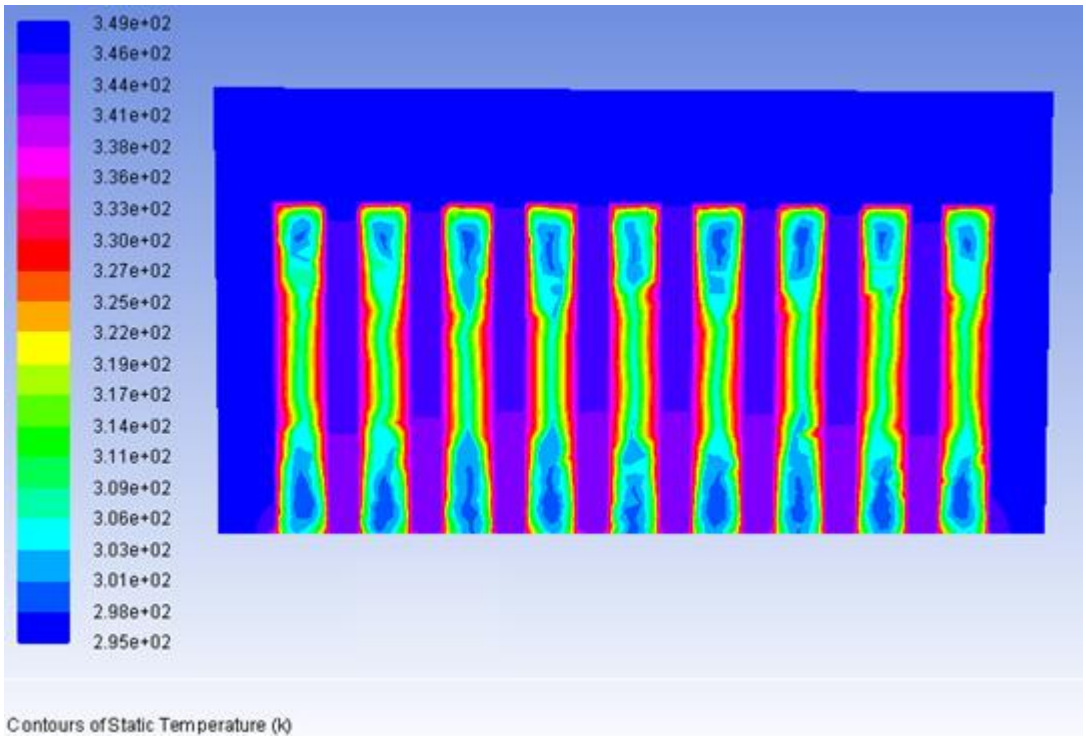

Figure D.25 The vertical half section (y direction) view temperature distribution of the fin block at 120 Watt two section heater and 6 m/s air velocity

CFD Result of the 20 PPI CU Foam Embedded Heat Sink

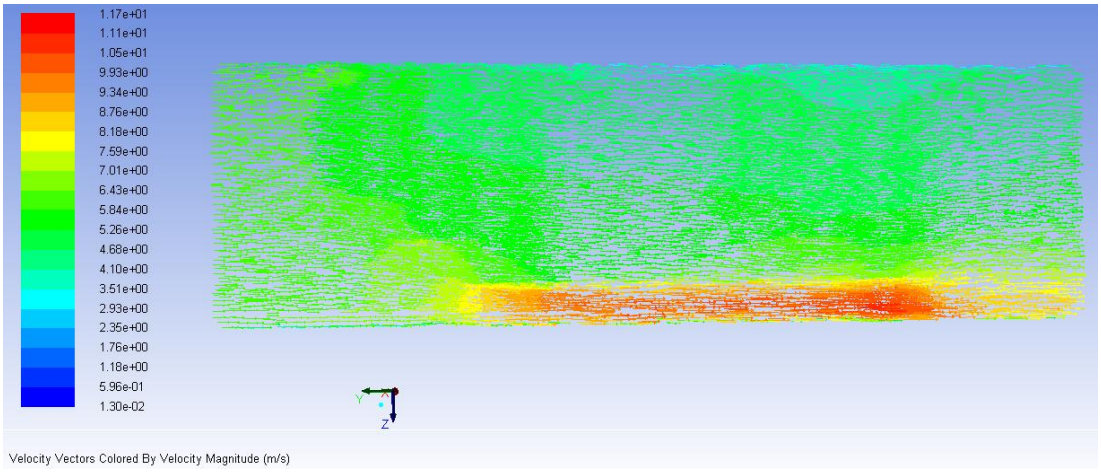

Figure D.26 The velocity vectors at the lateral half section (y direction) view of the 20 PPI CU embedded heat sink at 6 m/s air velocity and the viscous k-epsilon turbulent model solution

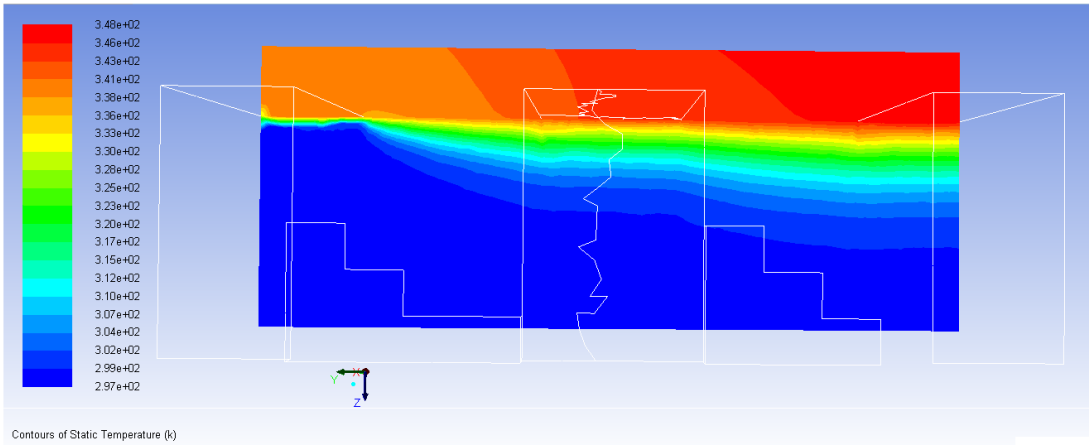

Figure D.27 The lateral half section (y direction) view temperature distribution of the 20 PPI CU embedded heat sink at the 160 W whole heater and 6 m/s air velocity at the laminar model solution

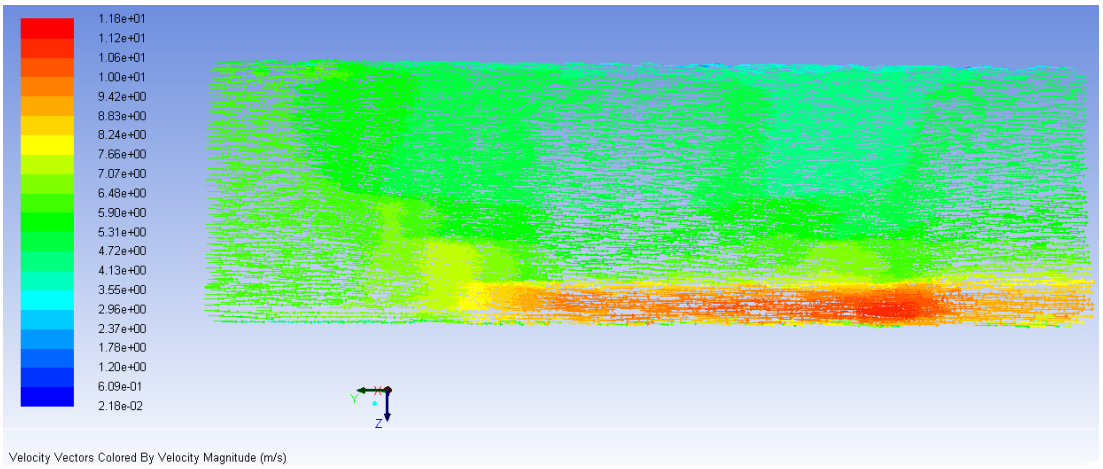

Figure D.28 The velocity vectors at the lateral half section (y direction) view of the 20 PPI CU embedded heat sink at 6 m/s air velocity and at the laminar model solution

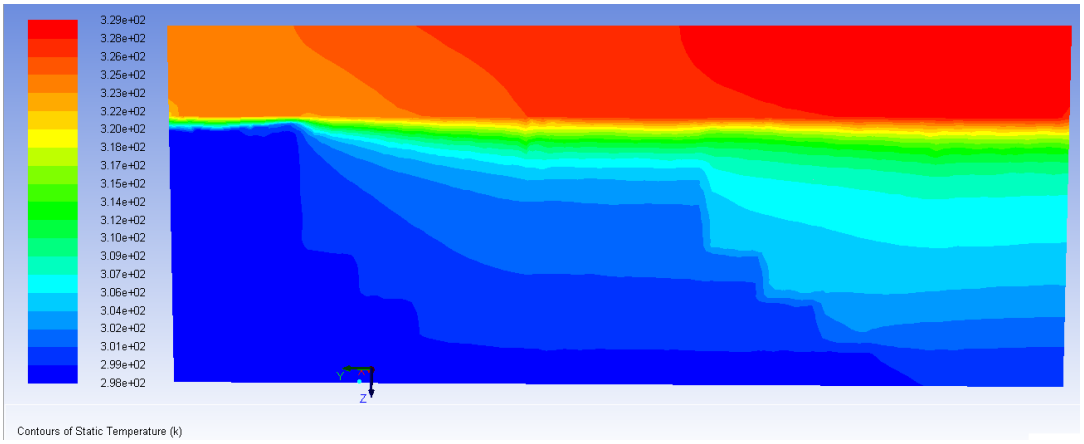

Figure D.29 The lateral half section (y direction) view temperature distribution of the 20 PPI CU embedded heat sink at the 120 W partial heater and 6 m/s air velocity at the k-epsilon turbulent model solution